



University of Copenhagen
Niels Bohr Institute

Investigating the morphologies of stars, gas and dust in star-forming galaxies at cosmic noon

Ditlev Frickmann, Francesca Rizzo & Sune Toft

Master's thesis



DAWN

Investigating the morphologies of stars, gas and dust in star-forming galaxies at cosmic noon

Master's thesis
October, 2022

By
Ditlev Frickmann

Copyright: Reproduction of this publication in whole or in part must include the customary bibliographic citation, including author attribution, report title, etc.

Cover photo: The Carina Nebula
by NASA, ESA, CSA, and STScI
<https://www.nasa.gov/webbfirstimages>


Published by: University of Copenhagen, Faculty of Science, Niels Bohr Institute
Jagtvej 155A, 2200 København, Denmark
<https://nbi.ku.dk/>

Approval

This thesis has been prepared over nine months at the Niels Bohr Institute at the Faculty of Science at the University of Copenhagen, UCPH, in partial fulfilment for the degree Master of Science in Physics, MSc Physics.

It is assumed that the reader has a basic knowledge in the areas of astronomy and astrophysics.

Ditlev Frickmann - rjs495



.....
Signature

Mon 31 Oct

.....
Date

Abstract

We compare the morphologies of dust, molecular gas, and stars in 30 star-forming galaxies at $0.5 \lesssim z \lesssim 3.5$, selected from the Atacama Large Millimetre/submillimetre Array (ALMA) archive of CO, [CI] and [CII]. Using public photometric catalogues, we perform spectral energy distribution fitting to recover their stellar masses and star formation rates, and we classify 27 of the galaxies in our sample according to the main sequence relation at their respective redshifts. About 37% of our sample lie ≥ 0.6 dex above the main-sequence, and we classify them as starburst galaxies. We classify the remaining galaxies in our sample as main sequence galaxies. We analyse spatially resolved ALMA and Hubble Space Telescope (HST) data to study how the morphologies and sizes of our sample changes as a function of wavelength. We use sub-arcsecond ALMA observations of CO, [CI] and [CII] line emission to probe the molecular gas, and we extract the dust continua from the spectral cubes. We have auxiliary sub-arcsecond observations in rest-frame near-infrared to near-ultraviolet from HST, probing the stellar population. We find that the the gas line emission and dust continuum emission have similar spatial extents, which is consistent with the commonly adopted assumption that the dust continuum traces the underlying molecular gas. We find that the stellar emission is more extended than the gas line emission and the dust continuum by a factor of $1.61_{-0.72}^{+1.04}$ and $1.61_{-0.43}^{+0.55}$ respectively. However, we find that the relative extent of the stellar emission to that of the gas line emission is very sensitive to the gas conditions probed by the emission line. Specifically, we find that the stellar emission is more extended than the emission coming from CO(2-1) and CO(3-2) by a factor of $1.11_{-0.30}^{+0.24}$ and $2.07_{-0.22}^{+1.09}$ respectively. Finally, for the stellar emission, gas line emission and dust continuum, we find no systemic trends in the relative shape of the Sérsic surface brightness profiles with respect to their degree of central concentration, given by the Sérsic index.

Acknowledgements

The nine months of writing this thesis has been intriguing, passionate and educational, but it has also been stressful, and at times, lonely. I could not have undertaken this journey without the help of some of the most brilliant, patient and committed people, that I have had the good fortune of becoming acquainted with.

I cannot begin to express my thanks to **Francesca Rizzo**, PhD, without whom, this thesis would not have been possible. Not only does her research lay out the foundation for this thesis, she has gone beyond and above with her unwavering support and guidance at every step of the way. There is not a section or result in this thesis, that she has not provided invaluable advice for. Finally, she has provided a great deal of encouragement and an astronomical amount of patience, that cannot be underestimated.

I am deeply indebted to **Vasily Kokorev**, PhD, and I would to extend my sincere thanks. He has been instrumental for the success of the SED fitting, which utilises his tool, STARDUST. He has gone above and beyond by providing unrelenting support and very helpful advice.

I would like to extend my deepest gratitude to **Gabriel Brammer**, PhD, who not only provided the HST mosaics, but also practical suggestions for analysing them. Additionally, he has been generous with his invaluable insight into SED fitting and stellar population templates.

I would like to express my deepest appreciation to **Francesco Maria Valentino**, PhD, whose door was always open. Remarkably, he has an unparalleled insight into any topic in astronomy and astrophysics, that I could not wrap my head around, and he has been very patient and eager to teach.

I am also grateful to **Georgios Magdis**, PhD, who provided valuable resources and insight into the $\langle U \rangle - z$ relation, and helpful advice to create meaningful assumptions.

Additionally, I would like to acknowledge the assistance of **Kasper Elm Heintz**, PhD, for providing resources concerning the gas and dust in the ISM.

Finally, I would like to thank my **friends, family** and **Fatimah**, for the tremendous amount of emotional support and the unparalleled encouragement, that they have extended to me. Without their unconditional love, astounding patience and monumental belief in me, I could never have dreamt of finishing this thesis.

Thank you.

This thesis has made use of the Spanish Virtual Observatory project funded by MCIN/AEI/10.13039/501100011033/ through grant PID2020-112949GB-I00.

This thesis has made use of the VizieR catalogue access tool, CDS, Strasbourg, France (DOI : 10.26093/cds/vizieR). The original description of the VizieR service was published in 2000, A&AS 143, 23.

Contents

Preface	ii
Abstract	iii
Acknowledgements	iv
1 Introduction	1
1.1 Galaxy formation in the Λ CDM Model	1
1.2 Baryons in Galaxies	2
1.2.1 Stars	2
1.2.2 The Interstellar Medium	2
1.3 Heating and Cooling of the ISM	4
1.4 Interstellar Heating Sources	4
1.5 Cooling of the ISM	6
1.5.1 Dust	9
1.6 Observations of Galaxies	13
1.6.1 The Initial Mass Function	14
1.6.2 Spectral Energy Distribution	14
1.6.3 Star Formation Rate Indicators	16
1.6.4 Galaxy Morphology	17
1.7 High Redshift Galaxies	18
1.7.1 Evolution of the Main Sequence	19
1.7.2 Evolution of the Mass-Size relations	21
1.7.3 Compact Molecular Gas Reservoirs	22
1.8 This Thesis	24
2 Sample	25
2.1 Photometry	26
2.2 Spatially Resolved Images	27
2.2.1 HST	27
2.2.2 ALMA	28
3 Methods & Analysis	32
3.1 SED fitting	32
3.1.1 Stardust	32
3.1.2 Fitting	34
3.2 Analytical Surface Brightness Profiles	35
3.2.1 Galfit	36
3.2.2 Data Preparation	36
3.2.3 Fitting	42
3.3 F-test for Additional Parameters	43
4 Results & Discussion	45
4.1 Indicative case	45
4.2 SED-Fitting	46
4.3 Surface brightness profiles	49
4.4 Discussion	53
5 Conclusion	59

References	61
Acronyms	68
Glossary	69
A HST Filters	70
B Extra Transmission Filters	71
C Datasheets	77
D Statistical Analyses	169
D.1 Spearman’s Rank Order Correlation	169
D.2 Monte Carlo Method	170

1 Introduction

Only a century ago, Edwin Hubble discovered these so-called “*island universes*” distributed across the entire sky and far beyond our Milky Way. Today we know, that galaxies are islands of stars, gas and dust that acts as fundamental building blocks of our Universe. However, for most of the last century, our study of galaxies has been limited to those in the nearby Universe. Albeit, we have developed a great understanding of the galaxies around us, the evolution of galaxies across cosmic time has been left to conjecture.

That is, until the 90’s with the launch of the Hubble Space Telescope (HST) providing sub-kilo-parsec resolution of galaxies billions of light years away. Probing observations with HST have opened up the early Universe, the undiscovered land of the Cosmos, in a way no other telescope had done or could have done. With HST we have gained a significant understanding of how the stellar population of galaxies evolve across cosmic time. However, auxiliary observations of galaxies targeting the dust and gas component has been challenging, and thus the complete picture has eluded us.

That is, until the Atacama Large Millimetre/submillimetre Array (ALMA) became fully operational in 2013. It allows us to study the missing parts, and to empirically test or formulate complete theories of cosmic evolution of galaxies. Recently, we have discovered that distant galaxies, at redshift $\sim 2 - 3$, produced stars at a rate that is tremendous compared to their present-day counterparts, and that the Star Formation Rate (SFR) has been steadily decreasing since then. This period of cosmic time is now commonly known as the cosmic noon. Furthermore, with the onset of sub-kilo-parsec resolution imaging of gas and dust in galaxies across the cosmic noon, we can now gain insight into the physical mechanisms shaping galaxies at important cosmological epochs.

1.1 Galaxy formation in the Λ CDM Model

The present day Universe, as described by the Λ Cold Dark Matter (Λ CDM) cosmological model, consists of $\sim 70\%$ dark energy, $\sim 25\%$ Cold Dark Matter (CDM) and $\lesssim 5\%$ baryonic matter. Baryonic matter is the *regular* type of matter, that we all know of. It makes up our bodies, the air that we breathe, the sun that we depend on, and so on. Additionally, it bends space-time, causing the effects of gravity, it interacts with electro-magnetic radiation, allowing us to observe it, and it interacts with itself through pressure. However, from observations of the gravitational effects of matter in our Universe, it has become clear, that the baryonic matter only makes up about 20% of the matter content of our Universe. Thus, a CDM component has been postulated to make up the remaining 80% of the matter. Similarly to baryonic matter, it bends space time around it, causing the effects of gravity. However, it is dark, meaning that it interacts weakly with baryonic matter and itself, such that it in essence is pressureless. Moreover, it does not interact with electromagnetic radiation, meaning that we cannot observe it directly. Additionally, it is cold, meaning that it moves slowly with respect to the speed of light.

If we go back in time, to immediately after the Big Bang, the Λ CDM model postulates that the Universe was a hot and dense fluid of coupled photons, baryons and CDM. It is known as the initial primordial density field, and in the hierarchical structure formation scenario, galaxies and large scale structures are thought to form from the overdensities of the field ([Kravtsov and Borgani 2012](#)). During the inflationary paradigm, quantum fluctuations of the field grew to macroscopic sizes. The resulting field is usually modelled as an isotropic Gaussian random field.

As the Universe kept expanding, the density of the radiation field decreased, and eventually the matter component decoupled from the radiation field. At that point in time, the CDM dominated the

expansion history of the Universe, and the baryonic matter fell freely into the CDM overdensities. Eventually, the CDM overdensities began to evolve non-linearly and collapsed into haloes, which are an approximately stable state in which the random motions of the constituents balance out gravity. Structures continued to grow in a bottom-up scenario, i.e. small haloes form first and merge into ever larger haloes (Joachimi et al. 2015).

As a CDM halo grows, so does its gravitational potential. In turn, baryonic matter accretes in to the gravitational well. As conditions evolve, the baryonic matter collapses into stars and gas clouds, which make up the early galaxies.

1.2 Baryons in Galaxies

The three major components of a galaxy's observational characteristics, are stars, gas and dust. The interplay between these components define the intrinsic Spectral Energy Distribution (SED) emitted by the galaxy, but the components also form, grow or change due to each other. Stars form from the molecular gas, which is shielded by the dust. When massive stars die, they enrich the Interstellar Medium (ISM) with heavier species, changing the observational characteristics. Additionally, the Ultraviolet (UV) radiation emitted by stars break apart dust and molecules and ionises atoms.

1.2.1 Stars

Stars form from the gravitational collapse of dense cores in molecular clouds (Stahler and Palla 2004). They are essentially factories for converting hydrogen into richer species in turn for hydrostatic equilibrium. Newly formed protostars evolve onto the main sequence of stars on the Hertzsprung-Russel (HR) diagram main sequence, and are in turn referred to as Zero Age Main Sequence (ZAMS). Stars on the main sequence convert hydrogen into helium, and their time on the main sequence is referred to as their lifetime. The more massive the star is, the more pressure is applied to its core. In turn, the density and temperature of the core is higher. Consequently, the thermonuclear fusion reaction is effective to a greater degree, which in turn means, that the star empties its reservoir of core-hydrogen quicker. As a result, more massive stars have shorter lifetimes. In essence, the evolutionary track of stars are set by their mass.

Additionally, the more heat that the star produces in the core, the more heat is transported to the surface and radiated away. As a result, the temperature and the spectrum of the star also changes. Stars approximately emit as black-bodies, according to Planck's law. In Fig. 1.1 we explore how the spectrum of a black-body changes with surface temperature. It is evident that warmer stars, corresponding to more massive stars, emit at shorter wavelengths. Additionally, they also emit more energy, than their low mass counterparts. This is expected, since they produce more energy from thermonuclear processes in their cores. Additionally, it is apparent that the radiation emitted by stars primarily set the shape of the UV and optical part of the SED. However, stars also indirectly affect the rest of the galaxy spectrum, due to being the most dominant source of heating for the ISM.

1.2.2 The Interstellar Medium

The ISM is a complex medium that consists of interstellar gas in a number of different phases and interstellar dust. In the following section, we describe the detailed properties of the ISM, mainly based on studies of local star-forming galaxies. A schematic of the ISM is illustrated in Fig. 1.2. As is evident from the schematic, there are four dominant phases of interstellar gas with different properties.

1. HII-regions and the Warm Ionized Medium (WIM)
2. The Warm Neutral Medium (WNM)
3. The Cold Neutral Medium (CNM)

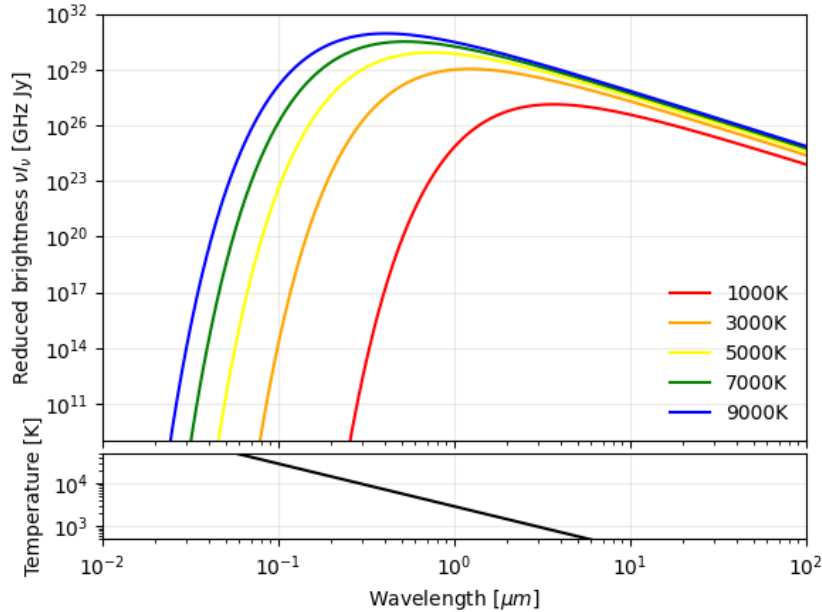


Figure 1.1: Exploring the intrinsic properties of black body emission. **Top:** SED of black body emission, as given by Planck's law, at different effective temperatures. **Bottom:** Temperature of black body given by Wien's displacement law.

4. Molecular clouds and Photo-Dissociation Regions (PDRs)

The HII-regions and the WIM are regions of interstellar ionised hydrogen. The former, also known as emission nebulae, are regions around newly exposed O-type stars, where the dominant Far Ultraviolet (FUV) emission photoionise the constituents, resulting in rich recombination spectra. The latter contain most of the total mass of interstellar HII. The typical temperature of HII are of the order 10^4 K, and it makes up about 10% of the volume of the ISM (Draine 2011, Wolfire et al. 2003).

The WNM primarily consists of atomic gas heated to temperatures of the order of ~ 5000 K and is quite diffuse with typical densities of about 0.6cm^{-3} . However, it is the largest component by volume fraction, making up about 40% of the ISM by volume (Draine 2011).

The Cold Neutral Medium (CNM) primarily consists of atomic gas at temperatures of the order of 10^2 K. At those temperatures, the CNM is about 50 times denser than the WNM. In turn, it only makes up about 1% of the volume of the ISM in nearby galaxies (Draine (2011)).

Lastly, the molecular gas of the interstellar medium is located in molecular clouds and PDRs. In the outer PDR the gas is more diffuse at densities of order 10^2cm^{-3} and temperatures of the order ~ 50 K while in the densest regions can have temperatures down to 10K and densities of the order 10^3 - 10^6cm^{-3} . In turn, the molecular gas only makes up about 0.01% of the volume of the ISM (Draine 2011).

The largest component, by mass, of the ISM is the CNM, closely followed by the WNM (Draine 2011), which permeates the space between the bulk of the stars of the galaxy, and which primarily consists of HI. The pressure, density, temperature and observational characteristics of a gassy medium is set by heating and cooling processes. Thus, we will now investigate the heating and cooling processes of the ISM.

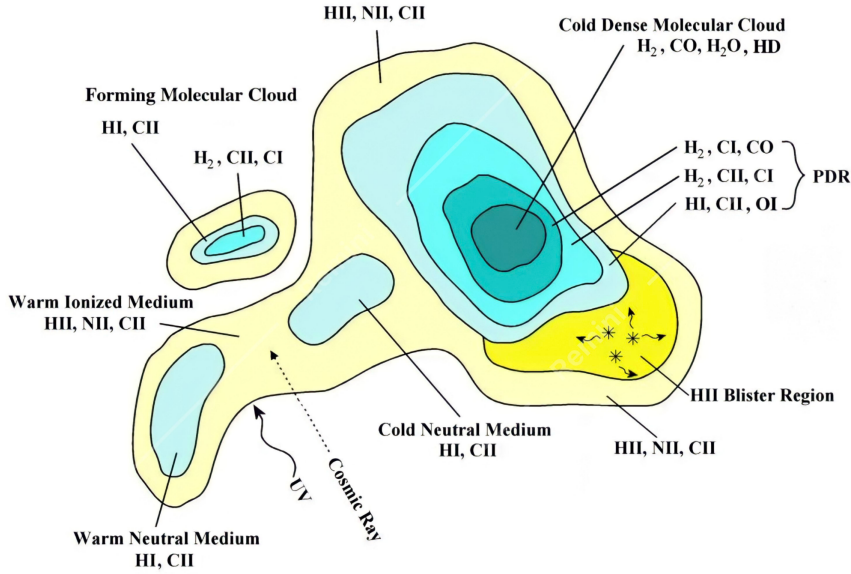


Figure 1.2: A schematic representation of the ISM components (Goldsmith et al. 2022, Fig. 2).

1.3 Heating and Cooling of the ISM

Radiation observed from the gaseous and dusty distribution of interstellar material relates to the cooling process of interstellar matter. The cooling of the ISM is naturally related to the heating, thus, to understand the observational characteristics of the ISM, we need to figure out how it is heated.

1.4 Interstellar Heating Sources

Firstly, the ISM is heated by cosmic rays, which mostly consist of relativistic protons, with a mixture of heavy elements and electrons. If the cosmic ray proton collides with H_2 , two different outcomes can come about. Firstly, the proton scatters inelastically, exciting the H_2 molecule to a higher electronic state. From the excited state, the H_2 molecule de-excites by dissociation. Secondly, and more commonly, the H_2 molecule is simply ionised by the impact of the cosmic ray proton (Stahler and Palla 2004, ch. 7), and additional energy is supplied as thermal kinetic energy.

Additionally, cosmic ray protons can collide with the diffuse interstellar protons of atomic hydrogen. When the protons collide, the most common result is ionisation (Stahler and Palla 2004, ch. 7). The free electron is ejected with an energy typically in the order of about 35 keV, and can secondarily scatter, consequently injecting the kinetic energy into the ambient cloud. The typical heating rate of atomic hydrogen and molecular hydrogen, due to cosmic rays, are (Stahler and Palla 2004, ch. 7),

$$\Gamma_{CR}(HI) = 1 \times 10^{-13} \left(\frac{n_{HI}}{10^3 \text{ cm}^{-3}} \right) \text{ eV cm}^{-3} \text{ s}^{-1}, \quad (1.1)$$

$$\Gamma_{CR}(H_2) = 2 \times 10^{-13} \left(\frac{n_{H_2}}{10^3 \text{ cm}^{-3}} \right) \text{ eV cm}^{-3} \text{ s}^{-1}, \quad (1.2)$$

where, n_{HI} is the density of atomic hydrogen, HI, and n_{H_2} is the density of molecular hydrogen, H_2 . Another important source of heating is the Interstellar Radiation Field (ISRF). It is a diffuse field of radiation that permeates the interstellar space of a galaxy. An example of an ISRF is shown in Fig. 1.3.

The ISRF can heat the ISM in various ways. Firstly, it can ionise hydrogen, carbon or other atoms by UV or X-ray photons.

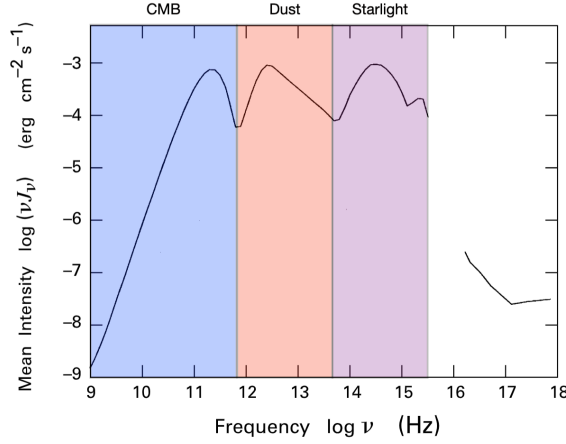


Figure 1.3: The mean intensity, over all solid angles in the sky, of the ISRF in the solar neighbourhood, expressed as a function of frequency, with the main constituents overlaid (Stahler and Palla (2004), Fig. 7.4).

The UV component of the ISRF is too weak to significantly ionise HI, with an ionisation potential of 13.6 eV, in the diffuse ISM. However, a number of heavier elements have lower ionisation potentials. Of these, CI is the most abundant, with a typical number density relative to HI of $n_{\text{CI}}/n_{\text{HI}} = 3 \times 10^{-4}$. Additionally, with an ionisation potential of 11.2 eV, it is not shielded by the abundant HI. Moreover, the CII in the diffuse ISM is not further ionised due to the fact that the UV component of the ISRF is too weak at its ionisation potential of 24.4 eV, and that any UV photons with these energies would ionise the much more abundant HI. As a result, any photon more energetic than 11.2 eV will ionise CI in the diffuse ISM, ejecting an electron. Since the kinetic energy of this electron quickly disperses to surrounding atoms through collisions, carbon ionisation is an effective heating mechanism.

The UV photons in the ISRF can also liberate electrons from H_2 . The heating mechanism of this process is similar to how cosmic rays heat the gas by releasing a free electron. The free electrons are ejected with a kinetic energy relative to the ionising photon, and the electron can then inject the kinetic energy into the ambient medium.

Secondly, the interstellar radiation can be absorbed by dust. The simplest way is the classical irradiation of the dust, where the photon is absorbed. A typical heating rate from irradiation of dust grains is (Stahler and Palla 2004, ch. 7),

$$\Gamma_{\text{IG}} = 2 \times 10^{-9} \left(\frac{n_{\text{H}}}{10^3 \text{ cm}^{-3}} \right) \text{ eV cm}^{-3} \text{ s}^{-1}. \quad (1.3)$$

However, if the photon is energetic enough, it can heat the ISM through the photo-electric effect. The UV and FUV photons release an electron from the surface of a dust grain through the photo-electric effect. A typical heating rate from the photo-electric effect is (Stahler and Palla 2004, ch. 7),

$$\Gamma_{\text{PE}} = 3 \times 10^{-11} \left(\frac{n_{\text{H}}}{10^3 \text{ cm}^{-3}} \right) \text{ eV cm}^{-3} \text{ s}^{-1}. \quad (1.4)$$

The electron then heats the surrounding gas. Especially small dust grains and Polycyclic Aromatic Hydrocarbon (PAH)s have large photo-electric efficiencies, and are the source of most of the photo-electric heating.

The main driver of the heating processes of the ISM are the stars. Especially the massive stars provide an important source of energy, which heats the interstellar matter through stellar winds, shocks and ionising photons. The bulk of the stars instead mainly provide heating through the irradiation of dust grains in the diffuse ISM, which is then propagated to the ambient medium.

1.5 Cooling of the ISM

Fine structure emission lines are the major coolants within the CNM and WNM. While hydrogen itself does not have fine-structure splitting of its ground electronic state, many species in the CNM and WNM do. Fine structure levels are easily excited by collisions with hydrogen. After collisionally exciting the fine-structure levels, the heat is then removed from the gas through the spontaneous emission of a photon, especially in environments where the density is lower than the critical density of the transition between the two fine-structure states. Especially OI and CII have fine-structure levels of their electronic ground state that can be excited through collisions at relatively low densities and temperatures. As discussed earlier in this chapter, we expect the ISRF to ionise CI to CII in the diffuse ISM. In turn, the CII content of the ISM must trace the diffuse atomic and ionised gas (Carilli and Walter 2013). The typical sub-critical cooling rates of the transition between the $^2P_{3/2} \rightarrow ^2P_{1/2}$ fine-structure splits of the electronic ground states of CII at $158\mu\text{m}$ (hereafter [CII]), in the diffuse atomic medium is (Stahler and Palla 2004, ch. 7),

$$\Lambda_{[\text{CII}]} = 3 \times 10^{-9} \left(\frac{n_H}{10^3 \text{ cm}^{-3}} \right)^2 \exp \left(-\frac{92 \text{ K}}{T_g} \right) \text{ eV cm}^{-3} \text{ s}^{-1}. \quad (1.5)$$

Note that while the heating rates, discussed in section 1.4, were proportional to the density, the cooling is proportional to the square of the density and the temperature of the gas T_g . Thus, the balance between the heating and cooling sets the temperature and density of the medium, and consequently, the pressure. Additionally, we can see from the temperature dependence of the cooling rates, what part of the neutral medium they trace. In general the [CII] fine structure emission plays a role for conditions where $10 \lesssim T_g \lesssim 10^4 \text{ K}$, while the [OI] $63\mu\text{m}$ plays a role for the neutral medium at conditions $T \gtrsim 100 \text{ K}$ (Draine 2011). Additionally, the critical density of the [CII] emission line is $\sim 4 \times 10^3 \text{ cm}^{-3}$. In turn, there is no significant collisional de-excitation of the upper levels. Moreover, warmer gas will have significantly populated $n = 2$ atomic hydrogen, and thus, it can also cool the gas directly by spontaneous emission through $\text{Ly}\alpha$.

Moving on, molecular hydrogen, H_2 , holds the key to accessing the star-forming reservoir of gas in galaxies. H_2 cannot exist in the diffuse ISM due to its dissociation energy of about 4.52 eV. As a result, the H_2 reservoirs of galaxies exist in conditions with high extinction of the ISRF. This is also seen in Fig. 1.2, where a PDR is located in the interface between the molecular cloud and the HII region caused by the O- and B-type ZAMS stars, that have been freed from their dust envelope. A PDR is illustrated in Fig. 1.4.

As mentioned in section 1.4, photons of the ISRF irradiate dust grains, that is, dust grains absorb the photons. As such, dust acts as an important extinction mechanism, and is one of the primary drivers of creating conditions for H_2 , and thus Star Formation (SF). While the dust is irradiated by FUV photons on the surface of a PDR the conditions leads to bright emission from [CII], [OI] $63\mu\text{m}$, and HI recombination lines.

As is illustrated on Fig. 1.4, as we go deeper into the cloud, less radiation penetrates, and a significant fraction of the HI is converted into H_2 . The dominant process of H_2 formation is grain catalysis (Draine 2011). In essence, a hydrogen atom is bound to the surface of a grain. At first it is a weak binding, enabling the H atom to diffuse across the surface, until it encounters a site in which it can be strongly bound. Subsequent H atoms that encounter the grain are also weakly bounded and can diffuse across the surface until they escape or encounter the strongly bound hydrogen atom, causing them to react, form H_2 and in the process, become freed from the grain. However, this process is more important at low temperatures within the cloud. At the edge, H_2 is primarily formed through gas phase formation. Because of the symmetry between two incident H atoms, there are no electric dipole moment, meaning that there are no electric dipole radiation that could leave the system and cause the atoms to be bound together. For this process to take place, the

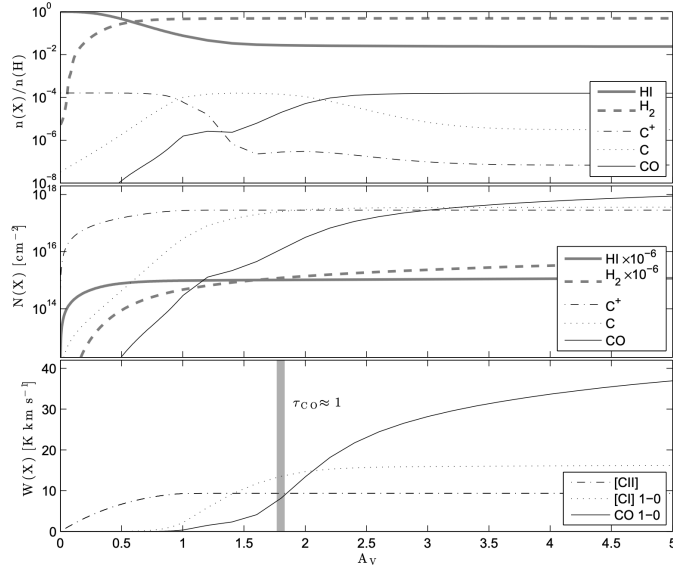


Figure 1.4: A schematic of a PDR (Bolatto et al. 2013, Fig. 1). It shows the calculated cloud structure as a function of optical depth. The top panel shows the fractional abundance of HI, H₂, C⁺, C, and CO. The middle panel shows their integrated column densities from the cloud edge. The bottom panel shows the emergent line intensity for [CII], [CI](1-0), and CO(1-0). The grey vertical bar shows where the CO(1-0) emission becomes optically thick.

hydrogen atom must first undergo radiative association in an encounter with a free electron. Next the negatively charged hydrogen ion can encounter a neutral hydrogen atom and form H₂ through associative detachment (Draine 2011).

The conversion to H₂ takes place quite quickly. As the first molecules form from the gas-phase, they begin to exhibit a phenomenon known as self-shielding. In essence, the outermost H₂ is easily dissociated by the radiation, but it dissociates through the process of spontaneous radiative dissociation. Thus only a small band of photon energies can actually photo-dissociate H₂, meaning that the shielding of the population of H₂ does not require the extinction of the entire UV spectrum of the ISRF. As the extinction of photons that can dissociate H₂ decreases, the population grows with the density of the cloud. And at low temperatures the grain catalysis of H₂ kicks in.

The electric quadrupole transitions of H₂ ensure that emission is optically thin up to high densities (Dionatos 2015). However, H₂ has a large rotational constant, causing its rotational energy levels to be widely spaced. In turn, even the lowest energy levels require high temperatures (~ 300 K) to be significantly collisionally populated. In turn, H₂ is a really inefficient coolant, in the conditions that it exists in within galaxies, meaning that we cannot observe it directly within the cloud. Inside the PDR, we also see that conditions evolve for CII to recombine into CI, and that the dominant coolant becomes the the CI $^3P_1 \rightarrow ^3P_0$ ground state fine structure transition line. In general the $^3P_1 \rightarrow ^3P_0$ (hereafter [CI](1-0)) and $^3P_2 \rightarrow ^3P_1$ (hereafter [CI](2-1)) fine structure transitions of the atomic carbon ground state are widely used for tracing H₂ (Carilli and Walter 2013). In the review by Carilli and Walter (2013), it is also mentioned that the CI properties of high-redshift galaxies does not seem to differ significantly from that of the low-redshift galaxies, including the Milky Way. Studies from the local universe show that [CI] traces the same conditions as carbon mono-oxide, CO, especially considering that the [CI](1-0) and the CO(1-0) emission lines have similar critical densities (Carilli and Walter 2013, Papadopoulos et al. 2004).

Further into the cloud we even reach conditions where the carbon and oxygen can combine into CO. It should be noted that CO also dissociates through spontaneous radiative dissociation, meaning

that it also exhibits the phenomenon of self-shielding. The CO molecule has permanent dipole moment ($d_p(\text{CO}) = 0.11$ Debye) that is more than an order of magnitude lower than the other common species in the ISM. It also has a ground rotational transition with a low excitation energy of $h\nu/k \approx 5.53\text{K}$ (Bolatto et al. 2013). With the low excitation energy and critical density, its ro-vibrational levels are excited even at very low temperatures, causing CO to become an effective coolant within the dense and cold molecular cloud. This is also seen in Fig. 1.2, where the CO(1-0), at $2600\mu\text{m}$, line becomes the most dominant coolant in the inner region of the cloud, where the $J = 1$ level is significantly populated, due to the fact that the density n , is larger than the critical density of CO(1-0) at $2600\mu\text{m}$ of $\sim 2200\text{cm}^{-3}$ (Bolatto et al. 2013).

If we treat diatomic molecules under the assumption of a rigid rotor with a fixed equilibrium separation, the angular momentum of the molecule can be described in the following way (Dionatos 2015, Carilli and Walter 2013),

$$L^2 = J(J+1) \left(\frac{h}{2\pi} \right)^2. \quad (1.6)$$

The levels are dictated by the rotational quantum number J . Using the classical equation for the energy of a rigid rotor, we get that the energy levels, of the discrete set of angular momentum, are,

$$E_{\text{rot}} = J(J+1) \left(\frac{h}{2\pi} \right)^2 \frac{1}{2I}, \quad (1.7)$$

$$= hBJ(J+1), \quad (1.8)$$

$$\propto J^2, \quad (1.9)$$

The selection rule for electric dipole transitions state that $\Delta J = \pm 1$ (Dionatos 2015), and that allows us to easily describe the frequencies of photons emitted or absorbed by rotational transitions. In the case where the transition is between $J \rightarrow (J-1)$, we find that

$$\nu = \frac{E_{\text{up}}(J) - E_{\text{low}}(J-1)}{h}, \quad (1.10)$$

$$= 2BJ, \quad (1.11)$$

$$\propto J. \quad (1.12)$$

In this treatment, we ignored vibrational levels, but if we relax the assumption of a rigid rotor with a fixed equilibrium separation, the diatomic molecules can also vibrate. Additionally, we get the effect that the separation distance increases with J due to centrifugal forces, causing the moment of inertia I , to increase with J , and in turn the rotational constant B to decrease with J . This effect leads to frequencies that are slightly lower than those predicted by the linear relation above (Carilli and Walter 2013).

However, to a first approximation, we can now investigate the conditions that are traced by different J -transitions. For example, for CO in conditions in which the density is much larger than the critical density, $n \gg n_{cr,J}$, and for temperatures larger than the excitation temperature $T_{ex,J} \gg E_J/k \approx 5.53 (J(J+1)/2) \text{K}$, the upper level of the $J \rightarrow (J-1)$ transition will be populated and the molecule will emit brightly (Bolatto et al. 2013). In Fig. 1.5 we illustrate the strength of the emission from different rotational transitions of CO, with respect to the CO(1-0), for different temperatures and densities. Note that increased temperatures leads to broader CO emission ladders, as a result of more and more high- J levels being populated according to the Boltzmann distribution. It is apparent, that different rotational transitions trace different physical conditions. When temperatures and densities increase, the upper levels are more significantly populated, and since their Einstein A coefficients are larger ($A \propto \nu^3 \propto J^3$), they become better coolants, and in turn

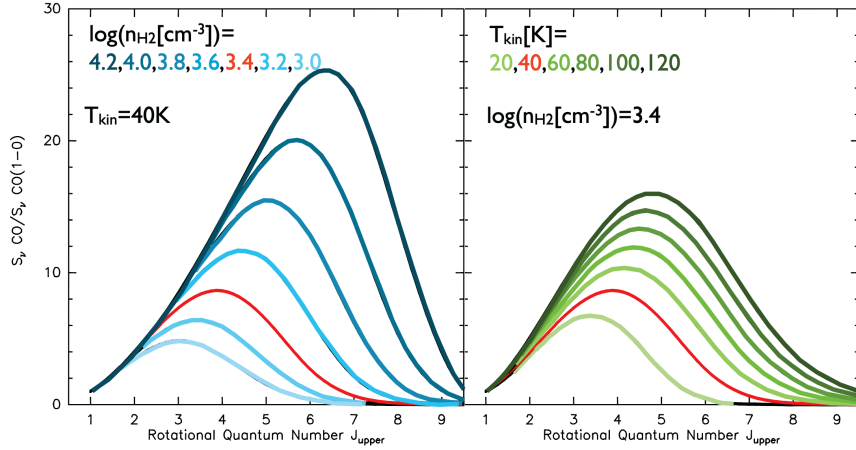


Figure 1.5: The CO emission ladder as a function of temperature and density (Carilli and Walter 2013, Fig. 3). **Left:** The CO ladder as a function of density, with a fixed temperature ($T_{\text{kin}} = 40\text{K}$). **Right:** The CO ladder as a function of temperature, with a fixed density ($\log(n(\text{H}_2)) = 3.4$). Both panels have been normalised to the CO(1-0) transition.

tracers of those conditions. Consequently, different gas components are traced with different rotational transitions. Low- J transitions trace cold and dense gas, while high J transitions trace a gas component of higher kinetic temperatures and densities.

To sum it up, the bulk of the H_2 is found in molecular clouds where the density is high, but the temperature is very low. We expect the low- J rotational transitions of CO ($J_{\text{up}}=1,2,3,4$), the fine-structure [CI](1-0), and potentially the fine structure [CII] emission to trace the bulk of the H_2 reservoirs. Each tracer has their trade-offs. The CO emission is most prominent within the cloud, but a certain fraction of H_2 is formed before the CO is formed, causing it to be *CO-faint*. The ionised carbon far-infrared fine structure [CII] is expected to trace the H_2 at low A_V . In turn, this emission line has the potential to trace the *CO-faint* H_2 , while it could have difficulties tracing the densest parts of the molecular clouds. CII has been found to trace to H_2 in PDRs in both the local Universe (e.g. Pineda et al. 2013, Velusamy and Langer 2014) and at high-redshift (e.g. Zanella et al. 2018, Vizgan et al. 2022).

Stars are created in cores of molecular clouds that have much higher densities than the bulk of the gas (Carilli and Walter 2013). As temperatures increase in areas of ongoing SF within the molecular clouds, the temperature increases, and in turn the higher J transitions of CO and the fine structure CI(2-1) line become more prominent coolants, and in turn tracers of the distribution of H_2 .

1.5.1 Dust

Dust plays a central role in the physical and chemical processes of the ISM. In addition, dust is a key driver in shaping the spectra of galaxies. Radiation at short wavelengths is absorbed or scattered, and the absorbed energy is re-radiated in the Infrared (IR) regime. It is estimated that $> 30\%$ of the energy emitted as starlight in the Universe is re-radiated by dust (Bernstein et al. 2002).

Interstellar dust consists of small solid particles, which are mainly less than $\sim 1\mu\text{m}$ in size (Draine 2011). The composition of interstellar dust is a controversial topic (Draine 2003). While meteorites provide some genuine specimens, these cannot be considered representative of the interstellar population. The most direct information on the composition that we have comes from spectral features in extinction and emission. In general, dust particles are described as poly-cyclic aromatic hydrocarbon molecules (e.g. Allamandola et al. 1989, Puget and Leger 1989) that at least display what appears to be graphite and silicate features (Clayton et al. 2003).

The basic interactions of photons and dust are sketched out in Fig. 1.6. The interaction is often called *extinction*. To describe the extinction caused by interstellar dust, we first distinguish

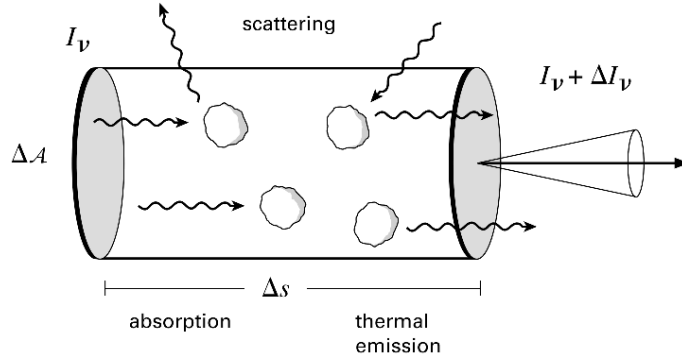


Figure 1.6: Schematic of the passage of light through an ensemble of dust grains (Stahler and Palla 2004, Fig. 2.9). Radiation with specific intensity I_ν enters an area ΔA at the left. By the time it travels a distance Δs , the intensity changes to $I_\nu + \Delta I_\nu$ through absorption, scattering and thermal emission by the grains.

between the properties of a single grain, and the properties of an ensemble of grains. A single individual grain is optically thick, if the size of the grain is larger than the wavelength of the incident radiation. However, an ensemble of grains can be optically thin, even though the individual grains are optically thick (Emerson 1996).

Individual grains interact with radiation according to their absorption cross section, σ_{abs} ,

$$\sigma_{\text{abs}} = \sigma Q_{\text{abs}}(\lambda), \quad (1.13)$$

Where σ is the physical cross section of the grain, and $Q_{\text{abs}}(\lambda)$ is the absorption efficiency. Let us assume, that the grain is immersed in an isotropic radiation field of black body radiation set by a temperature T_{rad} . Then, the power absorbed by the grain per unit frequency, per unit second, per unit solid angle is $\sigma B_\nu(T_{\text{rad}}) Q_{\text{abs}}(\lambda)$. By summing over the entire field of 4π sr, we get the absorbed power per unit frequency, P_{abs} ,

$$P_{\text{abs}} = 4\pi\sigma B_\nu(T_{\text{rad}}) Q_{\text{abs}}(\lambda). \quad (1.14)$$

Now, Assume that the radiation field produced by the grain is that of a black body, $I_\nu = B_\nu(T)$, with a certain efficiency, given by the emissivity Q_{em} . Moreover, the emergent flux of the perfect black body radiator, closely related to the second-order moment of the specific intensity, is simply,

$$F_\nu^+ = \int_{2\pi} I_\nu \cos \theta d\Omega = \pi I_\nu, \quad (1.15)$$

Because black body radiation is isotropic. Given the above, the emittance, S_ν , is simply

$$S_\nu = Q_{\text{em}}\pi B_\nu(T_G). \quad (1.16)$$

Thus, the emissivity, Q_{em} , is defined as the ratio of the emission of the grain surface to that of a perfect black body radiator. Assume, for simplicity's sake, that grains are spherical with a radius a , then the geometrical cross section of the grain is $\sigma = \pi a^2$ and the surface area of the grain is $4\pi a^2$. Now, the emitted power per unit frequency, P_{em} , of a grain is the product of the emittance and the surface area,

$$P_{\text{em}} = 4\pi a^2 Q_{\text{em}}\pi B_\nu(T_G). \quad (1.17)$$

Now, we switch our attention to that of ensembles of dust grains. To do this, we consider a special case where we ignore scattering, such that $\kappa_s = 0$, for a case that obeys the equation of radiative transfer under steady state in the plane-parallel approximation,

$$\cos \theta \frac{dI_\nu}{d\tau} = I_\nu - \left[\frac{j_\nu}{\kappa} + \frac{\omega}{4\pi} \int I_\nu \Phi d\Omega' \right], \quad (1.18)$$

Where the single scattering albedo, ω , is defined as,

$$\omega \equiv \frac{\kappa_s}{\kappa_a + \kappa_s}, \quad (1.19)$$

and the differential length along the line of sight is defined as,

$$ds = -\frac{d\tau}{\kappa\rho \cos \theta}. \quad (1.20)$$

Using eq. (1.20), we find that,

$$\cos \theta \frac{-1}{\kappa_a \rho \cos \theta} \frac{dI_\nu}{ds} = I_\nu - \frac{j_\nu}{\kappa_a}, \quad (1.21)$$

$$\frac{dI_\nu}{ds} = -\kappa_a \rho I_\nu + \rho j_\nu. \quad (1.22)$$

The first term, $-\kappa_a \rho I_\nu$, addresses the absorption, and the second term, ρj_ν , takes care of the emission. Additionally, let us consider a case, where a cavity is filled with an emitting ensemble of dust, that is in thermal equilibrium with the cavity itself, then $\frac{dI_\nu}{ds} = 0$. Since there is thermal equilibrium, the intensity everywhere should be $I_\nu = B_\nu(T)$, where T is the temperature of the cavity. In turn, we find that the emission coefficient is given by,

$$j_\nu = \kappa_a B_\nu(T), \quad (1.23)$$

meaning that the emission coefficient of a material in thermal equilibrium is defined only by the mass absorption coefficient and the temperature. Also, thermal equilibrium requires that the power emitted and absorbed by the grains are equal, and from eqs. (1.14) and (1.17) it is apparent that $Q_{\text{abs}}(\lambda) = Q_{\text{em}} = Q_\nu$.

Now, the emission coefficient per unit volume for an ensemble of grains, if there are N grains per unit volume, is given by (Emerson 1996),

$$\begin{aligned} j_\nu \rho &= \frac{1}{4\pi} (\text{number of grains per unit volume})(\text{emission per grain}), \\ &= \frac{1}{4\pi} (N) (P_{\text{em}}), \\ &= \frac{1}{4\pi} (N) (4\pi a^2 \pi Q_\nu B_\nu(T)), \\ &= N\pi a^2 Q_\nu B_\nu(T). \end{aligned} \quad (1.24)$$

Using eq. (1.23) we find that the absorption coefficient per unit volume is,

$$\kappa_a \rho = N\pi a^2 Q_\nu \quad (1.25)$$

If the grain material has a density of ρ_G , then we can describe the density of the cavity as,

$$\rho = (\text{Fraction of unit volume occupied by grains}) (\text{density of grain material}), \quad (1.26)$$

$$= (\text{volume of single grain}) (\text{grains per volume}) (\text{density of grain material}), \quad (1.27)$$

$$= \left(\frac{4}{3} \pi a^3 \right) (N) (\rho_G). \quad (1.28)$$

Now, we can describe the mass absorption coefficient as,

$$\kappa_a = \frac{N\pi a^2 Q_\nu}{\left(\frac{4}{3}\pi a^3\right) (N) (\rho_G)}, \quad (1.29)$$

$$= \frac{3Q_\nu}{4a\rho_G}, \quad (1.30)$$

$$\propto Q_\nu a^{-1}. \quad (1.31)$$

Given a constant emissivity, the mass absorption coefficient decreases with increasing size. Essentially, the opacity of the ensemble of grains increases as the size of the grains decreases. However, in reality, the emissivity decreases when the wavelength of the incident radiation becomes larger than the size of the grain. With this in mind, we conclude that grains are most efficient at absorbing radiation from the ISRF, when the size of the grains are of the same order of magnitude as the wavelength of the incident radiation.

Moreover, in reality, the grains in the ensemble will not all have the same size. In reality, the grain sizes follow a distribution, and the classical distribution used throughout literature is the MRN (Mathis et al. 1977) distribution. It describes the number of grains as a function of size as a power-law that roughly has a power-law index of -3.5 ,

$$dn \propto a^{-3.5} da \quad [50\text{\AA} < a < 2500\text{\AA}] \quad (1.32)$$

Using such a grain size distribution, and taking into account the shape and composition of the dust, one can create a so-called dust-opacity law, which describes the mass absorption coefficient as a function of wavelength. An example of dust opacity laws are shown in Fig. 1.7, which is taken from Webb et al. (2017), where they plot the absorption coefficient as a function of wavelength, for several dust models.

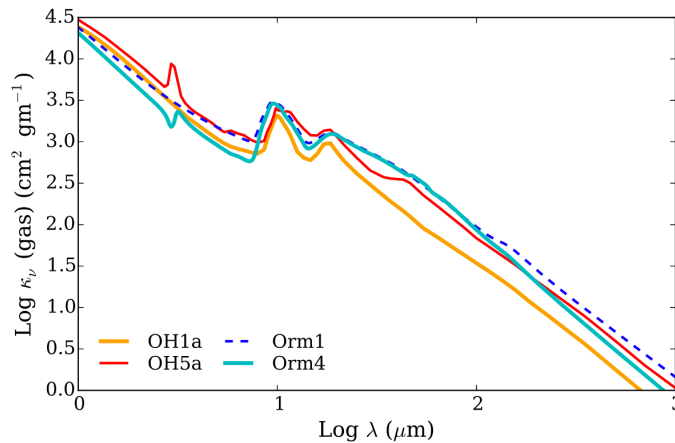


Figure 1.7: Dust extinction curves for different dust models (Webb et al. 2017, Fig. 2)

In general, dust opacity laws show a decline in the absorption coefficient as a function of wavelength. In the long-wavelength regime, this relationship approaches that of a power-law. With this in mind, we can conclude that interstellar dust grains are much more effective at absorbing short wavelength radiation. Referring to the description of the ISRF in Fig. 1.3, it becomes apparent that the absorption of dust mostly affects the stellar contribution to the ISRF. As a reference number, a modest optical attenuation of $A_V = 0.9$ produces a factor ten reduction in the UV continuum at $0.13\mu\text{m}$, if the Calzetti et al. (2000) dust attenuation law is applied (Falc3n-Barroso and Knapen 2013).

Scattering has been ignored in the above treatment of dust opacity. However, as mentioned, the dust extinction is also caused by scattering of light on dust grains. The cross section for scattering is given by $\sigma_{\text{sca}} = \sigma Q_{\text{sca}}(\lambda)$, where $Q_{\text{sca}}(\lambda)$ is the scattering efficiency. Thus the overall effect of extinction is given by the mass extinction coefficient (Emerson 1996),

$$\kappa_{\text{ext}}\rho = \kappa_{\text{abs}}\rho + \kappa_{\text{sca}}\rho = N\sigma Q_{\text{ext}}(\lambda) = N\sigma [(Q_{\text{sca}}(\lambda) + Q_{\text{abs}}(\lambda))] \quad (1.33)$$

In Emerson (1996), it is described that the framework of Mie Theory gives that strongly absorbing materials have refractive indices that are strongly dependant on wavelength, with shorter wavelengths being more efficiently scattered. Additionally, the theory states that at long wavelengths, the scattering and absorption efficiencies scale in the following way,

$$Q_{\text{abs}} \propto \frac{a}{\lambda} \quad (1.34)$$

$$Q_{\text{sca}} \propto \left(\frac{a}{\lambda}\right)^4 \quad (1.35)$$

When the wavelength becomes larger than the grain size, the scattering decreases in effectiveness much faster than the absorption, and both of them tend to zero at very long wavelengths.

1.6 Observations of Galaxies

In this thesis, we study galaxies across the cosmic noon, by investigating the radiation that they emit. When radiation arrives, from an astronomical source, at a detector, the situation can be schematised as illustrated in Fig. 1.8. From the schematic, it is hinted that, the energy carried by

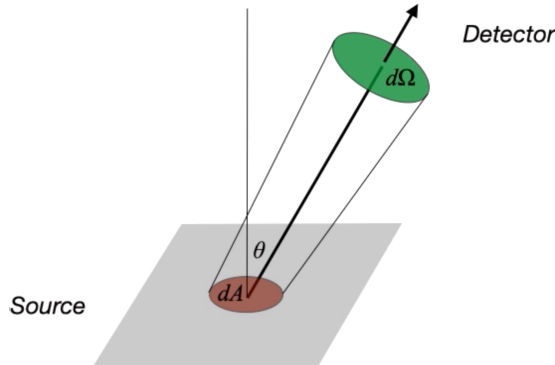


Figure 1.8: Radiation passing through a surface element of an astronomical source, picked up by a surface element of the detector.

the radiation through the detector surface element, dE_ν , is proportional to the solid angle of the detector surface element, $d\Omega$, that the signal is recorded through, and the area that the source surface element subtends on the sky, $dA \cos \theta$. The cosine enters to account for the source surface element inclination with respect to the detector. It comes from the dot product of the unit normal vector of the source plane, \mathbf{n} , and the unit vector describing the direction of propagation, Ω . Moreover, the energy is also proportional to the frequency interval, $d\nu$, and the integration time, dt . The proportionality factor between the energy carried by the radiation and these above properties is the specific intensity, I_ν , of the radiation,

$$dE_\nu = I_\nu \cos \theta dA dt d\nu d\Omega \quad (1.36)$$

Thus, the specific intensity is the energy emitted during the time dt , with a frequency between ν and $\nu + d\nu$, emitted at an angle θ , from the area dA , within solid angle $d\Omega$.

From an observing point of view, one is more interested in the specific flux density, F_ν , of the source surface element, which is the power emitted per unit area. In turn, the flux density takes the entire surface of the detector into account,

$$F_\nu = \frac{1}{dA d\nu dt} \int_S dE_\nu = \int_S I_\nu \cos \theta d\Omega \quad (1.37)$$

Observations of radiation emitted by baryons in galaxies used in this thesis will in general contain the flux density. Additionally, for observations of galaxies outside the local group, we do not resolve the individual stars, gas and dust particles. Instead, we observe the superposition of emission from all stars, gas species and dust particles in the galaxy.

1.6.1 The Initial Mass Function

The spectrum of the collection of stars in a galaxy, can be described by the superposition of all the spectra of all the stars within the galaxy, with their mass number distribution being the determining factor. Since we can already correlate their life time with their mass, we only need to know the mass distribution of newly formed stars, to model the entirety of the stellar spectrum. The combination of those factors is an empirical relationship describing the relative number of stars as a function of their mass in star forming regions, and it is called the Initial Mass Function (IMF). Many problems in modern astrophysics can be *solved* by invoking an IMF and a Star Formation History (SFH). However, the informative power of those *solutions* are rather poor without observational evidence for the invoked IMF (Bastian et al. 2010).

The IMF was originally modelled to empirical data of sun-like stars and giants, from the solar neighbourhood, as a steep power law in Salpeter (1955) on the form,

$$\Phi(\log m) = dN/d\log m \propto m^{-\Gamma}, \quad (1.38)$$

where m is the mass of a star, N is the number of stars in a logarithmic mass range $\log_{10}(m) + d\log_{10}(m)$ and Γ is the slope of the power law, which was originally modelled to be $\Gamma \sim 1.35$. There is no direct observational determination of the IMF. Instead, the integrated light of objects, the Luminosity Function (LF), is observed. Transforming that quantity into an IMF thus relies on theories of stellar evolution, namely the relation between mass, age and luminosity (Chabrier 2003).

By integrating the IMF and properly normalising it, we extract the number of stars within a logarithmic mass interval (Bastian et al. 2010). It is evident that the IMF is not constant with mass. Instead, lower mass stars are more easily formed, which can be attributed to the fact that lower mass stars require less H_2 . Later on, in the 1970s, it was recognised that SF had a *preferred mass*, the characteristic mass, meaning the IMF was not simply a power-law. Different modern IMFs are compared to the Salpeter (1955) IMF in Fig. 1.9.

Additionally, modern IMFs take into account the full stellar population all the way down to the M-dwarfs at the bottom of the main sequence of stars (Chabrier 2003). It is also shown that the characteristic mass of SF is subject to cosmic evolution, meaning that the characteristic mass has been decreasing with time (e.g. Chabrier 2003, Dokkum 2008).

With this in mind, we can now review the spectral fingerprint of galaxies, induced by all its constituents.

1.6.2 Spectral Energy Distribution

Together, the emission coming from the stars, gas and dust of a galaxy makes up the spectrum of a galaxy. The SED explains the power emitted with respect to wavelength or frequency. The reduced brightness is very useful when one wants to describe the SED of a source, as it allows one

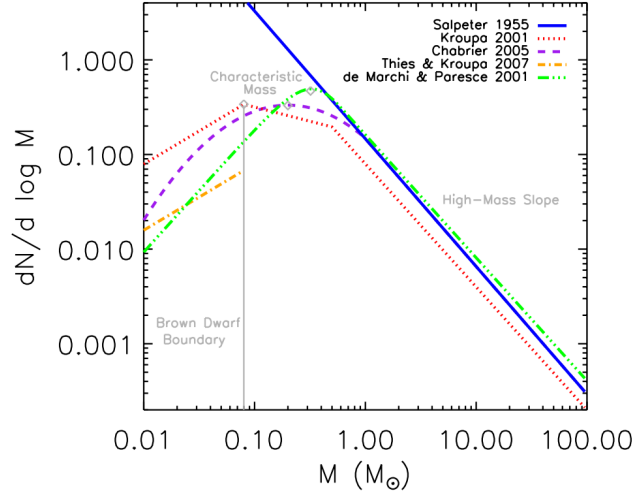


Figure 1.9: Functional forms of the IMF proposed by various authors from fits to galactic stellar data (Offner et al. 2014, Fig. 1). Except for the Salpeter slope, the curves are normalised such that the integral over mass is unity.

to easily identify at which wavelength or frequency a source emits most of its energy. This is a consequence of the following equation (Léna et al. 2012, ch. 3.1),

$$\int_{\Delta\nu} \nu I(\nu) d \ln \nu = \int_{\Delta\nu} I(\nu) d\nu \quad (1.39)$$

The integral of the reduced brightness over a logarithmic frequency unit in a given frequency range, is equal to the integral of the intensity integrated over that same frequency range. The SED is most often plotted as the reduced brightness against the frequency or wavelength. The area under the SED is thus directly related to the fraction of power emitted by the radiation at the given wavelength interval.

An illustration of a galaxy SED is given in Fig. 1.10. It is evident, that radiation from the youngest

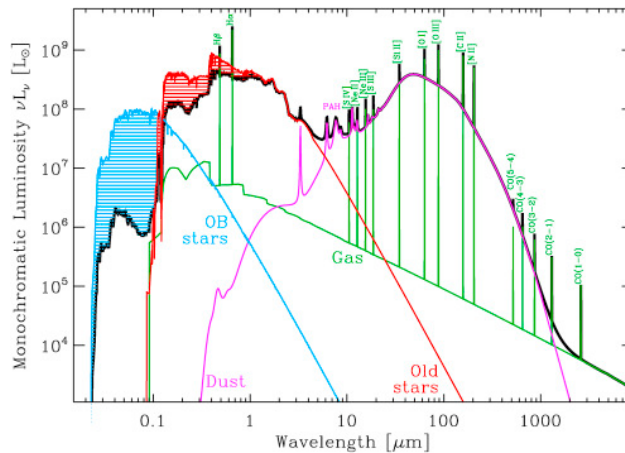


Figure 1.10: Typical SED of a nearby star-forming galaxy (Galliano 2017). The black curve represents the total superimposed SED, while the other curves represents modelled contributions from different components. Only the most widely observed gas lines have been shown. The hatched areas in the stellar spectra represent the fraction of light that has been absorbed by the ISM. This absorbed light is re-emitted by the dust component.

and most massive stars are primarily dominant in UV. Additionally, radiation coming from the bulk

of the stars are primarily dominant in optical and Near Infrared (NIR). Moreover, it is apparent that the gaseous component itself is not a dominant source of radiation, but must instead be observed through emission lines. Also, the radiation emerging from the warmest, and thus largest, brightest and youngest, stars, are most affected by absorption caused by interstellar dust. Thus the warm dust black-body emission primarily stems from the dust extinction of the O- and B-type stars and, thus traces ongoing SF. Moreover, it is apparent from Fig. 1.10, that the curves become almost linear towards their truncation in the log-log plot, meaning that they obey power laws. The complete spectrum exhibits this feature in the low energy Rayleigh–Jeans Tail ($h\nu \ll k_B T$), where cold diffuse dust, heated by the old stellar population (Kokorev et al. 2021), dominates the spectrum. This in turn means that a large part of the low energy continuum can be modelled by measurements in two separate energy bands. Furthermore, the same amount of power that is absorbed, represented by the hatched area, is re-emitted by the dust in IR. Thus there is an energy balance between these components, that allows for reconstruction of the hatched areas. This is indeed useful, when trying to infer the SFR of galaxies.

1.6.3 Star Formation Rate Indicators

In the Milky Way, the most common way to measure SFRs in resolved regions, are to count individual objects, or events like supernovae, that trace the recent SFR. However, for unresolved systems, we measure SFR through emission related to the stellar ensemble. Consequently, invoking an IMF is necessary, to make measurements of SFRs, such that the number of inferred massive stars, can be extrapolated to the total number of stars formed (Falcón-Barroso and Knapen 2013). Additionally, to make the conversion, we must also require that the observed SF has been constant over a certain period of time.

As mentioned, newly formed stars are the dominant sources of UV in galaxy SEDs. Therefore, UV emission ($\lesssim 0.3\mu\text{m}$) is widely used to infer SFRs. However, since they're very short-lived, the time-scale for constant SF, τ , in the UV relations are typically of the order $\sim 10 - 100\text{Myr}$ (Falcón-Barroso and Knapen 2013).

Another important and widely used method to infer SFRs are related to HII regions. The FUV radiation emitted by newly formed stars ionise the surrounding medium, and usually dominates over shock-ionisation (e.g. Calzetti et al. 2004, Hong et al. 2011). As a result, HII-regions display a wealth of recombination cascade lines. In turn, the $\text{H}\alpha$ line has been commonly used as way to infer SFR. However, only stars more massive than $\sim 20M_\odot$ produce a significant flux of ionising FUV photons (Falcón-Barroso and Knapen 2013). Additionally, after the burst of instantaneous massive SF, the ionising photon flux decreases by orders of magnitude in timescales as short as $\sim 5 - 10\text{Myr}$. Consequently, the assumed timescale τ , of the $\text{H}\alpha$ relations, must be on the same order (Falcón-Barroso and Knapen 2013).

Dust heavily obscures SF across the cosmic noon (e.g. Elbaz et al. 2011, Reddy et al. 2012), meaning that the SFRs inferred from UV and $\text{H}\alpha$ relations would be only a fraction of the total SFR. Consequently, the IR luminosity related to the re-emission by dust, can be used to infer the SFR. However, the IR luminosity will depend not only on the heating rate provided by the newly formed stars, but also on the bulk of the stars. Essentially, due to dust emitting as a black-body following the Planck function, hotter dust in thermal equilibrium has higher emissivity in IR than cooler dust. Furthermore, the cross-section of the dust grains for stellar light is higher in UV than in optical. Consequently, the dust heated by UV-luminous young stars, produce an IR SED that is more luminous and peaks at shorter wavelengths, than the dust heated by the bulk of the stars. Therefore, the mid- to far-IR dust continuum emission ($\sim 5 - 1000\mu\text{m}$), induced by dust absorption of UV radiation, is used to infer SFRs. In reality, due to dust emitting as a Planck function, one would need to integrate over the entire UV-heated dust continuum to map the stellar photons. Additionally, to acquire the SFR, one would need to know, or make a qualified assumption of, the

dust grain size distribution and dust grain chemical composition. Furthermore, timescales of the IR inferred SFRs can be much longer, depending on the part of the spectrum that is used, ranging from 2Myr all the way up to 10Gyr (Falc3n-Barroso and Knapen 2013).

Over the last ~ 20 years another approach have been gaining traction, due to the ever growing amount of photometric observations across a wide range of wavelengths. SED fitting entails fitting stellar templates, AGN templates and dust templates to photometric data from FUV to radio. The power of these techniques are related to the global galaxy parameters of the template libraries. Essentially, the templates are created assuming global properties, and by fitting the templates to photometric observations, the global properties can be scaled and retrieved. For a more detailed description, we refer to section 3.1.

1.6.4 Galaxy Morphology

Galaxies have canonically been divided into two types: Early-Type Galaxy (ETG) & Late-Type Galaxy (LTG). The naming scheme was originally devised by Edwin Hubble, and is quite counter-

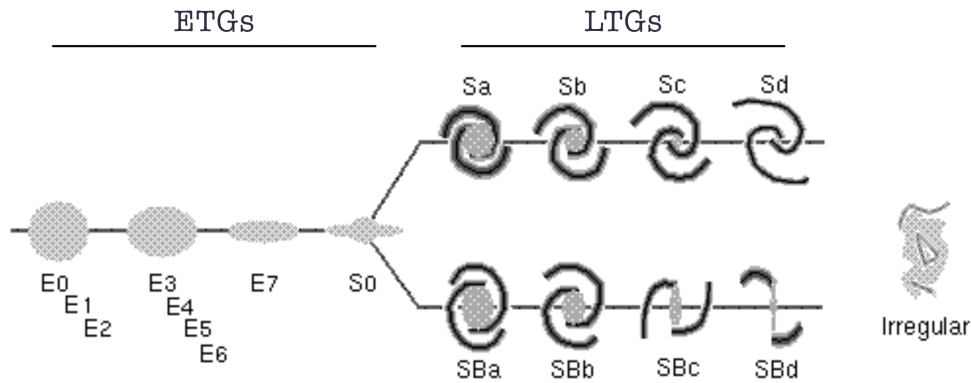


Figure 1.11: The Hubble Sequence, also known as the Tuning Fork Diagram (Strobel 2022). It is a classification scheme devised by Edwin Hubble for galaxies based on their morphologies, and the postulate that galaxies evolve from elliptical ETGs to spiral LTGs. In reality, this is not an evolutionary sequence.

intuitive, since our current understanding of galaxy evolution entails that galaxies mainly evolve from LTGs to ETGs.

LTGs refer to disk galaxies that at low redshift often have spiral arms. They are often blue due to ongoing SF in the disk, and they are typically larger than ETGs of similar mass. On the other hand, ETGs are often quiescent and as a result their stellar spectra are made up of old stars, making them much redder than their LTG counterparts.

Galaxies are overall thought to contain a disk and bulge structure. Since the ISM is a dissipative medium, that are affected by magneto-hydrodynamics, it is expected to have an exponential disk shape. However, since this is not the case for the stellar distribution, its distribution is expected to be more sharply peaked, corresponding to a central concentration.

The common way to model surface brightness profiles of bulges and disks are the De Vaucouleurs profile and the exponential luminosity profile respectively. Both of which are subsets of the S3ersic profiles (Padmanabhan 2002, ch. 1.6-1.7), given on the following form,

$$I(r) = I_e \exp \left\{ -b_n \left[\left(\frac{r}{r_e} \right)^{1/n} - 1 \right] \right\}, \quad (1.40)$$

where I_e is the intensity of the radiation emitted by the galaxy at the effective radius $r = r_e$. The effective radius r_e is the radius that encapsulates half the intensity of the model. The discrete index

n is known as the Sérsic index, and it is shown by [Graham and Driver \(2005\)](#), that the constant b_n is correlated to the Sérsic index by the following relation,

$$\Gamma(2n) = 2\gamma(2n; b_n) \quad (1.41)$$

The relation includes the gamma function and the lower incomplete gamma function.

$$\Gamma(n) = (n - 1)! \quad \gamma(s, x) = \int_0^x t^{s-1} e^{-t} dt \quad (1.42)$$

According to [Voigt and Bridle \(2010\)](#), b_n can analytically be approximated by the following relation,

$$b_n = 1.9992n - 0.3271 \quad [0.5 < n < 10] \quad (1.43)$$

The parameters defining the Sérsic profile are thus the effective radius, the intensity at the effective radius and the Sérsic index. Furthermore, the Sérsic index sets the central concentration, with higher values of the index corresponding to higher concentration. Fig. 1.12 illustrates the dependency of the Sérsic profile on the Sérsic index. It is apparent, that for a source with a given intensity,

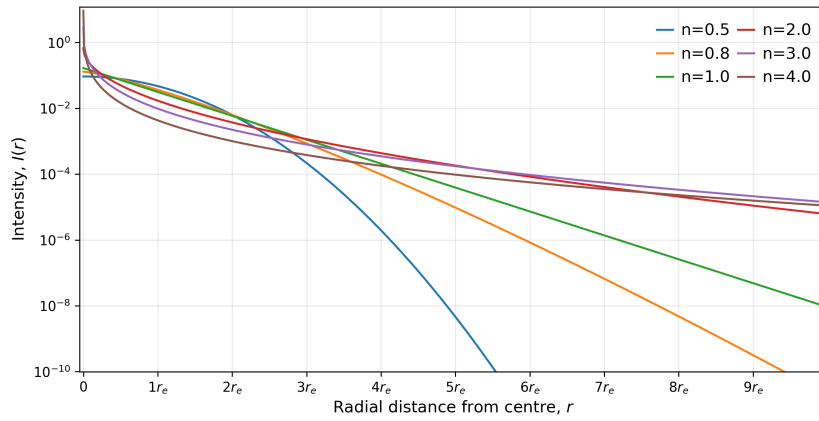


Figure 1.12: The Sérsic profile for different values of the Sérsic index, and in turn, the constant b_n as explained by eq. (1.43). The profiles are normalised such that $\int_0^{10r_e} I(r) dr = 1$.

the surface brightness profile is significantly different, for different values of the Sérsic index, n . Moreover, we see that $n = 1$ corresponds to an exponential profile and that $n = 4$ corresponds to a De Vaucouleurs profile. Additionally, well resolved local galaxies, containing a wide variety of bulge-to-disk ratios, are often modelled by at least two Sérsic profiles. However, for high-redshift galaxies the resolution of an observed galaxy are often too poor to separate the bulge and disk components, and they're consequently often well-modelled by a single Sérsic profile ([Graham and Driver 2005](#)).

1.7 High Redshift Galaxies

The structure of star-forming galaxies change with cosmic time and they grow inside-out, such that their size gradually increases as stars are formed over cosmic time (e.g. [Wuyts et al. 2011](#), [Nelson et al. 2016](#), [Suess et al. 2021](#)). In the canonical description, inside-out growth is a consequence of the properties of the galaxy CDM halo. As galaxies accrete gas from the cosmic web, and form galaxy mergers, it is assembled into a disk structure. As the gas cools in the disk, the galaxy forms stars with a radial distribution set by the angular momentum distribution of the halo ([van den Bosch 2001](#), [Nelson et al. 2016](#)). As a result, a Star Forming Galaxy (SFG) will continuously grow in

stellar mass and size over cosmic time as long as there's ongoing SF and an inflow of gas to the central bulge to replenish the molecular gas reservoirs.

However should the inflow stop, or another mechanism trigger the complete consumption or removal of the molecular reservoir, the SF of the galaxy will be quenched, and it will stop growing inside-out. We believe that those galaxies become spheroid ETGs (e.g. [Wuyts et al. 2010](#)).

Consequently, we arrive at the conclusion that galaxies do not grow in a self-similar way. While the inside-out growth might provide some similarity between the SFGs, the addition of merger-driven growth makes the properties of the global galaxy population vary a lot. Anyhow, lets take a look at some of the relations between galaxy properties and how they evolve with cosmic time.

1.7.1 Evolution of the Main Sequence

Galaxies can be categorised by their SF state. A SFG is a galaxy that actively form stars, while a quiescent galaxy is a galaxy where SF has been quenched. In turn SFGs and quiescent galaxies are closely related to their morphologies. Spheroid galaxies are typically quiescent, and they have red colours due to their old stellar population. Additionally, they have limited amounts of cold gas and dust, and as a result no active SF. On the other hand, SFGs are typically disk galaxies, with large reservoirs of molecular gas and dust. Consequently, they typically have blue colours due to their population of young massive stars ([Renzini 2006](#)).

For SFGs, there exists a correlation between their SFR and stellar mass, M_* , the so-called Main Sequence (MS) relation. Most SFGs fall within an observed scatter of 0.3 dex of the MS (e.g. [Rodighiero et al. 2011](#), [Sargent et al. 2012](#), [Speagle et al. 2014](#), [Schreiber et al. 2015](#)). Consequently, it is conjectured that SFGs will secularly evolve along the MS with cosmic time (e.g. [Genzel et al. 2015](#)), until some mechanism quench the active SF. Additionally, the MS moves to lower SFRs at lower redshifts (e.g. [Speagle et al. 2014](#), [Schreiber et al. 2015](#)), corresponding to the SFR decreasing with cosmic time, which is illustrated in Fig. 1.13. As a reference number, [Speagle et al. \(2014\)](#) found that the average SFR has decreased by a factor ~ 20 from $z \sim 2$ to $z = 0$.

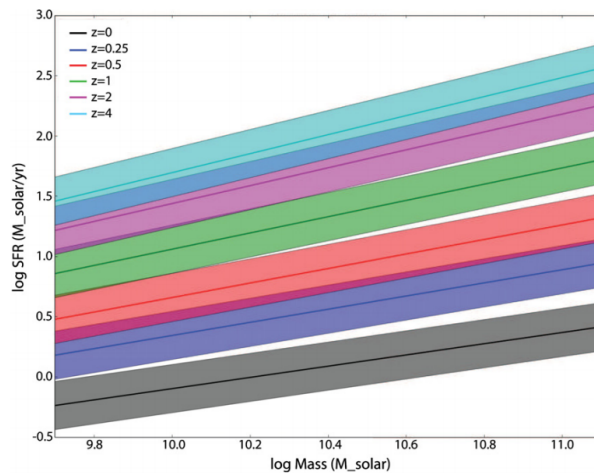


Figure 1.13: Empirical MS-relation between SFR and stellar mass at different redshifts, derived by fitting observations from literature ([Speagle et al. 2014](#)). The displayed widths of the distribution is set at the *true* 0.2 dex scatter, rather than the observed 0.3 dex scatter.

The SFR of a galaxy has been shown to correspond with the amount of gas available in the galaxy ([Schreiber et al. 2015](#)). Consequently, the decreasing SFR with cosmic time can potentially be explained by the fact that gas fractions at a given stellar mass slowly decrease with time because the cosmic inflow rate diminishes and the consumption rate increases (e.g. [Davé et al. 2011](#), [Cochrane](#)

et al. 2021). As evidence towards that hypothesis, measurements of galactic gas reservoirs yield gas fractions evolving from about 10% in the local Universe up to 60% at $z \approx 3$ (Schreiber et al. 2015). Furthermore, as illustrated in Fig. 1.14, recent studies have shown that the gas density has decreased since the cosmic noon. It is apparent, that the molecular mass content per volume

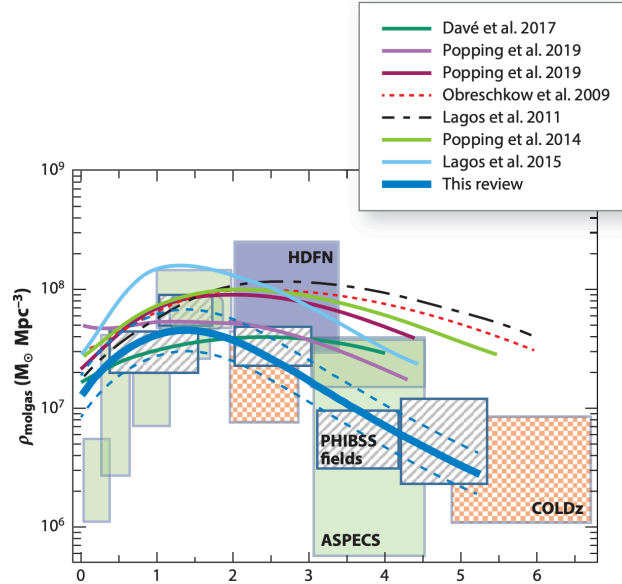


Figure 1.14: Empirical and theoretical estimates of the evolution of total molecular mass (H_2 and helium) (Tacconi et al. 2020, Fig. 7)

increases with increasing redshift, and it reaches a broad peak at $z_{\text{peak}} \sim 1.4 \pm 0.3$, and slowly drops toward higher redshift (Tacconi et al. 2020). When a SFG empties its molecular gas reservoirs the SF will effectively be quenched, causing the galaxy to move off of the MS.

Another hypothesis related to evolution from SFG to quiescent galaxy, is related to another mode of star formation. Galaxies can undergo Star Burst (SB) periods, where they have a significantly increased SFRs, much larger than the SFR expected from the MS relation and scatter. Such galaxies are grouped together and referred to as SB galaxies (SBG). In turn, the SBGs are much more efficient at converting gas into stars than they should be, leading to the swift consumption of their molecular gas reservoirs, quickly shooting the galaxy down to quiescent. The cause of SBGs are still debated in literature. However, there seems to be a theoretical and empirical agreement, that the SB mode is related to compact SF regions. As a result, it is theorised that SBGs are related to stochastic processes like major mergers, where the compression of the gas content of the galaxies, result in an intense period of SF (e.g. Silverman et al. 2015, Cibinel et al. 2019). This explanation is also supported by the fact that SB galaxies only represent a small percentage of the SFG population, and they seem to have a minor impact on the cosmic SFH (Rodighiero et al. 2011, Schreiber et al. 2015). However, they are more easily selected at high redshift due to being very luminous in the warm dust continuum at rest-frame mid IR, and in cases of dust poor conditions, the rest frame UV. However, studies have found that not all SBGs are mergers (e.g. Conselice et al. 2000, Blasco-Herrera et al. 2013). For those objects, their compact SF regions are explained by large cosmic inflows to the central region, which could be triggered by gravitational interactions (Moorwood 1996).

In this thesis, we parameterise the MS relation using eq. (9) of Schreiber et al. (2015):

$$\log_{10} (\text{SFR}_{\text{MS}} [\text{M}_{\odot}/\text{yr}]) = m - m_0 + a_0 r - a_1 [\max(0, m - m_1 - a_2 r)]^2, \quad (1.44)$$

Where,

$$r \equiv \log_{10}(1 + z), \quad (1.45)$$

$$m \equiv \log_{10}(M_*/10^9 M_\odot), \quad (1.46)$$

with $m_0 = 0.5 \pm 0.07$, $a_0 = 1.5 \pm 0.15$, $a_1 = 0.3 \pm 0.08$, $m_1 = 0.36 \pm 0.3$ and $a_2 = 2.5 \pm 0.6$.

Many studies has found that SFGs on the MS had much larger SFRs in the distant universe than they do today. In Fig. 1.15 we show the evolutionary track of SFGs assuming that they stay on the MS relation. It is clear that the cosmic SFR peaks at around $z = 2 - 3$, and that a subsequent

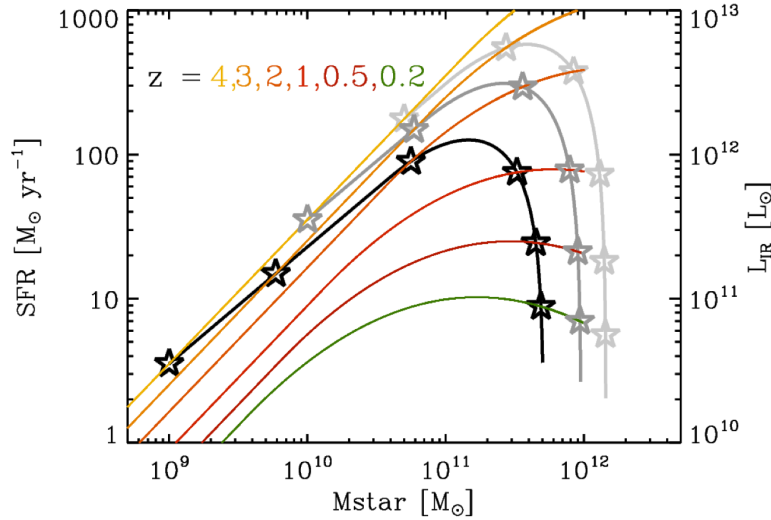


Figure 1.15: Credit to G. Magdis. The coloured lines indicate the MS relation of SF galaxies for the indicated redshifts. Additionally, three SFG SFHs has been illustrated by incremental calculations of their stellar mass and SFR over cosmic time, assuming they stay on the MS relation.

rapid quelling takes place down to $z = 0.2$. As a result, in the literature, the cosmic epoch at $z \sim 1 - 3$ for which the cosmic star formation history peaked has been coined the cosmic noon (Förster Schreiber and Wuyts 2020).

SFGs that follow the evolutionary track should evolve in a self-similar due to active SF, triggered by cold cosmic inflows. Additionally, some degeneracy is introduced with the addition of non-linear growth, due to the mergers. Consequently, we would expect that SFGs display a relation between size and stellar mass, albeit a scatter is to be expected.

1.7.2 Evolution of the Mass-Size relations

As a consequence of the inside-out growth, the stellar disk scale length of SFGs increase with stellar mass, which gives rise to the stellar mass-stellar size relation. In essence, galaxies with larger stellar masses have larger stellar radii (e.g. van der Wel et al. 2014, Shibuya et al. 2015, Pillepich et al. 2019). Consequently, a SFG, which grows its stellar mass over cosmic time, has a stellar size which also grows over cosmic time. Additionally, the size-mass relation indicates that galaxies with $M_* > 10^{10} M_\odot$, at a given stellar mass, are larger with decreasing redshift. However, the size of galaxies with $M_* < 10^{10} M_\odot$ show a weak redshift evolution between $z = 4$ and $z = 0.5$ for constant stellar mass (e.g. van der Wel et al. 2014, Shibuya et al. 2015, Pillepich et al. 2019).

Moreover, when galaxies stop forming stars, their stellar sizes appear to keep growing with time. It is suggested that this is caused by minor dry mergers (Suess et al. 2021). It has been shown that minor mergers fall onto the outskirts of massive compact galaxies, in turn causing their perceived

stellar size to grow alongside the addition of extra stellar mass. As a result, we see different size-mass relations of quiescent galaxies and SFGs. An empirical size-mass relation over cosmic time is presented in Fig. 1.16.

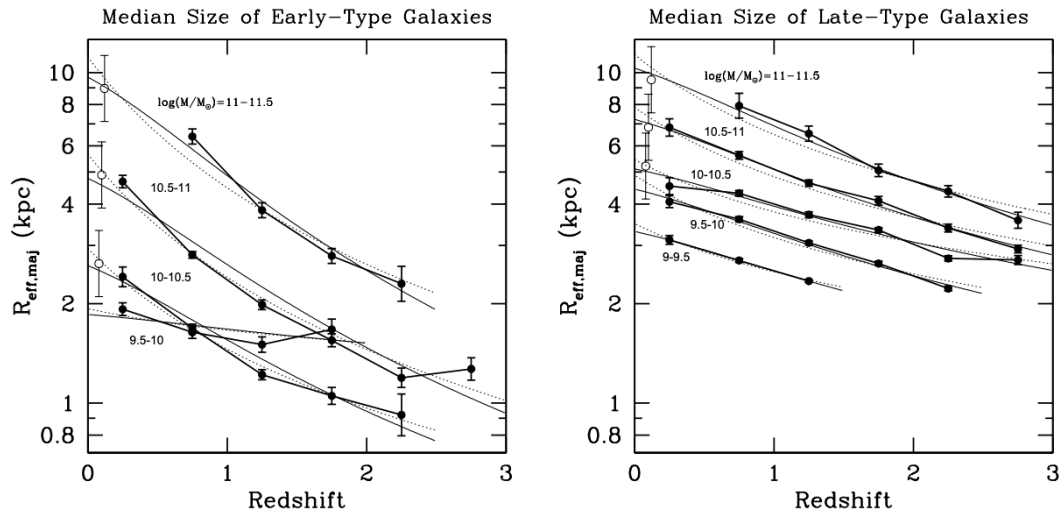


Figure 1.16: Median size as a function of stellar mass and redshift in black for quiescent spheroid galaxies (left) and for disk SFGs (right) (van der Wel et al. 2014, Fig. 9). Additionally, the relations are compared with Sloan Digital Sky Survey results, shown as open points. Fits to the median sizes are shown as dotted and solid lines.

We can interpret Fig. 1.16 by following an evolutionary track of a galaxy. Imagine a galaxy at $z = 2$ with $\log_{10} M_*/M_\odot > 10$. As time goes by, meaning the redshift decreases, the galaxy can only increase its stellar mass, since there are no mechanisms to significantly strip away the stellar population of a galaxy, and because the bulk of the stellar mass is made up of long-living low mass stars. The quiescent galaxies grow their stellar mass through minor mergers, while the SFGs also increase their stellar mass through SF. As we reach $z = 1$, the stellar mass has increased, and as a result the relation indicates that the stellar size of the galaxy should also be larger (van der Wel et al. 2014).

The major issue with the stellar mass-stellar size relation is the so-called progenitor bias. In essence, the selection criteria of quiescent galaxies and SFGs respectively trace different populations at different cosmic times. For example, the population of ETGs at $z = 0$ will contain most of the quiescent galaxies at $z = 2$, but additional quiescent galaxies would have been formed in between, from a universe in which conditions like temperature and density was very different from which the initial old population of quiescent galaxies at $z = 2$ were formed. This is called the progenitor bias due the fact that it is concerned with the difficulty of tracing observations of populations of objects across cosmic time.

To sum it up, there are two main scenarios to account for the size-mass relation of quiescent galaxies. The first being the actual growth through a series of minor dry merger events, and the second is ascribed to the continuous addition of larger, recently formed quenched galaxies at later epochs of cosmic history. In turn, the latter means that the size-mass relation of quiescent galaxies does not account for physical growth, but instead traces the change in population membership (Fagioli et al. 2016). In reality, both effects probably play a role in setting the slope of the relation.

1.7.3 Compact Molecular Gas Reservoirs

High-redshift galaxies have larger SFRs than their present day counterparts of equal stellar mass. However, to get more clues on the assembly mode of galaxies and their SFHs, it is important to study spatially resolved high-redshift galaxies. For instance, over the last few years, the enhanced

SFR has been observed to correlate with compact molecular gas reservoirs (e.g. Magnelli et al. 2020, Tadaki et al. 2020). The current paradigm suggests that compactness is caused by cosmic inflows to the central region of galaxies at $z \sim 2$. However, measurements of the gas size distribution are challenging as they require long integration times, even with ALMA. One way to overcome these limitations is to use the RJ tail of the dust continuum and assume that the thermal dust emission is spatially correlated with the H_2 (e.g. Genzel et al. 2015, Scoville et al. 2016, Tadaki et al. 2020).

Recent studies (Tadaki et al. 2017, Tadaki et al. 2020) investigated the dust continuum at $850\mu\text{m}$ of 85 massive ($> 10^{11} M_\odot$) galaxies at $1.9 < z < 2.5$ with ALMA at a resolution of $0.2''$. They found that the effective radius of the Far Infrared (FIR) emission is smaller by a factor of $2.3_{-1.0}^{+1.9}$ than the effective radius of the optical emission.

Recent extended configuration observations with ALMA have been used to compare the surface brightness distribution of various emission line tracers of H_2 in galaxies. Kaasinen et al. (2020) resolve the CO(2-1) or the CO(3-2) and the $870\mu\text{m}$ dust-continuum for three SFGs at $z = 1.4, 1.6, 2.7$ using ALMA. They find that the molecular gas size, traced by the CO emission, is $\gtrsim 30\%$ more compact than the stellar emission and that the dust continuum emission is more compact by $\gtrsim 50\%$ for two of the three galaxies. They explain the compactness as a combination of poor resolution and the central starburst scenario. Chen et al. (2017) investigate the CO(3-2) emission and the $870\mu\text{m}$ dust continuum emission of a $z = 2.12$ sub-mm galaxy using ALMA. They find that the dust continuum is 4-6 times more compact than the CO(3-2) emission. Calistro Rivera et al. (2018) examine the CO(3-2) emission and the rest-frame $250\mu\text{m}$ dust continuum emission of four galaxies at $z \sim 2 - 3$ with ALMA. They find that the cool molecular gas emission is more extended than the dust continuum emission by a factor of > 2 . Consequently, they state that morphological properties of the molecular gas phase is not easily derived from the dust continuum. Furthermore, Calistro Rivera et al. (2018) found that molecular gas sizes, traced by CO emission, was comparable to the stellar emission sizes.

From the theoretical perspective, recent studies have applied the radiative transfer code SKIRT (Camps and Baes 2015) on simulated galaxies, to simulate galaxy emission from UV to sub-mm.

Using high-redshift galaxies from the FIRE (Hopkins et al. 2014) simulations, Cochrane et al. (2019) predict that there is a clear difference between the morphologies in rest frame UV/optical, being more clumpy and extended, and for the dust in rest frame FIR, being more regular. Consequently, the rest frame UV/optical morphologies trace the holes in the dust distribution. In line with observations, they predict that the $870\mu\text{m}$ dust continuum emission is extremely compact, while being more extended than the physical stellar component. Moreover, they predict that the dust continuum has different sizes at different rest-frame wavelengths, with shorter wavelengths being more compact. Consequently comparing the observed $870\mu\text{m}$ dust continuum emission across increasing redshift, should naturally lead to more compact measurements.

Using high-redshift galaxies from the TNG50 (Nelson et al. 2019) simulations, Popping et al. (2021) predict that the $850\mu\text{m}$ dust continuum half light radius is up to $\sim 75\%$ larger than the stellar half-mass radius, but significantly more compact than the observed $1.6\mu\text{m}$ optical emission. This is driven by obscuration of stellar emission at the galaxy centres, in turn increasing the apparent $1.6\mu\text{m}$ sizes relative to that of the $850\mu\text{m}$ dust continuum emission. They find that the difference in relative extents increase with redshift, because the observed $1.6\mu\text{m}$ corresponds to shorter wavelength stellar emission with increasing redshift. As a result, they suggest that the compact dust-continuum emission observed in high-redshift galaxies is not necessarily evidence of compact star formation.

It is also predicted that the dust continuum emission is more compact than the actual dust mass component (Cochrane et al. 2019, Popping et al. 2021). This in turn means, that the dust continuum

emission is not a robust tracer of the spatial distribution of the underlying dust mass, because dust in the outer regions are not emitting. Additionally, it is predicted that the dust continuum size does not correlate very well with the H₂ size either. Instead, the dust continuum emission is more closely related to the ongoing star formation (Popping et al. 2021) or the recently formed stars (Cochrane et al. 2019). This is because the dust that emits strongly in the FIR is predominantly heated by young massive stars. Furthermore, Cochrane et al. (2019) observes, that measuring the dust continuum emission at a fixed observed wavelength, with increasing redshift, naturally leads to more compact size measurements, due to tracing further up the RJ tail, corresponding to warmer dust.

In conclusion, recent observations of high-redshift SFGs find that the dust continuum emission is more compact than the optical emission (e.g. Calistro Rivera et al. 2018, Magnelli et al. 2020, Tadaki et al. 2020, Kaasinen et al. 2020). However, it is suggested that these measurements are subject to systematic effects caused by poor resolution (Kaasinen et al. 2020). Recent simulations support the finding that the dust continuum is more compact than the optical emission, but finds that it does not necessarily correlate with compact star formation. It is suggested, that observed dust continuum compactness at the cosmic noon could be explained by dust continuum observations of warmer dust and changes in apparent stellar emission observations caused by tracing more dust obscured emission at shorter wavelengths. Furthermore, recent simulations find that the observed $\sim 850\mu\text{m}$ dust continuum primarily traces the on-going star formation at high redshifts. Additionally, a few recent high-resolution observations with ALMA, targeting H₂ emission line tracers, find that the dust continuum is more compact than the H₂ tracers, and that the optical stellar emission is only slightly larger than the H₂ gas size distribution.

1.8 This Thesis

The foundation of this thesis is laid out by the How to Use Measurements of Bright Line Emission (HUMBLE) project of Rizzo et al. (*In preparation*). HUMBLE is a large project based on the systematic mining of the ALMA public archive. The HUMBLE sample consists of 30 galaxies at $z = 0.5 - 3.5$ with ALMA observations of CO, [CI], or [CII] at high angular resolution. Furthermore, we have auxiliary data from HST in rest-frame optical for most of the targets. The aim of this thesis is first and foremost to parameterise the morphology of the superimposed light coming from stars, gas and dust of the HUMBLE galaxies. Secondly, we investigate how the sizes of molecular hydrogen varies across the cosmic noon with respect to the rest-frame optical emission and the dust continuum emission, and compare it to recent studies of empirical observations and simulations. Finally, we want to correlate those results with SFR and the MS of star-forming galaxies, by employing SED fitting to photometry in the literature.

The structure of this thesis is as follows. In chapter 2 we present our sample of HUMBLE galaxies. Additionally, we present the photometry and spatially resolved maps of our targets. In chapter 3 we present a detailed description on how we recover global galaxy parameters and parameterise morphologies. In chapter 4 we present our results and a detailed analysis of how our results compare to the literature. Finally, in chapter 5 we summarise our results.

2 Sample

We collected the sample of galaxies at $0.5 \lesssim z \lesssim 3.5$ by selecting from the ALMA public archive observations of CO, [CI] and [CII], with angular resolution $\lesssim 0.5''$, spectral resolution $\lesssim 50\text{kms}^{-1}$ and SNR $\gtrsim 3$. These criteria guarantees that a robust kinematic analysis can be performed on the HUMBLE sample, but consequently, we have selected galaxies for which the emission line tracing the molecular gas is bright, and as such should be biased towards SFGs and SBGs. The sample consists of 30 galaxies, and all our targets have spectroscopic redshifts based on optical or FIR/sub-mm spectroscopic campaigns. We present their assigned IDs, celestial coordinates and spectroscopic redshifts in Tbl. 2.1.

Table 2.1: An overview of the sample.

ID	Name	Reference	R.A. ° [ICRS]	DEC.	z
1	CDFS3 Ks 1 353	Olsen et al. (2006)	53.082 00	-27.839 87	0.561
2	COSMOS 2989680	Skelton et al. (2014)	150.431 92	2.802 61	0.625
3	COSMOS 1648673	Skelton et al. (2014)	149.981 45	2.253 20	1.448
4	ALMA0.3	Hayashi et al. (2018)	333.993 87	-17.629 93	1.453
5	ALMA0.10	Hayashi et al. (2018)	333.988 53	-17.631 51	1.454
6	ALMA0.8	Hayashi et al. (2018)	333.992 66	-17.639 50	1.457
7	ALMA0.1	Hayashi et al. (2018)	333.992 29	-17.633 30	1.466
8	ALMA0.6	Hayashi et al. (2018)	333.998 79	-17.633 06	1.467
9	ALMA0.13	Hayashi et al. (2018)	333.999 04	-17.637 97	1.471
10	SHiZELS-19	Gillman et al. (2019)	149.799 88	2.388 40	1.484
11	SpARCS J0225-371	Noble et al. (2017)	36.441 99	-3.924 38	1.590
12	SpARCS J025545	Noble et al. (2017)	36.439 83	-3.928 80	1.590
13	COSMOS 3182	Skelton et al. (2014)	150.075 97	2.211 83	2.000
14	Q2343-BX610	Schreiber et al. (2006)	356.539 32	12.822 01	2.210
15	XMM01 N	Fu et al. (2013)	35.069 22	-6.028 65	2.310
16	XMM01 S	Fu et al. (2013)	35.069 22	-6.028 65	2.310
17	HATLAS J084933-W	Iverson et al. (2013)	132.389 91	2.457 20	2.409
18	HATLAS J084933-T	Iverson et al. (2013)	132.387 36	2.244 35	2.407
19	CLJ1001-131077	Muzzin et al. (2013)	150.237 29	2.338 11	2.494
20	CLJ1001-130949	Muzzin et al. (2013)	150.236 92	2.335 75	2.503
21	CLJ1001-130901	Muzzin et al. (2013)	150.239 12	2.336 33	2.507
22	CLJ1001-130891	Muzzin et al. (2013)	150.239 83	2.336 44	2.512
24	Gal3	Cassata et al. (2020)	150.331 44	2.162 37	2.934
25	XMM05	Leung et al. (2019)	36.449 43	-4.297 44	2.980
26	ADF22.1	Umehata et al. (2017)	334.385 13	0.293 22	3.089
27	ADF22.7	Umehata et al. (2017)	334.384 17	0.293 22	3.094
28	ADF22.5	Umehata et al. (2017)	334.381 17	0.299 45	3.089
29	Gal5	Cassata et al. (2020)	149.877 18	2.283 88	3.329
30	Gal4	Cassata et al. (2020)	150.278 34	2.258 82	3.400

ID: the identification number of the target in this work.

Name: The name of the target in the referenced piece of work.

Reference: The reference to the work containing the name of the target.

R.A.: The right ascension of the target in degrees in the ICRS.

DEC.: The declination of the target in degrees in the ICRS.

z: The spectroscopic redshift of the target.

In this thesis, we work with four distinct types of data for each target. The availability for each type of data is presented in Tbl. 2.2. Furthermore, in section 2.1, the photometric catalogue is presented, while the high angular resolution data from ALMA and HST are described in section 2.2.

Table 2.2: An overview of the available data for our sample.

ID	HST	ALMA		Photometry
	Filter	Line	Continuum	
1	F160w	CO(3-2)	...	✓
2	F814w	CO(3-2)	✗	✓
3	F814w	CO(5-4)	✓	✓
4	F160w	CO(2-1)	...	(✓)
5	F160w	CO(2-1)	...	(✓)
6	F160w	CO(2-1)	...	(✓)
7	F160w	CO(2-1)	...	(✓)
8	F160w	CO(2-1)	...	(✓)
9	F160w	CO(2-1)	...	(✓)
10	F160w	CO(2-1)	✗	✓
11	F160w	CO(2-1)	✗	...
12	F160w	CO(2-1)	✗	...
13	F160w	[CI](2-1)	✓	✓
14	F140w	CO(4-3), [CI](1-0)	✓	✓
15	F110w	[CI](1-0)	✓	✓
16	F110w	[CI](1-0)	✓	✓
17	F110w	CO(4-3)	✓	✓
18	✗	CO(4-3)	✓	✓
19	F160w	CO(3-2)	✓	✓
20	F160w	CO(3-2)	✗	✓
21	F160w	CO(3-2)	✗	...
22	F160w	CO(3-2)	✗	✓
24	F160w	CO(5-4)	✓	✓
25	✗	[CII](1-0)	✓	✓
26	✗	CO(3-2)	✓	✓
27	F160w	CO(3-2)	✓	✓
28	✗	CO(3-2)	✓	...
29	✗	CO(5-4)	✓	✓
30	✗	CO(5-4)	✓	✓

HST: The HST filter (see Appendix A) used to image the stellar emission.

ALMA Line: The emission line imaged by ALMA.

ALMA Continuum: Availability of the ALMA dust continuum image.

Photometry: Availability of photometry in the literature.

(✓) Private photometry is included which is not tabulated in this thesis.

... Missing data.

✗ Target is not detected in the image.

2.1 Photometry

We have collected photometric observations for our targets from UV to radio, using public multi-wavelength catalogues and data from the literature. Ten of the galaxies are located in the COSMOS survey area, and have good coverage from optical to FIR. For the rest of the sample we use photometric data from public catalogues and the literature. In Tbl. 2.2 the photometry column indicates for each source whether we could acquire photometric data. All the photometric data can be found in Appendix C, but an example is presented in Tbl. 2.3

Table 2.3: Photometric data collected for source 2. The observation column lists the facility, instrument and filter used to make the observation. The code column connects the filter transmission curve with the correct one in Stardust. The reference column lists references to the works from which the observations were collected. Observations without an uncertainty corresponds to 3σ upper limits.

Observation	Flux [Jy]		Uncertainty [Jy]		Code	Reference
	Value	Order	Value	Order		
CFHT/MegaCam/u*	3.105	10^{-7}	2.047	10^{-8}	352	Weaver et al. (2022)
CFHT/MegaCam/u	2.840	10^{-7}	1.277	10^{-8}	353	Weaver et al. (2022)
Subaru/HSC/g	1.114	10^{-6}	1.624	10^{-8}	314	Weaver et al. (2022)
Subaru/HSC/r	4.441	10^{-6}	2.979	10^{-8}	315	Weaver et al. (2022)

Subaru/HSC/i	1.057	10 ⁻⁵	4.133	10 ⁻⁸	316	Weaver et al. (2022)
Subaru/HSC/z	1.609	10 ⁻⁵	5.968	10 ⁻⁸	317	Weaver et al. (2022)
Subaru/HSC/y	2.020	10 ⁻⁵	7.884	10 ⁻⁸	318	Weaver et al. (2022)
VISTA/VIRCAM/Y	2.260	10 ⁻⁵	5.379	10 ⁻⁸	256	Weaver et al. (2022)
VISTA/VIRCAM/J	3.372	10 ⁻⁵	6.781	10 ⁻⁸	257	Weaver et al. (2022)
VISTA/VIRCAM/H	5.758	10 ⁻⁵	9.454	10 ⁻⁸	258	Weaver et al. (2022)
VISTA/VIRCAM/Ks	8.213	10 ⁻⁵	1.357	10 ⁻⁷	259	Weaver et al. (2022)
Subaru/Suprime-Cam/IB427	5.802	10 ⁻⁷	6.580	10 ⁻⁸	181	Weaver et al. (2022)
Subaru/Suprime-Cam/IB464	8.739	10 ⁻⁷	1.050	10 ⁻⁷	183	Weaver et al. (2022)
Subaru/Suprime-Cam/IA484	1.175	10 ⁻⁶	4.982	10 ⁻⁸	184	Weaver et al. (2022)
Subaru/Suprime-Cam/IB505	1.297	10 ⁻⁶	6.713	10 ⁻⁸	185	Weaver et al. (2022)
Subaru/Suprime-Cam/IA527	1.644	10 ⁻⁶	5.579	10 ⁻⁸	186	Weaver et al. (2022)
Subaru/Suprime-Cam/IB574	2.322	10 ⁻⁶	9.186	10 ⁻⁸	188	Weaver et al. (2022)
Subaru/Suprime-Cam/IA624	4.220	10 ⁻⁶	5.241	10 ⁻⁸	190	Weaver et al. (2022)
Subaru/Suprime-Cam/IA679	7.082	10 ⁻⁶	8.870	10 ⁻⁸	192	Weaver et al. (2022)
Subaru/Suprime-Cam/IB709	8.082	10 ⁻⁶	8.020	10 ⁻⁸	193	Weaver et al. (2022)
Subaru/Suprime-Cam/IA738	9.715	10 ⁻⁶	7.852	10 ⁻⁸	194	Weaver et al. (2022)
Subaru/Suprime-Cam/IA767	1.078	10 ⁻⁵	1.147	10 ⁻⁷	195	Weaver et al. (2022)
Subaru/Suprime-Cam/IB827	1.250	10 ⁻⁵	1.027	10 ⁻⁷	197	Weaver et al. (2022)
Subaru/Suprime-Cam/NB711	8.327	10 ⁻⁶	1.121	10 ⁻⁷	322	Weaver et al. (2022)
Subaru/Suprime-Cam/NB816	1.237	10 ⁻⁵	1.017	10 ⁻⁷	319	Weaver et al. (2022)
VISTA/VIRCAM/NB118	3.053	10 ⁻⁵	3.543	10 ⁻⁷	321	Weaver et al. (2022)
Subaru/Suprime-Cam/B	7.200	10 ⁻⁷	1.498	10 ⁻⁸	114	Weaver et al. (2022)
Subaru/Suprime-Cam/V	1.916	10 ⁻⁶	2.926	10 ⁻⁸	115	Weaver et al. (2022)
Subaru/Suprime-Cam/r+	4.669	10 ⁻⁶	2.213	10 ⁻⁸	116	Weaver et al. (2022)
Subaru/Suprime-Cam/i+	1.040	10 ⁻⁵	3.478	10 ⁻⁸	117	Weaver et al. (2022)
Subaru/Suprime-Cam/z++	1.747	10 ⁻⁵	1.653	10 ⁻⁷	118	Weaver et al. (2022)
Spitzer/IRAC/ch1	8.675	10 ⁻⁵	4.332	10 ⁻⁷	18	Weaver et al. (2022)
Spitzer/IRAC/ch2	6.272	10 ⁻⁵	2.318	10 ⁻⁷	19	Weaver et al. (2022)
GALEX/GALEX/NUV	2.527	10 ⁻⁸	7.035	10 ⁻⁸	121	Weaver et al. (2022)
SPITZER/MIPS/24	3.642	10 ⁻⁴	2.221	10 ⁻⁵	325	Jin et al. (2018)
JCMT/SCUBA2/850GHz	2.871	10 ⁻³	2.038	10 ⁻³	324	Jin et al. (2018)
VLA/3GHz	2.950	10 ⁻⁵	2.800	10 ⁻⁶		Jin et al. (2018)
Meerkat/1.3GHz	1.912	10 ⁻⁴				Jin et al. (2018)
Herschel/PACS/100	1.193	10 ⁻²	1.867	10 ⁻³	329	Liu et al. (2019)
Herschel/PACS/160	2.580	10 ⁻²	3.688	10 ⁻³	330	Liu et al. (2019)
Herschel/SPIRE/250	1.870	10 ⁻²	3.543	10 ⁻³	331	Liu et al. (2019)

For each observation we list the corresponding filter curve used for the SED fitting with STARDUST¹.

2.2 Spatially Resolved Images

For the targets in our sample, we have spatially resolved image maps imaged by HST and ALMA respectively.

2.2.1 HST

The images are mosaics, produced by [Brammer \(2022\)](#), of HST observations, which have their background emission subtracted. For each source we select the reddest HST filter, in which the source is detected, to perform the data analysis². The selected HST filter is presented in the HST column of Tbl. 2.2. Alternatively, if the source is not detected by HST in any of the filters, it is marked with an 'X' in the HST column of Tbl. 2.2. In Fig. 2.1 we illustrate the targeted rest-frame wavelengths of the selected HST filters. It is apparent, that most of the observations fall within rest-frame optical. However, for a few annotated cases the HST observations fall within rest-frame NIR and NUV.

¹For more information on the transmission filters in STARDUST, we refer to Appendix B on page 71.

²Filter wavelengths are presented in Appendix A on page 70.

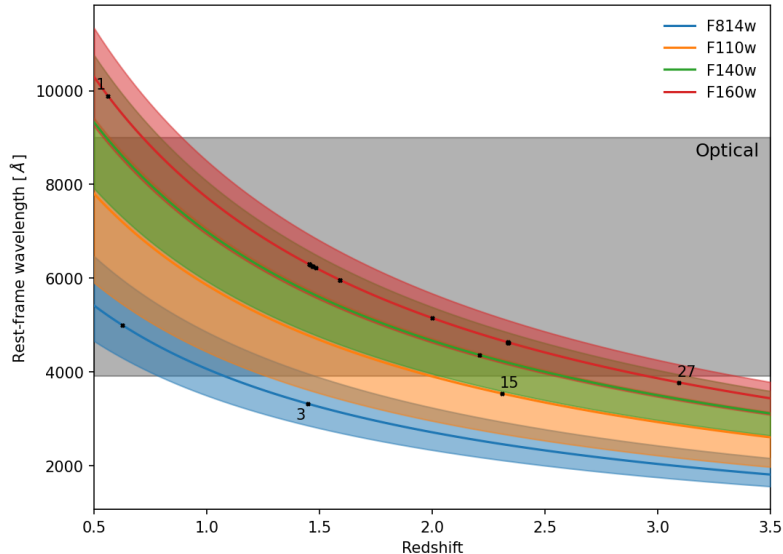


Figure 2.1: Rest-frame wavelengths targeted by the HST filters as a function of redshift in red to blue. The solid line refers to the central wavelength of the filter, and the shaded region displays the width of the filter, as described by *The SVO Filter Profile Service* (Rodrigo and Solano 2020). The black points represent the targeted rest-frame frequency for each of the targeted sources. The labelled targets fall outside the optical range and into either the NIR or the NUV.

Consequently, we are targeting the stellar emission of our targets with HST. And from Fig. 2.1 we are generally targeting shorter rest-frame wavelengths at larger redshifts.

2.2.2 ALMA

For most targets, we have CO(1-0), CO(2-1), CO(3-2), CO(4-3), [CI](1-0) or [CII](2-1) maps, which we expect to trace the molecular content of the galaxies. In some cases we have CO(5-4) and [CI](2-1) for which we expect to trace the high density molecular gas. Furthermore, in dust heavy systems, we extract the dust continuum. Images of the dust continuum and gas emission lines continuum were produced using the standard ALMA pipelines (*Rizzo et al. in preparation*, for details).

Targets for which the dust continuum could be extracted from the emission line spectral window, and the target is detected in the dust continuum map, are marked with a '✓' in the ALMA continuum column of Tbl. 2.2. Alternatively, sources, that are not detected in the dust continuum map, are marked with a '✗'.

In Fig. 2.2 to 2.6, we present the maps from HST and ALMA. We display the number of standard deviations. The coloured image illustrates the HST map. Moreover, the contours show the emission from the stellar population (black, HST data) and dust continuum (green, ALMA data) and the spectrally integrated gas emission lines (red, ALMA data). The lowest contour level is annotated in the top left, and each subsequent contour level is double the previous. Furthermore, the plot scale is displayed in the bottom left of each map. Also, the HST PSF and the ALMA beams are displayed in the bottom right of each map. However, since HST PSFs for the mosaics are not trivial, we instead show the half-maximum contour of a cubic interpolation of a point source in the HST mosaics. Finally, targets with red axes show galaxies that are classified as merging systems based on the analysis of their kinematics (*Rizzo et al. in preparation*).

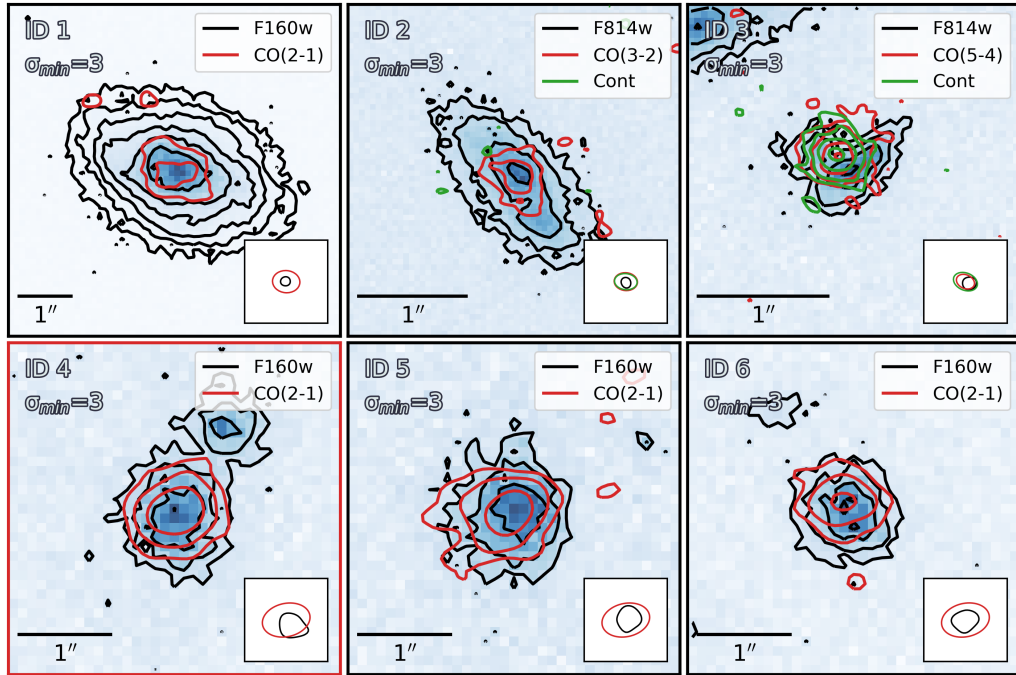


Figure 2.2: Data maps for source 1-6. The background shows the HST map in the filter indicated in Table ???. The black, red and green contours show the emission from stellar, gas and dust maps. The lowest contour level is annotated in the top left, and each subsequent contour corresponds to an increase by a factor of 2. The scale is shown in the bottom left. In the inset on the bottom right, the contours display the half maximum of the PSF and beams of HST and ALMA respectively. A red axis is used to mark merger systems.

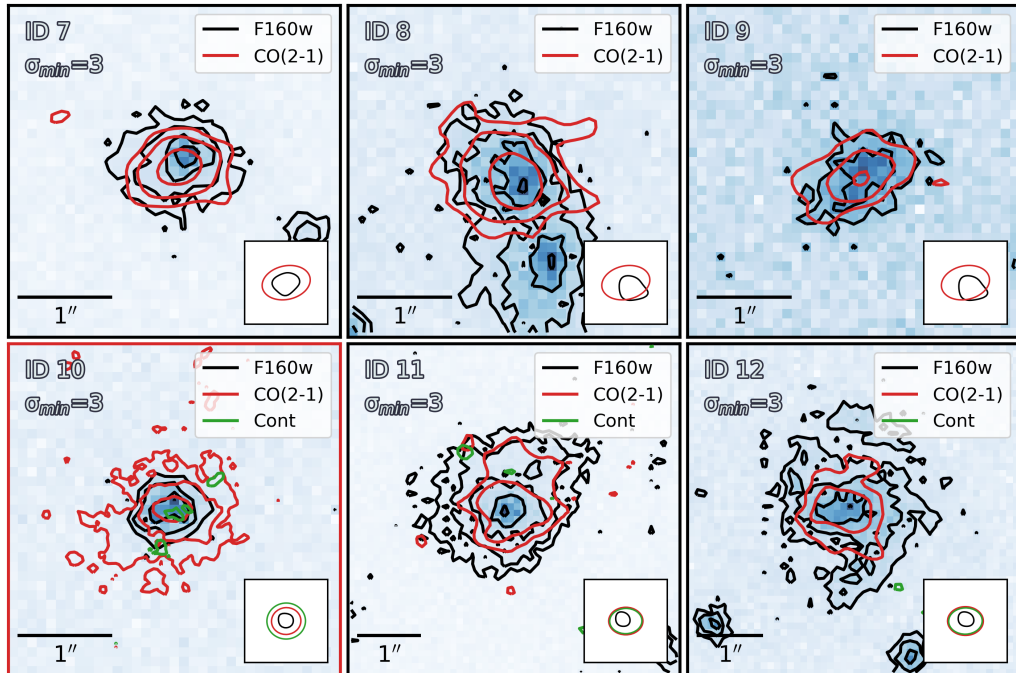


Figure 2.3: Same as Fig. 2.2, but for source 7-12.

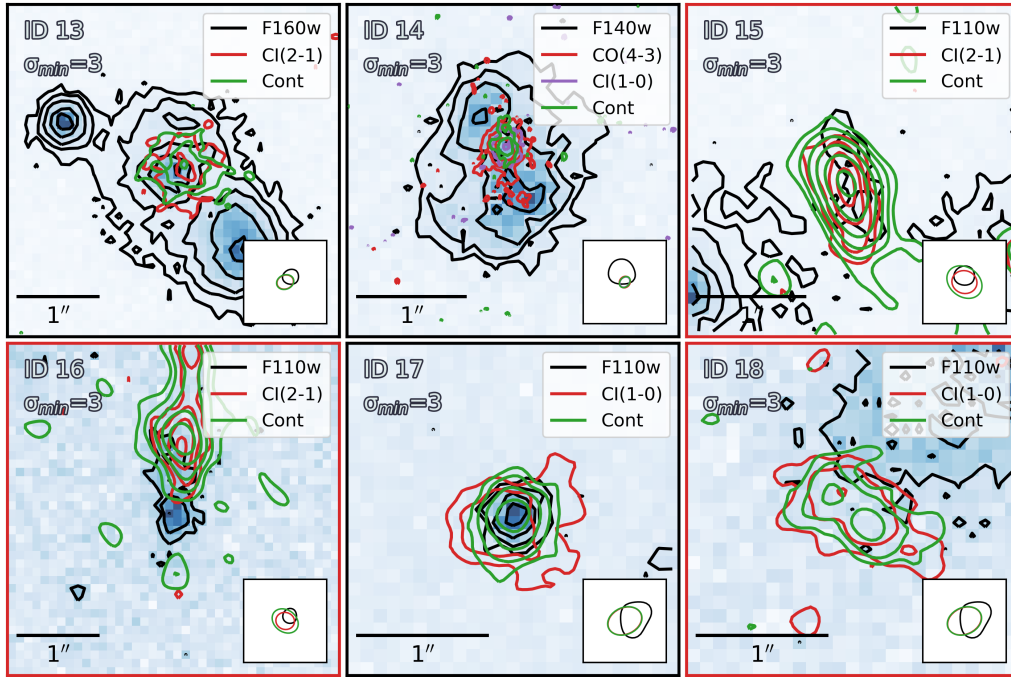


Figure 2.4: Same as Fig. 2.2, but for source 13-18.

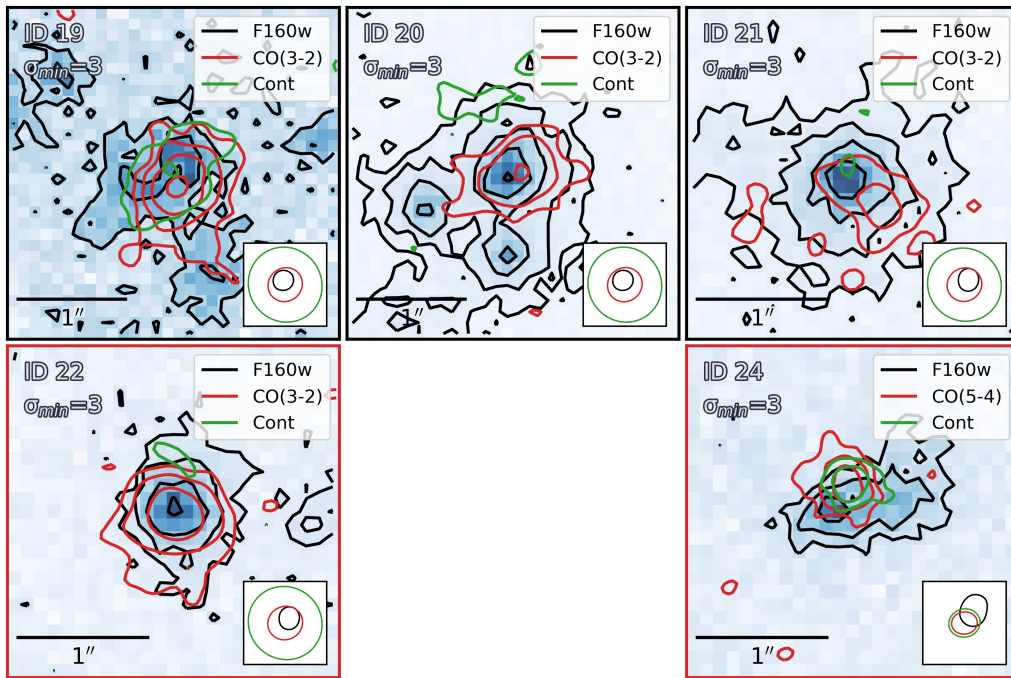


Figure 2.5: Same as Fig. 2.2, but for source 19-24.

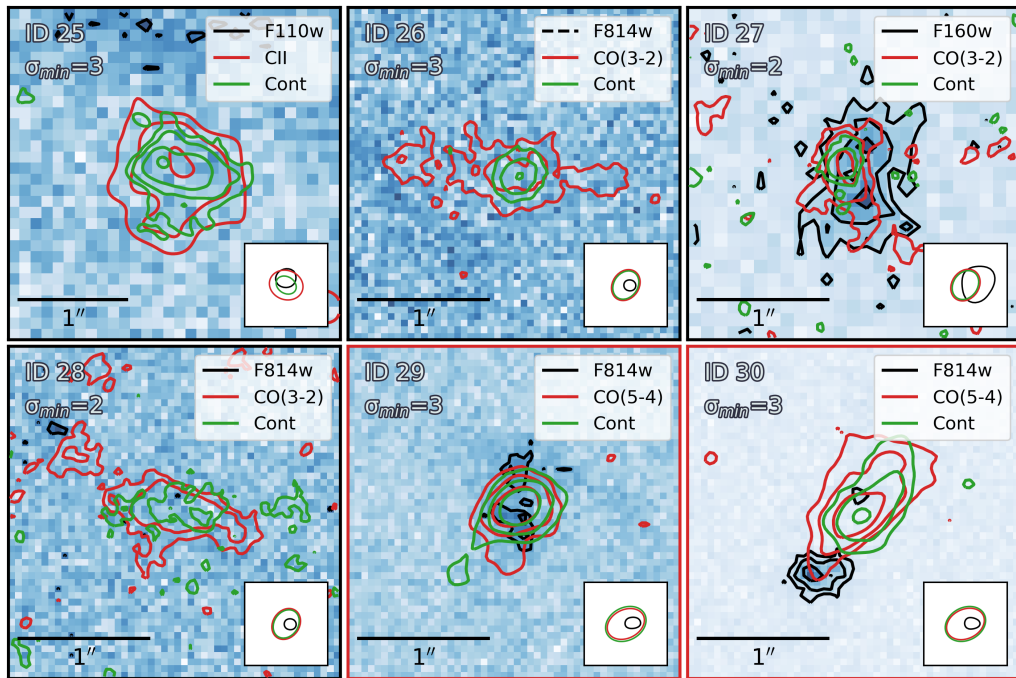


Figure 2.6: Same as Fig. 2.2, but for source 25-30.

3 Methods & Analysis

In this chapter, we present the methods and tools that we used to derive the SFRs, stellar masses and morphologies of our target galaxies.

3.1 SED fitting

Using the photometry that we have collected for the targets in our sample, we recover the stellar mass and SFR of each of our targets using SED fitting.

SED fitting codes widely used in the literature includes energy-balance routines such as CIGALE (Recently [Boquien et al. 2019](#)), MAGPHYS ([da Cunha et al. 2008](#)), SED3FIT ([Berta et al. 2013](#)). However, the informative power of these techniques are poor without proper template libraries and well established energy balance between the stellar and dust components of the SEDs. Recently, codes like STARDUST ([Kokorev et al. 2021](#)) employ an approach where the spectral templates of stellar population, dust continuum and AGNs are fitted independently, and then combined to reproduce the entire SED.

3.1.1 Stardust

STARDUST is a SED fitting algorithm that fits spectral templates to photometric observations. The code performs multi-component fits that linearly combines stellar libraries, AGN torus templates and IR models of dust emission arising from SF ([Kokorev et al. 2021](#)). Galaxies fitted in this thesis are assumed to not have AGNs, so we will only make use of the stellar- and dust templates.

The components are fit simultaneously, but independently from each other, without assuming an energy balance between the stellar population emission and the dust continuum emission.

In STARDUST, the stellar population is fitted with an updated version of the Stellar Population Synthesis (SPS) templates described in [Brammer et al. \(2008\)](#). SPS is a method of describing the stellar population as it evolves, by prescribing a SFH, through constant SFR in bins of cosmic time, under assumption of an IMF¹. Consequently, at each bin of cosmic time, the global SFR and stellar population is known. Additionally, the un-attenuated spectra of the entire stellar population can be extracted by keeping track of stellar evolution using stellar isochrones, and by assuming how the metallicity evolves over cosmic time. Furthermore, by assuming a dust attenuation law, an extra dimension is added to the template library, representing the amount of dust extinction, A_V . Consequently, the fitted template will carry information about the extinction, without having to derive it from the IR SED under the assumption of perfect energy balance ([Brammer et al. 2008](#)).

The stellar population templates in STARDUST are spectra of stellar populations ranging from rest-frame UV to NIR. The spectra are extracted from SPS models, and they represent a multivariate grid of stellar masses, SFRs, metallicities and dust extinction ([Brammer et al. 2008](#)). The templates have physical units of flux density, meaning that they can be directly fitted to photometric observations of galaxies. Consequently, the normalisation of that fitted template will scale the global stellar mass and SFR of the template.

However, galaxies can rarely be fitted adequately with a single stellar template. We know from the Milky Way that different components (i.e. the bulge and disk) have different stellar populations, SFHs, and metallicities. We also discussed in sec. 1.6 that while galaxies can evolve self-similarly, they are often subject to interactions with other galaxies. When we perform photometric measurements of distant galaxies, we essentially cover the whole galaxy with an aperture. Consequently, the observed emission is a coming from the sum of the different components with different SFHs.

¹STARDUST assumes a [Chabrier \(2003\)](#) IMF.

STARDUST solves this issue by having the stellar template library represent an optimised basis-set of models from a much larger parent template catalogue (Kokorev et al. 2021, Brammer et al. 2008). Consequently, non-negative linear combinations of the basis-set can reproduce any of the templates in the parent catalogue. This gives a much larger flexibility in fitting observed SEDs, and the global parameters like stellar mass and SFR can also be linearly combined.

Additionally, STARDUST fits not only the stellar population templates to the observed rest-frame UV-NIR photometry, but also fits the observed IR photometry to templates from an IR dust library.

To fit the rest-frame IR photometry, STARDUST uses the dust templates of Draine and Li 2007, with the addition of the updates described in Draine et al. (2014), hereafter DL07. These models describe the combined spectral contribution from warm dust and PAHs in PDRs, and the cold dust in the diffuse ISM heated by the bulk of the stellar population (Kokorev et al. 2021). Thus, the models explain a bimodal dust distribution, with the entire distribution being relevant for the dust mass, and the warm distribution being relevant for the SFR. The templates assume that the bulk of the dust mass is being heated by a radiation field of constant intensity U_{\min} . Additionally, a fraction of the total dust, γ , is being exposed to a gradient of radiation intensities ranging from U_{\min} to U_{\max} . Finally, they assume that a fraction of the dust, q_{PAH} , is locked in PAHs. STARDUST limits the templates to those having $U_{\max} = 10^6$ and a power-law index of the high-intensity regions of $\alpha = 2$. Consequently, there are three free parameters (U_{\min} , γ and q_{PAH}) for each dust continuum template in STARDUST, and the dust mass, M_{dust} , is retrieved from the normalisation of the template to the photometry². Moreover, from the parameterisation in Draine and Li (2007), we can relate the U_{\min} and γ parameter to the the average intensity of the radiation field, $\langle U \rangle$ of the STARDUST DL07 templates, in the following way,

$$\langle U \rangle = (1 - \gamma) U_{\min} + \left(\gamma \cdot U_{\min} \ln \left[\frac{10^6}{U_{\min}} \right] \right) \cdot \left(1 - \frac{U_{\min}}{10^6} \right)^{-1} \quad (3.1)$$

$$(3.2)$$

By integrating the SED of the fitted dust continuum template from 8 – 1000 μm , and if present, removing the AGN contribution, the IR luminosity is retrieved. Finally, it is converted to a SFR using the relation of Kennicutt 1998. Consequently, the IR SFR is only reliable if one can adequately constrain the location, peak and width of the dust continuum.

The uncertainties on the derived parameters are calculated by adding in quadrature the uncertainties coming from the linear combination fit of the SPS templates fit and the uncertainties coming from selecting the best DL07 template due to the uncertainty of the photometric data.

The linear combination uncertainties are calculated by a Monte Carlo (MC) simulation, re-sampling the best-fitted coefficients of the linear combination 10^4 times. For each iteration the global properties are calculated, and the upper and lower limit is defined as the 84th and 16th percentile respectively.

The uncertainties on the IR properties are calculated by considering all templates that fall within the 68% confidence interval range of the best fit DL07 template. The uncertainty on each IR global parameter is simply the width of that distribution with respect to the global parameter.

Consequently the uncertainties on the stellar mass is only estimated from the MC simulation. In cases where the algorithm is really certain of the linear combination of the SPS templates, the uncertainties will be very underestimated. However, we adopt a minimum uncertainty of 25% as described in Sorba and Sawicki (2015).

²Assuming a flat Λ CDM cosmology with $\Omega_{\text{m},0} = 0.3$, $\Omega_{\Lambda,0} = 0.7$ and $H_0 = 70 \text{ km s}^{-1} \text{ Mpc}^{-1}$.

3.1.2 Fitting

To convert our photometric observations collected from the literature into data sets that STARDUST can interpret, we have built the tool Cataloguer For Stardust (C4S)³. We use the tool to construct our photometric catalogue.

We divide our sample of galaxies into four groups, when fitting with STARDUST, as illustrated in Fig. 3.1

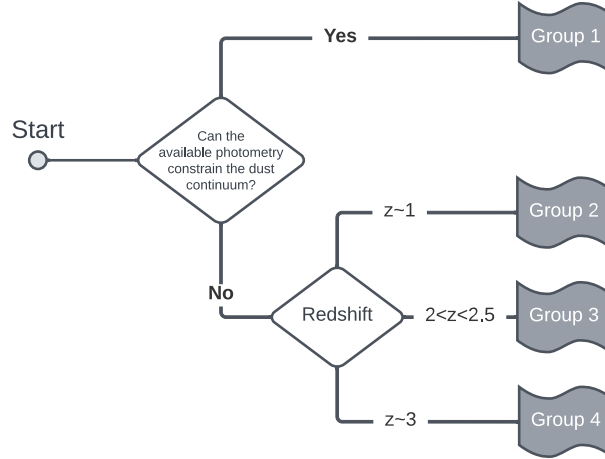


Figure 3.1: Illustration of how targets were divided into groups based on the available photometry, in preparation for the SED fitting with STARDUST.

For galaxies in group 2-4, we have to make assumptions about them to constrain the parameters, such that we get reasonable fits. In essence, it is not reasonable to fit four free parameters with < 5 data points. Recent studies have shown that for MS galaxies, the average intensity of the radiation field $\langle U \rangle$, or in this case equivalently U_{\min} (Schreiber et al. 2018), which is strongly correlated with the temperature of the dust, increases with redshift all the way up to $z \sim 4$ (e.g. Magdis et al. 2012, Béthermin et al. 2015, Béthermin et al. 2017, Schreiber et al. 2018, Kokorev et al. 2021). This is illustrated in Fig. 3.2. Consequently, we can restrict the template space when fitting with

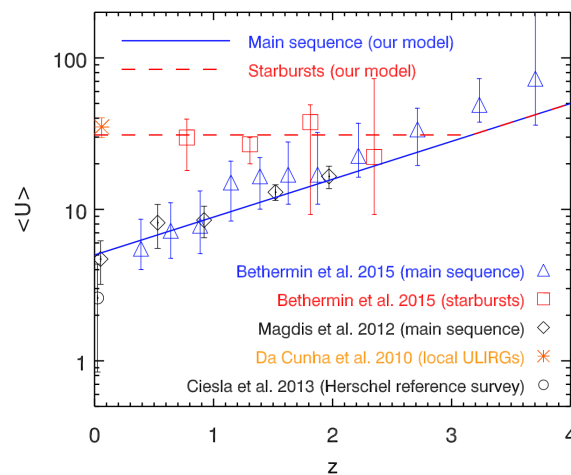


Figure 3.2: The evolution of the mean intensity of the radiation field, $\langle U \rangle$, as a function of redshift, z (Béthermin et al. 2017, Fig. 3). SBGs and MSGs are separated and plotted in red and blue respectively.

³The tool and the documentation pertaining to its usage can be found here: <https://github.com/skrrrlev/Cataloguer-4-Stardust>.

inadequate data, to match typical values of U_{\min} to that of MS galaxies at the given redshift or SB galaxies.

In Kokorev et al. (2021), SB galaxies are fitted by fixing $\langle U \rangle = 40$. However, it has been found that the $\langle U \rangle$ of SBGs can vary substantially to higher and lower values (e.g. Magdis et al. 2012, Tan et al. 2014, Béthermin et al. 2015). Consequently, we have assumed the range of $\langle U \rangle$ illustrated in Fig. 3.3. For all assumed SBGs in group 2-4, we derive the assumed $\langle U \rangle$ by selecting templates

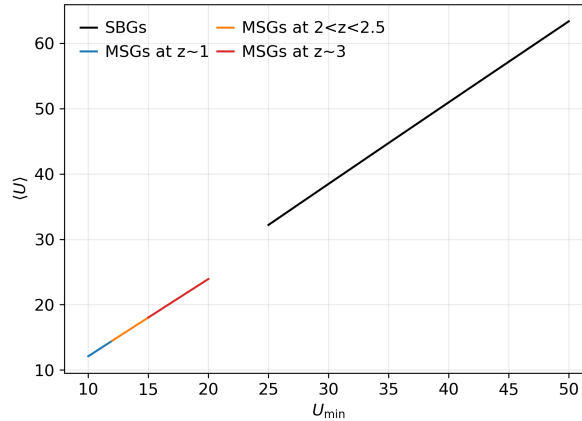


Figure 3.3: Assumptions of $\langle U \rangle$ as a function of U_{\min} and γ for galaxies in group 2-4. For SBGs $\gamma = 0.03$ and for MSGs $\gamma = 0.01$.

with $U_{\min} \geq 25$ and with $\gamma = 0.03$.

Furthermore, for all MSGs in group 2-4 we derive the assumed $\langle U \rangle$ ranges, illustrated in Fig. 3.3, by selecting templates with $\gamma = 0.01$ and $8 \leq U_{\min} \leq 10$, $10 \leq U_{\min} \leq 12$ and $12 \leq U_{\min} \leq 15$ respectively. Essentially, we're assuming increasing dust temperatures with increasing redshift, corresponding to increased IR luminosity and in turn increased IR SFR. We have compared our assumptions with other studies (Magdis et al. 2012, Béthermin et al. 2015), and find that our narrow range of assumed $\langle U \rangle$ values of MSGs are within their uncertainties.

Based on the values of SFRs and stellar masses from the literature, we fitted targets 15 and 16 under the assumption that they are SB galaxies and targets 13, 14, 19, 20, 22, 26 and 27 under the assumption that they are MS galaxies. Additionally, Targets 4, 5, 6, 7, 8 and 9 are all in the same galaxy cluster with limited amount of dust. We fit them as MSGs, but for those targets we retrieve the SFR from the optical photometry.

Finally, targets 1, 2, 3, 10, 17, 18, 24, 25, 29 and 30 are categorised as group 1 galaxies. In Béthermin et al. (2015), $\langle U \rangle \gtrsim 6$ for all galaxies with $z > 0.5$. Consequently, it does not make sense to fit the entire $\langle U \rangle$ parameter space, even when we have adequate data. Thus, for group 1 galaxies, we fit them assuming that $U_{\min} \geq 1.70$, corresponding to $\langle U \rangle > 2$ for $\gamma = 0.01$. However, we also keep γ as a free parameter, as the data is adequate to find a good fit.

3.2 Analytical Surface Brightness Profiles

As mentioned in section 1.6.4, the spatial light profile of a galaxy can be analytically modelled by the Sérsic profile, which is defined by three free parameters; the effective radius, the intensity at the effective radius and the Sérsic index. In this thesis, we employ GALFIT to fit Sérsic profiles to the spatially resolved surface brightness images.

3.2.1 Galfit

GALFIT is a tool for extracting information about galaxies, stars, globular cluster, stellar disks, etc., by using parametric functions to model objects as they appear in two-dimensional digital images (Peng et al. 2002). GALFIT employs the Levenberg-Marquardt (LM) non-linear least-squares fitting algorithm. Least-squares fitting algorithms determines the goodness of fit by calculating χ^2 , and computing how to adjust the parameters to minimise χ^2 . In GALFIT, the reduced χ^2 (χ_ν^2) is used, which is χ^2 normalised to the degree of freedom ν ,

$$\nu = N_{\text{pixels}} - N_{\text{args}} \quad (3.3)$$

$$= (nx \cdot ny) - N_{\text{args}}, \quad (3.4)$$

where N_{args} is the number of free parameters in the fit. In the GALFIT fit of the Sérsic surface brightness profiles, the centre pixel position, the axes ratio and the position angle are also fitted, adding 4 free parameters to the Sérsic profile.

$$\chi_\nu^2 = \frac{1}{\nu} \sum_{x=1}^{nx} \sum_{y=1}^{ny} \left(\frac{f_{\text{data}}(x, y) - [f_{\text{model}}(x, y, \text{args}) \otimes f_{\text{PSF}}(x', y')]}{\sigma(x, y)} \right)^2 \quad (3.5)$$

From eq. (3.5), it is obvious that GALFIT needs three types of input. First, $f_{\text{data}}(x, y)$ is the two-dimensional digital image of the galaxy, where x and y are discrete values used to identify each pixel. Secondly, $f_{\text{PSF}}(x', y')$ is the PSF or beam of the instrument that created the data. Lastly, $\sigma(x, y)$ is an image that contains the standard deviation for each of the pixels in the data image. Also, from eq. (3.5), it is obvious that χ_ν^2 is a function of the arguments that parameterises the analytical model(s).

The LM algorithm is combination of the The Gauss-Newton Method and the The Gradient Descent Method, and is based on a dampening parameter (Gavin 2019). By calculating the gradients with respect to the model parameters, these parameters can be changed towards the direction, which has the steepest decline in the value of χ_ν^2 . This is what happens for large values of the dampening parameter, and the parameter is initialised at a large value. As the solution approaches a minimum, the dampening parameter decreases, which makes the algorithm work like the Gauss-Newton Method. This method presumes that the solution to χ_ν^2 function is approximately quadratic near the optimal solution. Thus it makes a Taylor expansion of the model of a function of the parameters and a perturbation, and finds the value of the perturbation which yields the minimum of the quadratic χ_ν^2 function.

In GALFIT, the formal uncertainties of the reported fitting parameters are closely related to the covariance matrix. However, the formal uncertainties are only representative when the fluctuations in the residual map are caused by Poisson noise (Peng et al. 2010). Consequently, the uncertainties are representative only in idealised situations, such as image simulations. In real images, the residuals are caused by the structure of the galaxies and the PSFs, causing imperfect matches of analytical models to the data. These factors cause the formal uncertainties reported by GALFIT to be only lower estimates (Peng et al. 2010).

3.2.2 Data Preparation

As discussed, GALFIT takes at least three input. However, to ensure accurate results and low computational time, we make full use GALFIT's features. To prepare the data for fitting, we have developed a semi-automatic data preparation pipeline that builds all input to GALFIT for multiple data maps in parallel.

3.2.2.1 HST Images

Our HST images are wide Field Of View (FOV) mosaics made from multiple observations. They contain an image, which is a map where every pixel is represented by the flux density and a weight

map where every pixel contains σ_{pix}^{-2} , with σ_{pix} being the standard deviation for that pixel. An example is illustrated in Fig. 3.4

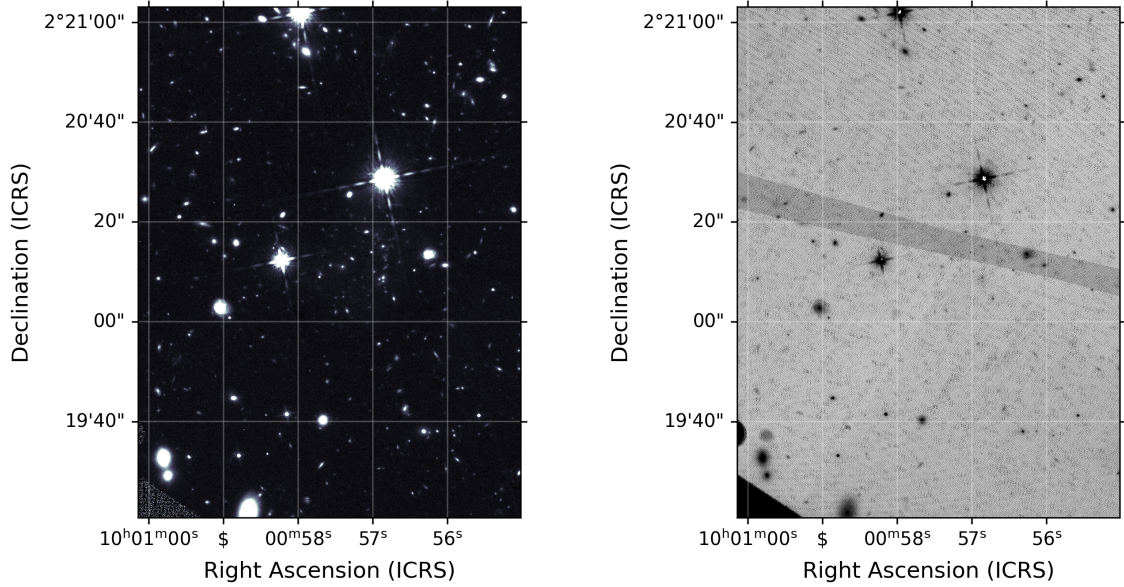


Figure 3.4: Illustration of the HST F160w mosaic for target 22 of our sample. On the left is the map containing the flux densities, and on the right is the weight map.

To save computational resources, we crop the flux-density image around the source. The resulting map acts as f_{data} in eq. (3.5). In Fig. 3.5 we illustrate the cropping of the flux-density map of Fig. 3.4. Additionally, we use the header of the fits file to reconstruct the AB magnitude zero-point, in

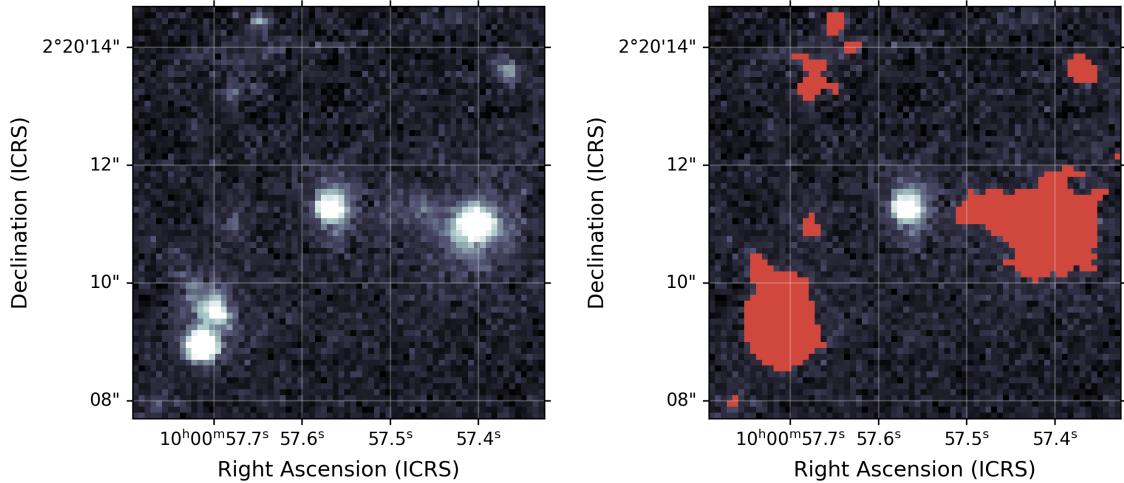


Figure 3.5: The left image is a plot of the cropped HST F160w mosaic for target 22 of our sample which, when fitting with GALFIT, corresponds to f_{data} in eq. (3.5). The right image is an illustration of the mask that we build for the left image. All pixels in red are non-zero values in the binary mask map.

the following way, depending on the available keywords.

$$ZP_{\text{ABmag}} = -2.5 \log_{10} (\text{PHOTOFNU}) + 8.9 \quad (3.6)$$

$$= -2.5 \log_{10} (\text{PHOTFLAM}) - 21.10 - 5 \log_{10} (\text{PHOTPLAM}) + 18.6921 \quad (3.7)$$

Next, we build a mask for the f_{data} map. Essentially, the mask is a binary map that instructs GALFIT to ignore any pixel in the f_{data} map that has a non-zero pixel-value in the mask map. We use it to mask out nearby sources in the FOV and dead pixels in the mosaic.

To build that map, we first build a binary dead pixel map for which a non-zero pixel value is assigned to every pixel that have value zero in the weight map. Then, we extract all astronomical sources in the image by building a segmentation map using SExtractor (Bertin and Arnouts 2010). Principally, a segmentation map is a map where every astronomical source is assigned a unique pixel value. Consequently, all pixels that have value zero in the segmentation map corresponds to pixels that do not contain significant emission from astronomical sources.

Finally we construct the mask in the following way. We apply the same crop that we applied to get f_{data} to the segmentation map and the dead pixel map. Next, we remove the target source from the segmentation map by identifying the unique value of the source in the segmentation map, and setting all pixels with that value to zero. Then we extract all non-zero pixels in the segmentation map. We apply a median filter⁴ to smooth the binary source mask. Lastly, we add all pixels in the dead pixel mask to the mask, so that galfit does not include dead pixels in the fitting procedure. An example of a binary mask is illustrated in Fig. 3.5.

Next, we construct the σ map that goes into GALFIT. The process is fairly simple: For all pixels in the weight map, that are not in the dead pixel map, we apply the following operation,

$$\sigma(x, y) = \sqrt{\frac{1}{K \cdot \text{weight}(x, y)}}, \quad (3.8)$$

Where K is a scaling constant that ensures the proper normalisation of the σ map. Additionally, all pixels that are marked by the dead pixel mask is set to an arbitrarily large value 10^6 . To derive the scaling constant K , we start out by constructing a noise pixel mask, which is a binary map, where all non-zero values correspond to pixels only influenced by noise. We start from the segmentation map, and we apply a binary dilation⁵. Essentially, the resulting binary mask has non-zero values for all pixels that are no further than 7 pixels away from a pixel containing significant contribution for astronomical sources. Consequently, the resulting binary map covers with high certainty all of the pixels influenced by astronomical sources in the image. Additionally, we add all the dead pixels to the binary map. Finally, we invert the map, so that all non-zero pixels are noise pixels. Then we extract all noise pixels from the full mosaic. In Fig. 3.6 we show the histogram of all noise pixel flux densities divided by the standard deviation.

If the mosaic is constructed correctly, the distribution should have a standard deviation of 1. Consequently, we extract the scaling constant as $K = \sigma_{\mathcal{N}}^{-2}$ where $\sigma_{\mathcal{N}}$ is the standard deviation of the fitted Normal distribution. Finally, we crop the σ map, to match that of the f_{data} map. We show an illustration of the derived σ map derived for source 22 in Fig. 3.6.

The final map that goes into eq. (3.5) is f_{PSF} , representing the PSF of the HST mosaic. The PSF of a mosaic is not a easy to model as a trivial analytical probability distribution. Instead, we represent the PSF by using a point source in the mosaic FOV, due to the fact that the resulting distribution of the point source is a discrete model of the PSF. We've gone through the mosaics of all our targets and identified sources displaying the classical airy disk and spike diffraction patterns. We select a point source as near the target galaxy as possible, and without other sources in the nearby FOV. This is illustrated in Fig. 3.7. We crop a region around the point source and use that map to construct the PSF. If there are any contribution not coming from the point source in the map, we manually mask it out. Additionally, we apply the same crop to the dead pixel mask and the full

⁴Using the `ndimage.median_filter` method from the SciPy package (Virtanen et al. 2020).

⁵Using the `ndimage.binary_dilation` method from the SciPy package (Virtanen et al. 2020).

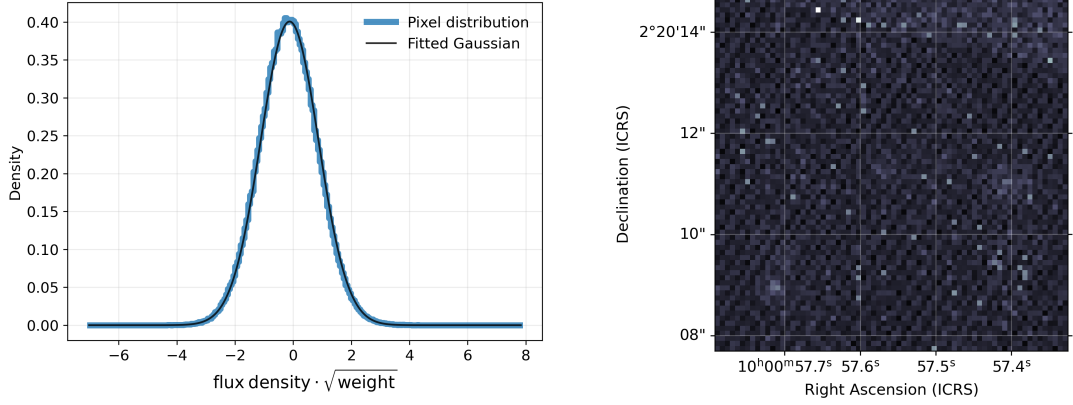


Figure 3.6: Illustration of the creation of the σ map for target 22 of our sample. The left figure shows the density histogram of the noise distribution, with a fitted Normal distribution used to derive the scaling factor K . Note that the weight map contains values of zero for all dead pixels and σ^{-2} for all other pixels. The right image shows the σ map created according to eq. (3.8).

FOV σ map. We use the dead pixel mask, to identify missing pixels in the point source map. In case there are any, we apply a linear interpolation⁶ to recover the missing pixel values. Next, we mask out the contribution coming from the noise. We create a simple binary mask by selecting all pixels that have $\text{SNR} < 3$. To avoid rough edges, we apply a median filter⁷ to smooth the binary mask. We select a pixel smoothing size of 3 pixels, and we further investigate the consequence of that decision in section 3.2.2.2. Next, we normalise the point source map, and centre it according to the requirements of GALFIT. The final result is the discrete map f_{PSF} which represents the discrete PSF of the mosaic, and it is illustrated in Fig. 3.8.

Now, we have constructed all the input files for GALFIT, however, we cannot quite proceed with the fitting yet. Since GALFIT is a χ^2 based least-squares fitting algorithm it is prone to local minima in the χ^2 distribution. Consequently, we will need to provide proper estimates of the parameters of the analytical Sérsic model to recover the best fit. First, we estimate the centre of the analytical model by selecting the pixel with the largest value from the f_{data} map. Secondly, we estimate the brightness of the target source in the f_{data} map. We do this by first creating a rough source mask by selecting all pixels with $\text{SNR} > 3$ in the f_{data} map and removing all pixels with non-zero values in the mask map. Next, we sum all the pixels in the rough source mask and use the calculated zero-point to calculate the estimated brightness of the target. Thirdly, we estimate the effective radius of the semi-major axis of the target source. From the centre defined above, we go along an array of pixels set by an angle from the positive x-axis. For an array of angles, we estimate the half-light radius by calculating the amount of pixels between the centre and the pixel with a value closest to half of the value of the centre pixel. Our estimate of the half-light radius is the average across the array of angles. For circular face-on sources this should be a good approximation, and for inclined sources we should slightly underestimate the actual half-light radius. Lastly, for the remaining parameters, the Sérsic index, the axis ratio and the position angle, we put 2, 0.5 and 0° respectively, and let GALFIT fit the proper values.

With that in mind, we can apply GALFIT to our HST mosaics. The first order of business is to estimate the effect of smoothing the binary mask used to create the PSF.

3.2.2.2 PSF Smoothing

As mentioned in section 3.2.1, the uncertainties outputted by GALFIT are not representative of the uncertainties coming from fitting empirical observations of galaxies with estimated PSFs. Conse-

⁶Using the `interpolate.griddata` method from the SciPy package (Virtanen et al. 2020).

⁷Using the `ndimage.median_filter` method from the SciPy package (Virtanen et al. 2020).

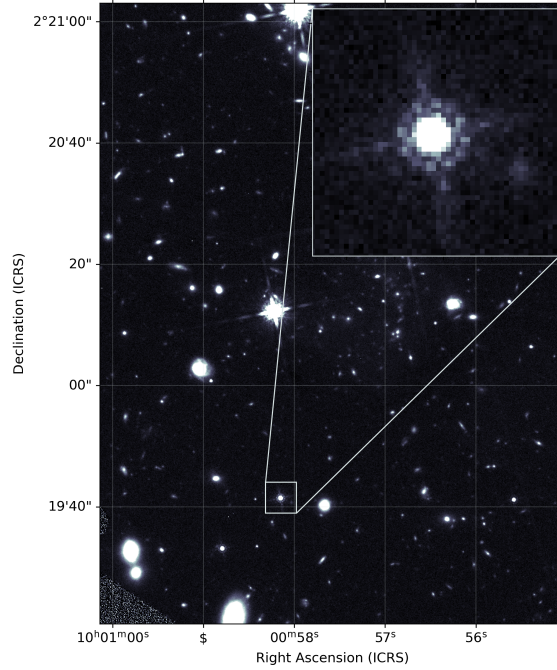


Figure 3.7: An illustration of how we manually selected a point source in the mosaic containing target 22, to act as a discrete representation of the PSF.

quently, we set out to estimate the uncertainties coming from fitting with different realisations of the discrete f_{PSF} with respect to the smoothing of the binary mask used to define f_{PSF} .

We adopt a Monte Carlo (MC)⁸ approach build around the point-source that we use for creating the PSF. We first create 7 realisations of the f_{PSF} map using different pixel sizes for the median filter smoothing of the binary mask. For each iteration, we create three analytical models of 2D Sérsic profiles by sampling the model parameter space. One model samples a space of unresolved effective radii ($\sim 0.4 \cdot \text{FWHM}_{\text{PSF}}$), and a space of Sérsic indices around $n \sim 4$. Another model samples a space of resolved effective radii ($\sim 1.5 \cdot \text{FWHM}_{\text{PSF}}$) and a space of Sérsic indices around $n \sim 1$. The last model samples the space of extended effective radii ($\sim 5 \cdot \text{FWHM}_{\text{PSF}}$) and Sérsic indices around $n \sim 1$. For each of the three 2D Sérsic models, we then convolve them with the non-smoothed PSF.

For each of the three models we add two realisations of noise, such that for each model we get a map in which the noise is low, corresponding to a high source SNR, and one in which the noise level is high, corresponding to a low source SNR. The high SNR and low SNR case are created by drawing noise samples from a Normal distribution for which the standard deviation is set dividing the peak flux density of the model with 100 and 25 respectively. As a result we have six different synthetic galaxy sources. We fit each of them with all realisations of the smoothed PSF, and we calculate the residual between the analytical parameters of the synthetic maps and the parameters retrieved by GALFIT. Finally, we average our results over every iteration, and we illustrate it Fig. 3.9. The plot shows the typical orders of uncertainties caused by fitting with PSFs that are not completely representative for the observed f_{data} . This will be the case for all of our fitting regardless, due to the fact that we use discrete representations of the PSF extracted from the mosaic. In general, uncertainties increase with smoothing factor, corresponding to uncertainties increasing with the applied PSF differing from the actual PSF. Consequently, we adopt a smoothing factor of 3 pixels, that will make sure the edges of the f_{PSF} map is not rough, and also does not differ too much from

⁸For more information on the MC method, we refer to Appendix D on page 169.

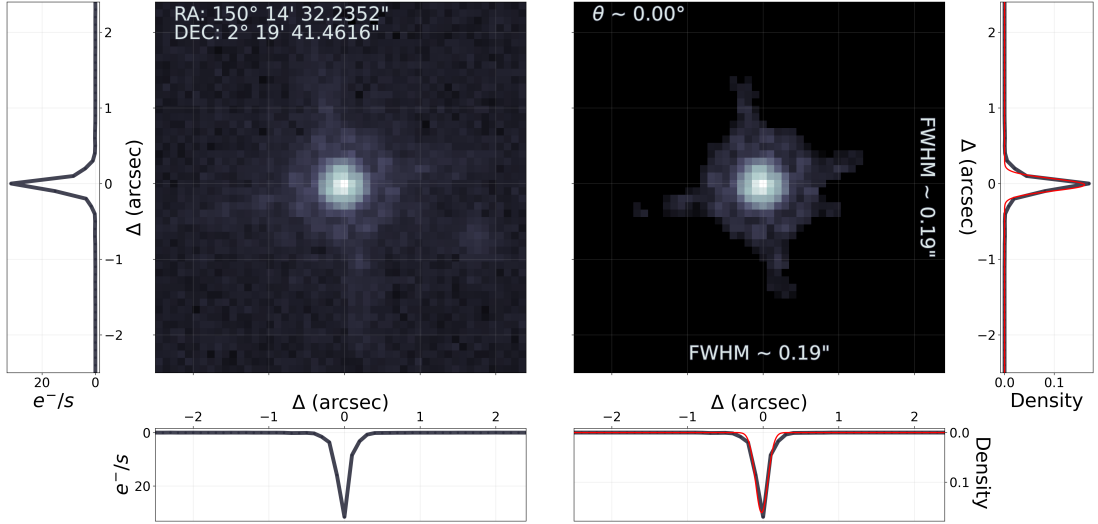


Figure 3.8: From point-source to PSF. **Left:** The map displays the source used to create the PSF in a logarithmic colour scale. The left and bottom panels shows the profile through the pixel of the highest value. The annotated coordinates are the coordinates of the centre of the map. **Right:** The map displays the PSF created from the left figure. The annotated FWHM along each axis are calculated by fitting a two-dimensional Gaussian to the map. The right and bottom panel shows the profile through the highest value pixel in black and the profile of the fitted two-dimensional Gaussian in red. The annotated angle describes the position angle of the fitted two-dimensional Gaussian counterclockwise from the positive x-axis.

the original discrete representation.

3.2.2.3 ALMA Images

Our ALMA images are single observation images, that contain a map where every pixel is represented by the velocity integrated flux density per beam. Consequently, an AB magnitude zero-point cannot be simply constructed to allow GALFIT to appropriately calculate the brightness.

For the ALMA maps we start by modelling the synthetic beam. Essentially, for each image we have the FWHM of the beam semi-major and semi-minor axis, and the position angle of the beam with respect to celestial north. We model the beam as a multivariate Normal distribution using that,

$$\text{FWHM} = 2\sqrt{(2 \ln 2)\sigma}. \quad (3.9)$$

Additionally, we centre the map according to the requirements of GALFIT. We use the resulting map as f_{PSF} in eq. (3.5). Additionally, we apply a crop to our data image, such that the width of the image is ~ 20 times the FWHM of the beam semi-major axis. We use that map as f_{data} in eq. (3.5). In Fig. 3.10 we show an example of a data map and a PSF map.

Next, we construct a noise pixel mask using an iterative approach. As for the HST images, we first construct a segmentation map using SExtractor and apply a binary dilation to all non-zero pixels. We invert the map to acquire a mask of all noise pixels. For all the noise pixels, we calculate the global mean and standard deviation. We then recompute the segmentation map, inputting the mean and standard deviation as the lower limit for source detection. Finally, we apply a binary dilation and invert the map to get the noise pixel mask.

Since we do not have a weight map for the ALMA data, we approximate the sigma image as a flat image with a value of the standard deviation of the noise pixel distribution. Additionally, we can construct the mask from the created segmentation map, by deselecting the source in the segmentation map, selecting all non-zero pixels and then inverting the map. With that in mind, we have all the input that we need to run GALFIT. Finally, we must estimate the parameters of the

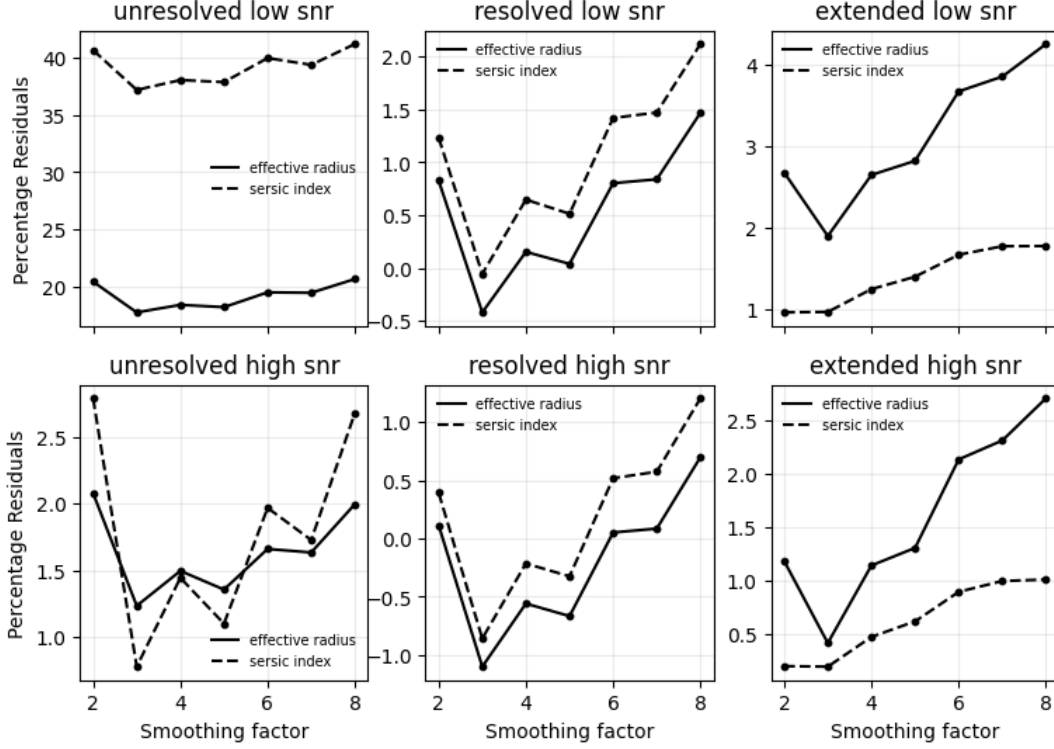


Figure 3.9: Average residuals between the analytical parameters of noisy synthetic 2D Sérsic models and the parameters recovered from fitting with GALFIT with different realisations of smoothed PSFs, for different size and noise realisations. The smoothing factor indicates the amount of pixels used by the median filter to smooth the binary mask which selects the pixels of the point source that goes into the discrete representation PSF.

analytical model, to get a good fit.

Instead of estimating the brightness of our source, we instead create a fake magnitude zero-point. Essentially, GALFIT only fits sources if the brightness of the source is $< 30 \text{ mag}_{AB}$, so we construct a zero-point that will make GALFIT fit the brightness to $\sim 25 \text{ mag}$. By selecting the source in the segmentation map we create a binary mask of the source. We smooth that mask using a median filter, to avoid rough edges. We select all pixels in f_{data} within the mask, and sum them. Then we calculate the fake zero-point in the following way,

$$ZP_{\text{fake}} = 25 + 2.5 \log_{10} \left(\sum \text{source pixels} \right). \quad (3.10)$$

For the remaining parameters of the Sérsic model, we estimate them in the same way we did for the HST models.

3.2.3 Fitting

When fitting our sources we simply run GALFIT with the previously defined input and parameter estimates, corresponding to fitting seven free parameters. We then calculate a normalised residual map in the following way,

$$f_{\text{residuals}}(x, y) = \frac{f_{\text{model}} - f_{\text{data}}}{f_{\text{data}}} \quad (3.11)$$

We visually inspect the map, to ensure that the fit is good. If not, we fix model parameters to better estimates, re-fit, and retrieve updates for the remaining parameters from the fitting. We iteratively apply this approach until we reach a solution that represents a good fit.

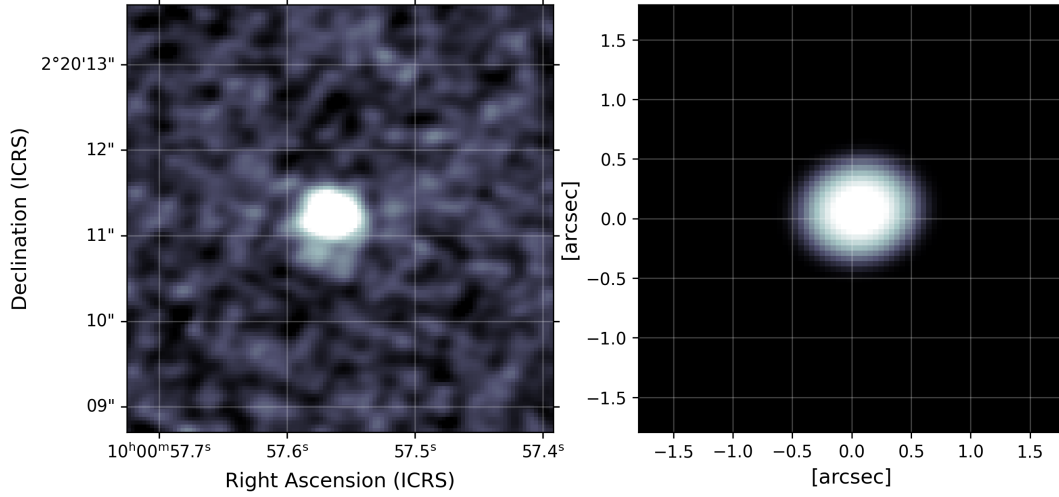


Figure 3.10: Input for GALFIT for the CO(3-2) emission line for target 22 of our sample. Note that the scale of the two images are different. **Left:** The cropped map representing f_{data} in eq. (3.5). **Right:** The synthetic beam representing f_{PSF} in eq. (3.5)

Since in some cases, there are systematic residuals in the central regions for HST maps, we add an unresolved co-spatial bulge with $r_e \ll \sigma_{\text{PSF}}$, $n = 4$, $b/a = 1$ and $\theta = 0$. Consequently, we add a single free parameter, the brightness of the unresolved co-spatial bulge, to the model. We fit that model and extract the χ^2 . Finally, we perform an F-test for additional parameters, to investigate whether the surface brightness profile is statistically better represented with a co-spatial unresolved bulge. We discuss the F-test for additional parameters in detail in sec. 3.3. Moreover, we adopt a 99.9% significance level for discarding the null-hypothesis.

For ALMA maps we additionally lock the Sérsic index to $n = 1/2$, corresponding to fitting a 2D Gaussian, and re-fit the map. Again, we perform an F-test for additional parameters, to investigate whether we have the resolution to properly model the shape of the surface brightness profile.

3.3 F-test for Additional Parameters

When carrying out the fitting of analytical surface brightness models to the data maps, it will be of interest whether or not it is statistically significant to fix a model parameter or add another model to the fit. However, since the degree of freedom changes between the two fits, the χ^2 's cannot be directly compared. Instead, we will carry out an F-test for additional parameters.

The F-test for additional parameters is based upon the fact that the ratio, f , of two χ^2_ν distributed statistics follows an F-distribution (Bevington and Robinson 2003, ch. 11.4).

$$f = \frac{\chi_1^2/\nu_1}{\chi_2^2/\nu_2}, \quad (3.12)$$

where χ_i^2 is the χ^2 statistic of distribution i with a degree of freedom of ν_i . The ratio f follows the F-distribution, which has a probability density function,

$$p_f(f; \nu_1, \nu_2) = \frac{\Gamma[(\nu_1 + \nu_2)/2]}{\Gamma(\nu_1/2)\Gamma(\nu_2/2)} \left(\frac{\nu_1}{\nu_2}\right)^{\nu_1/2} \frac{f^{1/2(\nu_1-2)}}{(1 + f\nu_1/\nu_2)^{1/2(\nu_1+\nu_2)}}. \quad (3.13)$$

In turn, the probability of getting a value of F or above from the null-hypothesis is given by,

$$P_F(F; \nu_1, \nu_2) = \int_F^\infty p_f(f; \nu_1, \nu_2) df. \quad (3.14)$$

Due to the nature of the χ^2 distribution, one can form a new χ^2 distribution by taking the difference between two other χ^2 distributions (Bevington and Robinson 2003, ch.11.4). So, if one fits a data map for which the fit has a degree of freedom ν . The goodness of fit can then be described as $\chi^2(\nu)$. Next, if k free parameters are added to the fit, then the degree of freedom for that fit is $\nu_k = \nu - k$ and the goodness of fit can be designated as $\chi^2(\nu - k) = \chi^2(\nu_k)$. Because of the additive nature of χ^2 distributions, the difference between those distribution yields a χ^2 distribution with a degree of freedom k .

$$\chi^2(k) = \chi^2(\nu) - \chi^2(\nu_k) \quad (3.15)$$

From that distribution, we can construct a null-hypothesis that states that the k added free parameters should be zero, corresponding to the fact that they should not be added. This is done by calculating the F-distributed ratio,

$$F_x = \frac{\chi^2(k)/k}{\chi^2(\nu_k)/\nu_k} \quad (3.16)$$

$$= \frac{(\chi^2(\nu) - \chi^2(\nu - k)) / k}{\chi^2(\nu - k) / (\nu - k)}, \quad (3.17)$$

which allows us to calculate the probability for which the null-hypothesis cannot be rejected by substituting $F = F_x$, $\nu_1 = k$ and $\nu_2 = \nu - k$ into eq. (3.14). However, in practice, it can be difficult to calculate this statistic when a large ν_k is involved, which is the case for data maps that has thousands of pixels. Instead, critical F-values are pre-calculated for different realisations of P_F , ν_1 and ν_2 . In this theses, we use tables and figures from Appendix C.5 in Bevington and Robinson (2003) to evaluate whether or not a computed F_x means that we can reject the null-hypothesis. In essence, if the computed F_x is larger than the critical F -value, the probability of getting F_x is lower than the probability, P_F , associated with the critical F -value, meaning that the null-hypothesis can be rejected with a significance level of $1 - P_F$

4 Results & Discussion

In this chapter we present the results of our analysis. For detailed results of every target galaxy, we refer to Appendix C. We first present an indicative case, by displaying the results of the SED and morphological fitting for target 22.

4.1 Indicative case

This section will present results of the analysis of source 22. Using STARDUST, we fit the photometry of the source using the stellar- and dust templates. The result of the fitting is illustrated in Fig. 4.1. As a result of the fitting, we get the SFR and stellar mass of $294 \pm 38 M_{\odot}/yr$ and

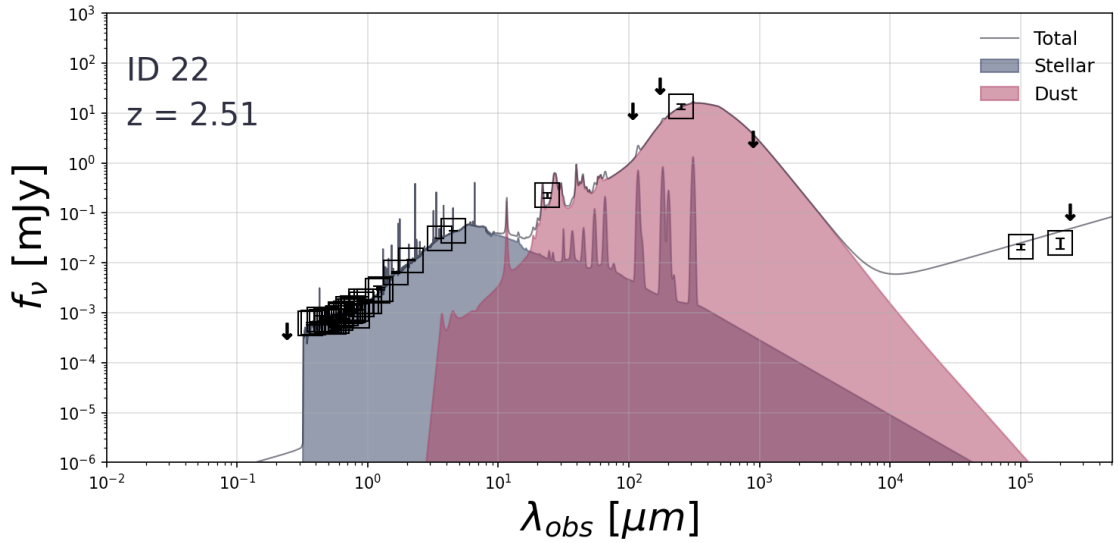


Figure 4.1: The SED of source 22 as fitted with STARDUST, assuming that there’s no significant AGN contribution. The squares are marked around observations with a $SNR > 3$. Arrows indicate 3σ upper limits of observations with $SNR < 3$ or non-detections.

$\log_{10} M_{\star}/M_{\odot} = 11.3 \pm 0.11$ respectively.

Using the relations describing the SFR of MSG from [Schreiber et al. \(2015\)](#), we can calculate the empirical SFR that a galaxy of this stellar mass and redshift would have, given that it is a main sequence galaxy.

$$SFR_{MS} = 346 \pm 166 M_{\odot}/yr \quad (4.1)$$

The uncertainties of the empirical MS SFR are primarily driven by the uncertainties of the parameterisation of the MS relation. Now, we can calculate the deviation from the main sequence, ΔMS , which simply describes the ratio of the measured SFR to the empirical MS SFR.

$$\Delta MS = SFR/SFR_{MS} \quad (4.2)$$

$$\Delta MS = 0.85 \pm 0.4 \quad (4.3)$$

Given the true scatter of the SFR- M_{\star} relation of 0.3 dex, corresponding to a $0.5 \lesssim \Delta MS \lesssim 2$, the galaxy is designated as a MSG.

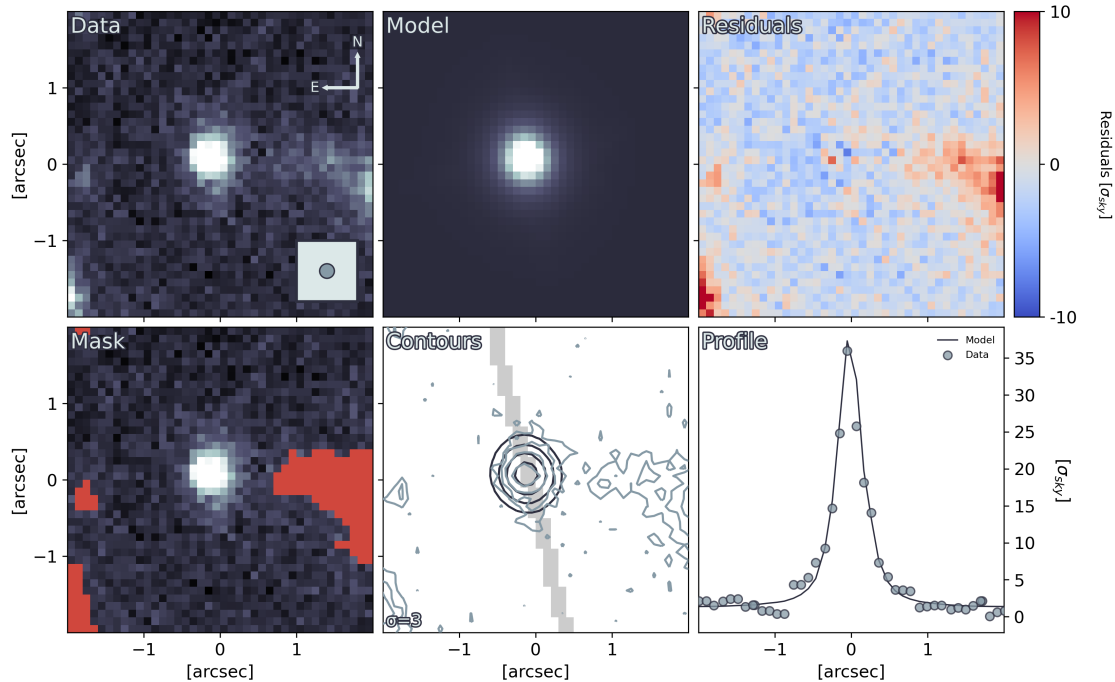


Figure 4.2: The results of fitting with GALFIT. **Data**: A cutout of the source. The colour scale for the *Data*, *Model* and *Mask* panels are defined from this map, using a linear scale. The direction towards celestial north and east are displayed by the arrows. An approximation of the FWHM of the PSF is displayed in the inset at the bottom right. **Mask**: Masked out sources and dead pixels are displayed in red. **Model**: The fitted model convolved with the PSF. **Contours**: Contours of the *Data* panel in blue. Contours of the *Model* panel in black. Contour levels start at the value annotated in the bottom left, and increase by a factor of two for each subsequent level. The shaded region indicates where the 1D profile was extracted from. **Residuals**: The *Data* subtracted by the *Model*. **Profile**: A one-dimensional profile extracted along the semi-major axis of the *Model*.

For source 22, we fitted the HST F160w map, corresponding to an observed wavelength of $1.544\mu\text{m}$. Consequently, we are investigating the spatial structure of the bulk of the stars in the galaxy. Fig. 4.2 illustrates the results of fitting, and compares the model to the original data.

The parameters extracted from the fit can be found in the tables of section 4.3. Here, we highlight that the fitted effective radius of the disk $r_e = 0.23'' \pm 0.014''$ and the fitted Sérsic index of the disk is $n = 2.22 \pm 0.28$. Next, we want to compare the size of the bulk of the stars with the size of the gas and dust.

In Fig. 4.3 we present the results of modelling the surface brightness profile of the image of the CO(3-2) emission line for target 22. The parameters extracted from the fit can be found in the tables of section 4.3. Here, we highlight that the fitted effective radius is $r_e = 0.44'' \pm 0.021''$ and the fitted Sérsic index is $n = 2.99 \pm 0.16$. Thus, the ratio of the effective radius of the stellar emission, to that of the gas emission line tracer, is ~ 0.5 . Additionally, from the Sérsic indices, we find that the stellar component is more disk-like than the molecular gas.

In the remainder of this chapter, we will focus on the trends of the sample as a whole. We will start by presenting the results of the SED-fitting, and classify our galaxies according to the MS relation.

4.2 SED-Fitting

The stellar masses and SFRs derived with STARDUST are presented in Tbl. 4.1. For all galaxies in the table, except target 25, we have enough photometric data to constrain the stellar masses.

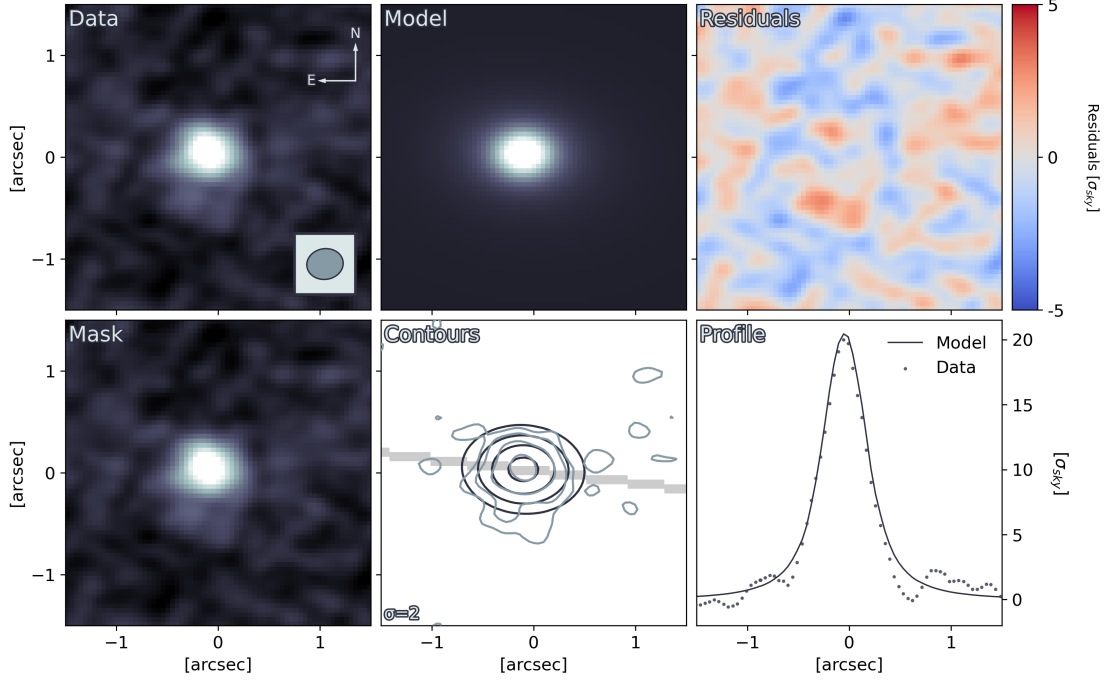


Figure 4.3: The results of fitting the CO(3-2) ALMA map for source 20 with GALFIT. **Data**: A cutout of the source. The colour scale for the *Data*, *Model* and *Mask* panels are defined from this map, using a linear scale. The direction towards celestial north and east are displayed by the arrows. The FWHM of the beam is displayed in inset in the lower right corner. **Mask**: Masked out sources and dead pixels are displayed in red. **Model**: The fitted model convolved with the PSF. **Contours**: Contours of the *Data* panel in blue. Contours of the *Model* panel in black. Contour levels start at $3\sigma_{\text{sky}}$, and increase by a factor of two for each subsequent level. The shaded region indicates where the 1D profile was extracted from. **Residuals**: The *Data* subtracted by the **Model**. **Profile**: A one-dimensional profile extracted along the semi-major axis of the *Model*.

Additionally, we calculate the empirical SFR of MSGs for each derived stellar mass and spectroscopic redshift. In turn, we can calculate the deviation from the MS, ΔMS , for each target. We also present those results in Tbl. 4.1.

Table 4.1: Global galaxy parameters derived from SED fitting.

ID	SED fitting		Schreiber et al. (2015)	
	Stellar mass [$\log_{10} M_{\odot}$]	SFR [M_{\odot}/yr]	MS SFR [M_{\odot}/yr]	ΔMS
1	10.2 ± 0.11	8 ± 1	9 ± 3	0.86 ± 0.3
2	10.8 ± 0.11	28 ± 3	23 ± 11	1.23 ± 0.6
3	10.6 ± 0.11	281 ± 6	42 ± 14	6.68 ± 2.2
4*	11.1 ± 0.11	54 ± 8	96 ± 45	0.56 ± 0.3
5*	10.5 ± 0.11	59 ± 2	40 ± 13	1.49 ± 0.5
6*	10.8 ± 0.11	53 ± 4	66 ± 24	0.80 ± 0.3
7*	10.8 ± 0.11	51 ± 1	65 ± 24	0.79 ± 0.3
8*	11.0 ± 0.11	31 ± 5	87 ± 37	0.36 ± 0.2
9*	10.6 ± 0.11	20 ± 4	46 ± 15	0.43 ± 0.2
10	10.7 ± 0.11	229 ± 6	55 ± 19	4.13 ± 1.4
13†	11.1 ± 0.11	220 ± 28	164 ± 69	1.34 ± 0.6
14†	10.8 ± 0.11	441 ± 78	102 ± 35	4.32 ± 1.7
15‡	11.3 ± 0.11	1350 ± 137	282 ± 136	4.78 ± 2.3
16‡	11.1 ± 0.11	1870 ± 111	215 ± 88	8.72 ± 3.6
17	11.2 ± 0.11	3480 ± 141	265 ± 115	13.12 ± 5.7
18	11.1 ± 0.11	1760 ± 1010	243 ± 100	7.26 ± 5.1
19†	10.8 ± 0.11	379 ± 15	132 ± 46	2.86 ± 1.0

Table 4.1 continued from previous page

ID	SED fitting		Schreiber et al. (2015)		Δ MS
	Stellar mass [$\log_{10} M_{\odot}$]	SFR [M_{\odot}/yr]	MS SFR [M_{\odot}/yr]		
20 [†]	11.4 ± 0.11	128 ± 170	380 ± 196	0.34 ± 0.5	
22 [†]	11.3 ± 0.11	294 ± 38	346 ± 166	0.85 ± 0.4	
24	10.8 ± 0.11	804 ± 313	155 ± 57	5.18 ± 2.8	
25	...	4370 ± 51	
26 [†]	12.1 ± 0.11	887 ± 32	1161 ± 986	0.76 ± 0.6	
27 [†]	10.7 ± 0.11	276 ± 13	125 ± 50	2.20 ± 0.9	
29	11.0 ± 0.11	983 ± 20	306 ± 112	3.21 ± 1.2	
30	11.0 ± 0.11	2150 ± 35	285 ± 105	7.54 ± 2.8	

The empirical SFRs of main sequence galaxies, MS SFR, are calculated using the fitted stellar mass and the MS parameterisation in Schreiber et al. (2015). The uncertainties of the MS SFRs and the deviation from the main sequence, Δ MS, are primarily driven by the uncertainties of the parameterisation of the MS relation.

[†] DL07 templates are constrained to match MS galaxies.

[‡] DL07 templates are constrained to match SB galaxies.

* SFRs are estimated from the optical photometry.

²⁵ We only had upper limits for the optical photometry for this target, and consequently could not fit the stellar mass.

For targets 11, 21 and 25, photometric data were not publicly available. For these, we supplement our sample with stellar masses and SFRs from the literature in Tbl. 4.2. Note that we have corrected for any difference in redshift and assumed cosmology between the literature and this work, such that,

$$M^* = M_{\text{lit}}^* \left(\frac{D_{\text{tw}}^L(z_{\text{tw}})}{D_{\text{lit}}^L(z_{\text{lit}})} \right)^2 \left(\frac{1 + z_{\text{lit}}}{1 + z_{\text{tw}}} \right), \quad (4.4)$$

where M^* is the stellar mass, D^L is the luminosity distance, z is the redshift, the “tw” subscript refers to this work, and the “lit” subscript refers to the literature.

Table 4.2: Stellar masses and SFRs adopted from literature.

ID	Reference	Literature		Schreiber et al. (2015)	
		Stellar mass [$\log_{10} M_{\odot}$]	SFR [M_{\odot}/yr]	MS SFR [M_{\odot}/yr]	Δ MS
11	Noble et al. (2017)	10.80 ± 0.11	174 ± 78	74 ± 24	2.3 ± 1.3
21	Xiao et al. (2022)	11.30 ± 0.15	300 ± 179	354 ± 181	0.8 ± 0.7
25	Leung et al. (2019)	11.86 ± 0.36	...	911 ± 659	4.8 ± 3.5

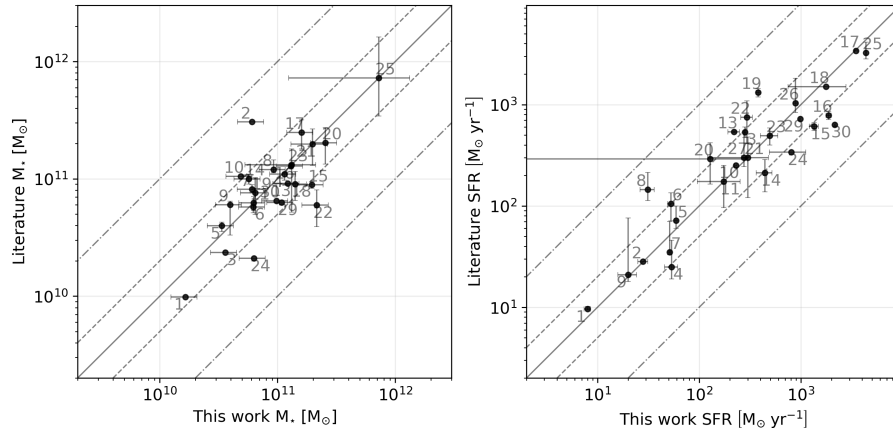
The empirical SFRs of main sequence galaxies, MS SFR, are calculated using the fitted stellar mass and the MS parameterisation in Schreiber et al. (2015). The uncertainties of the MS SFRs and the deviation from the main sequence, Δ MS, are primarily driven by the uncertainties of the parameterisation of the MS relation.

²⁵ The SFR of this target is given in Tbl. 4.1.

For targets 12 and 28 we could not find stellar masses and SFRs and consequently, we exclude them from our sample in this section. We also compare our derived global parameters to those in the literature, to investigate whether there is any systemic bias. We present those results in Fig. 4.4. When needed, we have converted the results to the Chabrier (2003) IMF using the conversion factors described in Madau and Dickinson (2014) Sec. 3.1. It is evident from Fig. 4.4 that there’s no systemic bias in our results with respect to those from the literature. The scatter observed between the global parameterisations of this work and global parameterisations of the literature can be attributed to different photometric data and SED fitting techniques.

Now, we can finally classify our targets according to the MS. In Fig. 4.5 we present visualisations of our targets with respect to the MS for the parameterisations of Schreiber et al. (2015).

Figure 4.4: Comparing fitted global galaxy parameters to values from the literature. The full line indicates the 1-1 relation. The dashed line indicates an offset of factor two. The dashed and dotted line indicates an offset of factor ten.



References to literature values: [Straatman et al. \(2016\)](#): 1, 13. [Liu et al. \(2019\)](#): 2, 3, 10. [Hayashi et al. \(2018\)](#): 4, 5, 6, 7, 8, 9. [Noble et al. \(2017\)](#): 11. [Bolatto et al. \(2015\)](#): 14. [Fu et al. \(2013\)](#): 15, 16. [Iverson et al. \(2013\)](#): 17, 18. [Xiao et al. \(2022\)](#): 19, 20, 21, 22. [Cassata et al. \(2020\)](#): 24, 29, 30. [Leung et al. \(2019\)](#): 25. [Umehata et al. \(2017\)](#): 26, 27.

In this thesis, following the approach of [Rodighiero et al. \(2011\)](#), we only classify galaxies as SBGs, if they are above 0.6 dex of the MS relation, corresponding to a SFR of ~ 4 times the expected empirical SFR of a MSG.

We classify targets 3, 10, 14, 15, 16, 17, 18, 24, 25 and 30, corresponding to $\sim 37\%$ of our sample, as SBGs. Of those, $3/5$ are merger systems. The rest of our sample is classified as MSGs. Of those, targets 1, 2, 4, 5, 6, 7, 8, 13, 21, 22 and 26, corresponding to $\sim 41\%$ of our sample, fall within the observed 0.3 dex scatter of the MS. Furthermore, $1/6$ of them are merger systems. Moreover, targets 11, 19, 27 and 29, corresponding to $\sim 15\%$, fall within the [0.3 dex, 0.6 dex] scatter range. Interestingly, $3/4$ of these targets are mergers. Lastly, targets 9 and 20 fall below the 0.3 dex scatter of the MS. None of those are merger systems.

As described in sec. 1.7.1, SBGs has been theorised to be related to stochastic processes like major mergers, where the compression of the gas content of the galaxies, result in an intense period of SF (e.g. [Silverman et al. 2015](#), [Cibinel et al. 2019](#)). In our sample, we conclude that $3/5$ of SBGs are related to merger events. In our limited sample we find 3 galaxies above the MS that does not have significant enough SF to be classified as SB galaxies, but they are all merger events. Additionally, 2 of our 12 MS galaxies are merger systems. If large merger events always cause SB periods, then we find that $\sim 19\%$ of our sample corresponds to galaxies transitioning into or away from a SB period.

4.3 Surface brightness profiles

We've fitted all the available data maps with GALFIT. For completeness, we first present the fitted centres in Tbl. 4.3. Previous studies have noticed that there are sometimes offsets between the dust continuum and stellar emission, causing issues with the energy balance assumption employed by some SED fitting techniques (e.g. [Chen et al. 2017](#), [Calistro Rivera et al. 2018](#)). However, since STARDUST does not work under that assumption, we do not investigate our results further.

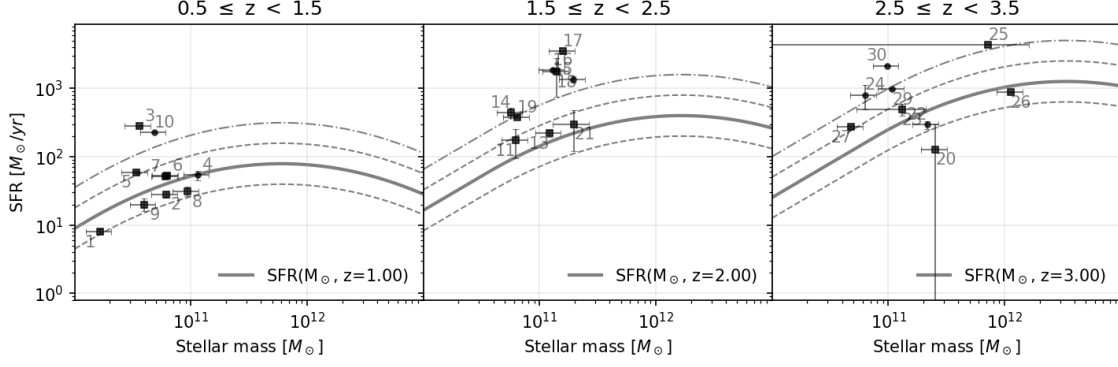


Figure 4.5: Overview of the SFR- M_* relation for the targets in our sample, where the MS, illustrated as a thick full line, is parameterised by the relation in Schreiber et al. (2015). The dashed line indicates the observed 0.3 dex scatter, and the dashed and dotted line indicates the 0.6 dex scatter that we use for SB classification. Dots are used for non-merging targets and squares are used for merger systems, as identified from the kinematic analysis in Rizzo et al. (In preparation).

Table 4.3: Centres of models fitted with GALFIT in the ICRS coordinate system. Values are presented in the unit of degrees and uncertainties are presented in the unit of arcseconds.

ID	Target	R.A. [$^{\circ} \pm ''$]	DEC. [$^{\circ} \pm ''$]
1	CO(2-1)	53.08206190 ± 0.0031	-27.83993020 ± 0.0026
1	F160w	53.08203653 ± 0.0011	-27.83993796 ± 0.0006
2	CO(3-2)	150.43185894 ± 0.0016	2.80260681 ± 0.0022
2 [†]	F814w	150.43186398	2.80262180
3	CO(5-4)	149.98144023 ± 0.0008	2.25320137 ± 0.0007
3	Continuum	149.98144315 ± 0.0009	2.25319923 ± 0.0008
3	F814w	149.98140023 ± 0.0018	2.25317525 ± 0.0011
4	CO(2-1)	333.99393973 ± 0.0025	-17.62990542 ± 0.0020
4	F160w	333.99392301 ± 0.0034	-17.62987443 ± 0.0042
5	CO(2-1)	333.98854464 ± 0.0034	-17.63150585 ± 0.0025
5	F160w	333.98849267 ± 0.0042	-17.63147795 ± 0.0049
6	CO(2-1)	333.99269262 ± 0.0043	-17.63951902 ± 0.0038
6	F160w	333.99263481 ± 0.0024	-17.63951386 ± 0.0029
7	CO(2-1)	333.99235290 ± 0.0036	-17.63738673 ± 0.0027
8	CO(2-1)	333.99881727 ± 0.0031	-17.63307444 ± 0.0027
8	F160w	333.99878982 ± 0.0032	-17.63303131 ± 0.0039
9	CO(2-1)	333.99910536 ± 0.0058	-17.63800002 ± 0.0034
9	F160w	333.99910593 ± 0.0087	-17.63796256 ± 0.0070
10	CO(2-1)	149.79819061 ± 0.0025	2.39006221 ± 0.0024
10	F160w	149.79817247 ± 0.0044	2.39007875 ± 0.0035
11	CO(2-1)	36.44192856 ± 0.0051	-3.92439517 ± 0.0054
11	F160w	36.44190950 ± 0.0020	-3.92439454 ± 0.0019
12	CO(2-1)	36.43974416 ± 0.0048	-3.92887820 ± 0.0046
12	F160w	36.43969502 ± 0.0064	-3.92885703 ± 0.0053
13	CI(2-1)	150.07595343 ± 0.0035	2.21179188 ± 0.0043
13	F160w	150.07598155 ± 0.0027	2.21180849 ± 0.0032
13	Continuum	150.07595603 ± 0.0024	2.21180768 ± 0.0018
14	CI(1-0)	356.53932526 ± 0.0015	12.82201451 ± 0.0020
14	F140w	356.53929997 ± 0.0034	12.82195522 ± 0.0056
14	CO(4-3)	356.53933174 ± 0.0006	12.82200795 ± 0.0009
14	Continuum	356.53932951 ± 0.0015	12.82201177 ± 0.0016
15	CI(2-1)	35.06939347 ± 0.0008	-6.02832257 ± 0.0017
15	Continuum	35.06937953 ± 0.0003	-6.02830395 ± 0.0005
15	Briggs	35.06939363 ± 0.0005	-6.02831268 ± 0.0008
15	F110w	35.06936771 ± 0.0069	-6.02825890 ± 0.0226
16	CI(2-1)	35.06907520 ± 0.0011	-6.02905929 ± 0.0017
16	Continuum	35.06906145 ± 0.0005	-6.02905388 ± 0.0006
16	Briggs	35.06907309 ± 0.0008	-6.02906587 ± 0.0010
16	F110w	35.06908825 ± 0.0075	-6.02928764 ± 0.0105
17	CI(1-0)	132.38995557 ± 0.0029	2.24572996 ± 0.0024
17	Continuum	132.38995373 ± 0.0007	2.24573820 ± 0.0008

Table 4.3 continued from previous page

ID	Target	R.A. [$^{\circ} \pm ''$]	DEC. [$^{\circ} \pm ''$]
17	F110w	132.38994031 \pm 0.0083	2.24576504 \pm 0.0081
18	CI(1-0)	132.38730555 \pm 0.0030	2.24437646 \pm 0.0019
18	Continuum	132.38728471 \pm 0.0026	2.24433583 \pm 0.0017
19	CO(3-2)	150.23727173 \pm 0.0013	2.33813759 \pm 0.0014
19	Continuum	150.23730403 \pm 0.0065	2.33816261 \pm 0.0055
19	F160w	150.23728234 \pm 0.0139	2.33817340 \pm 0.0119
20	CO(3-2)	150.23691250 \pm 0.0031	2.33576711 \pm 0.0024
20	F160w	150.23691409 \pm 0.0016	2.33578037 \pm 0.0019
21	CO(3-2)	150.23916140 \pm 0.0076	2.33630530 \pm 0.0052
21	F160w	150.23918039 \pm 0.0030	2.33639082 \pm 0.0027
22	CO(3-2)	150.23986787 \pm 0.0022	2.33644111 \pm 0.0017
22	F160w	150.23985529 \pm 0.0032	2.33646850 \pm 0.0033
24	CO(5-4)	150.33139722 \pm 0.0011	2.16239302 \pm 0.0010
24	F160w	150.33138240 \pm 0.0102	2.16233445 \pm 0.0049
24	Continuum	150.33138634 \pm 0.0024	2.16239439 \pm 0.0019
25	CII	36.44934291 \pm 0.0012	-4.29747788 \pm 0.0012
25	Continuum	36.44934022 \pm 0.0010	-4.29747578 \pm 0.0006
26	CO(3-2)	334.38506904 \pm 0.0054	0.29550681 \pm 0.0022
26	Continuum	334.38505634 \pm 0.0021	0.29550362 \pm 0.0018
27	CO(3-2)	334.38416592 \pm 0.0021	0.29321710 \pm 0.0035
27	Continuum	334.38416553 \pm 0.0030	0.29323772 \pm 0.0029
27	F160w	334.38413992 \pm 0.0091	0.29321409 \pm 0.0154
28	CO(3-2)	334.38121335 \pm 0.0050	0.29946161 \pm 0.0018
28	Continuum	334.38117902 \pm 0.0141	0.29946440 \pm 0.0039
29	CO(5-4)	149.87724904 \pm 0.0011	2.28386801 \pm 0.0009
29	Continuum	149.87723284 \pm 0.0012	2.28387692 \pm 0.0009
30	CO(5-4)	150.27828889 \pm 0.0013	2.25884715 \pm 0.0013
30	Continuum	150.27826143 \pm 0.0017	2.25885470 \pm 0.0023

† Fitted with fixed centre.

In Tbls. 4.4 and 4.5 we show the best-fit parameters obtained by fitting HST and ALMA maps using GALFIT.

Table 4.4: Sérsic surface brightness profiles fitted to HST maps.

ID	Target	Component	Magnitude [AB]	Effective radius [$''$]	Sérsic index	Axes ratio	Position angle [$^\circ$]
1	F160w	Bulge [†]	22.99 ± 0.040				
1	F160w	Disk	19.93 ± 0.003	0.71 ± 0.002	0.86 ± 0.01	0.57 ± 0.002	73.5 ± 0.2
2	F814w	System	21.17 ± 0.009	0.58 ± 0.007	1.27 ± 0.02	0.43 ± 0.003	37.3 ± 0.3
3	F814w	System	22.89 ± 0.022	0.33 ± 0.012	2.31 ± 0.10	0.47 ± 0.010	-61.4 ± 0.9
4	F160w	System	21.63 ± 0.030	0.50 ± 0.020	1.46 ± 0.07	0.73 ± 0.016	-15.4 ± 2.6
5	F160w	System	21.69 ± 0.025	0.48 ± 0.016	1.25 ± 0.06	0.85 ± 0.017	-1.8 ± 4.9
6	F160w	System	21.94 ± 0.019	0.33 ± 0.008	1.26 ± 0.08	0.71 ± 0.018	36.0 ± 2.5
8	F160w	System	21.49 ± 0.035	0.56 ± 0.027	1.61 ± 0.08	0.75 ± 0.017	28.4 ± 2.9
9	F160w	System	22.57 ± 0.042	0.52 ± 0.029	1.04 ± 0.08	0.65 ± 0.027	-52.5 ± 3.6
10	F160w	System	21.41 ± 0.032	0.25 ± 0.010	1.56 ± 0.17	0.68 ± 0.030	-76.8 ± 4.0
11	F160w	Bulge [†]	22.56 ± 0.020				
11	F160w	Disk	21.15 ± 0.012	0.74 ± 0.009	0.58 ± 0.03	0.88 ± 0.014	-67.2 ± 3.8
12	F160w	Bulge [†]	24.82 ± 0.149				
12	F160w	Disk	21.17 ± 0.046	1.07 ± 0.041	1.13 ± 0.07	0.78 ± 0.015	76.1 ± 2.6
13	F160w	System	21.71 ± 0.130	1.14 ± 0.211	3.57 ± 0.35	0.83 ± 0.014	-15.9 ± 4.4
14	F140w	System	22.16 ± 0.010	0.57 ± 0.007	0.49 ± 0.02	0.56 ± 0.006	14.0 ± 0.8
15 [‡]	F110w	System	22.98 ± 0.050	0.52 ± 0.030	0.50	0.19 ± 0.018	16.8 ± 1.4
16 ^{‡‡}	F110w	System	22.13 ± 0.102	0.88 ± 0.126	4.00	0.40 ± 0.044	-6.9 ± 3.3
17*	F110w	System	21.80 ± 0.018	0.03	0.50	1.00	0.0
19	F160w	System	23.55 ± 0.083	0.80 ± 0.075	1.19 ± 0.13	0.63 ± 0.035	-49.8 ± 4.2
20	F160w	Bulge [†]	23.88 ± 0.052				
20	F160w	Disk	22.16 ± 0.176	1.38 ± 0.293	2.90 ± 0.61	0.70 ± 0.018	-25.9 ± 2.1
21	F160w	Bulge [†]	23.69 ± 0.274				
21	F160w	Disk	22.62 ± 0.243	1.55 ± 0.375	1.90 ± 0.51	0.67 ± 0.024	82.0
22	F160w	System	23.70 ± 0.041	0.23 ± 0.014	2.22 ± 0.28	0.86 ± 0.041	13.6 ± 11.4
24	F160w	System	22.98 ± 0.023	0.47 ± 0.016	0.62 ± 0.07	0.37 ± 0.013	-73.7 ± 1.3
27	F160w	System	23.92 ± 0.046	0.48 ± 0.032	0.86 ± 0.11	0.50 ± 0.027	-5.7 ± 3.1

Position angle is measured counterclockwise from celestial north.

Effective radius is measured along the semi-major axis.

¹⁶ *Rizzo et al. (in preparation)* finds that this is two separate galaxies that are interacting. We only fit the southern.

[†] Unresolved co-spatial bulge fitted with $r_e \ll \sigma_{\text{PSF}}$, $n = 4$, $b/a = 1$ and $\theta = 0$.

[‡] Fitted with fixed $n = 1/2$ due to the fact that $n \rightarrow 0$ in the fit.

^{‡‡} Fitted with fixed $n = 4$ due to the fact that $n \rightarrow \infty$ in the fit.

* Unresolved source fitted with $r_e \ll \sigma_{\text{PSF}}$, $n = 0.5$, $b/a = 1$ and $\theta = 0$.

Table 4.5: Sérsic surface brightness profiles fitted to ALMA maps.

ID	Target	Effective radius	Sérsic index	Axes ratio	Position angle
1	CO(2-1)	0.83 ± 0.015	1.35 ± 0.03	0.62 ± 0.007	45.59 ± 0.89
2	CO(3-2)	0.23 ± 0.004	0.67 ± 0.04	0.64 ± 0.011	24.54 ± 1.50
3	CO(5-4)	0.23 ± 0.004	1.52 ± 0.03	0.87 ± 0.008	-48.08 ± 2.54
3	Continuum	0.14 ± 0.003	1.59 ± 0.06	0.93 ± 0.017	-14.19 ± 7.77
4	CO(2-1)	0.25 ± 0.005	1.71 ± 0.12	0.99 ± 0.024	27.14 ± 54.34
5	CO(2-1)	0.38 ± 0.010	1.44 ± 0.07	0.77 ± 0.016	-58.79 ± 2.94
6	CO(2-1)	0.58 ± 0.071	4.08 ± 0.50	0.58 ± 0.032	27.97 ± 2.70
7	CO(2-1)	0.26 ± 0.006	0.81 ± 0.09	0.80 ± 0.019	-74.16 ± 4.15
8	CO(2-1)	0.48 ± 0.008	1.14 ± 0.03	0.83 ± 0.012	49.24 ± 2.75
9	CO(2-1)	0.53 ± 0.021	1.55 ± 0.10	0.50 ± 0.015	-68.57 ± 1.42
10	CO(2-1)	1.08 ± 0.032	2.18 ± 0.05	0.93 ± 0.011	51.91 ± 6.12
11	CO(2-1)	0.89 ± 0.024	1.41 ± 0.04	0.88 ± 0.015	-10.08 ± 4.85
12	CO(2-1)	0.57 ± 0.014	1.01 ± 0.05	0.92 ± 0.019	16.18 ± 9.36
13	CI(2-1)	0.43 ± 0.006	0.53 ± 0.02	0.79 ± 0.009	1.29 ± 2.17
13	Continuum	0.41 ± 0.006	0.89 ± 0.02	0.71 ± 0.007	60.28 ± 1.30
14	CI(1-0)	0.20 ± 0.005	0.98 ± 0.04	0.76 ± 0.013	-23.36 ± 2.77
14	CO(4-3)	0.29 ± 0.004	1.51 ± 0.02	0.67 ± 0.006	9.78 ± 0.77
14 [‡]	Continuum	0.29	2.20 ± 0.07	0.97 ± 0.029	35.22 ± 30.00
15	CI(2-1)	0.31 ± 0.004	1.00 ± 0.03	0.25 ± 0.005	11.94 ± 0.30
15	Continuum	0.25 ± 0.001	0.94 ± 0.02	0.29 ± 0.003	15.83 ± 0.15
16	CI(2-1)	0.47 ± 0.017	2.47 ± 0.09	0.37 ± 0.007	-1.14 ± 0.53

Table 4.5 continued from previous page

ID	Target	Effective radius	Sérsic index	Axes ratio	Position angle
16	Continuum	0.44 ± 0.011	4.25 ± 0.10	0.40 ± 0.005	-0.90 ± 0.32
17	CI(1-0)	0.35 ± 0.005	0.68 ± 0.02	0.85 ± 0.009	-75.60 ± 3.15
17	Continuum	0.20 ± 0.003	1.86 ± 0.06	0.71 ± 0.011	5.21 ± 1.38
18	CI(1-0)	0.52 ± 0.008	0.82 ± 0.02	0.46 ± 0.005	55.31 ± 0.54
18	Continuum	0.33 ± 0.009	1.24 ± 0.05	0.48 ± 0.011	53.98 ± 1.06
19	CO(3-2)	0.49 ± 0.018	3.13 ± 0.12	0.65 ± 0.012	-8.39 ± 1.24
19 [‡]	Continuum	0.49	2.17 ± 0.25	0.65	-42.40 ± 3.84
20	CO(3-2)	0.34 ± 0.006	0.72 ± 0.04	0.76 ± 0.011	-66.76 ± 2.16
21	CO(3-2)	0.57 ± 0.012	0.66 ± 0.03	0.66 ± 0.011	88.28 ± 1.79
22	CO(3-2)	0.44 ± 0.021	2.99 ± 0.16	0.66 ± 0.015	83.40 ± 1.72
24	CO(5-4)	0.26 ± 0.007	1.77 ± 0.06	0.78 ± 0.014	35.84 ± 2.57
24	Continuum	0.15 ± 0.006	1.88 ± 0.25	0.65 ± 0.034	67.72 ± 3.74
25	CII	0.45 ± 0.002	0.54 ± 0.01	0.84 ± 0.004	42.48 ± 1.13
25	Continuum	0.32 ± 0.002	0.60 ± 0.01	0.58 ± 0.002	77.08 ± 0.32
26	CO(3-2)	0.66 ± 0.011	0.82 ± 0.03	0.34 ± 0.004	84.48 ± 0.44
26	Continuum	0.43 ± 0.055	4.36 ± 0.42	0.63 ± 0.027	80.40 ± 2.63
27	CO(3-2)	0.26 ± 0.007	1.00 ± 0.07	0.43 ± 0.015	11.82 ± 1.22
27	Continuum	0.79 ± 0.524	8.75 ± 2.76	0.51 ± 0.051	-59.74 ± 3.96
28 [†]	CO(3-2)	0.40 ± 0.006	0.50	0.23 ± 0.007	75.38 ± 0.48
28 [†]	Continuum	0.47 ± 0.017	0.50	0.18 ± 0.012	89.48 ± 0.84
29	CO(5-4)	0.19 ± 0.007	2.59 ± 0.16	0.80 ± 0.017	-51.10 ± 3.29
29	Continuum	0.11 ± 0.003	1.81 ± 0.22	0.69 ± 0.022	-45.73 ± 2.98
30	CO(5-4)	0.36 ± 0.005	1.22 ± 0.03	0.42 ± 0.005	-40.85 ± 0.46
30 [‡]	Continuum	0.36	1.47 ± 0.07	0.38 ± 0.010	-32.41 ± 0.75

Position angle is measured counterclockwise from celestial north.

Effective radius is measured along the semi-major axis.

¹⁶ *Rizzo et al. (in preparation)* finds that this is two separate galaxies that are interacting.

We only fit the southern galaxy.

[†] Fitted with fixed $n = 1/2$ due to the fact that $n \rightarrow 0$ in the fit.

[‡] Source is barely resolved.

As discussed in sec. 3.2.1, we note that the formal uncertainties reported by GALFIT and presented in Tbl. 4.3, 4.4 and 4.5 are underestimated.

4.4 Discussion

Finally, we compare our results to recent findings in the literature. In sec. 1.7.3 we discussed that recent observations and simulations of high redshift galaxies have compact molecular reservoirs. Additionally, we discussed that simulations predict that the dust continuum traces ongoing star formation, contrary to the assumption that it traces the molecular reservoirs.

Thus, we first compare our derived sizes of respective galaxy components. We adopt the approach of circularising the effective radius (e.g. [Ricciardelli et al. 2010](#), [Smith et al. 2019](#)).

$$r_e^{\text{circ}} = r_e^{\text{semi-major}} \sqrt{(b/a)} \quad (4.5)$$

We present our results in Fig. 4.6, where we compare the stellar emission size to the gas line tracer size, the stellar emission size to the dust continuum size and the gas line tracer size to the dust continuum size. To distinguish between the rest-frame targets of our observations, we plot rest-frame NIR and optical observations of the stellar emission in red, and rest-frame NUV observations in blue. Additionally, we plot low- J^1 gas line tracers with circles and high- J^2 with squares. Additionally, we show merging systems, for which the analytical surface brightness profiles are not physically meaningful, as transparent data points. To discuss the results, we define the following

¹CO(1-0), CO(2-1), CO(3-2), CO(4-3), [CI](1-0), [CII]

²CO(5-4), [CI](2-1)

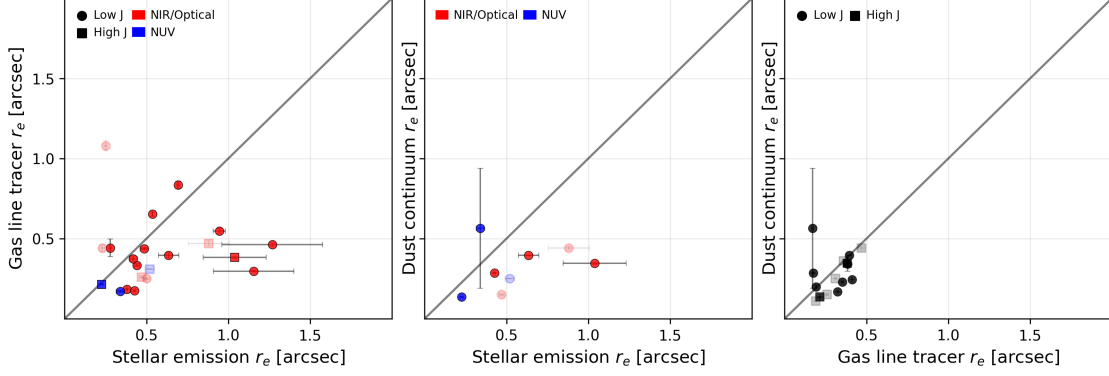


Figure 4.6: Comparison between derived circularised observed sizes of emission from the stellar ensemble, dust continuum and gas lines. The stellar emission sizes are plotted in red, when targeting rest-frame NIR/Optical and in blue when targeting rest-frame NUV. The gas line tracer emission sizes are plotted with circles when corresponding to CO(1-0), CO(2-1), CO(3-2), CO(4-3), [CI](1-0) or [CII] and with squares when corresponding to CO(5-4) and [CI](2-1). The 1-1 relation is illustrated as a full line. Transparent data points correspond to merger systems, for which the surface brightness modelling is not physically meaningful.

ratios,

$$\mathcal{R}_G^S \equiv \frac{\text{Stellar emission } r_e}{\text{Gas line tracer } r_e} \quad (4.6)$$

$$\mathcal{R}_D^S \equiv \frac{\text{Stellar emission } r_e}{\text{Dust continuum } r_e} \quad (4.7)$$

$$\mathcal{R}_D^G \equiv \frac{\text{Gas line tracer } r_e}{\text{Dust continuum } r_e} \quad (4.8)$$

Additionally, we quantify the global ratios of our sample, of galaxies that are not classified as merging systems (*Rizzo et al. in preparation*), using the median, and we denote them as $\tilde{\mathcal{R}}$. For uncertainties, we add in quadrature the 84th percentile and the weighted average of the errors for the upper limit, and we add in quadrature the 16th percentile and the weighted average of the errors for the lower limit. The spread of the distribution is the primary driver of the uncertainties.

For our sample, we find that $\tilde{\mathcal{R}}_G^S = 1.61^{+1.04}_{-0.72}$, meaning that the stellar emission is more extended than the gas line tracer, with unity being within the uncertainties. Interestingly, we recover gas line emission that is less extended, with respect to the stellar emission, than other recent empirical studies (*Calistro Rivera et al. 2018*, *Kaasinen et al. 2020*). *Calistro Rivera et al. (2018)* find $\tilde{\mathcal{R}}_G^S \sim 1$, where the gas line emission size is measured using CO(3-2), and *Kaasinen et al. (2020)* find $\tilde{\mathcal{R}}_G^S \gtrsim 1.4$, also using CO(3-2) as a tracer for the gas. We have 15 targets for which we have measurements of \mathcal{R}_G^S . Interestingly, for seven out of fifteen, we target CO(2-1), corresponding to lower densities and kinetic temperatures than CO(3-2). Additionally, for five out of fifteen we target the CO(3-2) line and for the remaining three, we target emission lines tracing higher densities and kinetic temperatures than CO(3-2). As most of our sample targets gas emission at lower densities and kinetic temperatures than CO(3-2), one would naturally assume that our estimate of $\tilde{\mathcal{R}}_G^S$ would also be biased to lower values than those targeting CO(3-2). However, this is not the case. Therefore, we investigate the effects of targeting different gas conditions, by splitting our sample into observations of CO(2-1) and CO(3-2) respectively. We find the following result,

$$\tilde{\mathcal{R}}_G^S = \begin{cases} 1.11^{+0.24}_{-0.30} & \text{for CO(2-1)} \\ 2.07^{+1.09}_{-0.22} & \text{for CO(3-2)} \\ 2.45^{+0.18}_{-0.95} & \text{for CO(4-3), CO(5-4) and [CI](2-1)}^\dagger \end{cases} \quad (4.9)$$

Intuitively, we find that $\tilde{\mathcal{R}}_G^S$ increases, when targeting higher densities and kinetic temperatures. Additionally, we find a higher value of $\tilde{\mathcal{R}}_G^S$ than the previously mentioned studies, when considering the same gas conditions (Calistro Rivera et al. (2018), Kaasinen et al. 2020). Consequently, we show that the measurement of \mathcal{R}_G^S is very sensitive to the conditions of the gas that the emission line traces. Additionally, we note that our observations of CO(3-2) are typically at higher redshift than our observations of CO(2-1). Furthermore, we in general target shorter rest-frame wavelengths of the stellar emission with increasing redshift (i.e. Fig. 2.1). One would assume that the decrease of observed rest-frame stellar emission would similarly correspond to a decrease in the observed stellar size, due to targeting fewer stars at higher stellar masses. However, a recent study into simulated galaxies suggest that tracing shorter wavelengths³ of the stellar emission will make it appear to be more extended (Popping et al. 2021). Consequently, it is hard to evaluate how the difference in the targeted rest-frame stellar emission affects our measurements of \mathcal{R}_G^S . Nonetheless, we do note that we have ALMA resolution that is ~ 4 times better than Calistro Rivera et al. (2018) and ~ 3 times better than Kaasinen et al. (2020) at the given redshifts of their observations. Additionally, we cover 15 targets, while those studies only cover 4 and 3 targets respectively.

For our sample, we find that $\tilde{\mathcal{R}}_D^G = 1.11_{-0.40}^{+0.55}$, meaning that we essentially recover that the size of the emission coming from gas line tracers and the dust continuum respectively, are similar in size. In turn, we find that the dust continuum is a robust tracer of the underlying molecular gas as traced by emission lines.

Interestingly, recent results suggest that the dust continuum⁴ in general is less extended than the molecular gas traced by CO(3-2) (Chen et al. 2017, Calistro Rivera et al. 2018, Kaasinen et al. 2020). Chen et al. (2017) find $\mathcal{R}_D^G \sim 4 - 6$, Calistro Rivera et al. (2018) find $\tilde{\mathcal{R}}_D^G \gtrsim 2$, and Kaasinen et al. (2020) find $\tilde{\mathcal{R}}_D^G \sim 1.4$. For our results ^{4/9} of our data points are targeting the same gas emission line tracer, CO(3-2), and the dust continuum at $\sim 870\mu\text{m}$. The remainder of our data targets higher-J gas emission line tracers, corresponding to higher densities and kinetic temperatures, and dust continuum at shorter wavelengths. More specifically, we target the dust continuum at $\sim 610-650\mu\text{m}$ together with gas traced by CO(4-3) and [CI](1-0), $\sim 430\mu\text{m}$ together with CO(5-4), and $158\mu\text{m}$ together with [CII]. Curiously, our highest values of \mathcal{R}_D^G , comes from the observations at $\lesssim 430\mu\text{m}$, while our $\sim 870\mu\text{m}$ dust continuum measurements together with our CO(3-2) observations have $\mathcal{R}_D^G \sim 1$, meaning that the dust continuum size in general is comparable to the gas line emission. That trend is in line with a recent study of simulated galaxies across the cosmic noon (Cochrane et al. 2019). They find that when tracing further up the Rayleigh–Jeans Tail of the dust continuum, the apparent size of the dust continuum decreases, which would make \mathcal{R}_D^G increase. However, we also expect the molecular gas to appear more compact, when probing higher densities and kinetic temperatures. But there might be a degeneracy between the decrease of size across the gas and dust components, when moving to hotter dust and gas, such that the apparent dust continuum size decreases more than the apparent gas emission line size, corresponding to the increase in \mathcal{R}_D^G .

Finally, in line with the above results, we find $\tilde{\mathcal{R}}_D^S = 1.61_{-0.43}^{+0.55}$, meaning that the stellar emission is more extended than the dust continuum emission. In recent observations of high-redshift galaxies, the dust continuum⁵ has been shown to be more compact than the stellar emission (e.g. Calistro Rivera et al. 2018, Tadaki et al. 2020, Kaasinen et al. 2020). Interestingly, Kaasinen et al. (2020) find $\tilde{\mathcal{R}}_D^S \gtrsim 2$, Calistro Rivera et al. 2018 find $\tilde{\mathcal{R}}_D^S > 2$, and Tadaki et al. (2020) find $\tilde{\mathcal{R}}_D^S = 2.3_{-1.0}^{+1.9}$. While unity between our result and the results from the literature is within the uncertainties, we do on average find a lower value of $\tilde{\mathcal{R}}_D^S$, corresponding to the fact that the dust continuum is

[†] Note that we only have a single measurement of \mathcal{R}_G^S for each of the three cases.

³based on an observed wavelength of $1.6\mu\text{m}$

⁴at $870\mu\text{m}$, $250\mu\text{m}$, $870\mu\text{m}$ respectively

⁵at $250\mu\text{m}$, $850\mu\text{m}$, $870\mu\text{m}$ respectively

less extended, with respect to the stellar emission. We have two data points also targeting the $\sim 870\mu\text{m}$ dust continuum, and one data point each targeting $\sim 650\mu\text{m}$, $\sim 430\mu\text{m}$, $\sim 370\mu\text{m}$ dust continuum respectively. As mentioned above, [Cochrane et al. \(2019\)](#) predicted that the apparent dust continuum size would decrease when tracing shorter rest-frame wavelengths, so one would naturally assume that we find higher values of $\tilde{\mathcal{R}}_D^S$ than in the studies mentioned above. However, as discussed above, we also in general target shorter rest-frame wavelengths of the stellar emission, when targeting shorter rest-frame wavelengths of the dust continuum. Additionally, with only five data points, we cannot identify any degeneracy between the decrease in apparent relative size between the stellar emission and the dust continuum, caused by tracing shorter rest-frame wavelengths.

Next, we investigate how our measurements of \mathcal{R}_G^S for our sample correlate with redshift. We present our results in Fig. 4.7. From visual inspection, it seems that there is a positive monotonic

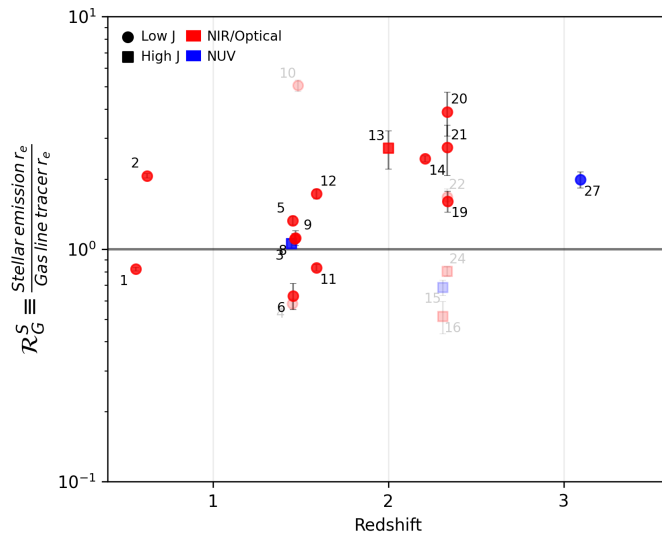


Figure 4.7: Comparison between the observed circularised sizes of emission from the stellar ensemble and gas emission line tracers across the cosmic noon. The stellar emission sizes are plotted in red, when targeting rest-frame NIR/Optical and in blue when targeting rest-frame NUV. The gas line tracer emission sizes are plotted with circles when corresponding to CO(1-0), CO(2-1), CO(3-2), CO(4-3), [CI](1-0) or [CII] and with squares when corresponding to CO(5-4) or [CI](2-1). The 1-1 relation is illustrated as a full line. Transparent data points correspond to merger systems, for which the surface brightness modelling is not physically meaningful.

trend between \mathcal{R}_G^S and redshift, meaning that the gas emission line appears to be more compact with respect to the stellar emission, with increasing redshift across the cosmic noon. To quantify it, we perform a MC simulation performing the Spearman’s rank order correlation in each iteration⁶. For each \mathcal{R}_G^S , we draw values from a Normal distribution with a mean set by the derived \mathcal{R}_G^S value, and a standard deviation set by the uncertainty. From the analysis, we find a Spearman’s rank order correlation of $\rho = 0.6 \pm 0.04$ with a p-value of $p = 0.02 \pm 0.01$. Consequently, we can say with a $\gtrsim 97\%$ significance level, that there is a moderate positive monotonic relation between \mathcal{R}_G^S and redshift. This is in line with recent results suggesting that compactness of molecular gas reservoirs increase with redshift due to cosmic inflows, in turn explaining why galaxies at cosmic noon have enhanced SFRs with respect to present-day galaxies (e.g. [Magnelli et al. 2020](#), [Tadaki et al. 2020](#)). However, the relation might not correspond to a physical evolution. As discussed, we showed that \mathcal{R}_G^S is very sensitive to the conditions of the gas that is traced, and in general, we trace higher densities and kinetic temperatures with increasing redshift. Additionally, we trace

⁶For more information on the MC method and Spearman’s rank order correlation, we refer to Appendix D

shorter rest-frame stellar emission at higher redshift, but as discussed above, we cannot concretely measure how that affects our results. To gather concrete empirical evidence, future studies should target the same rest-frame wavelength for both the stellar emission and dust continuum emission, and the same conditions of the gas, with increasing redshift .

In sec. 1.7.1 we discussed that non-merging SBGs are associated with large cosmic inflows of gas into the central region of the galaxy, in turn forming very compact SF regions. Additionally, we discussed that SFR should increase with the compactness of the SF regions, for all SFGs. Thus, we investigate the relation between our measured size ratios, and the deviation from the MS. We present our results in Fig. 4.8, where we show the relation between the deviation from the MS, ΔMS , with respect to \mathcal{R}_G^S , \mathcal{R}_D^S and \mathcal{R}_D^G respectively. To distinguish between the rest-frame targets of our observations, we plot rest-frame NIR and optical observations of the stellar emission in red, and rest-frame NUV observations in blue. Additionally, we plot low- J^7 gas line tracers with circles and high- J^8 with squares. Moreover, we show merging systems, for which the analytical surface brightness profiles are not likely to be physically meaningful, as transparent data points. At first

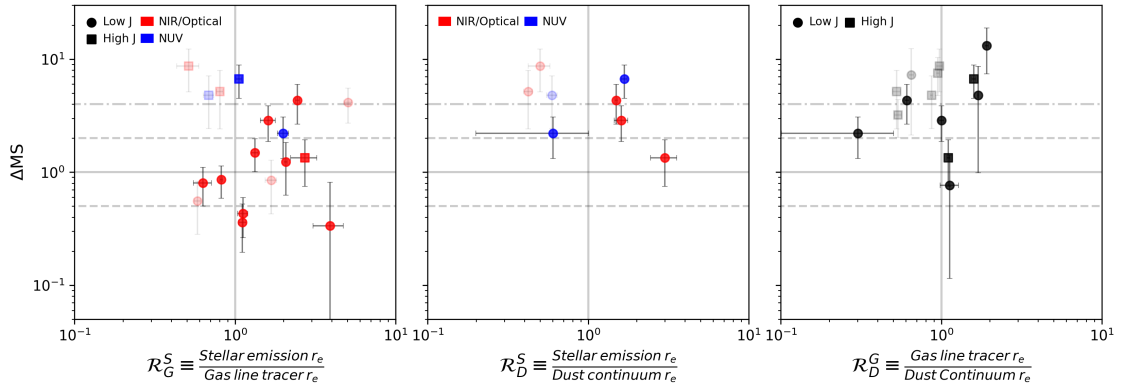


Figure 4.8: Comparison between the observed circularised sizes of emission from the stellar ensemble, gas emission line tracers and the dust continuum with respect to the deviation from the main sequence, ΔMS . The stellar emission sizes are plotted in red, when targeting rest-frame NIR/Optical and in blue when targeting rest-frame NUV. The gas line tracer emission sizes are plotted with circles when corresponding to CO(1-0), CO(2-1), CO(3-2), CO(4-3), [CI](1-0) or [CII] and with squares when corresponding to CO(5-4) or [CI](2-1). The 1-1 relations are illustrated as full lines. The 0.3 dex scatter is illustrated with a dashed line. The 0.6 dex SB classification line is illustrated as a dashed and dotted line. Transparent data points correspond to merger systems, for which the surface brightness modelling is not physically meaningful.

glance, there does not seem to be any meaningful correlations. To quantify this, we once again calculate Spearman's rank order correlation in a MC simulation. For the non-merging systems in Fig. 4.8 from left to right, we find Spearman's rank order correlation p-values of 0.6 ± 0.2 , 0.7 ± 0.2 and 0.3 ± 0.3 respectively. Consequently, we do not find any significant statistical correlations between the deviation from the MS and \mathcal{R}_G^S , \mathcal{R}_D^S and \mathcal{R}_D^G respectively.

In sec. 1.6, we discussed that we would expect different morphology of galaxy components. The dissipative ISM is expected to be more *disky*, while the non-dissipative stellar ensemble is expected to have emission that is more *bulgy*. However, we do not find any trends of this in our results. Moreover, if the compactness of the molecular reservoirs scale with enhanced SF, then we would expect less *disky* emission from galaxies above the MS. We investigate that in Fig. 4.9, where we compare the deviation of the main sequence, ΔMS , with the fitted Sérsic indices of our fitted analytical surface brightness profiles. Interestingly, for our sample of non-merging galaxies, we find Spearman's rank order correlations $\rho < 0$, however, the p-values are 0.5 ± 0.2 , 0.3 ± 0.2 and

⁷CO(1-0), CO(2-1), CO(3-2), CO(4-3), [CI](1-0) and [CII]

⁸CO(5-4) and [CI](2-1)

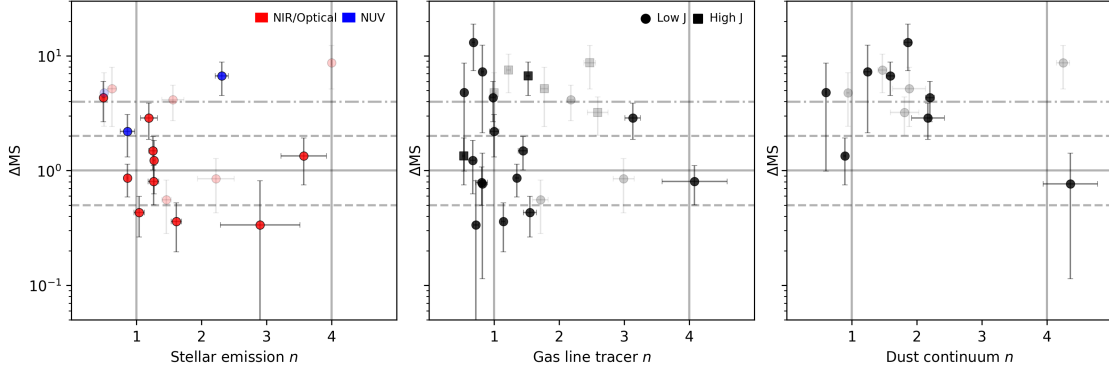


Figure 4.9: Comparison between the Sérsic indices, n , of our fitted surface brightness profiles on emission from the stellar ensemble, gas emission line tracers and the dust continuum with respect to the deviation from the main sequence, Δ_{MS} . The stellar emission is plotted in red, when targeting rest-frame NIR/Optical and in blue when targeting rest-frame NUV. The gas line tracer emission is plotted with circles when corresponding to CO(1-0), CO(2-1), CO(3-2), CO(4-3), [CI](1-0) or [CII] and with squares when corresponding to CO(5-4) or [CI](2-1). The $\Delta_{\text{MS}} = 1$ relation is illustrated as full lines. The 0.3 dex scatter is illustrated with a dashed line. The 0.6 dex SB classification line is illustrated as a dashed and dotted line. Transparent data points correspond to merger systems, for which the surface brightness modelling is not physically meaningful.

0.3 ± 0.3 respectively for the stellar emission, gas emission line tracer and dust continuum with respect to the deviation from the MS. Thus, we once again find no statistical significant correlations for our sample of non-merging galaxies.

5 Conclusion

In this thesis, we investigated the morphologies of stars, gas and dust in a sample of 30 star-forming galaxies at cosmic noon ($0.5 \lesssim z \lesssim 3.5$). Using public photometric catalogues, we perform Spectral Energy Distribution (SED) fitting to derive the Star Formation Rate (SFR) and stellar mass for our targets. We found that our sample consist of $17/27$ main sequence galaxies and $10/27$ starbursts. We could not classify the remaining three due to the lack of good estimates of their stellar masses.

We traced the stellar emission in rest-frame near-infrared to near-ultraviolet using spatially resolved images from the Hubble Space Telescope (HST). Additionally, we traced the molecular gas using images from the Atacama Large Millimetre/submillimetre Array (ALMA) of gas emission line tracers of CO, [CI] and [CII]. Finally, we investigated the dust continuum, from images of the dust continuum extracted from the spectral cubes of the images containing the emission lines.

We fit the surface brightness profiles of our targets using Galfit. We found that the size of the stellar emission of our sample was $1.61_{-0.72}^{+1.04}$ and $1.61_{-0.43}^{+0.55}$ times that of the molecular gas emission line tracers and the dust continuum respectively. The fact that the stellar emission is more extended than the dust continuum is in line with recent observations of galaxies at cosmic noon. However, we found that the stellar emission is less extended than other recent studies.

Recent studies comparing the stellar emission size to the size of the gas emission as traced by CO(3-2) find that the stellar emission is either comparable to the size of the gas emission line or slightly more extended. For our subsample targeting the same emission line, we find that the stellar emission is more extended than the gas emission line by a factor of $2.07_{-0.22}^{+1.09}$. We additionally find, that the relative extents of the stellar emission and the gas emission lines are very sensitive to the conditions traced by the emission line.

Furthermore, we found that the size of the gas emission lines of our sample was $1.11_{-0.40}^{+0.55}$ times that of the dust continuum. This is in line with the commonly adopted assumption that the dust continuum traces the underlying molecular gas.

The results obtained using this sample may be biased because of the following reasons: (i) there is no homogeneous coverage of the stellar emission, because we trace different rest-frame near-infrared to near-ultraviolet emission with HST; (ii) there is no homogeneous coverage of gas densities and kinetic temperatures, because we trace the molecular gas emission using different gas emission line tracers with ALMA; (iii) Our sample is not representative of star-forming galaxies, as it is subject to selection bias, resulting from selecting galaxies with high Signal-To-Noise Ratio (SNR) in the ALMA archive of CO, [CI] and [CII]; (iv) In the future, better constraints should be obtained by ensuring homogeneous stellar emission coverage with the James Webb Space Telescope and gas conditions by observing the same gas emission line tracers with ALMA.

References

- Allamandola, L. J., A. G. G. M. Tielens, and J. R. Barker (Dec. 1989). “Interstellar Polycyclic Aromatic Hydrocarbons: The Infrared Emission Bands, the Excitation/Emission Mechanism, and the Astrophysical Implications”. In: *apjs* 71, p. 733. DOI: 10.1086/191396.
- Bastian, Nate, Kevin R. Covey, and Michael R. Meyer (Aug. 2010). “A Universal Stellar Initial Mass Function? A Critical Look at Variations”. In: *Annual Review of Astronomy and Astrophysics* 48.1, pp. 339–389. DOI: 10.1146/annurev-astro-082708-101642. URL: <https://doi.org/10.1146%2Fannurev-astro-082708-101642>.
- Bernstein, Rebecca A., Wendy L. Freedman, and Barry F. Madore (May 2002). “The First Detections of the Extragalactic Background Light at 3000, 5500, and 8000 Å”. In: *The Astrophysical Journal* 571.1, pp. 56–84. DOI: 10.1086/339422. URL: <https://doi.org/10.1086/339422>.
- Berta, S. et al. (Mar. 2013). “Panchromatic spectral energy distributions of Herschel sources”. In: *aap* 551, A100, A100. DOI: 10.1051/0004-6361/201220859. arXiv: 1301.4496 [astro-ph.CO].
- Bertin, E. and S. Arnouts (Oct. 2010). *SExtractor: Source Extractor*. Astrophysics Source Code Library, record ascl:1010.064. ascl: 1010.064.
- B  thermin, Matthieu et al. (Jan. 2015). “Evolution of the dust emission of massive galaxies up to $z = 4$ and constraints on their dominant mode of star formation”. In: *aap* 573, A113, A113. DOI: 10.1051/0004-6361/201425031. arXiv: 1409.5796 [astro-ph.GA].
- B  thermin, Matthieu et al. (Nov. 2017). “The impact of clustering and angular resolution on far-infrared and millimeter continuum observations”. In: *aap* 607, A89, A89. DOI: 10.1051/0004-6361/201730866. arXiv: 1703.08795 [astro-ph.GA].
- Bevington, Philip R. and D. Keith Robinson (2003). *Data reduction and error analysis for the physical sciences*. URL: <http://experimentationlab.berkeley.edu/sites/default/files/pdfs/Bevington.pdf>.
- Blasco-Herrera, J. et al. (Sept. 2013). “Ha kinematics of 11 starburst galaxies selected from the Sloan Digital Sky Survey”. In: *Monthly Notices of the Royal Astronomical Society* 435.3, pp. 1958–1983. ISSN: 0035-8711. DOI: 10.1093/mnras/stt1387. eprint: <https://academic.oup.com/mnras/article-pdf/435/3/1958/3353142/stt1387.pdf>. URL: <https://doi.org/10.1093/mnras/stt1387>.
- Bolatto, A. D. et al. (Aug. 2015). “High-resolution Imaging of PHIBSS $z \sim 2$ Main-sequence Galaxies in CO J = 1 \rightarrow 0”. In: *ApJ* 809.2, 175, p. 175. DOI: 10.1088/0004-637X/809/2/175. arXiv: 1507.05652 [astro-ph.GA].
- Bolatto, Alberto D., Mark Wolfire, and Adam K. Leroy (Aug. 2013). “The CO-to-H₂ Conversion Factor”. In: *ARAA* 51.1, pp. 207–268. DOI: 10.1146/annurev-astro-082812-140944. arXiv: 1301.3498 [astro-ph.GA].
- Boquien, M. et al. (Feb. 2019). “CIGALE: a python Code Investigating GALaxy Emission”. In: *aap* 622, A103, A103. DOI: 10.1051/0004-6361/201834156. arXiv: 1811.03094 [astro-ph.GA].
- Brammer, Gabriel (June 2022). *grizli*. Version 1.5.0. DOI: 10.5281/zenodo.5012699. URL: <https://github.com/gbrammer/grizli>.
- Brammer, Gabriel B., Pieter G. van Dokkum, and Paolo Coppi (Oct. 2008). “EAZY: A Fast, Public Photometric Redshift Code”. In: *ApJ* 686.2, pp. 1503–1513. DOI: 10.1086/591786. arXiv: 0807.1533 [astro-ph].
- Brisbin, Drew et al. (Aug. 2019). “Neutral carbon and highly excited CO in a massive star-forming main sequence galaxy at $z = 2.2$ ”. In: *aap* 628, A104, A104. DOI: 10.1051/0004-6361/201935148. arXiv: 1907.04936 [astro-ph.GA].
- Bussmann, R. S. et al. (Oct. 2015). “HerMES: ALMA Imaging of Herschel-selected Dusty Star-forming Galaxies”. In: *ApJ* 812.1, 43, p. 43. DOI: 10.1088/0004-637X/812/1/43. arXiv: 1504.05256 [astro-ph.GA].
- Calistro Rivera, Gabriela et al. (Aug. 2018). “Resolving the ISM at the Peak of Cosmic Star Formation with ALMA: The Distribution of CO and Dust Continuum in $z \sim 2.5$ Submillimeter Galaxies”. In: *ApJ* 863.1, 56, p. 56. DOI: 10.3847/1538-4357/aacffa. arXiv: 1804.06852 [astro-ph.GA].
- Calzetti, Daniela et al. (Apr. 2000). “The Dust Content and Opacity of Actively Star-forming Galaxies”. In: *ApJ* 533.2, pp. 682–695. DOI: 10.1086/308692. arXiv: astro-ph/9911459 [astro-ph].
- Calzetti, Daniela et al. (Mar. 2004). “The Ionized Gas in Local Starburst Galaxies: Global and Small-Scale Feedback from Star Formation”. In: *aj* 127.3, pp. 1405–1430. DOI: 10.1086/382095. arXiv: astro-ph/0312385 [astro-ph].
- Camps, P. and M. Baes (Mar. 2015). “SKIRT: An advanced dust radiative transfer code with a user-friendly architecture”. In: *Astronomy and Computing* 9, pp. 20–33. DOI: 10.1016/j.ascom.2014.10.004. arXiv: 1410.1629 [astro-ph.IM].
- Carilli, C. L. and F. Walter (Aug. 2013). “Cool Gas in High-Redshift Galaxies”. In: *ARAA* 51.1, pp. 105–161. DOI: 10.1146/annurev-astro-082812-140953. arXiv: 1301.0371 [astro-ph.CO].
- Cassata, Paolo et al. (Mar. 2020). “ALMA Reveals the Molecular Gas Properties of Five Star-forming Galaxies across the Main Sequence at $z = 3$ ”. In: *ApJ* 891.1, 83, p. 83. DOI: 10.3847/1538-4357/ab7452. arXiv: 2002.04040 [astro-ph.GA].
- Chabrier, Gilles (July 2003). “Galactic Stellar and Substellar Initial Mass Function”. In: 115.809, pp. 763–795. DOI: 10.1086/376392. arXiv: astro-ph/0304382 [astro-ph].

- Chen, Chian-Chou et al. (Sept. 2017). “A Spatially Resolved Study of Cold Dust, Molecular Gas, H II Regions, and Stars in the $z = 2.12$ Submillimeter Galaxy ALESS67.1”. In: *ApJ* 846.2, 108, p. 108. DOI: 10.3847/1538-4357/aa863a. arXiv: 1708.08937 [astro-ph.GA].
- Cibinel, A. et al. (June 2019). “Early- and late-stage mergers among main sequence and starburst galaxies at $0.2 \leq z \leq 2$ ”. In: *mnras* 485.4, pp. 5631–5651. DOI: 10.1093/mnras/stz690. arXiv: 1809.00715 [astro-ph.GA].
- Clayton, Geoffrey C. et al. (May 2003). “Dust Grain Size Distributions from MRN to MEM”. In: *The Astrophysical Journal* 588.2, pp. 871–880. DOI: 10.1086/374316. URL: <https://doi.org/10.1086/374316>.
- Cochrane, R K et al. (Feb. 2021). “Resolving a dusty, star-forming SHiZELS galaxy at $z = 2.2$ with HST, ALMA, and SINFONI on kiloparsec scales”. In: *Monthly Notices of the Royal Astronomical Society* 503.2, pp. 2622–2638. ISSN: 1365-2966. DOI: 10.1093/mnras/stab467. URL: <http://dx.doi.org/10.1093/mnras/stab467>.
- Cochrane, R. K. et al. (Sept. 2019). “Predictions for the spatial distribution of the dust continuum emission in $1 < z < 5$ star-forming galaxies”. In: *mnras* 488.2, pp. 1779–1789. DOI: 10.1093/mnras/stz1736. arXiv: 1905.13234 [astro-ph.GA].
- Conselice, C. J., M. A. Bershadsky, and III Gallagher J. S. (Feb. 2000). “Physical morphology and triggers of starburst galaxies”. In: *aap* 354, pp. L21–L24. arXiv: astro-ph/0001195 [astro-ph].
- da Cunha, Elisabete, Stéphane Charlot, and David Elbaz (Aug. 2008). “A simple model to interpret the ultraviolet, optical and infrared emission from galaxies”. In: *mnras* 388.4, pp. 1595–1617. DOI: 10.1111/j.1365-2966.2008.13535.x. arXiv: 0806.1020 [astro-ph].
- Davé, Romeel, Kristian Finlator, and Benjamin D. Oppenheimer (Sept. 2011). “Galaxy evolution in cosmological simulations with outflows - II. Metallicities and gas fractions”. In: *mnras* 416.2, pp. 1354–1376. DOI: 10.1111/j.1365-2966.2011.19132.x. arXiv: 1104.3156 [astro-ph.CO].
- Dionatos, Odysseas (Jan. 2015). “Gas line observations of disks”. In: *EPJ Web of Conferences* 102, p. 00008. DOI: 10.1051/epjconf/201510200008.
- Dokkum, Pieter G. van (Feb. 2008). “Evidence of Cosmic Evolution of the Stellar Initial Mass Function”. In: *The Astrophysical Journal* 674.1, pp. 29–50. DOI: 10.1086/525014. URL: <https://doi.org/10.1086/525014>.
- Draine, B. T. and Aigen Li (Mar. 2007). “Infrared Emission from Interstellar Dust. IV. The Silicate-Graphite-PAH Model in the Post-Spitzer Era”. In: *ApJ* 657.2, pp. 810–837. DOI: 10.1086/511055. arXiv: astro-ph/0608003 [astro-ph].
- Draine, B. T. et al. (Jan. 2014). “Andromeda’s Dust”. In: *ApJ* 780.2, 172, p. 172. DOI: 10.1088/0004-637X/780/2/172. arXiv: 1306.2304 [astro-ph.CO].
- Draine, B.T. (2003). “Interstellar Dust Grains”. In: *Annual Review of Astronomy and Astrophysics* 41.1, pp. 241–289. DOI: 10.1146/annurev.astro.41.011802.094840. eprint: <https://doi.org/10.1146/annurev.astro.41.011802.094840>. URL: <https://doi.org/10.1146/annurev.astro.41.011802.094840>.
- Draine, Bruce T. (2011). *Physics of the Interstellar and Intergalactic Medium*. Princeton University Press. ISBN: 9780691122144. URL: <http://www.jstor.org/stable/j.ctvc4m4hrz.4> (visited on 10/04/2022).
- Elbaz, D. et al. (Sept. 2011). “GOODS-Herschel: an infrared main sequence for star-forming galaxies”. In: *aap* 533, A119, A119. DOI: 10.1051/0004-6361/201117239. arXiv: 1105.2537 [astro-ph.CO].
- Emerson, D. (1996). *Interpreting Astronomical Spectra*.
- Erb, Dawn K. et al. (July 2006). “The Stellar, Gas, and Dynamical Masses of Star-forming Galaxies at $z \sim 2$ ”. In: *apj* 646.1, pp. 107–132. DOI: 10.1086/504891. arXiv: astro-ph/0604041 [astro-ph].
- Fagioli, Martina et al. (Nov. 2016). “Minor Mergers or Progenitor Bias? The Stellar Ages of Small and Large Quenched Galaxies”. In: *ApJ* 831.2, 173, p. 173. DOI: 10.3847/0004-637X/831/2/173. arXiv: 1607.03493 [astro-ph.GA].
- Falcón-Barroso, Jesús and Johan H. Knapen (2013). *Secular Evolution of Galaxies*.
- Förster Schreiber, Natascha M. and Stijn Wuyts (Aug. 2020). “Star-Forming Galaxies at Cosmic Noon”. In: *ARAA* 58, pp. 661–725. DOI: 10.1146/annurev-astro-032620-021910. arXiv: 2010.10171 [astro-ph.GA].
- Fu, Hai et al. (May 2013). “The rapid assembly of an elliptical galaxy of 400 billion solar masses at a redshift of 2.3”. In: *Nature* 498.7454, pp. 338–341. DOI: 10.1038/nature12184. URL: <https://doi.org/10.1038%5C%2Fnature12184>.
- Galliano, F. (Dec. 2017). “Some insights on the dust properties of nearby galaxies, as seen with Herschel”. In: 149, pp. 38–44. DOI: 10.1016/j.pss.2017.09.006.
- Gavin, Henri P. (2019). “The Levenberg-Marquardt algorithm for nonlinear least squares curve-fitting problems”. In: *Department of Civil and Environmental Engineering at Duke University*. URL: <http://people.duke.edu/~hpgavin/ce281/lm.pdf>.
- Genzel, R. et al. (Feb. 2015). “Combined CO and Dust Scaling Relations of Depletion Time and Molecular Gas Fractions with Cosmic Time, Specific Star-formation Rate, and Stellar Mass”. In: *ApJ* 800.1, 20, p. 20. DOI: 10.1088/0004-637X/800/1/20. arXiv: 1409.1171 [astro-ph.GA].
- Gillman, S et al. (2019). “The dynamics and distribution of angular momentum in HiZELS star-forming galaxies at $z = 0.8-3.3$ ”. In: *Monthly Notices of the Royal Astronomical Society* 486.1, pp. 175–194.
- Goldsmith, Paul et al. (Oct. 2022). “The Space Terahertz Observatory (STO): A 10-meter-class Far-Infrared Telescope for Origins Research”. In:
- Graham, Alister W. and Simon P. Driver (2005). “A Concise Reference to (Projected) Sérsic $R1/n$ Quantities, Including Concentration, Profile Slopes, Petrosian Indices, and Kron Magnitudes”. In: *Publications of the Astronomical Society*

- of Australia* 22.2, pp. 118–127. ISSN: 1448-6083. DOI: 10.1071/as05001. URL: <http://dx.doi.org/10.1071/AS05001>.
- Guo, Yicheng et al. (Aug. 2013). “CANDELS Multi-wavelength Catalogs: Source Detection and Photometry in the GOODS-South Field”. In: *apjs* 207.2, 24, p. 24. DOI: 10.1088/0067-0049/207/2/24. arXiv: 1308.4405 [astro-ph.CO].
- Hayashi, Masao et al. (Apr. 2018). “Molecular Gas Reservoirs in Cluster Galaxies at $z = 1.46$ ”. In: *ApJ* 856.2, 118, p. 118. DOI: 10.3847/1538-4357/aab3e7. arXiv: 1803.00298 [astro-ph.GA].
- Hong, Sungryong et al. (Apr. 2011). “Large-scale Shock-ionized and Photoionized Gas in M83: The Impact of Star Formation”. In: *ApJ* 731.1, 45, p. 45. DOI: 10.1088/0004-637X/731/1/45. arXiv: 1102.2444 [astro-ph.CO].
- Hopkins, Philip F. et al. (Nov. 2014). “Galaxies on FIRE (Feedback In Realistic Environments): stellar feedback explains cosmologically inefficient star formation”. In: *mnras* 445.1, pp. 581–603. DOI: 10.1093/mnras/stu1738. arXiv: 1311.2073 [astro-ph.CO].
- Iverson, R. J. et al. (Aug. 2013). “Herschel-ATLAS: A Binary HyLIRG Pinpointing a Cluster of Starbursting Protoellipticals”. In: *ApJ* 772.2, 137, p. 137. DOI: 10.1088/0004-637X/772/2/137. arXiv: 1302.4436 [astro-ph.CO].
- Jin, Shuowen et al. (Aug. 2018). ““Super-deblended” Dust Emission in Galaxies. II. Far-IR to (Sub)millimeter Photometry and High-redshift Galaxy Candidates in the Full COSMOS Field”. In: *The Astrophysical Journal* 864.1, p. 56. DOI: 10.3847/1538-4357/aad4af. URL: <https://doi.org/10.3847/1538-4357/aad4af>.
- Joachimi, Benjamin et al. (July 2015). “Galaxy Alignments: An Overview”. In: *Space Science Reviews* 193.1-4, pp. 1–65. ISSN: 1572-9672. DOI: 10.1007/s11214-015-0177-4. URL: <http://dx.doi.org/10.1007/s11214-015-0177-4>.
- Kaasinen, Melanie et al. (Aug. 2020). “A Comparison of the Stellar, CO, and Dust-continuum Emission from Three Star-forming HUDF Galaxies at $z \sim 2$ ”. In: *The Astrophysical Journal* 899.1, p. 37. DOI: 10.3847/1538-4357/aba438. URL: <https://doi.org/10.3847/1538-4357/aba438>.
- Kennicutt Robert C., Jr. (Jan. 1998). “Star Formation in Galaxies Along the Hubble Sequence”. In: *ARAAS* 36, pp. 189–232. DOI: 10.1146/annurev.astro.36.1.189. arXiv: astro-ph/9807187 [astro-ph].
- Kokorev, Vasily I. et al. (Nov. 2021). “The Evolving Interstellar Medium of Star-forming Galaxies, as Traced by Stardust”. In: *ApJ* 921.1, 40, p. 40. DOI: 10.3847/1538-4357/ac18ce. arXiv: 2109.06209 [astro-ph.GA].
- Kravtsov, Andrey V. and Stefano Borgani (Sept. 2012). “Formation of Galaxy Clusters”. In: *Annual Review of Astronomy and Astrophysics* 50.1, pp. 353–409. ISSN: 1545-4282. DOI: 10.1146/annurev-astro-081811-125502. URL: <http://dx.doi.org/10.1146/annurev-astro-081811-125502>.
- Laigle, C. et al. (June 2016). “The COSMOS2015 Catalog: Exploring the $1 < z < 6$ Universe with Half a Million Galaxies”. In: *apjs* 224.2, 24, p. 24. DOI: 10.3847/0067-0049/224/2/24. arXiv: 1604.02350 [astro-ph.GA].
- Lasker, Barry M. et al. (Aug. 2008). “The Second-Generation Guide Star Catalog: Description and Properties”. In: 136.2, pp. 735–766. DOI: 10.1088/0004-6256/136/2/735. arXiv: 0807.2522 [astro-ph].
- Léna, Pierre et al. (2012). *Observational Astrophysics*. DOI: 10.1007/978-3-642-21815-6.
- Leung, T. K. Daisy et al. (Jan. 2019). “The ISM Properties and Gas Kinematics of a Redshift 3 Massive Dusty Star-forming Galaxy”. In: *The Astrophysical Journal* 871.1, p. 85. DOI: 10.3847/1538-4357/aaf860. URL: <https://doi.org/10.3847/1538-4357/aaf860>.
- Liu, Daizhong et al. (Oct. 2019). “Automated Mining of the ALMA Archive in the COSMOS Field (A³COSMOS). I. Robust ALMA Continuum Photometry Catalogs and Stellar Mass and Star Formation Properties for ~ 700 Galaxies at $z = 0.5-6$ ”. In: *apjs* 244.2, 40, p. 40. DOI: 10.3847/1538-4365/ab42da. arXiv: 1910.12872 [astro-ph.GA].
- Lutz, D. et al. (Aug. 2011). “PACS Evolutionary Probe (PEP) - A Herschel key program”. In: *aap* 532, A90, A90. DOI: 10.1051/0004-6361/201117107. arXiv: 1106.3285 [astro-ph.CO].
- Madau, Piero and Mark Dickinson (Aug. 2014). “Cosmic Star-Formation History”. In: *Annual Review of Astronomy and Astrophysics* 52.1, pp. 415–486. DOI: 10.1146/annurev-astro-081811-125615. URL: <https://doi.org/10.1146/annurev-astro-081811-125615>.
- Magdis, Georgios E. et al. (Nov. 2012). “The Evolving Interstellar Medium of Star-forming Galaxies since $z = 2$ as Probed by Their Infrared Spectral Energy Distributions”. In: *apj* 760.1, 6, p. 6. DOI: 10.1088/0004-637X/760/1/6. arXiv: 1210.1035 [astro-ph.CO].
- Magnelli, Benjamin et al. (Mar. 2020). “The ALMA Spectroscopic Survey in the HUDF: The Cosmic Dust and Gas Mass Densities in Galaxies up to $z \sim 3$ ”. In: *ApJ* 892.1, 66, p. 66. DOI: 10.3847/1538-4357/ab7897. arXiv: 2002.08640 [astro-ph.GA].
- Marocco, Federico et al. (Mar. 2021). “The CatWISE2020 Catalog”. In: *apjs* 253.1, 8, p. 8. DOI: 10.3847/1538-4365/abd805. arXiv: 2012.13084 [astro-ph.IM].
- Mathis, J. S., W. Rumpl, and K. H. Nordsieck (Oct. 1977). “The size distribution of interstellar grains.” In: *ApJ* 217, pp. 425–433. DOI: 10.1086/155591.
- Moorwood, Alan F. M. (Aug. 1996). “Starburst Galaxies”. In: *ssr* 77.3-4, pp. 303–366. DOI: 10.1007/BF00226226.
- Muzzin, Adam et al. (May 2013). “A PUBLIC K -SELECTED CATALOG IN THE COSMOS/ULTRAVISTA FIELD: PHOTOMETRY, PHOTOMETRIC REDSHIFTS, AND STELLAR POPULATION PARAMETERS”. In: *The Astrophysical Journal Supplement Series* 206.1, p. 8. DOI: 10.1088/0067-0049/206/1/8. URL: <https://doi.org/10.1088/0067-0049/206/1/8>.

- Nayyeri, H. et al. (Jan. 2017). “CANDELS Multi-wavelength Catalogs: Source Identification and Photometry in the CANDELS COSMOS Survey Field”. In: *apjs* 228.1, 7, p. 7. DOI: 10.3847/1538-4365/228/1/7. arXiv: 1612.07364 [astro-ph.GA].
- Nelson, Dylan et al. (Dec. 2019). “First results from the TNG50 simulation: galactic outflows driven by supernovae and black hole feedback”. In: *mnras* 490.3, pp. 3234–3261. DOI: 10.1093/mnras/stz2306. arXiv: 1902.05554 [astro-ph.GA].
- Nelson, Erica June et al. (Sept. 2016). “Where Stars Form: Inside-out Growth and Coherent Star Formation from HST H α Maps of 3200 Galaxies across the Main Sequence at $0.7 < z < 1.5$ ”. In: *ApJ* 828.1, 27, p. 27. DOI: 10.3847/0004-637X/828/1/27. arXiv: 1507.03999 [astro-ph.GA].
- Noble, AG et al. (2017). “ALMA Observations of Gas-rich Galaxies in $z \sim 1.6$ Galaxy Clusters: Evidence for Higher Gas Fractions in High-density Environments”. In: *The Astrophysical Journal Letters* 842.2, p. L21.
- Offner, S. S. R. et al. (Jan. 2014). “The Origin and Universality of the Stellar Initial Mass Function”. In: *Protostars and Planets VI*. Ed. by Henrik Beuther et al., p. 53. DOI: 10.2458/azu_uapress_9780816531240-ch003. arXiv: 1312.5326 [astro-ph.SR].
- Olsen, LF et al. (2006). “ESO imaging survey: infrared observations of CDF-S and HDF-S”. In: *Astronomy & Astrophysics* 452.1, pp. 119–129.
- Padmanabhan, T. (2002). *Theoretical astrophysics. Galaxies and cosmology*. First. Vol. Third. Cambridge University Press.
- Papadopoulos, P. P., W. -F. Thi, and S. Viti (June 2004). “CI lines as tracers of molecular gas, and their prospects at high redshifts”. In: *mnras* 351.1, pp. 147–160. DOI: 10.1111/j.1365-2966.2004.07762.x. arXiv: astro-ph/0403092 [astro-ph].
- Peng, Chien Y. et al. (July 2002). “Detailed Structural Decomposition of Galaxy Images”. In: 124.1, pp. 266–293. DOI: 10.1086/340952. arXiv: astro-ph/0204182 [astro-ph].
- (June 2010). “Detailed Decomposition of Galaxy Images. II. Beyond Axisymmetric Models”. In: 139.6, pp. 2097–2129. DOI: 10.1088/0004-6256/139/6/2097. arXiv: 0912.0731 [astro-ph.CO].
- Pillepich, Annalisa et al. (Dec. 2019). “First results from the TNG50 simulation: the evolution of stellar and gaseous discs across cosmic time”. In: *mnras* 490.3, pp. 3196–3233. DOI: 10.1093/mnras/stz2338. arXiv: 1902.05553 [astro-ph.GA].
- Pineda, J. L. et al. (June 2013). “A Herschel [C ii] Galactic plane survey. I. The global distribution of ISM gas components”. In: *aap* 554, A103, A103. DOI: 10.1051/0004-6361/201321188. arXiv: 1304.7770 [astro-ph.GA].
- Popping, Gergö et al. (Nov. 2021). “The dust-continuum size of TNG50 galaxies at $z = 1-5$: a comparison with the distribution of stellar light, stars, dust, and H $_2$ ”. In: *Monthly Notices of the Royal Astronomical Society* 510.3, pp. 3321–3334. ISSN: 1365-2966. DOI: 10.1093/mnras/stab3312. URL: <http://dx.doi.org/10.1093/mnras/stab3312>.
- Puget, J. L. and A. Leger (Jan. 1989). “A new component of the interstellar matter: small grains and large aromatic molecules.” In: *ARAA* 27, pp. 161–198. DOI: 10.1146/annurev.aa.27.090189.001113.
- Reddy, Naveen A. et al. (July 2012). “The Characteristic Star Formation Histories of Galaxies at Redshifts $z \sim 2-7$ ”. In: *ApJ* 754.1, 25, p. 25. DOI: 10.1088/0004-637X/754/1/25. arXiv: 1205.0555 [astro-ph.CO].
- Renzini, Alvio (Sept. 2006). “Stellar Population Diagnostics of Elliptical Galaxy Formation”. In: *ARAA* 44.1, pp. 141–192. DOI: 10.1146/annurev.astro.44.051905.092450. arXiv: astro-ph/0603479 [astro-ph].
- Ricciardelli, E. et al. (July 2010). “The evolutionary sequence of submillimetre galaxies: from diffuse discs to massive compact ellipticals?” In: *mnras* 406.1, pp. 230–236. DOI: 10.1111/j.1365-2966.2010.16693.x. arXiv: 1003.3252 [astro-ph.CO].
- Rodighiero, G. et al. (Oct. 2011). “The Lesser Role of Starbursts in Star Formation at $z = 2$ ”. In: *apjl* 739.2, L40, p. L40. DOI: 10.1088/2041-8205/739/2/L40. arXiv: 1108.0933 [astro-ph.CO].
- Rodrigo, C. and E. Solano (July 2020). “The SVO Filter Profile Service”. In: *XIV.0 Scientific Meeting (virtual) of the Spanish Astronomical Society*, p. 182.
- Salpeter, Edwin E. (Jan. 1955). “The Luminosity Function and Stellar Evolution.” In: *ApJ* 121, p. 161. DOI: 10.1086/145971.
- Sargent, M. T. et al. (Mar. 2012). “The Contribution of Starbursts and Normal Galaxies to Infrared Luminosity Functions at $z < 2$ ”. In: *apjl* 747.2, L31, p. L31. DOI: 10.1088/2041-8205/747/2/L31. arXiv: 1202.0290 [astro-ph.CO].
- Schreiber, C. et al. (Mar. 2015). “The Herschel view of the dominant mode of galaxy growth from $z = 4$ to the present day”. In: *aap* 575, A74, A74. DOI: 10.1051/0004-6361/201425017. arXiv: 1409.5433 [astro-ph.GA].
- Schreiber, C. et al. (Jan. 2018). “Dust temperature and mid-to-total infrared color distributions for star-forming galaxies at $0 < z < 4$ ”. In: *aap* 609, A30, A30. DOI: 10.1051/0004-6361/201731506. arXiv: 1710.10276 [astro-ph.GA].
- Schreiber, N. M. Förster et al. (Sept. 2011). “CONSTRAINTS ON THE ASSEMBLY AND DYNAMICS OF GALAXIES. II. PROPERTIES OF KILOPARSEC-SCALE CLUMPS IN REST-FRAME OPTICAL EMISSION”. In: *The Astrophysical Journal* 739.1, p. 45. DOI: 10.1088/0004-637x/739/1/45. URL: <https://doi.org/10.1088/0004-637x/739/1/45>.
- Schreiber, NM Förster et al. (2006). “SINFONI integral field spectroscopy of $z \sim 2$ UV-selected galaxies: rotation curves and dynamical evolution”. In: *The Astrophysical Journal* 645.2, p. 1062.

- Scoville, N. et al. (Apr. 2016). “ISM Masses and the Star formation Law at $Z = 1$ to 6: ALMA Observations of Dust Continuum in 145 Galaxies in the COSMOS Survey Field”. In: *ApJ* 820.2, 83, p. 83. DOI: 10.3847/0004-637X/820/2/83. arXiv: 1511.05149 [astro-ph.GA].
- Shibuya, Takatoshi, Masami Ouchi, and Yuichi Harikane (Aug. 2015). “Morphologies of $\sim 190,000$ Galaxies at $z = 0-10$ Revealed with HST Legacy Data. I. Size Evolution”. In: *apjs* 219.2, 15, p. 15. DOI: 10.1088/0067-0049/219/2/15. arXiv: 1503.07481 [astro-ph.GA].
- Silverman, J. D. et al. (Sept. 2015). “The FMOS-COSMOS Survey of Star-forming Galaxies at $z \sim 1.6$. III. Survey Design, Performance, and Sample Characteristics”. In: *apjs* 220.1, 12, p. 12. DOI: 10.1088/0067-0049/220/1/12. arXiv: 1409.0447 [astro-ph.GA].
- Skelton, Rosalind E et al. (2014). “3D-HST WFC3-selected photometric catalogs in the five CANDELS/3D-HST fields: photometry, photometric redshifts, and stellar masses”. In: *The Astrophysical Journal Supplement Series* 214.2, p. 24.
- Smith, Mark D. et al. (May 2019). “WISDOM project - IV. A molecular gas dynamical measurement of the supermassive black hole mass in NGC 524”. In: *mnras* 485.3, pp. 4359–4374. DOI: 10.1093/mnras/stz625. arXiv: 1903.03124 [astro-ph.GA].
- Smolčić, V. et al. (June 2017). “The VLA-COSMOS 3 GHz Large Project: Continuum data and source catalog release”. In: *aap* 602, A1, A1. DOI: 10.1051/0004-6361/201628704. arXiv: 1703.09713 [astro-ph.GA].
- Sorba, R. and M. Sawicki (July 2015). “Missing stellar mass in SED fitting: spatially unresolved photometry can underestimate galaxy masses”. In: *Monthly Notices of the Royal Astronomical Society* 452.1, pp. 235–245. ISSN: 0035-8711. DOI: 10.1093/mnras/stv1235. eprint: <https://academic.oup.com/mnras/article-pdf/452/1/235/13769293/stv1235.pdf>. URL: <https://doi.org/10.1093/mnras/stv1235>.
- Speagle, Joshua et al. (Apr. 2014). “A Highly Consistent Framework for the Evolution of the Star-Forming ”Main Sequence” from $z = 0-6$ ”. In: *Astrophysical Journal Supplement Series* 214.
- Spitzer Science Center (SSC) and Infrared Science Archive (IRSA) (Mar. 2021). “VizieR Online Data Catalog: The Spitzer (SEIP) source list (SSTSL2) (Spitzer Science Center, 2021)”. In: *VizieR Online Data Catalog*, II/368, pp. II/368.
- Stahler, Steven W. and Francesco Palla (2004). *The Formation of Stars*.
- Straatman, Caroline M. S. et al. (Oct. 2016). “The FourStar Galaxy Evolution Survey (ZFOURGE): Ultraviolet to Far-infrared Catalogs, Medium-bandwidth Photometric Redshifts with Improved Accuracy, Stellar Masses, and Confirmation of Quiescent Galaxies to $z \sim 3.5$ ”. In: *ApJ* 830.1, 51, p. 51. DOI: 10.3847/0004-637X/830/1/51. arXiv: 1608.07579 [astro-ph.GA].
- Strobel, Nick (2022). *Astronomy Notes*. Accessed: 2022-10-26. URL: <https://www.astronomynotes.com/galaxy/s3.htm>.
- Suess, Katherine A. et al. (July 2021). “Dissecting the Size-Mass and Σ_1 -Mass Relations at $1.0 < z < 2.5$: Galaxy Mass Profiles and Color Gradients as a Function of Spectral Shape”. In: *ApJ* 915.2, 87, p. 87. DOI: 10.3847/1538-4357/abf1e4. arXiv: 2101.05820 [astro-ph.GA].
- Tacconi, Linda J., Reinhard Genzel, and Amiel Sternberg (Aug. 2020). “The Evolution of the Star-Forming Interstellar Medium Across Cosmic Time”. In: *araa* 58, pp. 157–203. DOI: 10.1146/annurev-astro-082812-141034. arXiv: 2003.06245 [astro-ph.GA].
- Tadaki, Ken-ichi et al. (Jan. 2017). “BULGE-FORMING GALAXIES WITH AN EXTENDED ROTATING DISK AT $z \sim 2$ ”. In: *The Astrophysical Journal* 834.2, p. 135. DOI: 10.3847/1538-4357/834/2/135. URL: <https://doi.org/10.3847/1538-4357/834/2/135>.
- Tadaki, Ken-ichi et al. (Sept. 2020). “Structural Evolution in Massive Galaxies at $z \sim 2$ ”. In: *The Astrophysical Journal* 901.1, p. 74. DOI: 10.3847/1538-4357/abaf4a. URL: <https://doi.org/10.3847/1538-4357/abaf4a>.
- Tamura, Y. et al. (Dec. 2010). “Submillimeter Array Identification of the Millimeter-selected Galaxy SSA22-AzTEC1: A Protoquasar in a Protocluster?” In: *apj* 724.2, pp. 1270–1282. DOI: 10.1088/0004-637X/724/2/1270. arXiv: 1010.1267 [astro-ph.CO].
- Tan, Q. et al. (Sept. 2014). “Dust and gas in luminous proto-cluster galaxies at $z = 4.05$: the case for different cosmic dust evolution in normal and starburst galaxies”. In: *aap* 569, A98, A98. DOI: 10.1051/0004-6361/201423905. arXiv: 1403.7992 [astro-ph.GA].
- Umehata, Hideki et al. (2017). “ALMA deep field in SSA22: source catalog and number counts”. In: *The Astrophysical Journal* 835.1, p. 98.
- van den Bosch, Frank C. (Nov. 2001). “The origin of the density distribution of disc galaxies: a new problem for the standard model of disc formation”. In: *mnras* 327.4, pp. 1334–1352. DOI: 10.1046/j.1365-8711.2001.04861.x. arXiv: astro-ph/0107195 [astro-ph].
- van der Wel, A. et al. (June 2014). “3D-HST+CANDELS: The Evolution of the Galaxy Size-Mass Distribution since $z = 3$ ”. In: *ApJ* 788.1, 28, p. 28. DOI: 10.1088/0004-637X/788/1/28. arXiv: 1404.2844 [astro-ph.GA].
- Velusamy, T. and W. D. Langer (Dec. 2014). “Origin and z -distribution of Galactic diffuse [C II] emission”. In: *aap* 572, A45, A45. DOI: 10.1051/0004-6361/201424350. arXiv: 1409.4788 [astro-ph.GA].
- Virtanen, Pauli et al. (Oct. 2020). *scipy/scipy: SciPy 1.5.3*. Zenodo. Version v1.5.3. DOI: 10.5281/zenodo.4100507.
- Vizgan, D. et al. (Apr. 2022). “Tracing Molecular Gas Mass in $z \leq 6$ Galaxies with [C II]”. In: *ApJ* 929.1, 92, p. 92. DOI: 10.3847/1538-4357/ac5cba. arXiv: 2203.05316 [astro-ph.GA].

- Voigt, L. M. and S. L. Bridle (Mar. 2010). “Limitations of model-fitting methods for lensing shear estimation”. In: *Monthly Notices of the Royal Astronomical Society*. ISSN: 1365-2966. DOI: 10.1111/j.1365-2966.2010.16300.x. URL: <http://dx.doi.org/10.1111/j.1365-2966.2010.16300.x>.
- Weaver, J. R. et al. (Jan. 2022). “COSMOS2020: A Panchromatic View of the Universe to $z \sim 10$ from Two Complementary Catalogs”. In: *The Astrophysical Journal Supplement Series* 258.1, p. 11. DOI: 10.3847/1538-4365/ac3078. URL: <https://doi.org/10.3847/1538-4365/ac3078>.
- Webb, K. A. et al. (Oct. 2017). “Constraining the Dust Opacity Law in Three Small and Isolated Molecular Clouds”. In: *The Astrophysical Journal* 849.1, p. 13. DOI: 10.3847/1538-4357/aa901c. URL: <https://doi.org/10.3847/1538-4357/aa901c>.
- Wolfire, Mark G. et al. (Apr. 2003). “Neutral Atomic Phases of the Interstellar Medium in the Galaxy”. In: *ApJ* 587.1, pp. 278–311. DOI: 10.1086/368016. arXiv: astro-ph/0207098 [astro-ph].
- Wuyts, Stijn et al. (Oct. 2010). “On Sizes, Kinematics, M/L Gradients, and Light Profiles of Massive Compact Galaxies at $z \sim 2$ ”. In: *apj* 722.2, pp. 1666–1684. DOI: 10.1088/0004-637X/722/2/1666. arXiv: 1008.4127 [astro-ph.CO].
- Wuyts, Stijn et al. (Dec. 2011). “Galaxy Structure and Mode of Star Formation in the SFR-Mass Plane from $z \sim 2.5$ to $z \sim 0.1$ ”. In: *ApJ* 742.2, 96, p. 96. DOI: 10.1088/0004-637X/742/2/96. arXiv: 1107.0317 [astro-ph.CO].
- Xiao, M. -Y. et al. (Aug. 2022). “Starbursts with suppressed velocity dispersion revealed in a forming cluster at $z = 2.51$ ”. In: *aap* 664, A63, A63. DOI: 10.1051/0004-6361/202142843. arXiv: 2205.07909 [astro-ph.GA].
- Zanella, A. et al. (Dec. 2018). “The [C II] emission as a molecular gas mass tracer in galaxies at low and high redshifts”. In: *mnras* 481.2, pp. 1976–1999. DOI: 10.1093/mnras/sty2394. arXiv: 1808.10331 [astro-ph.GA].
- Zavala, J. A. et al. (Dec. 2019). “On the Gas Content, Star Formation Efficiency, and Environmental Quenching of Massive Galaxies in Protoclusters at $z \approx 2.0-2.5$ ”. In: *The Astrophysical Journal* 887.2, p. 183. DOI: 10.3847/1538-4357/ab5302. URL: <https://doi.org/10.3847/1538-4357/ab5302>.

Acronyms

Λ CDM Λ Cold Dark Matter. 1, 33

ACS Advanced Camera for Surveys. 70

AGN Active Galactic Nucleus. 32, 69, 78, 81, 84, 88, 91, 94, 97, 99, 102, 105, 112, 116, 121, 125, 129, 133, 136, 140, 145, 148, 152, 155, 158, 164, 167

ALMA Atacama Large Millimetre/submillimetre Array. iii, 1, 23–29, 41, 43, 47, 52, 55, 59, 79, 82, 85, 86, 89, 92, 95, 97, 100, 103, 106, 108, 110, 113, 114, 117–119, 122, 123, 126, 127, 130, 131, 133, 134, 137, 138, 141, 143, 146, 149, 150, 152, 153, 155, 156, 159–162, 164, 165, 167, 168

CDM Cold Dark Matter. 1, 2, 18

CNM Cold Neutral Medium. 3, 6

DEC. Declination. 25, 50, 51

ETG Early-Type Galaxy. 17, 19, 22

FIR Far Infrared. 23, 24, 26

FOV Field Of View. 36, 38, 39

FUV Far Ultraviolet. 3, 5, 6, 16, 17

FWHM Full Width at Half-Maximum. 41, 46, 47, 78, 79, 81, 82, 84–86, 88, 89, 91, 92, 94, 95, 97, 99, 100, 102, 103, 105–110, 112–114, 116–119, 121–123, 125–127, 129–131, 133, 134, 136–138, 140–143, 145, 146, 148–150, 152, 153, 155, 156, 158–162, 164, 165, 167, 168

HST Hubble Space Telescope. iii, 1, 24–29, 36–39, 41–43, 46, 52, 59, 70

HUMBLE How to Use Measurements of Bright Line Emission. 24, 25

ICRS International Celestial Reference System. 25

IMF Initial Mass Function. 14–16, 32, 48

IR Infrared. 9, 16, 17, 32, 33, 35, 69

ISM Interstellar Medium. 2–6, 8, 9, 17, 33, 57

ISRF Interstellar Radiation Field. 4–7, 12

LF Luminosity Function. 14

LM Levenberg-Marquardt. 36

LTG Late-Type Galaxy. 17

MC Monte Carlo. 33, 40, 56, 57, 170

MS Main Sequence. 19–21, 24, 34, 35, 45–50, 57, 58

NIR Near Infrared. 16, 27, 32, 33, 53, 54, 56–58

NUV Near Ultraviolet. 27, 53, 54, 56–58

PAH Polycyclic Aromatic Hydrocarbon. 5, 33

PDR Photodissociation regions. 3, 6, 7, 9, 33

R.A. Right Ascension. 25, 50, 51

RJ Rayleigh–Jeans. 23, 24, 69

SB Star Burst. 20, 25, 34, 35, 48–50, 57, 58

SED Spectral Energy Distribution. 2, 3, 14–17, 24, 32–34, 45, 47, 49, 59, 69, 71, 77, 78, 81, 84, 88, 91, 94, 97, 99, 102, 105, 112, 116, 121, 125, 129, 133, 136, 140, 145, 148, 152, 155, 158, 164, 167

SF Star Formation. 6, 14, 16, 17, 19–22, 32, 49, 57

SFG Star Forming Galaxy. 18–25, 57

SFH Star Formation History. 14, 20–22, 32

SFR Star Formation Rate. 1, 16, 17, 19–24, 32, 33, 35, 45–50, 56, 57, 59

SNR Signal-To-Noise Ratio. 39, 40, 59

SPS Stellar Population Synthesis. 32, 33

sub-mm sub-millimetre. 23

SVO Spanish Virtual Observatory. 28, 70, 72–76

UV Ultraviolet. 2, 4, 5, 7, 12, 15, 16, 20, 23, 26, 32, 33

WFC3 Wide Field Camera 3. 70

WIM Warm Ionized Medium. 3

WNM Warm Neutral Medium. 3, 6

ZAMS Zero Age Main Sequence. 2, 6

Glossary

- [CII]** Referring to the ${}^2P_{3/2} \rightarrow {}^2P_{1/2}$ fine structure transition of the singly ionised carbon ground state at $158\mu\text{m}$. 6, 7, 9, 28, 53–58
- [CI](1-0)** Referring to the ${}^3P_1 \rightarrow {}^3P_0$ fine structure transition of the atomic carbon ground state at $610\mu\text{m}$. 7, 9, 28, 53–58
- [CI](2-1)** Referring to the ${}^3P_2 \rightarrow {}^3P_1$ fine structure transition of the atomic carbon ground state at $370\mu\text{m}$. 7, 28, 53, 54, 56–58
- C4S** Cataloguer For Stardust is a tool for easily and automatically building catalogues for SED fitting algorithms, and in case of STARDUST and EAZY, linking the photometric observations with internal transmission filter curves. The tool and documentation for the tool can be found here: <https://github.com/skrrrlev/Cataloguer-4-Stardust>. 34
- COSMOS** The Cosmic Evolution Survey (COSMOS) is an astronomical survey. The survey covers a 2 square degree equatorial field with spectroscopy and X-ray to radio imaging by most of the major space-based telescopes and a number of large ground based telescopes. 26
- DL07** Refers to the [Draine and Li \(2007\)](#) dust templates, with the addition of the [Draine et al. \(2014\)](#) update, employed by STARDUST in the rest-frame IR regime. 33, 48
- Galfit** GALFIT is a tool for parameterising the spatial structure of galaxies, stars, globular cluster, stellar disks, etc., by using parametric functions to model objects as they appear in two-dimensional digital images ([Peng et al. 2002](#)). 35–43, 46, 47, 49, 50, 52, 53, 59, 78, 79, 81, 82, 84–86, 88, 89, 91, 92, 94, 95, 97, 99, 100, 102, 103, 105–110, 112–114, 116–119, 121–123, 125–127, 129–131, 133, 134, 136–138, 140–143, 145, 146, 148–150, 152, 153, 155, 156, 158–162, 164, 165, 167, 168, 170
- PSF** The Point Spread Function characterises how radiation, from a point source, incident on an imaging system, is spread over the detector area. 28, 29, 36, 38–42, 46, 47, 78, 79, 81, 82, 84–86, 88, 89, 91, 92, 94, 95, 97, 99, 100, 102, 103, 105–110, 112–114, 116–119, 121–123, 125–127, 129–131, 133, 134, 136–138, 140–143, 145, 146, 148–150, 152, 153, 155, 156, 158–162, 164, 165, 167, 168, 170
- Rayleigh–Jeans Tail** The RJ tail of a black body distribution is in the region where the inequality $h\nu \ll kT$ holds true. In this regime, the Planck function can be simplified by allowing $\exp(h\nu/k_B T) \approx 1 + h\nu/k_B T$, which in turn means that the specific intensity is proportional to ν^2 . Consequently, this corresponds to the linear regime of a SED plot. 16, 55
- Stardust** STARDUST is a panchromatic galaxy SED fitting algorithm, that models the emission from stars, AGN, and dust, without relying on energy balance assumptions. It is designed to extract galaxy properties by fitting their multi-wavelength photometry data to a set of linearly combined templates ([Kokorev et al. 2021](#)). 26, 27, 32–34, 45, 46, 49, 69, 71, 77, 78, 80, 81, 83, 84, 87, 88, 90, 91, 93, 94, 96–99, 101, 102, 104, 105, 111, 112, 115, 116, 120, 121, 124, 125, 128, 129, 132, 133, 135, 136, 139, 140, 144, 145, 147, 148, 151, 152, 154, 155, 157, 158, 163, 164, 166, 167

A HST Filters

In this appendix we list the observed wavelengths of the HST instrument+filters used for the spatially resolved data.

Table A.1: Wavelengths of the HST filters used in this section

Filter	λ_{ref} [Å]	λ_{mean} [Å]	λ_{eff} [Å]	Instrument
F606w	5887.08	6000.37	5776.43	ACS, HRC
F814w	8029.30	8117.36	7954.84	WFC3, UVIS2
F850lp	9169.95	9207.49	9148.57	WFC3, UVIS2
F105w	10550.25	10651.00	10430.83	WFC3, IR
F110w	11534.46	11797.14	11200.52	WFC3, IR
F125w	12486.07	12576.18	12363.55	WFC3, IR
F140w	13923.21	14061.91	13734.66	WFC3, IR
F160w	15370.34	15436.30	15278.47	WFC3, IR

Data provided by the SVO (Rodrigo and Solano 2020).

B Extra Transmission Filters

The complete list of STARDUST transmission filters used in this thesis can be found at <https://github.com/VasilyKokorev/stardust> at commit 026d7ee. For any observation with a STARDUST code that are > 351 , the filter transmission curve is manually added to STARDUST. This appendix chapter contains the transmission filters that were used for SED fitting but was not included in the default version of STARDUST.

Transmission Filter 352

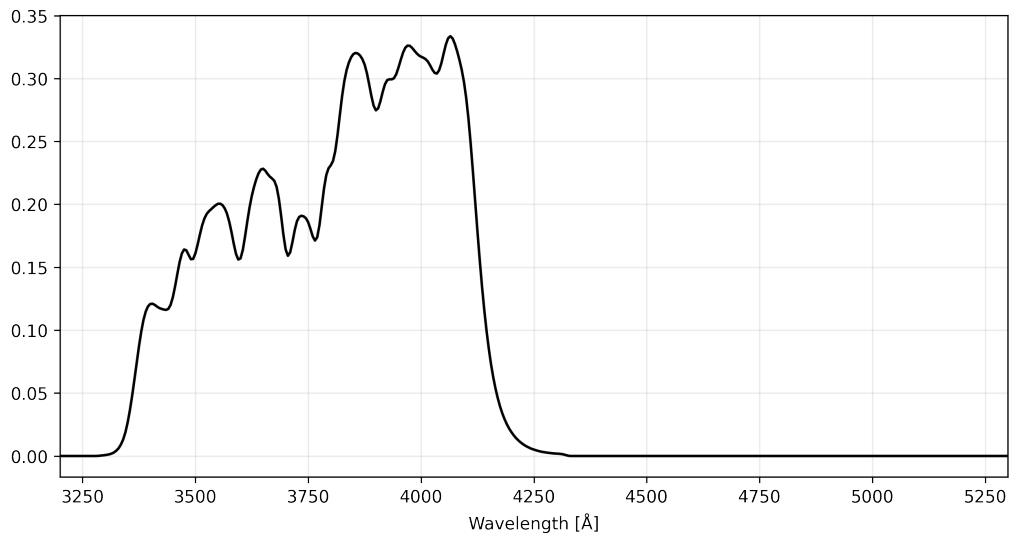


Figure B.1: Transmission filter with code 352: Canada France Hawaii Telescope (CFHT) MegaCam update for filter u^* found in EAZY (Brammer et al. 2008)

Transmission Filter 353

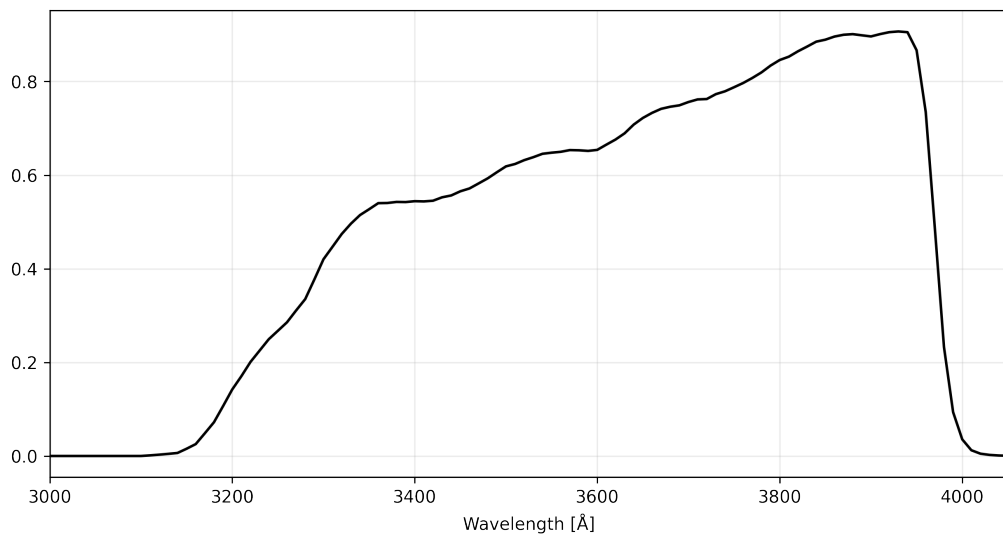


Figure B.2: Transmission filter with code 353: Canada France Hawaii Telescope (CFHT) MegaCam update for filter u found in EAZY (Brammer et al. 2008)

Transmission Filter 354

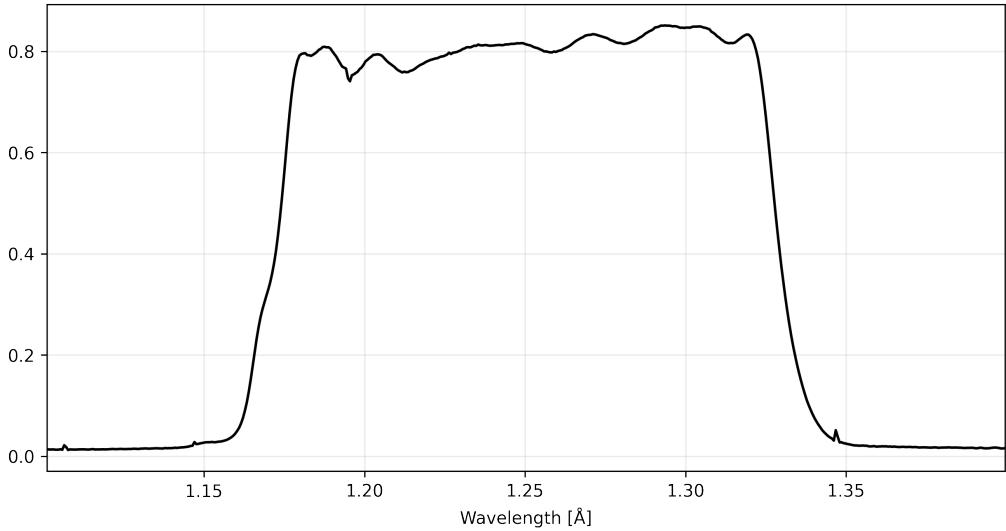


Figure B.3: Transmission filter with code 354: The William Herschel Telescope (WHT) LRIS J-band provided by the SVO (Rodrigo and Solano 2020)

Transmission Filter 355

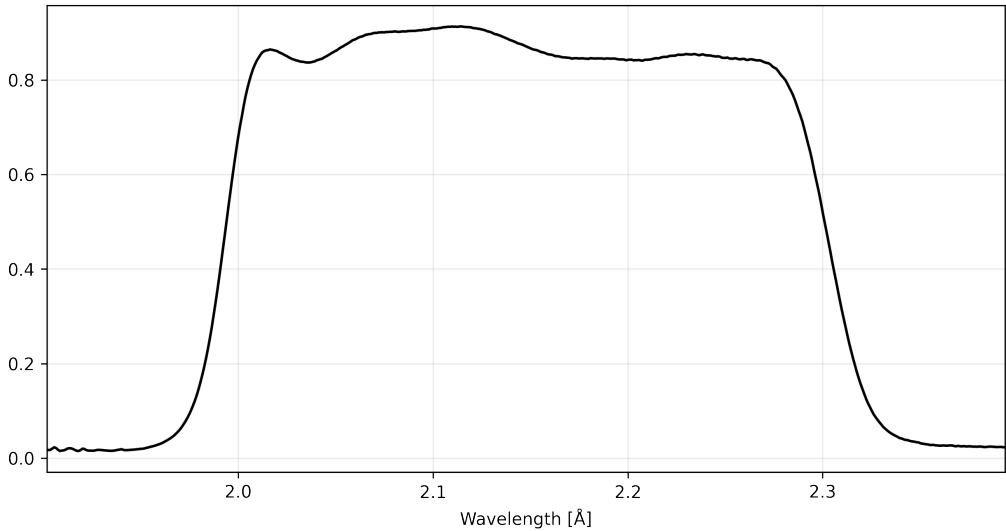


Figure B.4: Transmission filter with code 355: The William Herschel Telescope (WHT) LRIS Ks-band provided by the SVO (Rodrigo and Solano 2020)

Transmission Filter 356

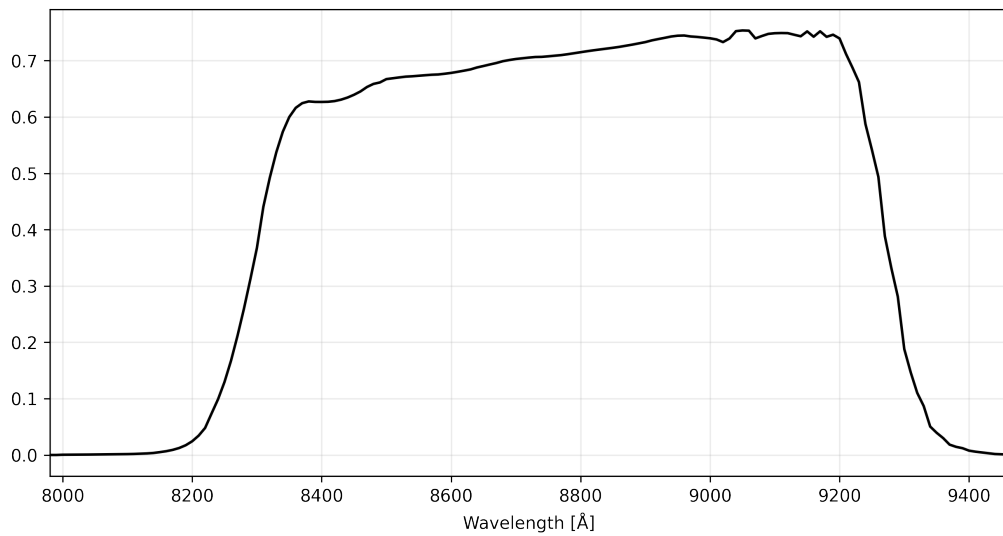


Figure B.5: Transmission filter with code 356: European Southern Observatory's Cerro Paranal Observatory Vista Z-band provided by the SVO (Rodrigo and Solano 2020)

Transmission Filter 357

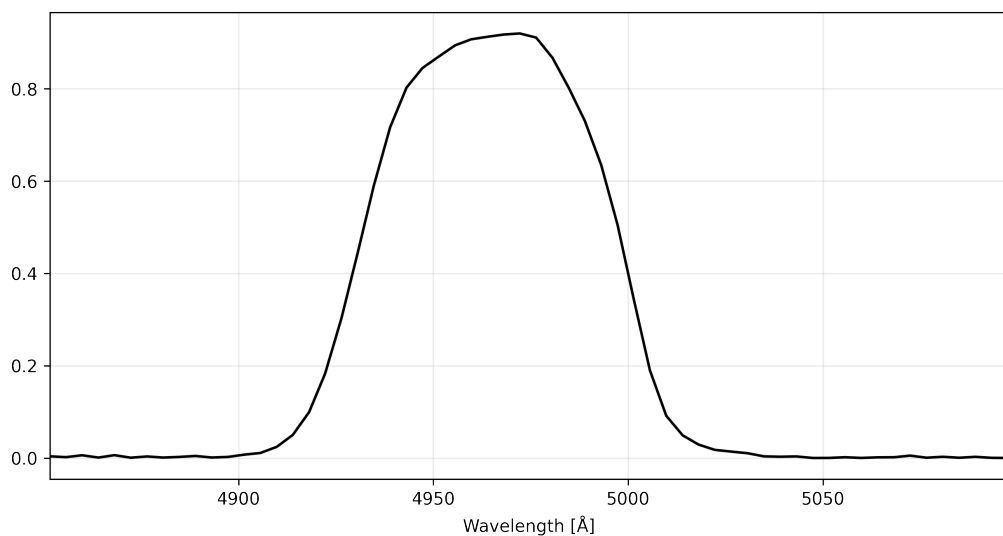


Figure B.6: Transmission filter with code 357: Subaru Hyper Suprime-Cam (HSC) NB497 provided by the SVO (Rodrigo and Solano 2020)

Transmission Filter 358

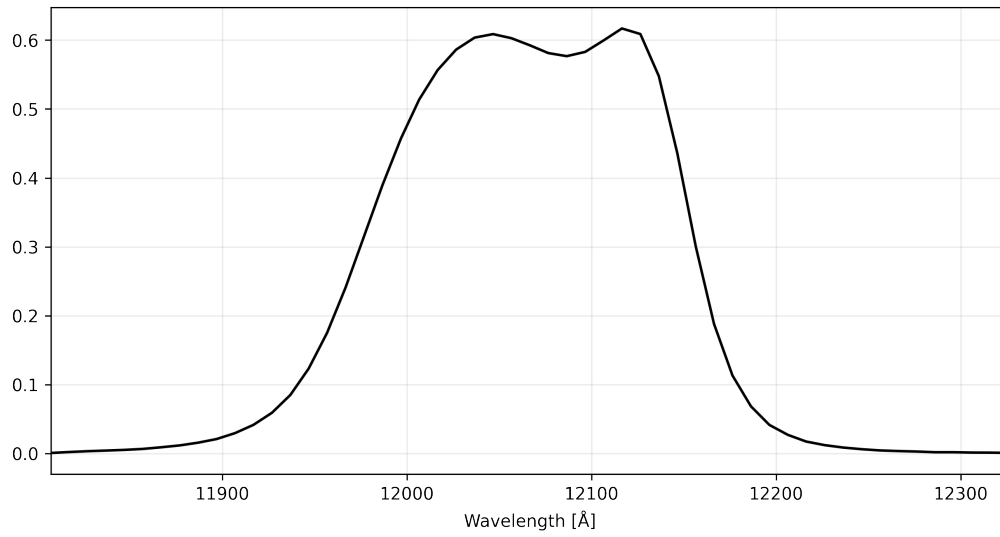


Figure B.7: Transmission filter with code 358: Palomar Observatory Wide-Field Infrared Camera (WIRC) J-band provided by the SVO (Rodrigo and Solano 2020)

Transmission Filter 359

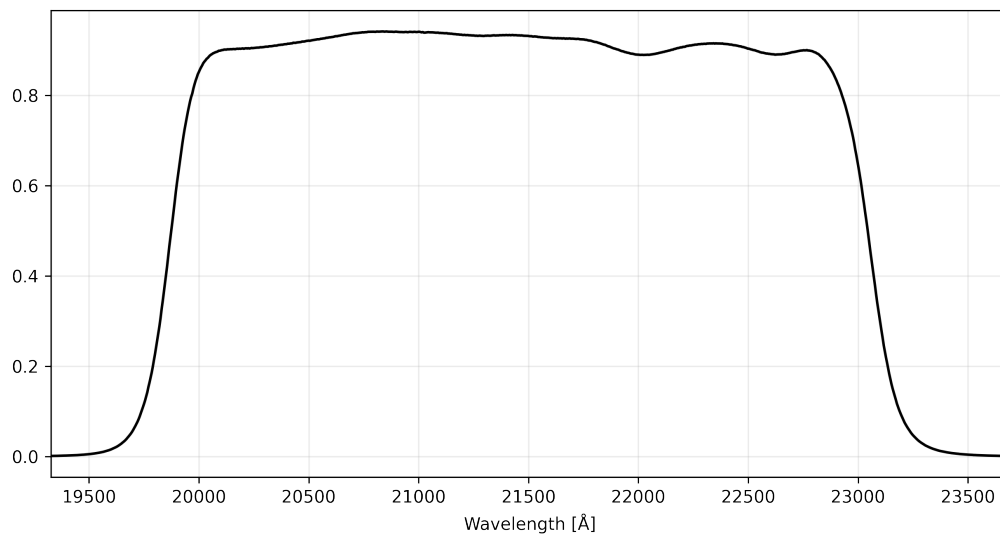


Figure B.8: Transmission filter with code 359: Palomar Observatory Wide-Field Infrared Camera (WIRC) Ks-band provided by the SVO (Rodrigo and Solano 2020)

Transmission Filter 360

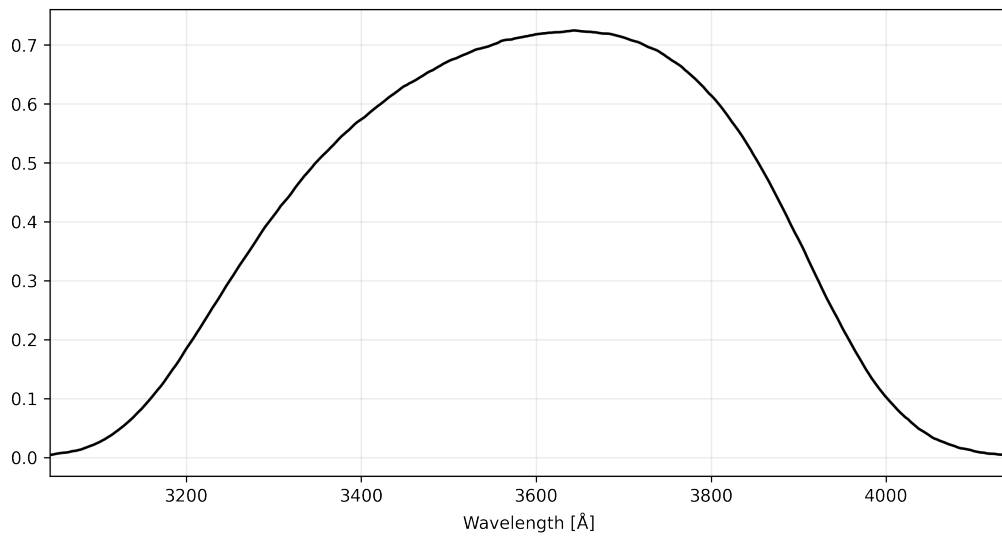


Figure B.9: Transmission filter with code 360: Cerro Tololo Inter-American Observatory (CTIO) Mosaic U-band provided by the SVO (Rodrigo and Solano 2020)

Transmission Filter 361

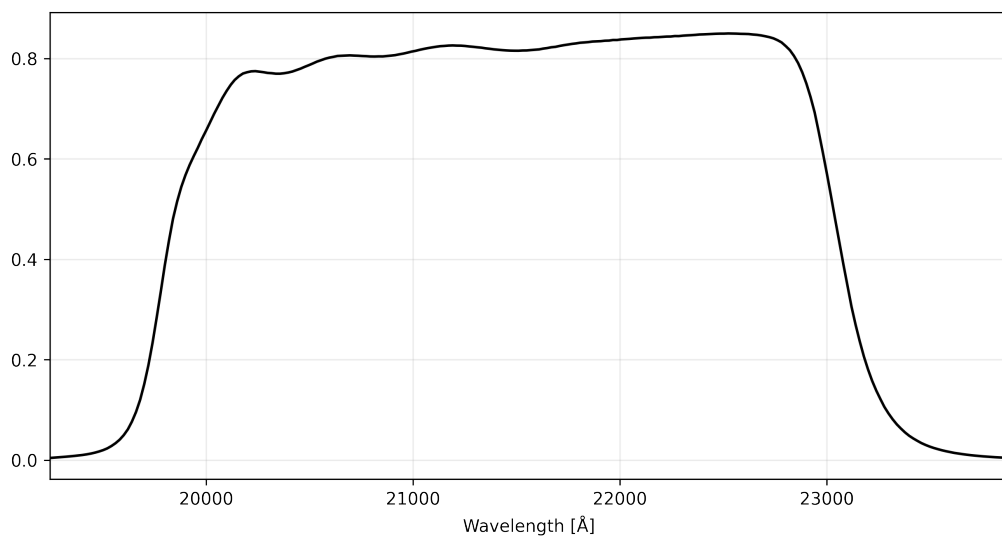


Figure B.10: Transmission filter with code 361: European Southern Observatory (ESO) HAWK-I Ks-band provided by the SVO (Rodrigo and Solano 2020)

Transmission Filter 362

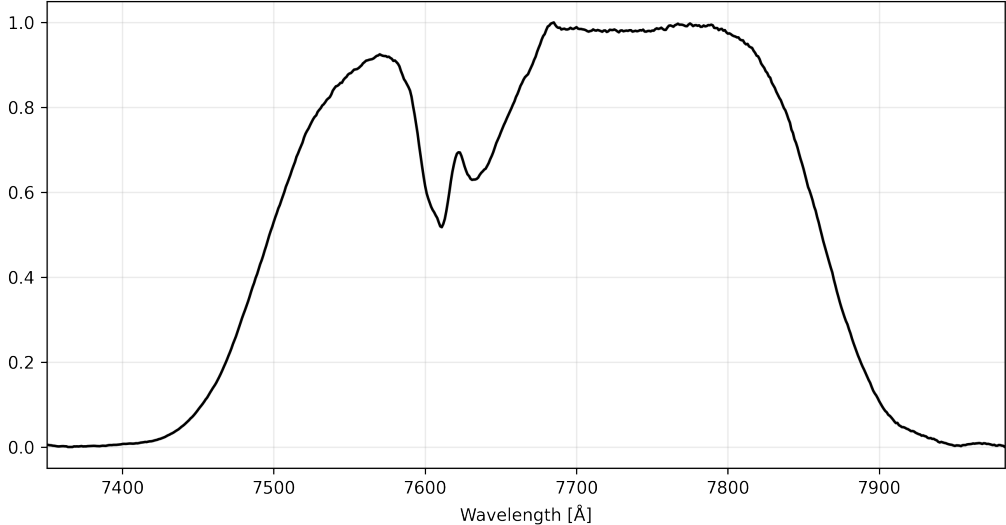


Figure B.11: Transmission filter with code 362: Subaru Suprime-Cam IB767 provided by the SVO (Rodrigo and Solano 2020)

C Datasheets

This appendix chapter contains data sheets for each of the targets in our sample. Each data sheet contains available photometry, the SED, and analytical fits of the surface brightness profile of the stellar emission, gas line emission and dust continuum.

Source 1

Table C.1: Photometric data collected for source 1. The observation column lists the facility, instrument and filter used to make the observation. The code column connects the filter transmission curve with the correct one in Stardust. The reference column lists references to the works from which the observations were collected. Observations without an uncertainty corresponds to 3σ upper limits.

Observation	Flux [Jy]		Uncertainty [Jy]		Code	Reference
	Value	Order	Value	Order		
CTIO/Mosaic/U	3.226	10^{-6}	2.226	10^{-8}	360	Guo et al. 2013
VLT/VIMOS/U	3.425	10^{-6}	1.873	10^{-8}	103	Guo et al. 2013
HST/ACS/F435W	4.606	10^{-6}	6.889	10^{-8}	1	Guo et al. 2013
HST/ACS/F606W	9.960	10^{-6}	4.609	10^{-8}	4	Guo et al. 2013
HST/ACS/F775W	1.820	10^{-5}	9.848	10^{-8}	5	Guo et al. 2013
HST/ACS/F814W	1.928	10^{-5}	5.115	10^{-8}	6	Guo et al. 2013
HST/ACS/F850LP	2.278	10^{-5}	1.088	10^{-7}	7	Guo et al. 2013
HST/WFC3/F125W	3.051	10^{-5}	4.584	10^{-8}	203	Guo et al. 2013
HST/WFC3/F160W	4.024	10^{-5}	5.390	10^{-8}	205	Guo et al. 2013
ESO/ISAAC/Ks	5.451	10^{-5}	1.394	10^{-7}	37	Guo et al. 2013
ESO/HAWK-I/Ks	5.445	10^{-5}	4.983	10^{-8}	361	Guo et al. 2013
IRAC/ch1	5.030	10^{-5}	6.081	10^{-8}	18	Guo et al. 2013
IRAC/ch2	3.748	10^{-5}	7.855	10^{-8}	19	Guo et al. 2013
IRAC/ch3	3.841	10^{-5}	3.025	10^{-7}	20	Guo et al. 2013
IRAC/ch4	3.708	10^{-5}	3.244	10^{-7}	21	Guo et al. 2013
Herschel/PACS/70	1.060	10^{-3}	3.000	10^{-4}	328	Lutz et al. 2011
Herschel/PACS/100	4.430	10^{-3}	2.000	10^{-4}	329	Elbaz et al. 2011
Herschel/PACS/160	8.190	10^{-3}	7.600	10^{-4}	330	Elbaz et al. 2011
SPITZER/MIPS/24	1.720	10^{-4}	2.000	10^{-6}	325	Elbaz et al. 2011

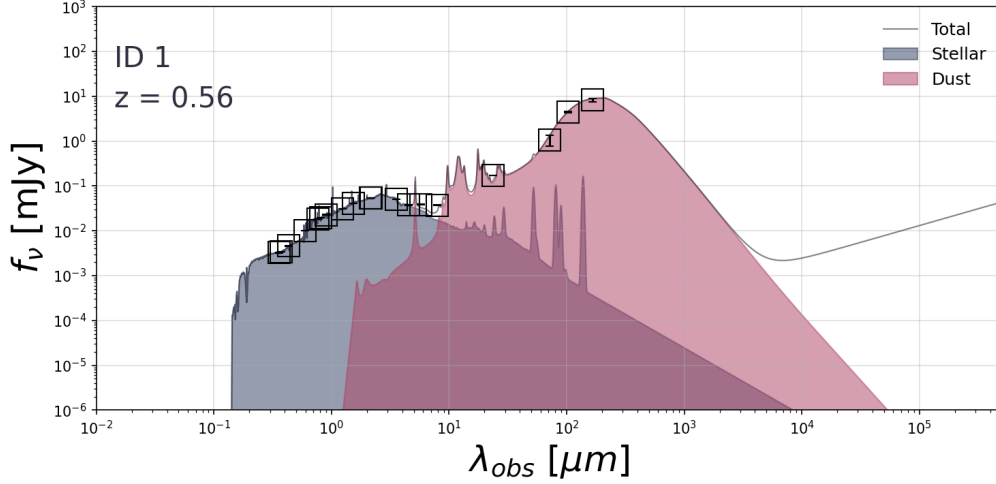


Figure C.1: The SED of source 1 as fitted with STARDUST, assuming that there's no significant AGN contribution. The squares are marked around observations with a SNR > 3. Arrows indicate 3σ upper limits of observations with SNR < 3 or non-detections.

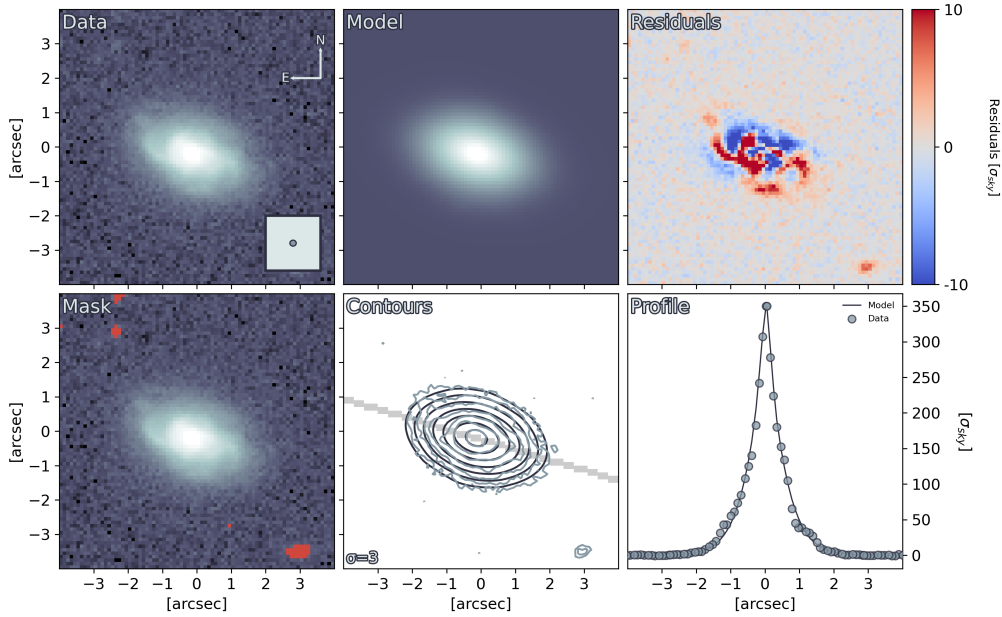


Figure C.2: The results of fitting source 1 with GALFIT. **Data**: A cutout of the source. The colour scale for the *Data*, *Model* and *Mask* panels are defined from this map, using a logarithmic scale. The direction towards celestial north and east are displayed by the arrows. The fitted FWHM of the PSF is displayed in the inset in the bottom right. **Mask**: Masked out sources and dead pixels are displayed in red. **Model**: The fitted model convolved with the PSF. **Contours**: Contours of the *Data* panel in blue. Contours of the *Model* panel in black. Contour levels start at the value annotated in the bottom left, and increase by a factor of two for each subsequent level. The shaded region indicates where the 1D profile was extracted from. **Residuals**: The *Data* subtracted by the *Model*. **Profile**: A one-dimensional profile extracted along the semi-major axis of the *Model*.

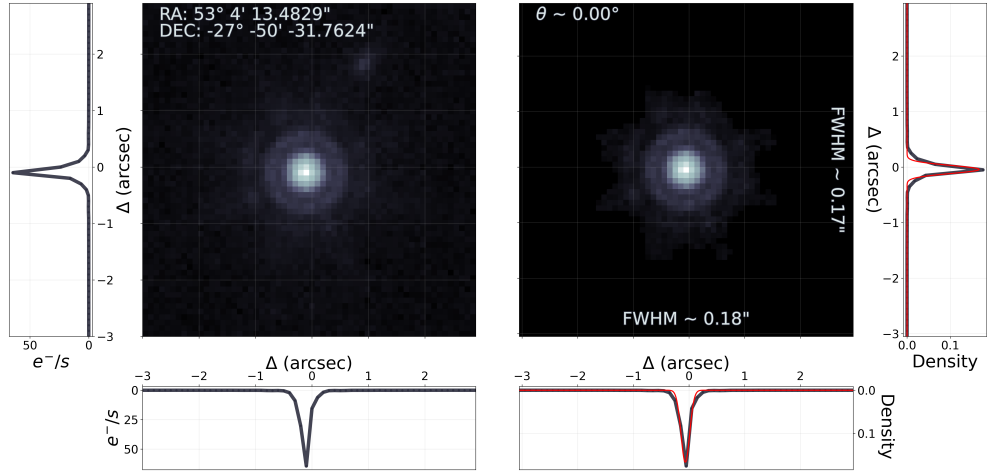


Figure C.3: From point-source to PSF. **Left:** The map displays the source used to create the PSF, for the mosaic containing source 1, in a logarithmic colour scale. The left and bottom panels shows the profile through the pixel of the highest value. The annotated coordinates are the coordinates of the centre of the map. **Right:** The map displays the PSF created from the left figure. The annotated FWHM along each axis are calculated by fitting a two-dimensional Gaussian to the map. The right and bottom panel shows the profile through the highest value pixel in black and the profile of the fitted two-dimensional Gaussian in red. The annotated angle describes the position angle of the fitted two-dimensional Gaussian counterclockwise from the positive x-axis.

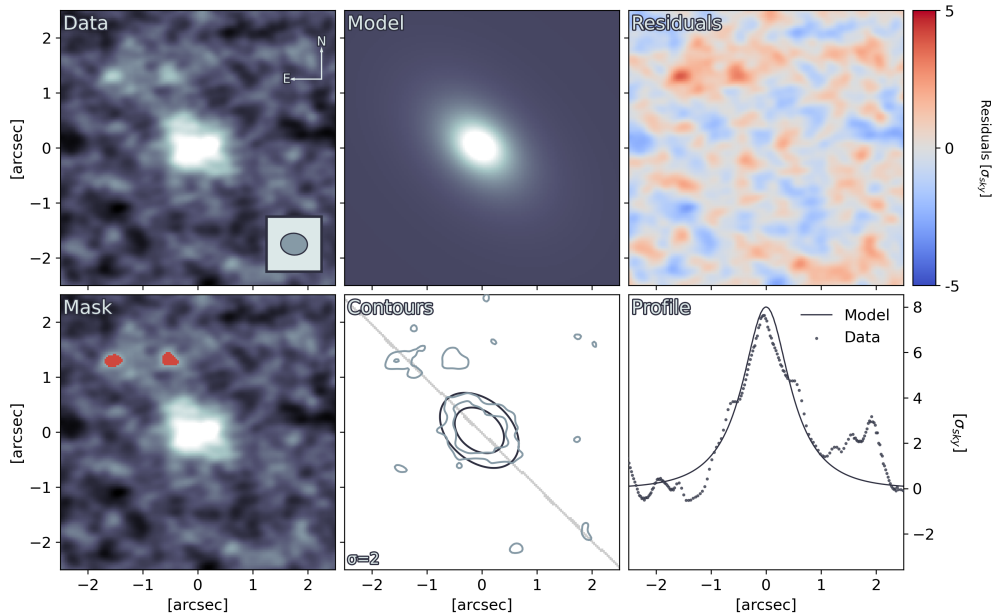


Figure C.4: The results of fitting the CO(2-1) ALMA map for source 1 with GALFIT. **Data:** A cutout of the source. The colour scale for the *Data*, *Model* and *Mask* panels are defined from this map, using a linear scale. The direction towards celestial north and east are displayed by the arrows. The FWHM of the synthetic beam is displayed in the inset on the lower right. **Mask:** Masked out sources and dead pixels are displayed in red. **Model:** The fitted model convolved with the PSF. **Contours:** Contours of the *Data* panel in blue. Contours of the *Model* panel in black. Contour levels start at the value annotated in the bottom left, and increase by a factor of two for each subsequent level. The shaded region indicates where the 1D profile was extracted from. **Residuals:** The *Data* subtracted by the *Model*. **Profile:** A one-dimensional profile extracted along the semi-major axis of the *Model*.

Source 2

Table C.2: Photometric data collected for source 2. The observation column lists the facility, instrument and filter used to make the observation. The code column connects the filter transmission curve with the correct one in Stardust. The reference column lists references to the works from which the observations were collected. Observations without an uncertainty corresponds to 3σ upper limits.

Observation	Flux [Jy]		Uncertainty [Jy]		Code	Reference
	Value	Order	Value	Order		
CFHT/MegaCam/u*	3.105	10^{-7}	2.047	10^{-8}	352	Weaver et al. 2022
CFHT/MegaCam/u	2.840	10^{-7}	1.277	10^{-8}	353	Weaver et al. 2022
Subaru/HSC/g	1.114	10^{-6}	1.624	10^{-8}	314	Weaver et al. 2022
Subaru/HSC/r	4.441	10^{-6}	2.979	10^{-8}	315	Weaver et al. 2022
Subaru/HSC/i	1.057	10^{-5}	4.133	10^{-8}	316	Weaver et al. 2022
Subaru/HSC/z	1.609	10^{-5}	5.968	10^{-8}	317	Weaver et al. 2022
Subaru/HSC/y	2.020	10^{-5}	7.884	10^{-8}	318	Weaver et al. 2022
VISTA/VIRCAM/Y	2.260	10^{-5}	5.379	10^{-8}	256	Weaver et al. 2022
VISTA/VIRCAM/J	3.372	10^{-5}	6.781	10^{-8}	257	Weaver et al. 2022
VISTA/VIRCAM/H	5.758	10^{-5}	9.454	10^{-8}	258	Weaver et al. 2022
VISTA/VIRCAM/Ks	8.213	10^{-5}	1.357	10^{-7}	259	Weaver et al. 2022
Subaru/Suprime-Cam/IB427	5.802	10^{-7}	6.580	10^{-8}	181	Weaver et al. 2022
Subaru/Suprime-Cam/IB464	8.739	10^{-7}	1.050	10^{-7}	183	Weaver et al. 2022
Subaru/Suprime-Cam/IA484	1.175	10^{-6}	4.982	10^{-8}	184	Weaver et al. 2022
Subaru/Suprime-Cam/IB505	1.297	10^{-6}	6.713	10^{-8}	185	Weaver et al. 2022
Subaru/Suprime-Cam/IA527	1.644	10^{-6}	5.579	10^{-8}	186	Weaver et al. 2022
Subaru/Suprime-Cam/IB574	2.322	10^{-6}	9.186	10^{-8}	188	Weaver et al. 2022
Subaru/Suprime-Cam/IA624	4.220	10^{-6}	5.241	10^{-8}	190	Weaver et al. 2022
Subaru/Suprime-Cam/IA679	7.082	10^{-6}	8.870	10^{-8}	192	Weaver et al. 2022
Subaru/Suprime-Cam/IB709	8.082	10^{-6}	8.020	10^{-8}	193	Weaver et al. 2022
Subaru/Suprime-Cam/IA738	9.715	10^{-6}	7.852	10^{-8}	194	Weaver et al. 2022
Subaru/Suprime-Cam/IA767	1.078	10^{-5}	1.147	10^{-7}	195	Weaver et al. 2022
Subaru/Suprime-Cam/IB827	1.250	10^{-5}	1.027	10^{-7}	197	Weaver et al. 2022
Subaru/Suprime-Cam/NB711	8.327	10^{-6}	1.121	10^{-7}	322	Weaver et al. 2022
Subaru/Suprime-Cam/NB816	1.237	10^{-5}	1.017	10^{-7}	319	Weaver et al. 2022
VISTA/VIRCAM/NB118	3.053	10^{-5}	3.543	10^{-7}	321	Weaver et al. 2022
Subaru/Suprime-Cam/B	7.200	10^{-7}	1.498	10^{-8}	114	Weaver et al. 2022
Subaru/Suprime-Cam/V	1.916	10^{-6}	2.926	10^{-8}	115	Weaver et al. 2022
Subaru/Suprime-Cam/r+	4.669	10^{-6}	2.213	10^{-8}	116	Weaver et al. 2022
Subaru/Suprime-Cam/i+	1.040	10^{-5}	3.478	10^{-8}	117	Weaver et al. 2022
Subaru/Suprime-Cam/z++	1.747	10^{-5}	1.653	10^{-7}	118	Weaver et al. 2022
Spitzer/IRAC/ch1	8.675	10^{-5}	4.332	10^{-7}	18	Weaver et al. 2022
Spitzer/IRAC/ch2	6.272	10^{-5}	2.318	10^{-7}	19	Weaver et al. 2022
GALEX/GALEX/NUV	2.527	10^{-8}	7.035	10^{-8}	121	Weaver et al. 2022
SPITZER/MIPS/24	3.642	10^{-4}	2.221	10^{-5}	325	Jin et al. 2018
JCMT/SCUBA2/850GHz	2.871	10^{-3}	2.038	10^{-3}	324	Jin et al. 2018
VLA/3GHz	2.950	10^{-5}	2.800	10^{-6}		Jin et al. 2018
Meerkat/1.3GHz	1.912	10^{-4}				Jin et al. 2018
Herschel/PACS/100	1.193	10^{-2}	1.867	10^{-3}	329	Liu et al. 2019
Herschel/PACS/160	2.580	10^{-2}	3.688	10^{-3}	330	Liu et al. 2019
Herschel/SPIRE/250	1.870	10^{-2}	3.543	10^{-3}	331	Liu et al. 2019

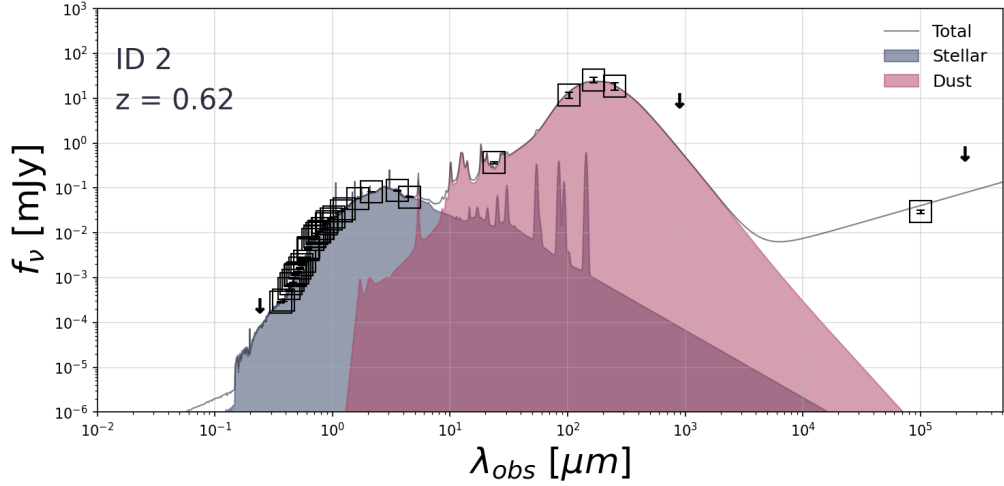


Figure C.5: The SED of source 2 as fitted with STARDUST, assuming that there's no significant AGN contribution. The squares are marked around observations with a SNR > 3. Arrows indicate 3σ upper limits of observations with SNR < 3 or non-detections.

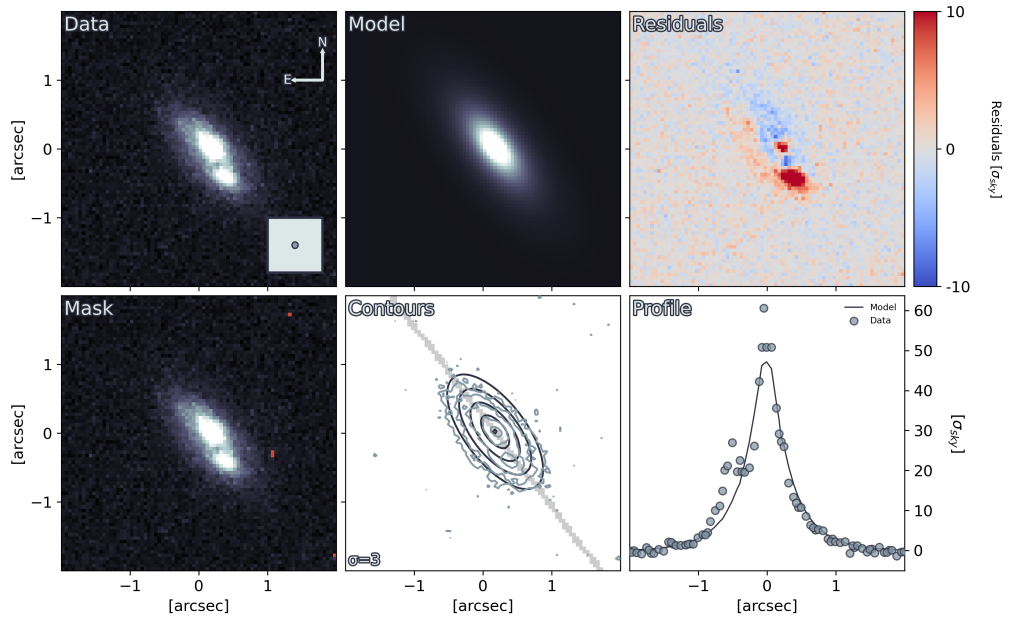


Figure C.6: The results of fitting source 2 with GALFIT. **Data**: A cutout of the source. The colour scale for the *Data*, *Model* and *Mask* panels are defined from this map, using a linear scale. The direction towards celestial north and east are displayed by the arrows. The fitted FWHM of the PSF is displayed in the inset in the bottom right. **Mask**: Masked out sources and dead pixels are displayed in red. **Model**: The fitted model convolved with the PSF. **Contours**: Contours of the *Data* panel in blue. Contours of the *Model* panel in black. Contour levels start at the value annotated in the bottom left, and increase by a factor of two for each subsequent level. The shaded region indicates where the 1D profile was extracted from. **Residuals**: The *Data* subtracted by the *Model*. **Profile**: A one-dimensional profile extracted along the semi-major axis of the *Model*.

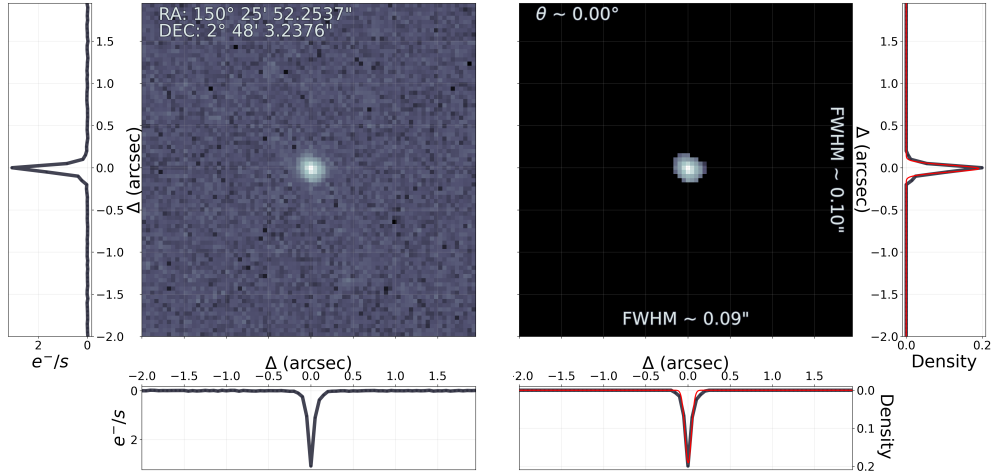


Figure C.7: From point-source to PSF. **Left:** The map displays the source used to create the PSF, for the mosaic containing source 2, in a logarithmic colour scale. The left and bottom panels shows the profile through the pixel of the highest value. The annotated coordinates are the coordinates of the centre of the map. **Right:** The map displays the PSF created from the left figure. The annotated FWHM along each axis are calculated by fitting a two-dimensional Gaussian to the map. The right and bottom panel shows the profile through the highest value pixel in black and the profile of the fitted two-dimensional Gaussian in red. The annotated angle describes the position angle of the fitted two-dimensional Gaussian counterclockwise from the positive x-axis.

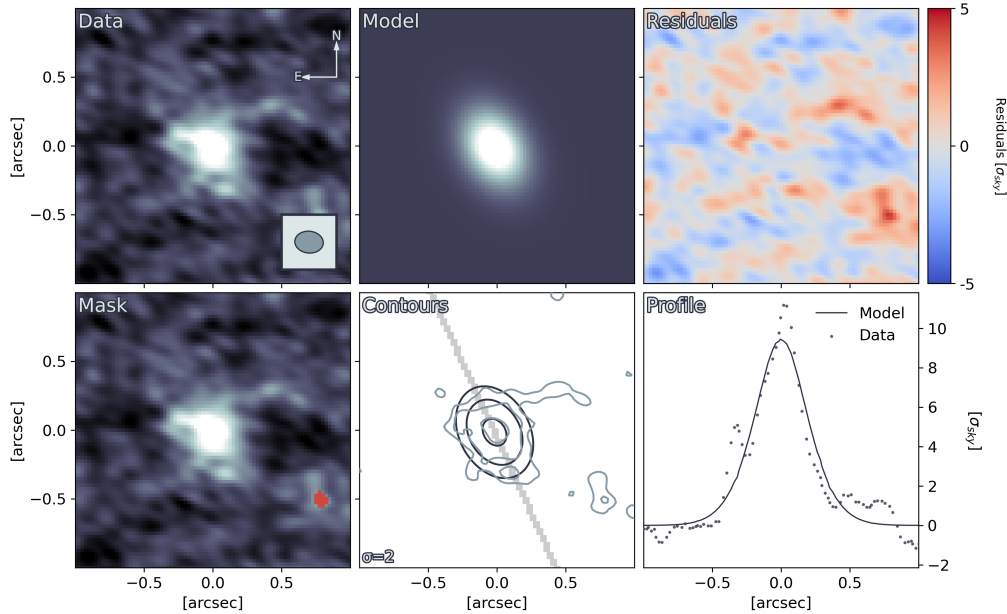


Figure C.8: The results of fitting the CO(3-2) ALMA map for source 2 with GALFIT. **Data:** A cutout of the source. The colour scale for the *Data*, *Model* and *Mask* panels are defined from this map, using a linear scale. The direction towards celestial north and east are displayed by the arrows. The FWHM of the synthetic beam is displayed in the inset on the lower right. **Mask:** Masked out sources and dead pixels are displayed in red. **Model:** The fitted model convolved with the PSF. **Contours:** Contours of the *Data* panel in blue. Contours of the *Model* panel in black. Contour levels start at the value annotated in the bottom left, and increase by a factor of two for each subsequent level. The shaded region indicates where the 1D profile was extracted from. **Residuals:** The *Data* subtracted by the *Model*. **Profile:** A one-dimensional profile extracted along the semi-major axis of the *Model*.

Source 3

Table C.3: Photometric data collected for source 3. The observation column lists the facility, instrument and filter used to make the observation. The code column connects the filter transmission curve with the correct one in Stardust. The reference column lists references to the works from which the observations were collected. Observations without an uncertainty corresponds to 3σ upper limits.

Observation	Flux [Jy]		Uncertainty [Jy]		Code	Reference
	Value	Order	Value	Order		
CFHT/MegaCam/u*	1.030	10^{-6}	8.369	10^{-9}	352	Weaver et al. 2022
CFHT/MegaCam/u	9.507	10^{-7}	1.348	10^{-8}	353	Weaver et al. 2022
Subaru/HSC/g	1.344	10^{-6}	1.682	10^{-8}	314	Weaver et al. 2022
Subaru/HSC/r	1.846	10^{-6}	1.924	10^{-8}	315	Weaver et al. 2022
Subaru/HSC/i	2.687	10^{-6}	2.113	10^{-8}	316	Weaver et al. 2022
Subaru/HSC/z	4.072	10^{-6}	3.080	10^{-8}	317	Weaver et al. 2022
Subaru/HSC/y	5.587	10^{-6}	4.455	10^{-8}	318	Weaver et al. 2022
VISTA/VIRCAM/Y	6.294	10^{-6}	1.002	10^{-7}	256	Weaver et al. 2022
VISTA/VIRCAM/J	9.032	10^{-6}	1.193	10^{-7}	257	Weaver et al. 2022
VISTA/VIRCAM/H	1.533	10^{-5}	1.730	10^{-7}	258	Weaver et al. 2022
VISTA/VIRCAM/Ks	1.831	10^{-5}	1.094	10^{-7}	259	Weaver et al. 2022
Subaru/Suprime-Cam/IB427	1.152	10^{-6}	6.053	10^{-8}	181	Weaver et al. 2022
Subaru/Suprime-Cam/IB464	1.445	10^{-6}	1.105	10^{-7}	183	Weaver et al. 2022
Subaru/Suprime-Cam/IA484	1.312	10^{-6}	4.314	10^{-8}	184	Weaver et al. 2022
Subaru/Suprime-Cam/IB505	1.469	10^{-6}	6.704	10^{-8}	185	Weaver et al. 2022
Subaru/Suprime-Cam/IA527	1.596	10^{-6}	4.876	10^{-8}	186	Weaver et al. 2022
Subaru/Suprime-Cam/IB574	1.841	10^{-6}	8.977	10^{-8}	188	Weaver et al. 2022
Subaru/Suprime-Cam/IA624	2.017	10^{-6}	4.727	10^{-8}	190	Weaver et al. 2022
Subaru/Suprime-Cam/IA679	2.170	10^{-6}	8.051	10^{-8}	192	Weaver et al. 2022
Subaru/Suprime-Cam/IB709	2.578	10^{-6}	8.416	10^{-8}	193	Weaver et al. 2022
Subaru/Suprime-Cam/IA738	2.699	10^{-6}	7.211	10^{-8}	194	Weaver et al. 2022
Subaru/Suprime-Cam/IA767	2.612	10^{-6}	1.134	10^{-7}	195	Weaver et al. 2022
Subaru/Suprime-Cam/IB827	3.245	10^{-6}	1.099	10^{-7}	197	Weaver et al. 2022
Subaru/Suprime-Cam/NB711	2.445	10^{-6}	1.000	10^{-7}	322	Weaver et al. 2022
Subaru/Suprime-Cam/NB816	3.144	10^{-6}	8.423	10^{-8}	319	Weaver et al. 2022
Subaru/Suprime-Cam/B	1.313	10^{-6}	1.479	10^{-8}	114	Weaver et al. 2022
Subaru/Suprime-Cam/V	1.646	10^{-6}	2.678	10^{-8}	115	Weaver et al. 2022
Subaru/Suprime-Cam/r+	2.015	10^{-6}	2.282	10^{-8}	116	Weaver et al. 2022
Subaru/Suprime-Cam/i+	2.830	10^{-6}	2.557	10^{-8}	117	Weaver et al. 2022
Subaru/Suprime-Cam/z++	4.768	10^{-6}	1.255	10^{-7}	118	Weaver et al. 2022
Spitzer/IRAC/ch1	2.802	10^{-5}	4.388	10^{-8}	18	Weaver et al. 2022
Spitzer/IRAC/ch2	4.067	10^{-5}	6.404	10^{-8}	19	Weaver et al. 2022
GALEX/GALEX/FUV	3.561	10^{-8}	4.269	10^{-8}	120	Weaver et al. 2022
GALEX/GALEX/NUV	1.215	10^{-7}	8.303	10^{-8}	121	Weaver et al. 2022
SPITZER/MIPS/24	1.201	10^{-4}	1.513	10^{-5}	325	Jin et al. 2018
JCMT/SCUBA2/850GHz	3.908	10^{-3}	4.378	10^{-3}	324	Jin et al. 2018
VLA/3GHz	5.850	10^{-5}	3.900	10^{-6}		Jin et al. 2018
VLA/1.5GHz	8.551	10^{-5}	1.453	10^{-5}		Jin et al. 2018
Meerkat/1.3GHz	3.978	10^{-4}				Jin et al. 2018
Herschel/PACS/100	2.794	10^{-2}	3.646	10^{-3}	329	Liu et al. 2019
Herschel/PACS/160	1.640	10^{-8}	7.675	10^{-3}	330	Liu et al. 2019
Herschel/SPIRE/250	2.520	10^{-2}	4.258	10^{-3}	331	Liu et al. 2019
Subaru/Suprime-Cam/IB679	2.270	10^{-6}	7.000	10^{-8}	192	Laigle et al. 2016

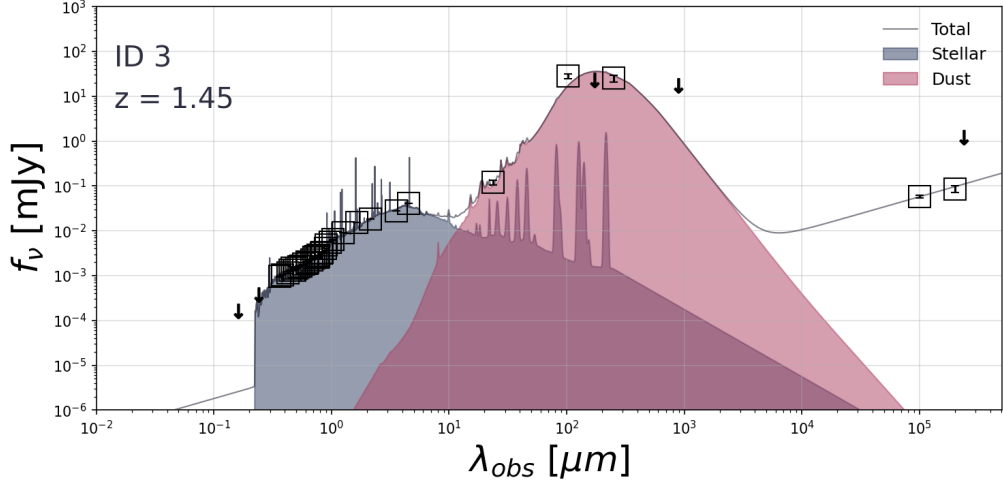


Figure C.9: The SED of source 3 as fitted with STARDUST, assuming that there's no significant AGN contribution. The squares are marked around observations with a SNR > 3. Arrows indicate 3σ upper limits of observations with SNR < 3 or non-detections.

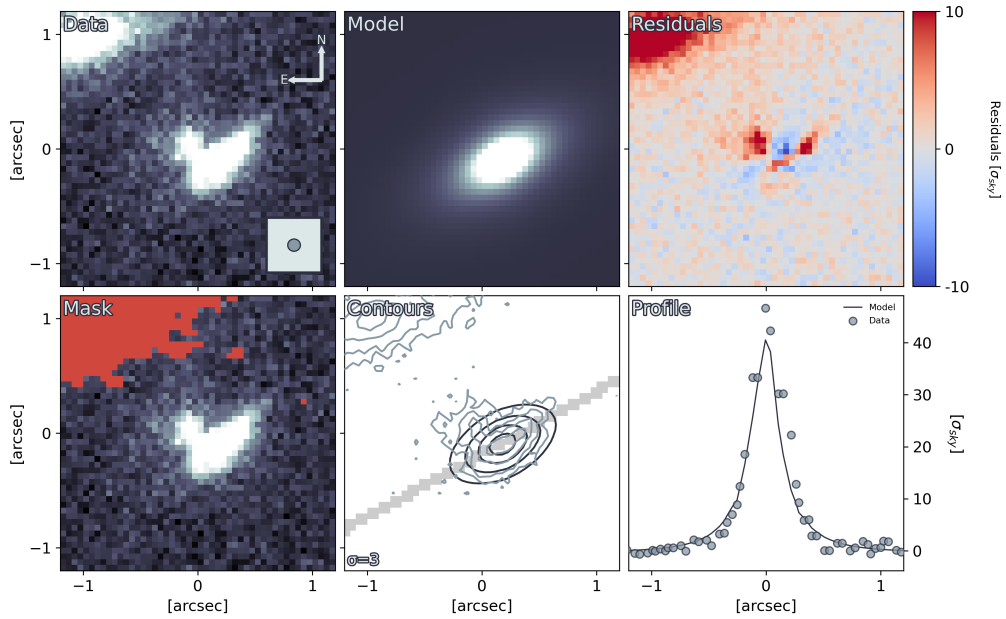


Figure C.10: The results of fitting source 3 with GALFIT. **Data**: A cutout of the source. The colour scale for the *Data*, *Model* and *Mask* panels are defined from this map, using a linear scale. The direction towards celestial north and east are displayed by the arrows. The fitted FWHM of the PSF is displayed in the inset in the bottom right. **Mask**: Masked out sources and dead pixels are displayed in red. **Model**: The fitted model convolved with the PSF. **Contours**: Contours of the *Data* panel in blue. Contours of the *Model* panel in black. Contour levels start at the value annotated in the bottom left, and increase by a factor of two for each subsequent level. The shaded region indicates where the 1D profile was extracted from. **Residuals**: The *Data* subtracted by the *Model*. **Profile**: A one-dimensional profile extracted along the semi-major axis of the *Model*.

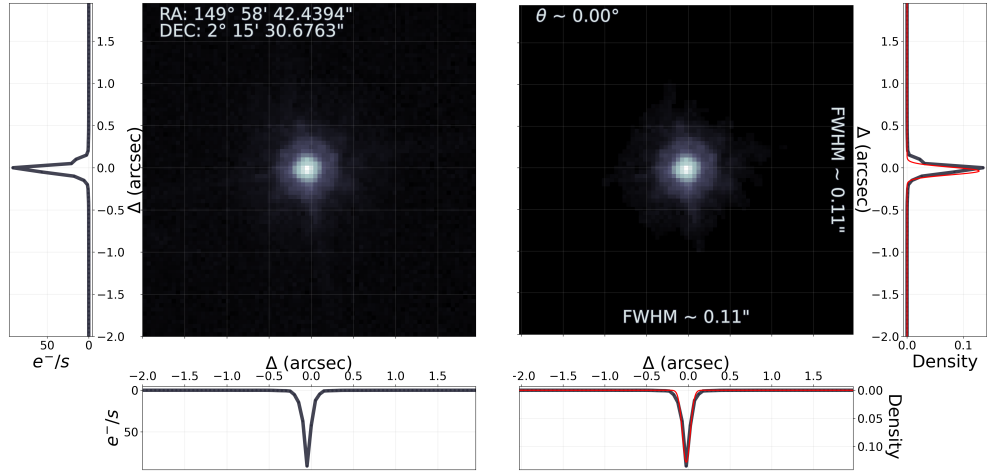


Figure C.11: From point-source to PSF. **Left:** The map displays the source used to create the PSF, for the mosaic containing source 3, in a logarithmic colour scale. The left and bottom panels shows the profile through the pixel of the highest value. The annotated coordinates are the coordinates of the centre of the map. **Right:** The map displays the PSF created from the left figure. The annotated FWHM along each axis are calculated by fitting a two-dimensional Gaussian to the map. The right and bottom panel shows the profile through the highest value pixel in black and the profile of the fitted two-dimensional Gaussian in red. The annotated angle describes the position angle of the fitted two-dimensional Gaussian counterclockwise from the positive x-axis.

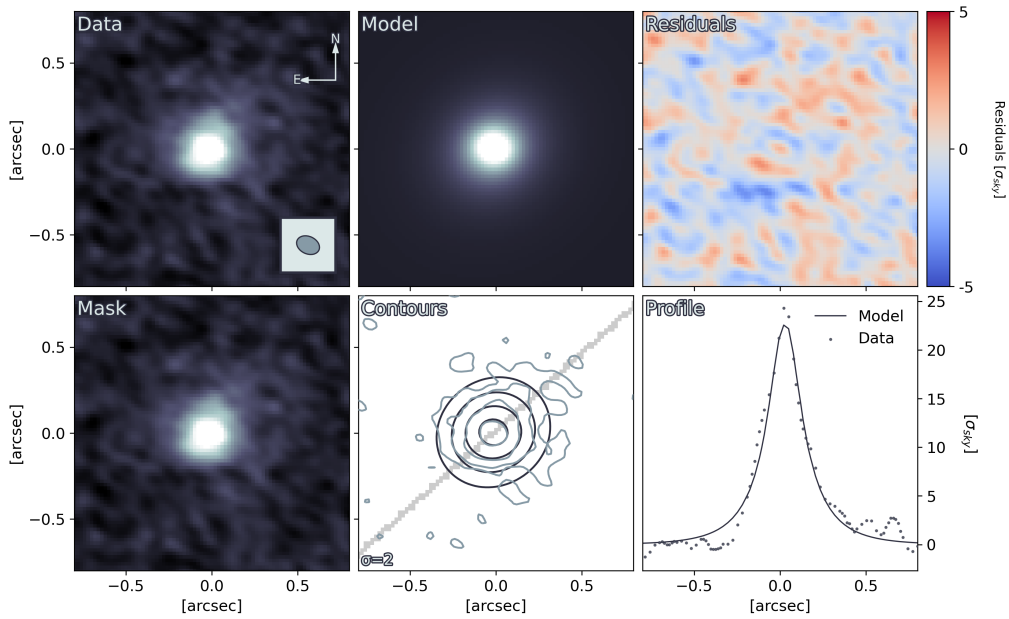


Figure C.12: The results of fitting the CO(5-4) ALMA map for source 3 with GALFIT. **Data:** A cutout of the source. The colour scale for the *Data*, *Model* and *Mask* panels are defined from this map, using a linear scale. The direction towards celestial north and east are displayed by the arrows. The FWHM of the synthetic beam is displayed in the inset on the lower right. **Mask:** Masked out sources and dead pixels are displayed in red. **Model:** The fitted model convolved with the PSF. **Contours:** Contours of the *Data* panel in blue. Contours of the *Model* panel in black. Contour levels start at the value annotated in the bottom left, and increase by a factor of two for each subsequent level. The shaded region indicates where the 1D profile was extracted from. **Residuals:** The *Data* subtracted by the *Model*. **Profile:** A one-dimensional profile extracted along the semi-major axis of the *Model*.

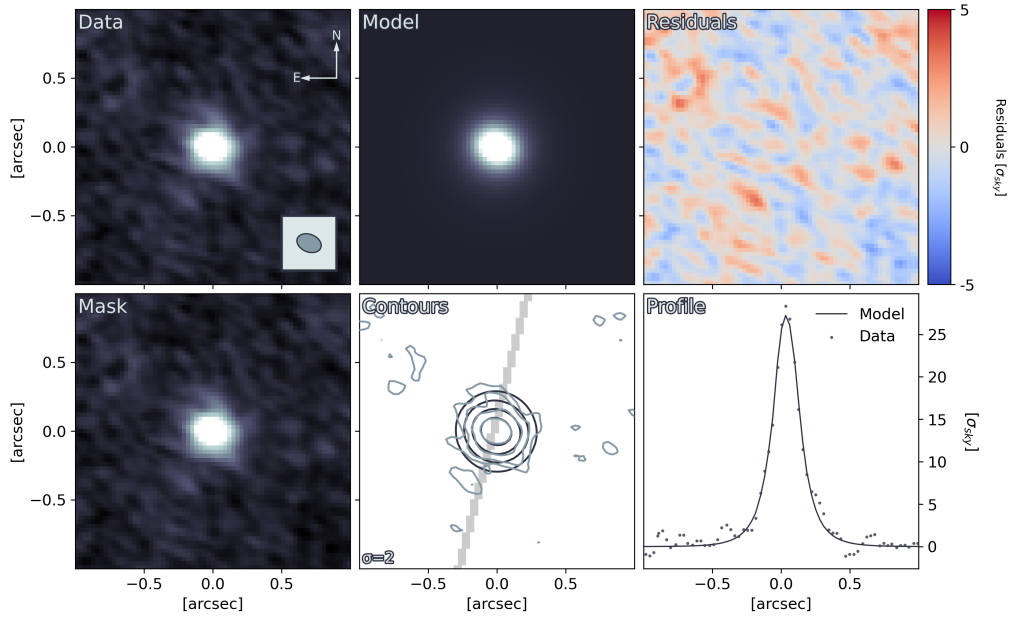


Figure C.13: The results of fitting the dust continuum ALMA map for source 3 with GALFIT. **Data**: A cutout of the source. The colour scale for the *Data*, *Model* and *Mask* panels are defined from this map, using a linear scale. The direction towards celestial north and east are displayed by the arrows. The FWHM of the synthetic beam is displayed in the inset on the lower right. **Mask**: Masked out sources and dead pixels are displayed in red. **Model**: The fitted model convolved with the PSF. **Contours**: Contours of the *Data* panel in blue. Contours of the *Model* panel in black. Contour levels start at the value annotated in the bottom left, and increase by a factor of two for each subsequent level. The shaded region indicates where the 1D profile was extracted from. **Residuals**: The *Data* subtracted by the *Model*. **Profile**: A one-dimensional profile extracted along the semi-major axis of the *Model*.

Source 4

Table C.4: Photometric data collected for source 4. The observation column lists the facility, instrument and filter used to make the observation. The code column connects the filter transmission curve with the correct one in Stardust. The reference column lists references to the works from which the observations were collected. Observations without an uncertainty corresponds to 3σ upper limits.

Observation	Flux [Jy]		Uncertainty [Jy]		Code	Reference
	Value	Order	Value	Order		
MegaCam/u					353	Private
Subaru/Suprime-Cam/B					114	Private
MegaCam/g					89	Private
Subaru/Suprime-Cam/Rc					285	Private
Subaru/Suprime-Cam/i'					82	Private
Subaru/Suprime-Cam/z'					83	Private
Subaru/Suprime-Cam/NBB921					320	Private
HST/WFC3/F125W					203	Private
HST/WFC3/F140W					204	Private
HST/WFC3/F160W					205	Private
WIRCam/J					220	Private
WIRCam/H					221	Private
WIRCam/Ks					222	Private
IRAC/ch1					18	Private
IRAC/ch2					19	Private
IRAC/ch3					20	Private
ALMA/870um	2.580	10^{-3}	2.300	10^{-4}		Hayashi et al. 2018
WISE/band-1	5.030	10^{-5}	5.100	10^{-6}	244	Lasker et al. 2008
WISE/band-2	7.370	10^{-5}	1.130	10^{-5}	245	Lasker et al. 2008
WISE/band-3	5.030	10^{-5}	5.100	10^{-6}	244	Lasker et al. 2008
WISE/band-4	7.370	10^{-5}	1.130	10^{-5}	245	Lasker et al. 2008

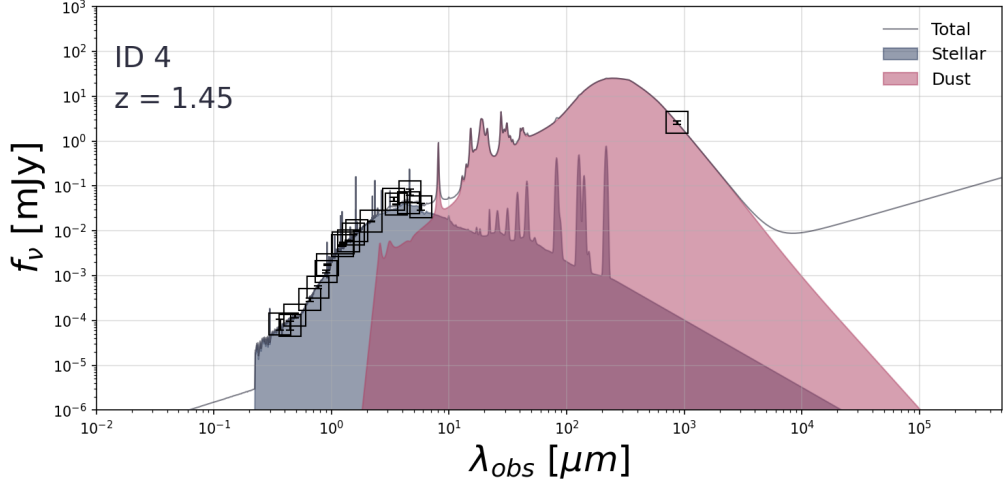


Figure C.14: The SED of source 4 as fitted with STARDUST, assuming that there's no significant AGN contribution. The squares are marked around observations with a SNR > 3. Arrows indicate 3σ upper limits of observations with SNR < 3 or non-detections.

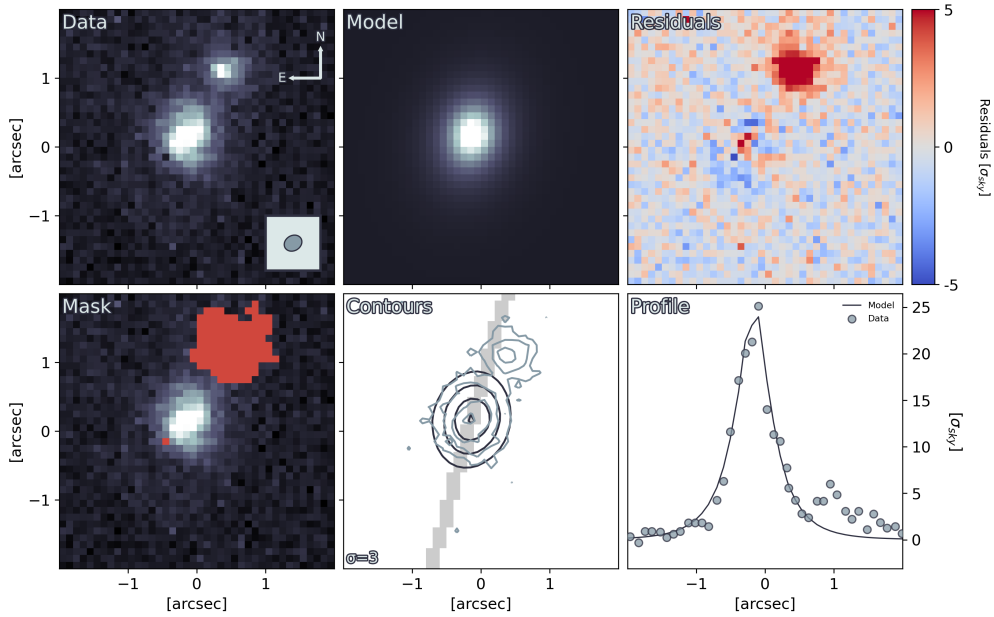


Figure C.15: The results of fitting source 4 with GALFIT. **Data**: A cutout of the source. The colour scale for the *Data*, *Model* and *Mask* panels are defined from this map, using a linear scale. The direction towards celestial north and east are displayed by the arrows. The fitted FWHM of the PSF is displayed in the inset in the bottom right. **Mask**: Masked out sources and dead pixels are displayed in red. **Model**: The fitted model convolved with the PSF. **Contours**: Contours of the *Data* panel in blue. Contours of the *Model* panel in black. Contour levels start at the value annotated in the bottom left, and increase by a factor of two for each subsequent level. The shaded region indicates where the 1D profile was extracted from. **Residuals**: The *Data* subtracted by the *Model*. **Profile**: A one-dimensional profile extracted along the semi-major axis of the *Model*.

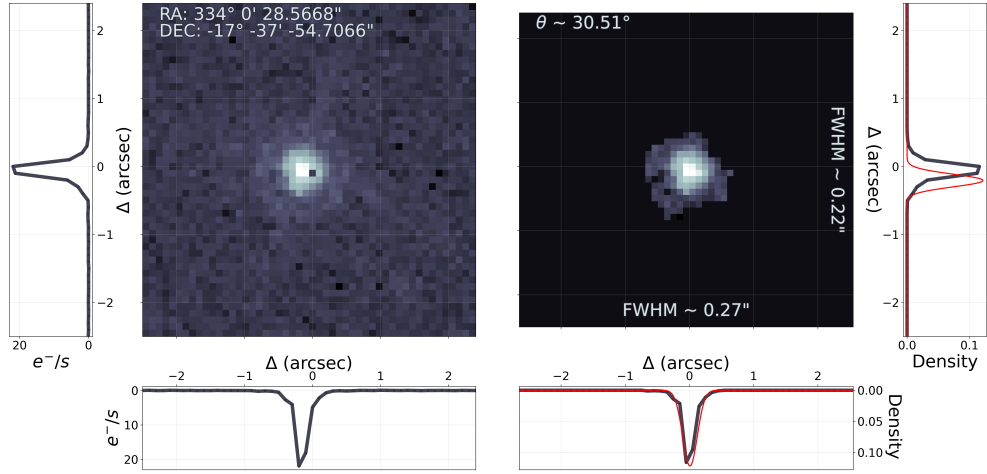


Figure C.16: From point-source to PSF. **Left:** The map displays the source used to create the PSF, for the mosaic containing source 4, in a logarithmic colour scale. The left and bottom panels shows the profile through the pixel of the highest value. The annotated coordinates are the coordinates of the centre of the map. **Right:** The map displays the PSF created from the left figure. The annotated FWHM along each axis are calculated by fitting a two-dimensional Gaussian to the map. The right and bottom panel shows the profile through the highest value pixel in black and the profile of the fitted two-dimensional Gaussian in red. The annotated angle describes the position angle of the fitted two-dimensional Gaussian counterclockwise from the positive x-axis.

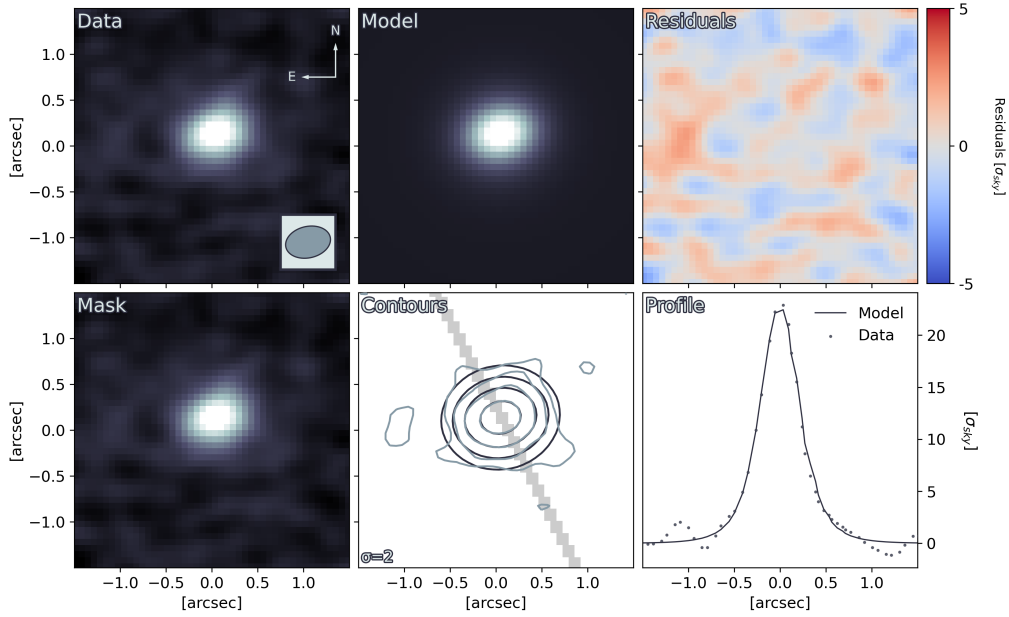


Figure C.17: The results of fitting the CO(2-1) ALMA map for source 4 with GALFIT. **Data:** A cutout of the source. The colour scale for the *Data*, *Model* and *Mask* panels are defined from this map, using a linear scale. The direction towards celestial north and east are displayed by the arrows. The FWHM of the synthetic beam is displayed in the inset on the lower right. **Mask:** Masked out sources and dead pixels are displayed in red. **Model:** The fitted model convolved with the PSF. **Contours:** Contours of the *Data* panel in blue. Contours of the *Model* panel in black. Contour levels start at the value annotated in the bottom left, and increase by a factor of two for each subsequent level. The shaded region indicates where the 1D profile was extracted from. **Residuals:** The *Data* subtracted by the *Model*. **Profile:** A one-dimensional profile extracted along the semi-major axis of the *Model*.

Source 5

Table C.5: Photometric data collected for source 5. The observation column lists the facility, instrument and filter used to make the observation. The code column connects the filter transmission curve with the correct one in Stardust. The reference column lists references to the works from which the observations were collected. Observations without an uncertainty corresponds to 3σ upper limits.

Observation	Flux [Jy]		Uncertainty [Jy]		Code	Reference
	Value	Order	Value	Order		
MegaCam/u					353	Private
Subaru/Suprime-Cam/B					114	Private
MegaCam/g					89	Private
Subaru/Suprime-Cam/Rc					285	Private
Subaru/Suprime-Cam/i'					82	Private
Subaru/Suprime-Cam/z'					83	Private
Subaru/Suprime-Cam/NBB921					320	Private
HST/WFC3/F125W					203	Private
HST/WFC3/F140W					204	Private
HST/WFC3/F160W					205	Private
WIRCam/J					220	Private
WIRCam/H					221	Private
WIRCam/Ks					222	Private
IRAC/ch1					18	Private
IRAC/ch2					19	Private
IRAC/ch3					20	Private
ALMA/870um	1.080	10^{-3}	1.300	10^{-4}		Hayashi et al. 2018
ALMA/24um	1.250	10^{-4}	1.000	10^{-5}		Hayashi et al. 2018

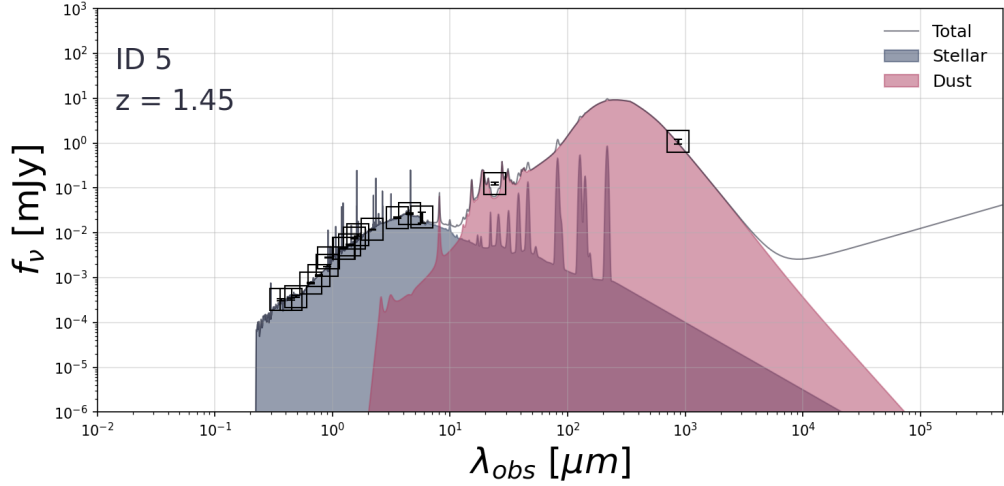


Figure C.18: The SED of source 5 as fitted with STARDUST, assuming that there's no significant AGN contribution. The squares are marked around observations with a $\text{SNR} > 3$. Arrows indicate 3σ upper limits of observations with $\text{SNR} < 3$ or non-detections.

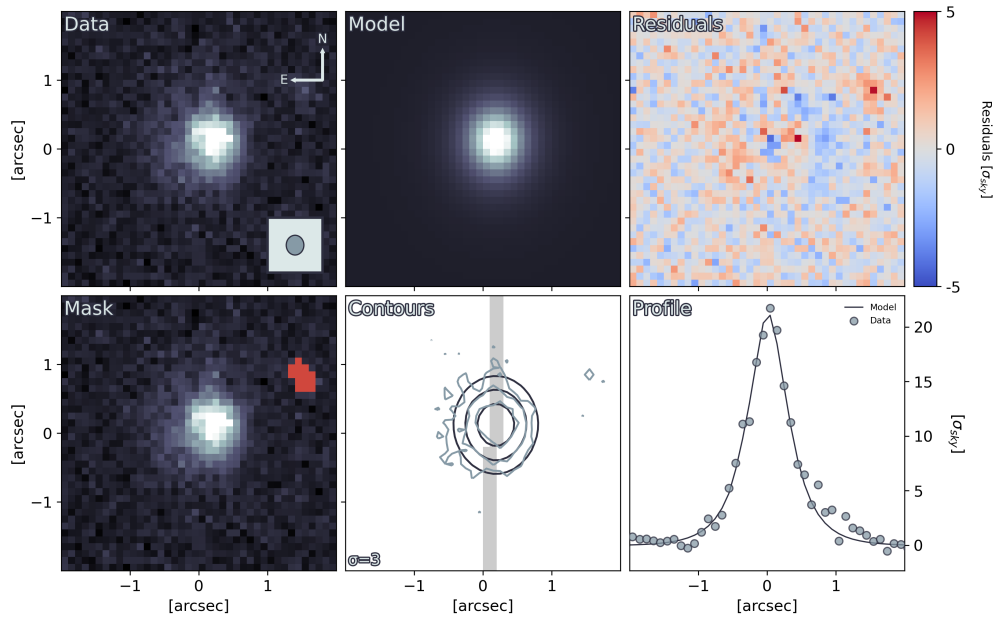


Figure C.19: The results of fitting source 5 with GALFIT. **Data**: A cutout of the source. The colour scale for the *Data*, *Model* and *Mask* panels are defined from this map, using a linear scale. The direction towards celestial north and east are displayed by the arrows. The fitted FWHM of the PSF is displayed in the inset in the bottom right. **Mask**: Masked out sources and dead pixels are displayed in red. **Model**: The fitted model convolved with the PSF. **Contours**: Contours of the *Data* panel in blue. Contours of the *Model* panel in black. Contour levels start at the value annotated in the bottom left, and increase by a factor of two for each subsequent level. The shaded region indicates where the 1D profile was extracted from. **Residuals**: The *Data* subtracted by the *Model*. **Profile**: A one-dimensional profile extracted along the semi-major axis of the *Model*.

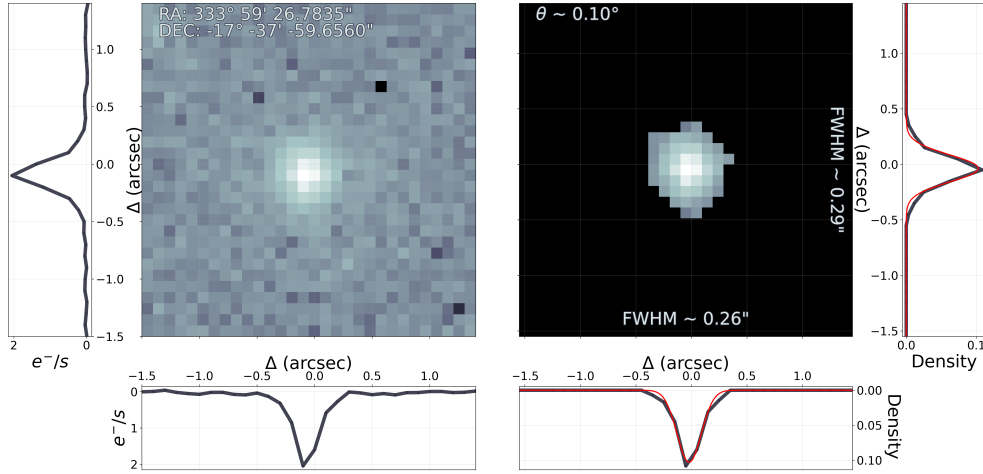


Figure C.20: From point-source to PSF. **Left:** The map displays the source used to create the PSF, for the mosaic containing source 5, in a logarithmic colour scale. The left and bottom panels shows the profile through the pixel of the highest value. The annotated coordinates are the coordinates of the centre of the map. **Right:** The map displays the PSF created from the left figure. The annotated FWHM along each axis are calculated by fitting a two-dimensional Gaussian to the map. The right and bottom panel shows the profile through the highest value pixel in black and the profile of the fitted two-dimensional Gaussian in red. The annotated angle describes the position angle of the fitted two-dimensional Gaussian counterclockwise from the positive x-axis.

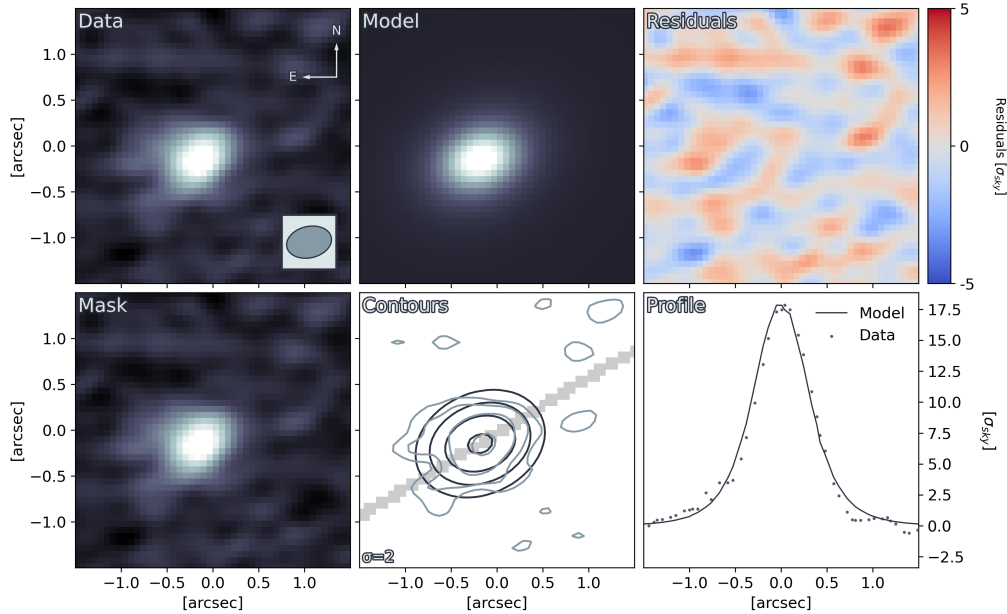


Figure C.21: The results of fitting the CO(2-1) ALMA map for source 5 with GALFIT. **Data:** A cutout of the source. The colour scale for the *Data*, *Model* and *Mask* panels are defined from this map, using a linear scale. The direction towards celestial north and east are displayed by the arrows. The FWHM of the synthetic beam is displayed in the inset on the lower right. **Mask:** Masked out sources and dead pixels are displayed in red. **Model:** The fitted model convolved with the PSF. **Contours:** Contours of the *Data* panel in blue. Contours of the *Model* panel in black. Contour levels start at the value annotated in the bottom left, and increase by a factor of two for each subsequent level. The shaded region indicates where the 1D profile was extracted from. **Residuals:** The *Data* subtracted by the *Model*. **Profile:** A one-dimensional profile extracted along the semi-major axis of the *Model*.

Source 6

Table C.6: Photometric data collected for source 6. The observation column lists the facility, instrument and filter used to make the observation. The code column connects the filter transmission curve with the correct one in Stardust. The reference column lists references to the works from which the observations were collected. Observations without an uncertainty corresponds to 3σ upper limits.

Observation	Flux [Jy]		Uncertainty [Jy]		Code	Reference
	Value	Order	Value	Order		
MegaCam/u					353	Private
Subaru/Suprime-Cam/B					114	Private
MegaCam/g					89	Private
Subaru/Suprime-Cam/Rc					285	Private
Subaru/Suprime-Cam/i'					82	Private
Subaru/Suprime-Cam/z'					83	Private
Subaru/Suprime-Cam/NBB921					320	Private
HST/WFC3/F125W					203	Private
HST/WFC3/F140W					204	Private
HST/WFC3/F160W					205	Private
WIRCam/J					220	Private
WIRCam/H					221	Private
WIRCam/Ks					222	Private
IRAC/ch1					18	Private
IRAC/ch2					19	Private
IRAC/ch3					20	Private
ALMA/24um	8.800	10^{-5}	1.000	10^{-5}		Hayashi et al. 2018
WISE/band-1	3.570	10^{-5}	2.400	10^{-6}	244	Marocco et al. 2021
WISE/band-2	5.090	10^{-5}	4.300	10^{-6}	245	Marocco et al. 2021

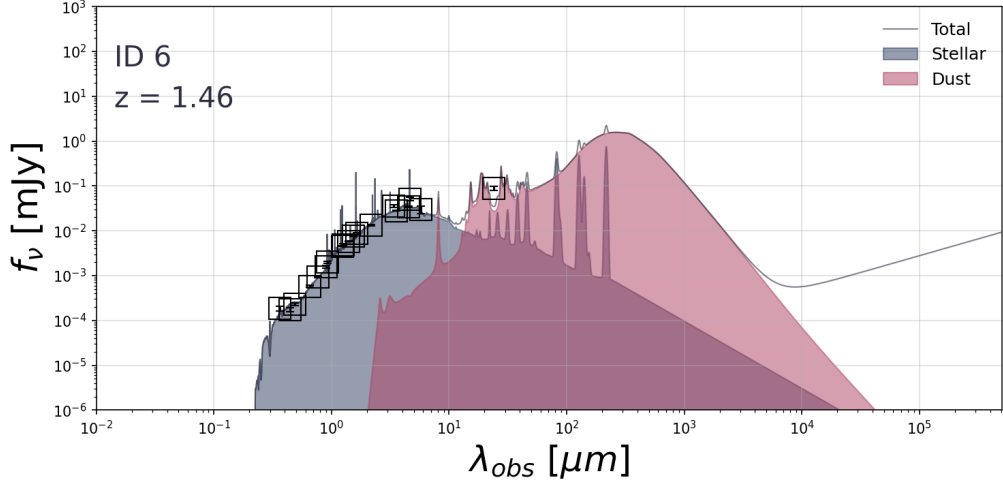


Figure C.22: The SED of source 6 as fitted with STARDUST, assuming that there's no significant AGN contribution. The squares are marked around observations with a SNR > 3. Arrows indicate 3σ upper limits of observations with SNR < 3 or non-detections.

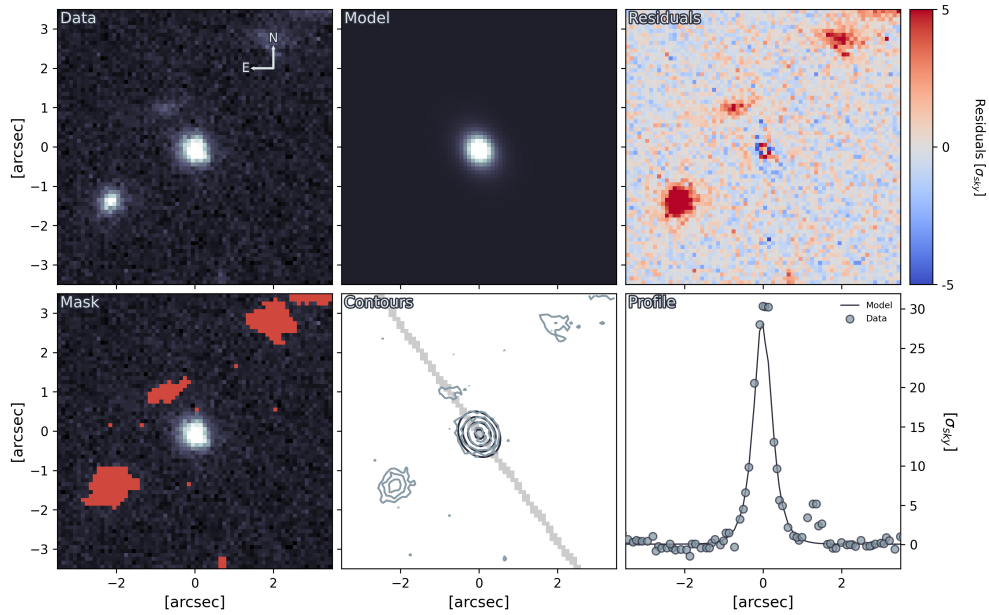


Figure C.23: The results of fitting source 6 with GALFIT. **Data**: A cutout of the source. The colour scale for the *Data*, *Model* and *Mask* panels are defined from this map, using a linear scale. The direction towards celestial north and east are displayed by the arrows. The fitted FWHM of the PSF is displayed in the inset in the bottom right. **Mask**: Masked out sources and dead pixels are displayed in red. **Model**: The fitted model convolved with the PSF. **Contours**: Contours of the *Data* panel in blue. Contours of the *Model* panel in black. Contour levels start at the value annotated in the bottom left, and increase by a factor of two for each subsequent level. The shaded region indicates where the 1D profile was extracted from. **Residuals**: The *Data* subtracted by the *Model*. **Profile**: A one-dimensional profile extracted along the semi-major axis of the *Model*.

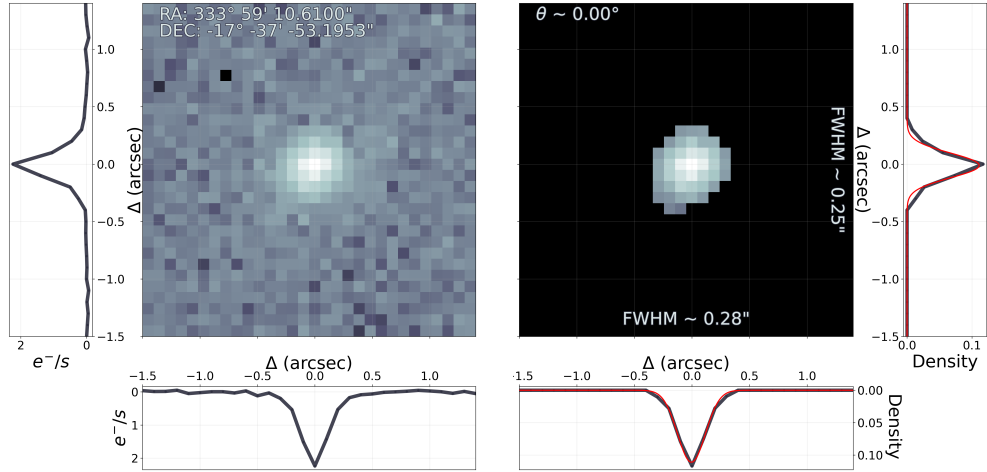


Figure C.24: From point-source to PSF. **Left:** The map displays the source used to create the PSF, for the mosaic containing source 6, in a logarithmic colour scale. The left and bottom panels shows the profile through the pixel of the highest value. The annotated coordinates are the coordinates of the centre of the map. **Right:** The map displays the PSF created from the left figure. The annotated FWHM along each axis are calculated by fitting a two-dimensional Gaussian to the map. The right and bottom panel shows the profile through the highest value pixel in black and the profile of the fitted two-dimensional Gaussian in red. The annotated angle describes the position angle of the fitted two-dimensional Gaussian counterclockwise from the positive x-axis.

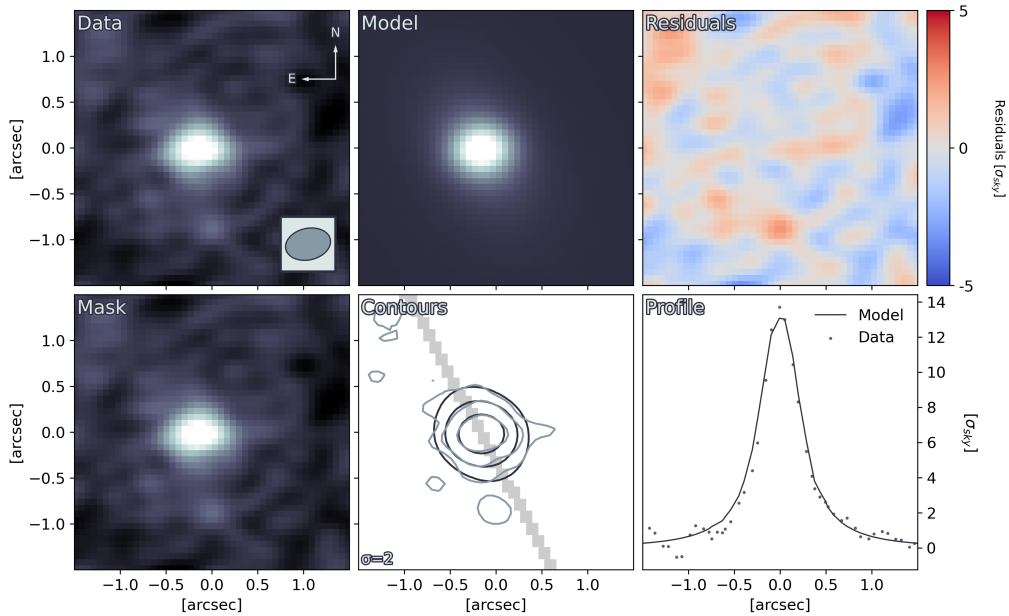


Figure C.25: The results of fitting the CO(2-1) ALMA map for source 6 with GALFIT. **Data:** A cutout of the source. The colour scale for the *Data*, *Model* and *Mask* panels are defined from this map, using a linear scale. The direction towards celestial north and east are displayed by the arrows. The FWHM of the synthetic beam is displayed in the inset on the lower right. **Mask:** Masked out sources and dead pixels are displayed in red. **Model:** The fitted model convolved with the PSF. **Contours:** Contours of the *Data* panel in blue. Contours of the *Model* panel in black. Contour levels start at the value annotated in the bottom left, and increase by a factor of two for each subsequent level. The shaded region indicates where the 1D profile was extracted from. **Residuals:** The *Data* subtracted by the *Model*. **Profile:** A one-dimensional profile extracted along the semi-major axis of the *Model*.

Source 7

Table C.7: Photometric data collected for source 7. The observation column lists the facility, instrument and filter used to make the observation. The code column connects the filter transmission curve with the correct one in Stardust. The reference column lists references to the works from which the observations were collected. Observations without an uncertainty corresponds to 3σ upper limits.

Observation	Flux [Jy]		Uncertainty [Jy]		Code	Reference
	Value	Order	Value	Order		
MegaCam/u					353	Private
Subaru/Suprime-Cam/B					114	Private
MegaCam/g					89	Private
Subaru/Suprime-Cam/Rc					285	Private
Subaru/Suprime-Cam/i'					82	Private
Subaru/Suprime-Cam/z'					83	Private
Subaru/Suprime-Cam/NBB921					320	Private
HST/WFC3/F125W					203	Private
HST/WFC3/F140W					204	Private
HST/WFC3/F160W					205	Private
WIRCam/J					220	Private
WIRCam/H					221	Private
WIRCam/Ks					222	Private
IRAC/ch1					18	Private
IRAC/ch2					19	Private
IRAC/ch3					20	Private
ALMA/24um	1.250	10^{-4}	1.000	10^{-5}		Hayashi et al. 2018

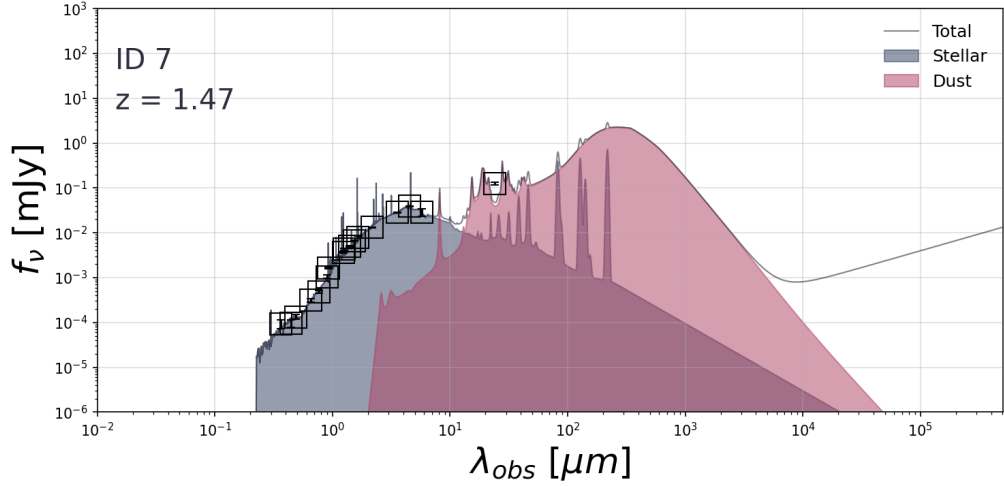


Figure C.26: The SED of source 7 as fitted with STARDUST, assuming that there's no significant AGN contribution. The squares are marked around observations with a $\text{SNR} > 3$. Arrows indicate 3σ upper limits of observations with $\text{SNR} < 3$ or non-detections.

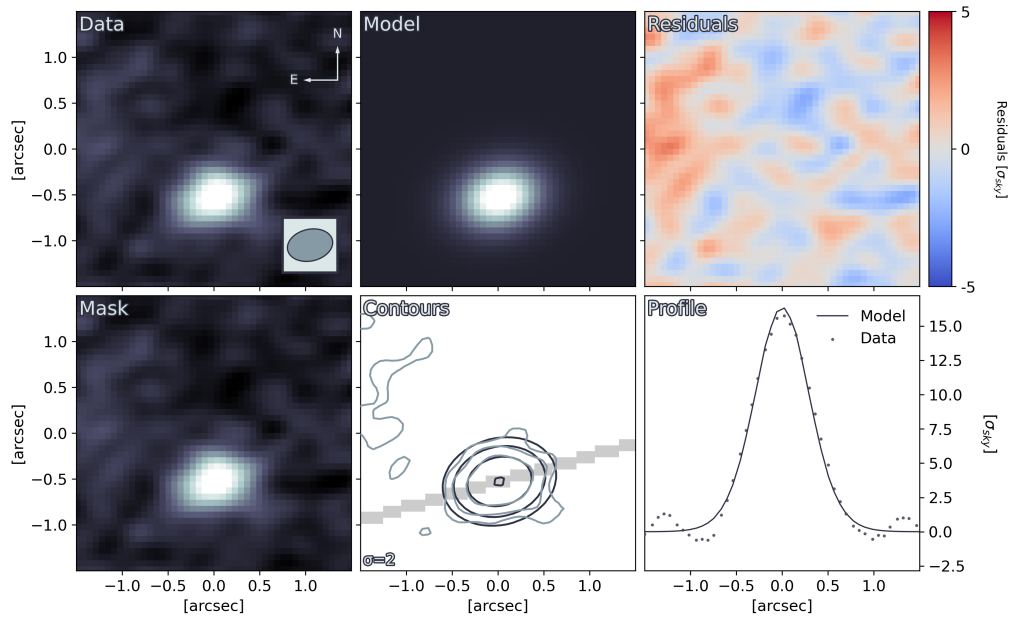


Figure C.27: The results of fitting the CO(2-1) ALMA map for source 7 with GALFIT. **Data**: A cutout of the source. The colour scale for the *Data*, *Model* and *Mask* panels are defined from this map, using a linear scale. The direction towards celestial north and east are displayed by the arrows. The FWHM of the synthetic beam is displayed in the inset on the lower right. **Mask**: Masked out sources and dead pixels are displayed in red. **Model**: The fitted model convolved with the PSF. **Contours**: Contours of the *Data* panel in blue. Contours of the *Model* panel in black. Contour levels start at the value annotated in the bottom left, and increase by a factor of two for each subsequent level. The shaded region indicates where the 1D profile was extracted from. **Residuals**: The *Data* subtracted by the *Model*. **Profile**: A one-dimensional profile extracted along the semi-major axis of the *Model*.

Source 8

Table C.8: Photometric data collected for source 8. The observation column lists the facility, instrument and filter used to make the observation. The code column connects the filter transmission curve with the correct one in Stardust. The reference column lists references to the works from which the observations were collected. Observations without an uncertainty corresponds to 3σ upper limits.

Observation	Flux [Jy]		Uncertainty [Jy]		Code	Reference
	Value	Order	Value	Order		
MegaCam/u					353	Private
Subaru/Suprime-Cam/B					114	Private
MegaCam/g					89	Private
Subaru/Suprime-Cam/Rc					285	Private
Subaru/Suprime-Cam/i'					82	Private
Subaru/Suprime-Cam/z'					83	Private
Subaru/Suprime-Cam/NBB921					320	Private
HST/WFC3/F125W					203	Private
HST/WFC3/F140W					204	Private
HST/WFC3/F160W					205	Private
WIRCam/J					220	Private
WIRCam/H					221	Private
WIRCam/Ks					222	Private
IRAC/ch1					18	Private
IRAC/ch2					19	Private
IRAC/ch3					20	Private
ALMA/24um	1.800	10^{-4}	1.100	10^{-5}		Hayashi et al. 2018

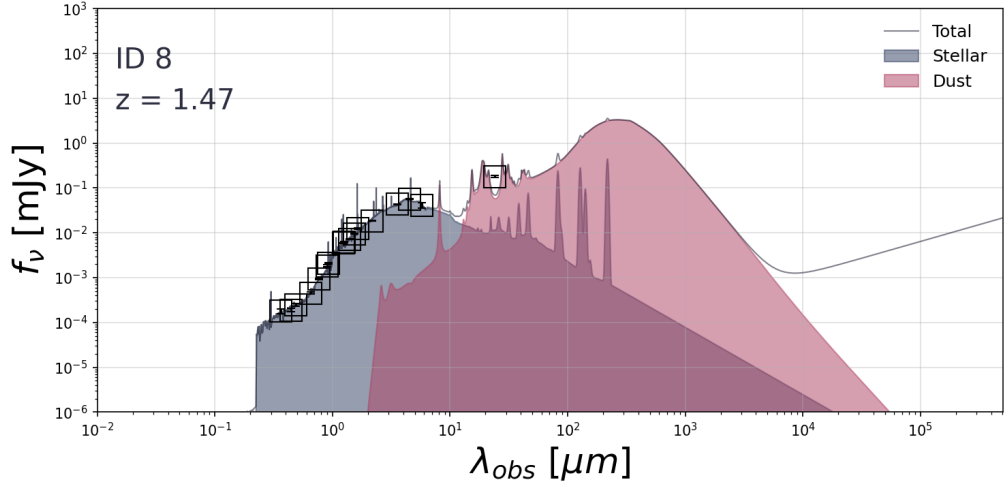


Figure C.28: The SED of source 8 as fitted with STARDUST, assuming that there's no significant AGN contribution. The squares are marked around observations with a $\text{SNR} > 3$. Arrows indicate 3σ upper limits of observations with $\text{SNR} < 3$ or non-detections.

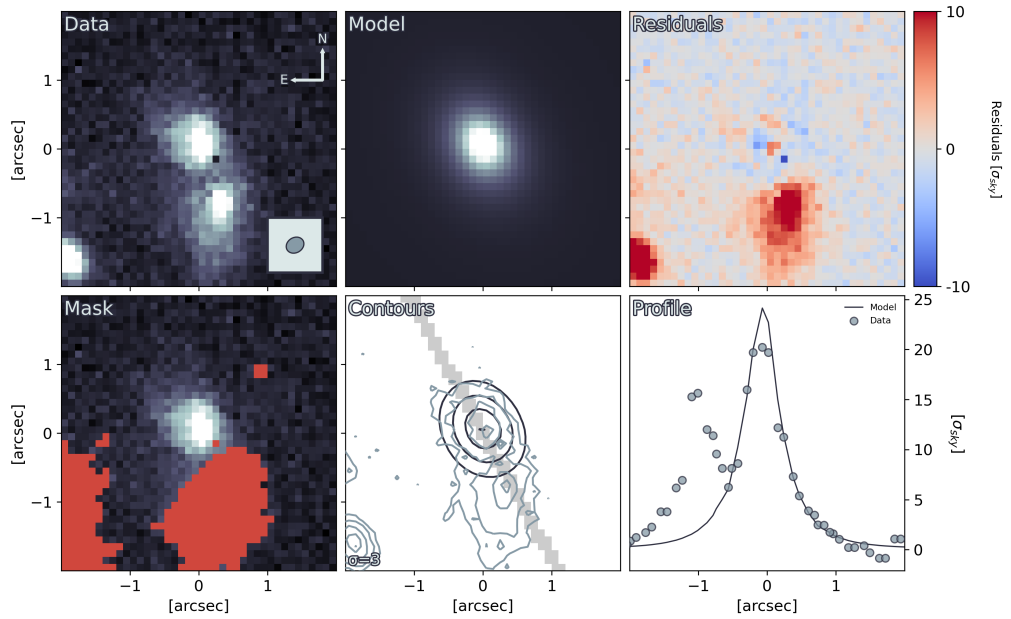


Figure C.29: The results of fitting source 8 with GALFIT. **Data**: A cutout of the source. The colour scale for the *Data*, *Model* and *Mask* panels are defined from this map, using a linear scale. The direction towards celestial north and east are displayed by the arrows. The fitted FWHM of the PSF is displayed in the inset in the bottom right. **Mask**: Masked out sources and dead pixels are displayed in red. **Model**: The fitted model convolved with the PSF. **Contours**: Contours of the *Data* panel in blue. Contours of the *Model* panel in black. Contour levels start at the value annotated in the bottom left, and increase by a factor of two for each subsequent level. The shaded region indicates where the 1D profile was extracted from. **Residuals**: The *Data* subtracted by the *Model*. **Profile**: A one-dimensional profile extracted along the semi-major axis of the *Model*.

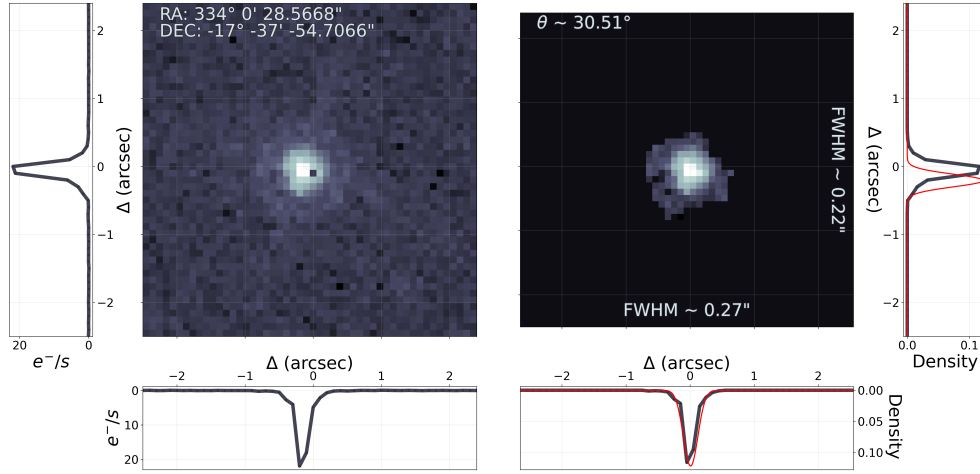


Figure C.30: From point-source to PSF. **Left:** The map displays the source used to create the PSF, for the mosaic containing source 8, in a logarithmic colour scale. The left and bottom panels shows the profile through the pixel of the highest value. The annotated coordinates are the coordinates of the centre of the map. **Right:** The map displays the PSF created from the left figure. The annotated FWHM along each axis are calculated by fitting a two-dimensional Gaussian to the map. The right and bottom panel shows the profile through the highest value pixel in black and the profile of the fitted two-dimensional Gaussian in red. The annotated angle describes the position angle of the fitted two-dimensional Gaussian counterclockwise from the positive x-axis.

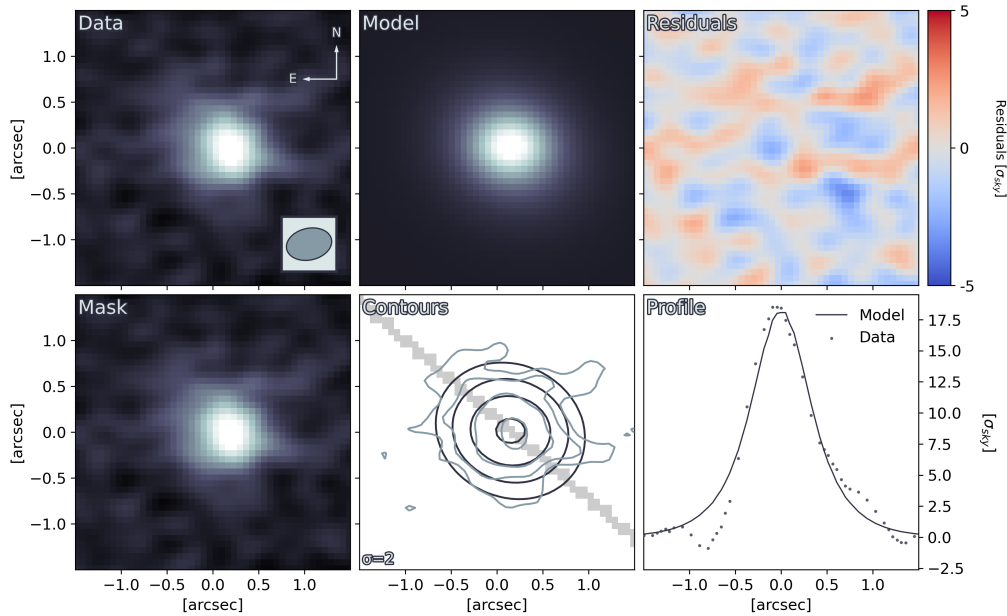


Figure C.31: The results of fitting the CO(2-1) ALMA map for source 8 with GALFIT. **Data:** A cutout of the source. The colour scale for the *Data*, *Model* and *Mask* panels are defined from this map, using a linear scale. The direction towards celestial north and east are displayed by the arrows. The FWHM of the synthetic beam is displayed in the inset on the lower right. **Mask:** Masked out sources and dead pixels are displayed in red. **Model:** The fitted model convolved with the PSF. **Contours:** Contours of the *Data* panel in blue. Contours of the *Model* panel in black. Contour levels start at the value annotated in the bottom left, and increase by a factor of two for each subsequent level. The shaded region indicates where the 1D profile was extracted from. **Residuals:** The *Data* subtracted by the *Model*. **Profile:** A one-dimensional profile extracted along the semi-major axis of the *Model*.

Source 9

Table C.9: Photometric data collected for source 9. The observation column lists the facility, instrument and filter used to make the observation. The code column connects the filter transmission curve with the correct one in Stardust. The reference column lists references to the works from which the observations were collected. Observations without an uncertainty corresponds to 3σ upper limits.

Observation	Flux [Jy]		Uncertainty [Jy]		Code	Reference
	Value	Order	Value	Order		
MegaCam/u					353	Private
Subaru/Suprime-Cam/B					114	Private
MegaCam/g					89	Private
Subaru/Suprime-Cam/Rc					285	Private
Subaru/Suprime-Cam/i'					82	Private
Subaru/Suprime-Cam/z'					83	Private
Subaru/Suprime-Cam/NBB921					320	Private
HST/WFC3/F125W					203	Private
HST/WFC3/F140W					204	Private
HST/WFC3/F160W					205	Private
WIRCam/J					220	Private
WIRCam/H					221	Private
WIRCam/Ks					222	Private
IRAC/ch1					18	Private
IRAC/ch2					19	Private
IRAC/ch3					20	Private
ALMA/24um	6.000	10^{-5}	1.000	10^{-5}		Hayashi et al. 2018

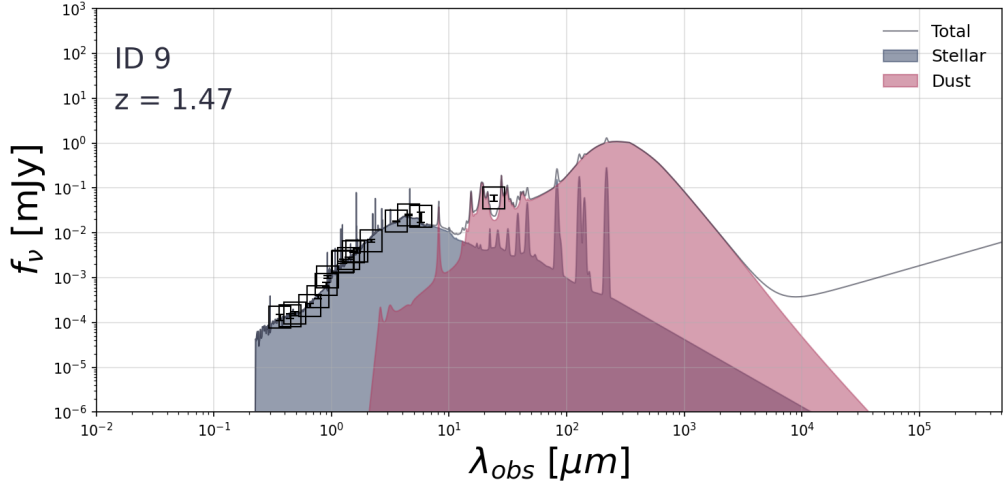


Figure C.32: The SED of source 9 as fitted with STARDUST, assuming that there's no significant AGN contribution. The squares are marked around observations with a SNR > 3. Arrows indicate 3σ upper limits of observations with SNR < 3 or non-detections.

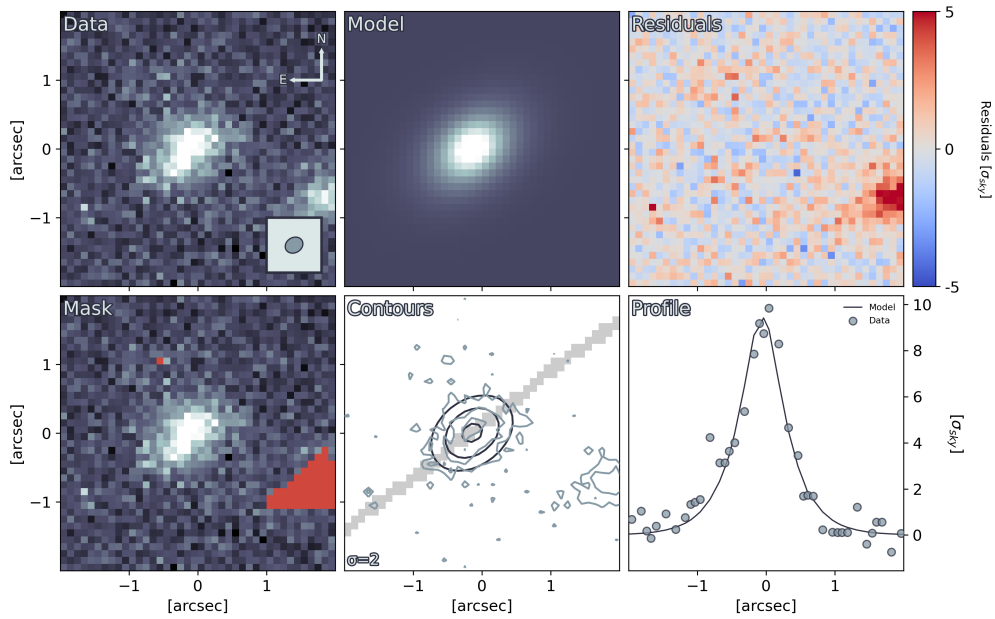


Figure C.33: The results of fitting source 9 with GALFIT. **Data**: A cutout of the source. The colour scale for the *Data*, *Model* and *Mask* panels are defined from this map, using a linear scale. The direction towards celestial north and east are displayed by the arrows. The fitted FWHM of the PSF is displayed in the inset in the bottom right. **Mask**: Masked out sources and dead pixels are displayed in red. **Model**: The fitted model convolved with the PSF. **Contours**: Contours of the *Data* panel in blue. Contours of the *Model* panel in black. Contour levels start at the value annotated in the bottom left, and increase by a factor of two for each subsequent level. The shaded region indicates where the 1D profile was extracted from. **Residuals**: The *Data* subtracted by the *Model*. **Profile**: A one-dimensional profile extracted along the semi-major axis of the *Model*.

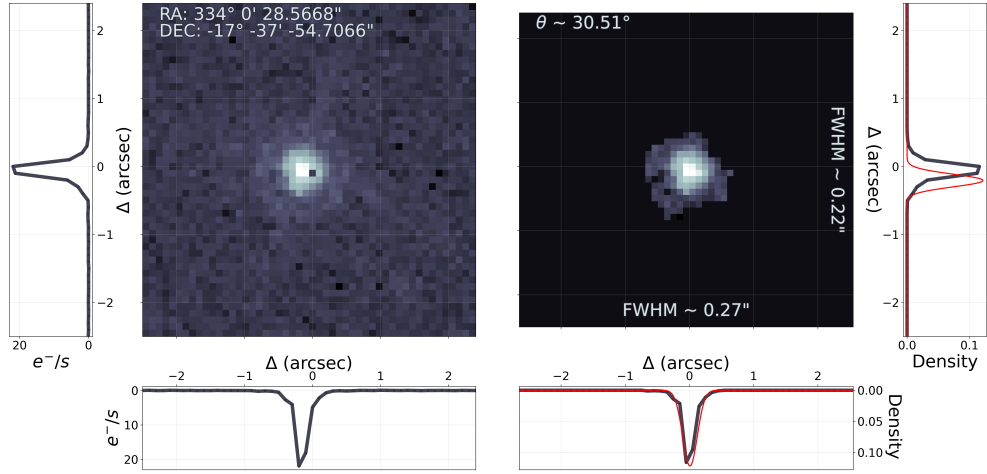


Figure C.34: From point-source to PSF. **Left:** The map displays the source used to create the PSF, for the mosaic containing source 9, in a logarithmic colour scale. The left and bottom panels shows the profile through the pixel of the highest value. The annotated coordinates are the coordinates of the centre of the map. **Right:** The map displays the PSF created from the left figure. The annotated FWHM along each axis are calculated by fitting a two-dimensional Gaussian to the map. The right and bottom panel shows the profile through the highest value pixel in black and the profile of the fitted two-dimensional Gaussian in red. The annotated angle describes the position angle of the fitted two-dimensional Gaussian counterclockwise from the positive x-axis.

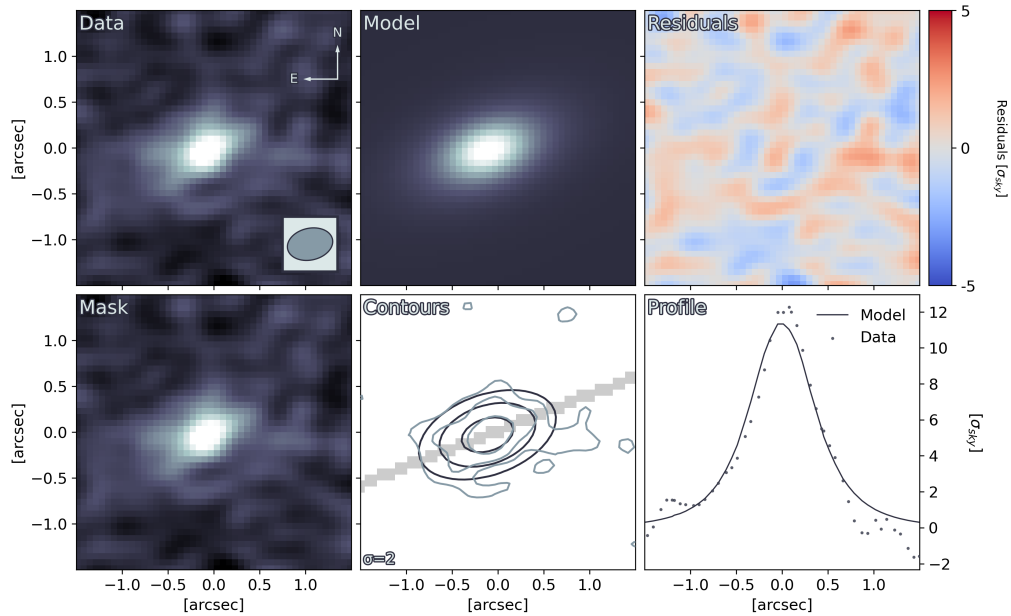


Figure C.35: The results of fitting the CO(2-1) ALMA map for source 8 with GALFIT. **Data:** A cutout of the source. The colour scale for the *Data*, *Model* and *Mask* panels are defined from this map, using a linear scale. The direction towards celestial north and east are displayed by the arrows. The FWHM of the synthetic beam is displayed in the inset on the lower right. **Mask:** Masked out sources and dead pixels are displayed in red. **Model:** The fitted model convolved with the PSF. **Contours:** Contours of the *Data* panel in blue. Contours of the *Model* panel in black. Contour levels start at the value annotated in the bottom left, and increase by a factor of two for each subsequent level. The shaded region indicates where the 1D profile was extracted from. **Residuals:** The *Data* subtracted by the *Model*. **Profile:** A one-dimensional profile extracted along the semi-major axis of the *Model*.

Source 10

Table C.10: Photometric data collected for source 10. The observation column lists the facility, instrument and filter used to make the observation. The code column connects the filter transmission curve with the correct one in Stardust. The reference column lists references to the works from which the observations were collected. Observations without an uncertainty corresponds to 3σ upper limits.

Observation	Flux [Jy]		Uncertainty [Jy]		Code	Reference
	Value	Order	Value	Order		
WISE/band-1	2.230	10^{-5}	2.300	10^{-6}	244	Marocco et al. 2021
WISE/band-2	2.400	10^{-5}	4.100	10^{-6}	245	Marocco et al. 2021
Herschel/SPIRE/250	2.210	10^{-2}	8.000	10^{-4}	331	Laigle et al. 2016
Herschel/SPIRE/350	1.590	10^{-2}	9.000	10^{-4}	332	Laigle et al. 2016
Herschel/PACS/100	1.220	10^{-2}	1.400	10^{-3}	329	Laigle et al. 2016
GALEX/GALEX/NUV	1.000	10^{-8}	7.000	10^{-8}	121	Laigle et al. 2016
SPITZER/MIPS/24	2.060	10^{-4}	1.300	10^{-5}	325	Laigle et al. 2016
CFHT/WIRCAM/Ks	1.590	10^{-5}	4.000	10^{-7}	222	Laigle et al. 2016
CFHT/WIRCAM/H	1.150	10^{-5}	4.000	10^{-7}	221	Laigle et al. 2016
VISTA/VIRCAM/Y	6.030	10^{-6}	4.000	10^{-8}	256	Laigle et al. 2016
VISTA/VIRCAM/J	8.350	10^{-6}	6.000	10^{-8}	257	Laigle et al. 2016
VISTA/VIRCAM/H	1.330	10^{-5}	1.000	10^{-7}	258	Laigle et al. 2016
VISTA/VIRCAM/Ks	1.700	10^{-5}	1.000	10^{-7}	259	Laigle et al. 2016
Subaru/Suprime-Cam/B	8.810	10^{-7}	2.500	10^{-8}	78	Laigle et al. 2016
Subaru/Suprime-Cam/V	1.450	10^{-6}	5.000	10^{-8}	79	Laigle et al. 2016
Subaru/Suprime-Cam/r	1.790	10^{-6}	4.000	10^{-8}	81	Laigle et al. 2016
Subaru/Suprime-Cam/i	2.510	10^{-6}	5.000	10^{-8}	82	Laigle et al. 2016
Subaru/Suprime-Cam/z	4.150	10^{-6}	4.000	10^{-8}	83	Laigle et al. 2016
Subaru/Suprime-Cam/IB827	2.870	10^{-6}	8.000	10^{-8}	197	Laigle et al. 2016
Subaru/Suprime-Cam/NB816	2.270	10^{-6}	8.000	10^{-8}	319	Laigle et al. 2016
Subaru/Suprime-Cam/IB767	2.170	10^{-6}	1.000	10^{-7}	362	Laigle et al. 2016
Subaru/Suprime-Cam/IB738	2.480	10^{-6}	1.000	10^{-7}	194	Laigle et al. 2016
Subaru/Suprime-Cam/NB711	1.890	10^{-6}	1.600	10^{-7}	322	Laigle et al. 2016
Subaru/Suprime-Cam/IB709	2.110	10^{-6}	7.000	10^{-8}	193	Laigle et al. 2016
Subaru/Suprime-Cam/IB624	2.170	10^{-6}	8.000	10^{-8}	190	Laigle et al. 2016
Subaru/Suprime-Cam/IB574	1.050	10^{-6}	7.000	10^{-8}	188	Laigle et al. 2016
Subaru/Suprime-Cam/IB527	1.260	10^{-6}	6.000	10^{-8}	186	Laigle et al. 2016
Subaru/Suprime-Cam/IB505	1.040	10^{-6}	8.000	10^{-8}	185	Laigle et al. 2016
Subaru/Suprime-Cam/IB484	1.250	10^{-6}	6.000	10^{-8}	184	Laigle et al. 2016
Subaru/Suprime-Cam/IB464	9.230	10^{-7}	6.000	10^{-8}	183	Laigle et al. 2016
Subaru/Suprime-Cam/IB427	7.040	10^{-7}	5.500	10^{-8}	181	Laigle et al. 2016
Spitzer/IRAC/ch1	3.190	10^{-5}	2.000	10^{-7}	18	Laigle et al. 2016
Spitzer/IRAC/ch2	4.150	10^{-5}	2.000	10^{-7}	19	Laigle et al. 2016
Spitzer/IRAC/ch3	3.950	10^{-5}	3.800	10^{-6}	20	Laigle et al. 2016
Spitzer/IRAC/ch4	2.650	10^{-5}	5.100	10^{-6}	21	Laigle et al. 2016
CFHT/MegaCam/u	6.380	10^{-7}	2.000	10^{-8}	72	Laigle et al. 2016
VLA/3GHz	2.540	10^{-5}	2.700	10^{-6}		Smolčić et al. 2017

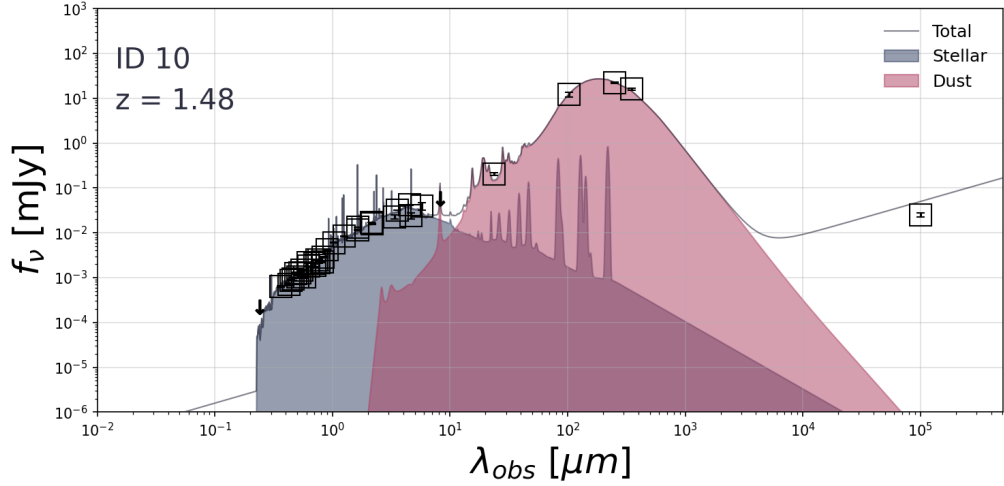


Figure C.36: The SED of source 10 as fitted with STARDUST, assuming that there's no significant AGN contribution. The squares are marked around observations with a $\text{SNR} > 3$. Arrows indicate 3σ upper limits of observations with $\text{SNR} < 3$ or non-detections.

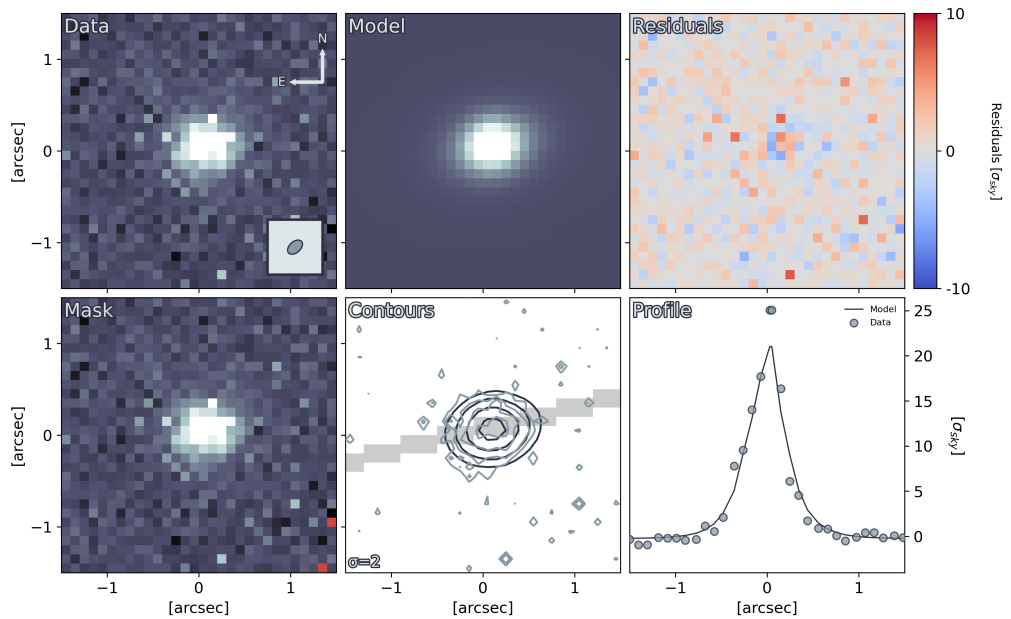


Figure C.37: The results of fitting source 10 with GALFIT. **Data**: A cutout of the source. The colour scale for the *Data*, *Model* and *Mask* panels are defined from this map, using a linear scale. The direction towards celestial north and east are displayed by the arrows. The fitted FWHM of the PSF is displayed in the inset in the bottom right. **Mask**: Masked out sources and dead pixels are displayed in red. **Model**: The fitted model convolved with the PSF. **Contours**: Contours of the *Data* panel in blue. Contours of the *Model* panel in black. Contour levels start at the value annotated in the bottom left, and increase by a factor of two for each subsequent level. The shaded region indicates where the 1D profile was extracted from. **Residuals**: The *Data* subtracted by the *Model*. **Profile**: A one-dimensional profile extracted along the semi-major axis of the *Model*.

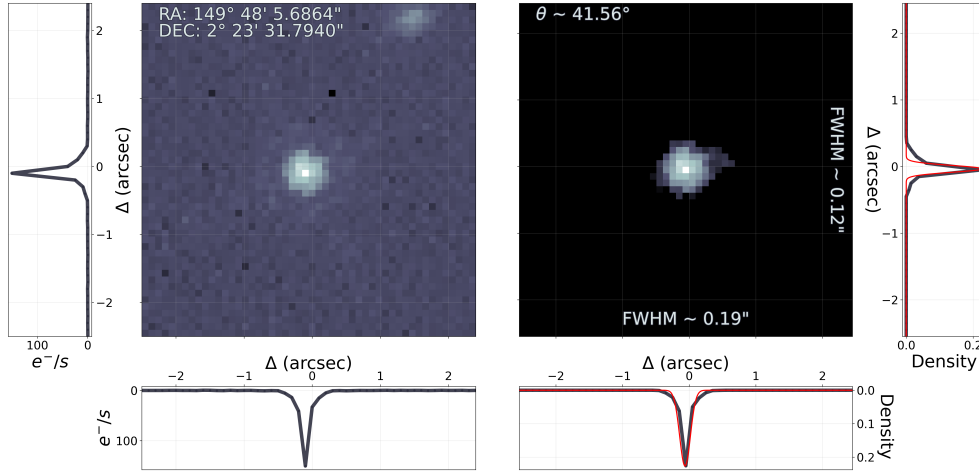


Figure C.38: From point-source to PSF. **Left:** The map displays the source used to create the PSF, for the mosaic containing source 10, in a logarithmic colour scale. The left and bottom panels shows the profile through the pixel of the highest value. The annotated coordinates are the coordinates of the centre of the map. **Right:** The map displays the PSF created from the left figure. The annotated FWHM along each axis are calculated by fitting a two-dimensional Gaussian to the map. The right and bottom panel shows the profile through the highest value pixel in black and the profile of the fitted two-dimensional Gaussian in red. The annotated angle describes the position angle of the fitted two-dimensional Gaussian counterclockwise from the positive x-axis.

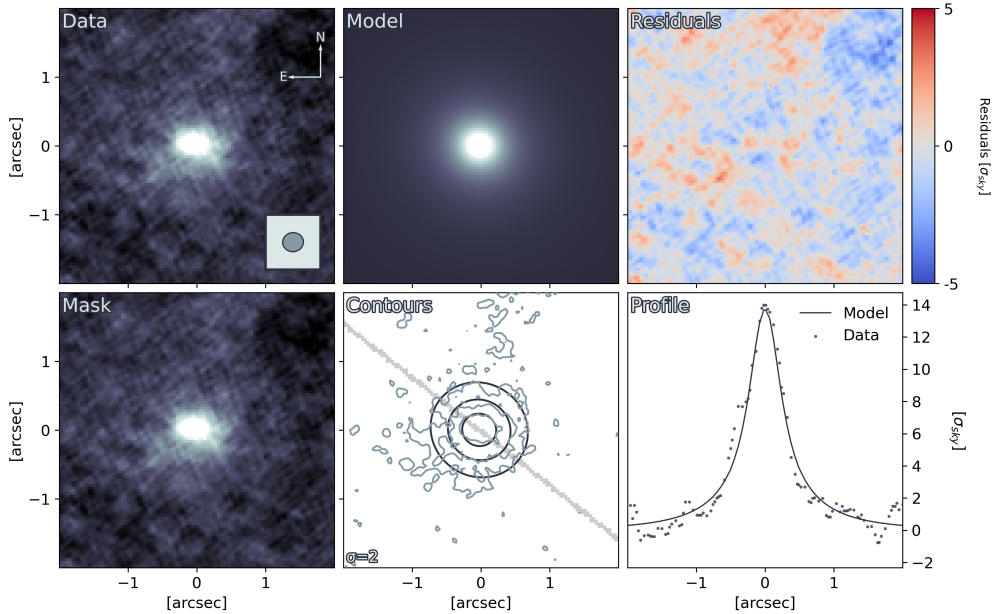


Figure C.39: The results of fitting the CO(2-1) ALMA map for source 10 with GALFIT. **Data:** A cutout of the source. The colour scale for the *Data*, *Model* and *Mask* panels are defined from this map, using a linear scale. The direction towards celestial north and east are displayed by the arrows. The FWHM of the synthetic beam is displayed in the inset on the lower right. **Mask:** Masked out sources and dead pixels are displayed in red. **Model:** The fitted model convolved with the PSF. **Contours:** Contours of the *Data* panel in blue. Contours of the *Model* panel in black. Contour levels start at the value annotated in the bottom left, and increase by a factor of two for each subsequent level. The shaded region indicates where the 1D profile was extracted from. **Residuals:** The *Data* subtracted by the *Model*. **Profile:** A one-dimensional profile extracted along the semi-major axis of the *Model*.

Source 11

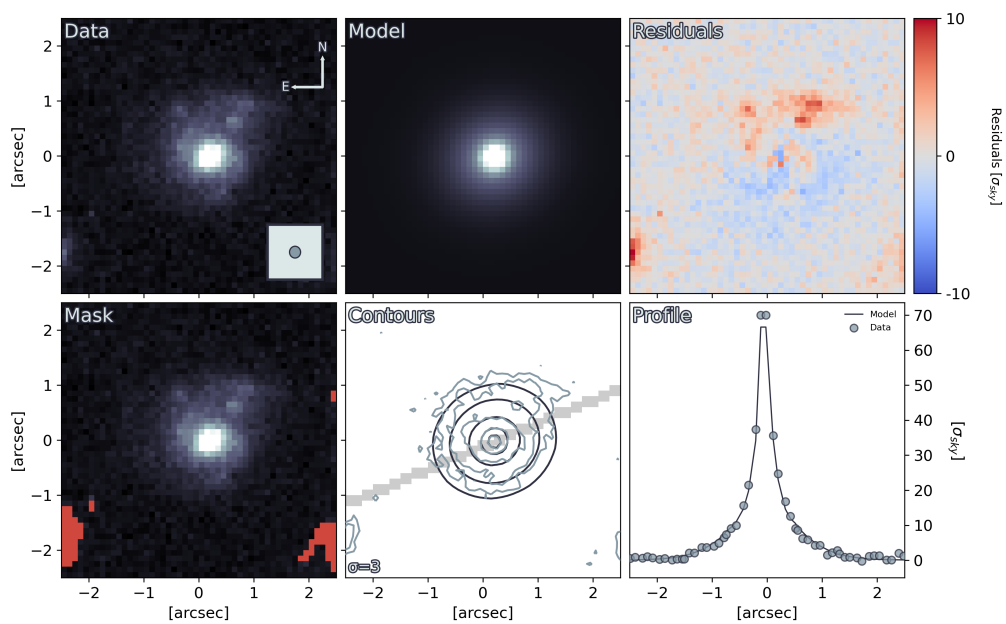


Figure C.40: The results of fitting source 11 with GALFIT. **Data**: A cutout of the source. The colour scale for the *Data*, *Model* and *Mask* panels are defined from this map, using a linear scale. The direction towards celestial north and east are displayed by the arrows. The fitted FWHM of the PSF is displayed in the inset in the bottom right. **Mask**: Masked out sources and dead pixels are displayed in red. **Model**: The fitted model convolved with the PSF. **Contours**: Contours of the *Data* panel in blue. Contours of the *Model* panel in black. Contour levels start at the value annotated in the bottom left, and increase by a factor of two for each subsequent level. The shaded region indicates where the 1D profile was extracted from. **Residuals**: The *Data* subtracted by the *Model*. **Profile**: A one-dimensional profile extracted along the semi-major axis of the *Model*.

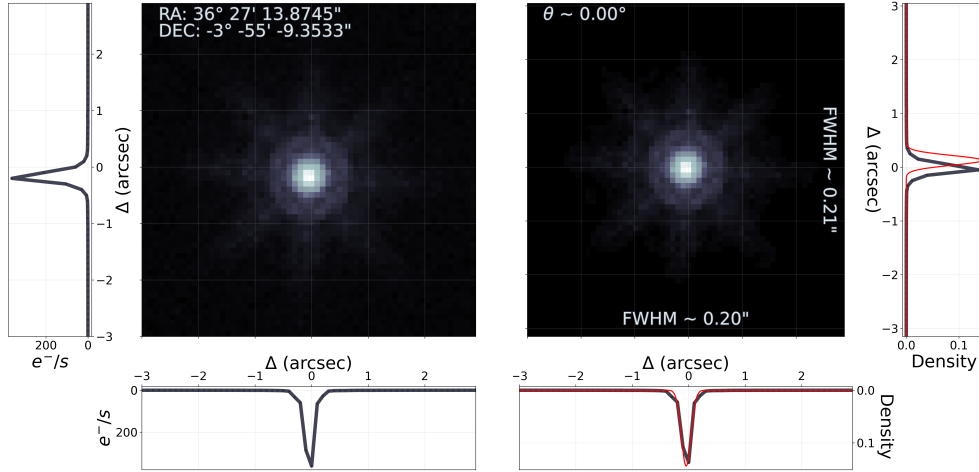


Figure C.41: From point-source to PSF. **Left:** The map displays the source used to create the PSF, for the mosaic containing source 11, in a logarithmic colour scale. The left and bottom panels shows the profile through the pixel of the highest value. The annotated coordinates are the coordinates of the centre of the map. **Right:** The map displays the PSF created from the left figure. The annotated FWHM along each axis are calculated by fitting a two-dimensional Gaussian to the map. The right and bottom panel shows the profile through the highest value pixel in black and the profile of the fitted two-dimensional Gaussian in red. The annotated angle describes the position angle of the fitted two-dimensional Gaussian counterclockwise from the positive x-axis.

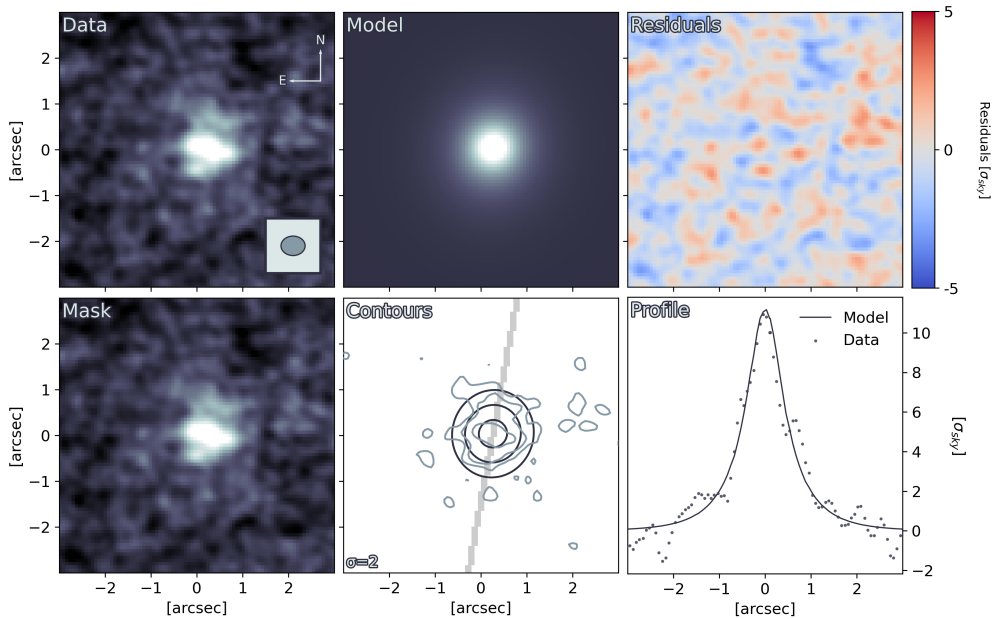


Figure C.42: The results of fitting the CO(2-1) ALMA map for source 11 with GALFIT. **Data:** A cutout of the source. The colour scale for the *Data*, *Model* and *Mask* panels are defined from this map, using a linear scale. The direction towards celestial north and east are displayed by the arrows. The FWHM of the synthetic beam is displayed in the inset on the lower right. **Mask:** Masked out sources and dead pixels are displayed in red. **Model:** The fitted model convolved with the PSF. **Contours:** Contours of the *Data* panel in blue. Contours of the *Model* panel in black. Contour levels start at the value annotated in the bottom left, and increase by a factor of two for each subsequent level. The shaded region indicates where the 1D profile was extracted from. **Residuals:** The *Data* subtracted by the *Model*. **Profile:** A one-dimensional profile extracted along the semi-major axis of the *Model*.

Source 12

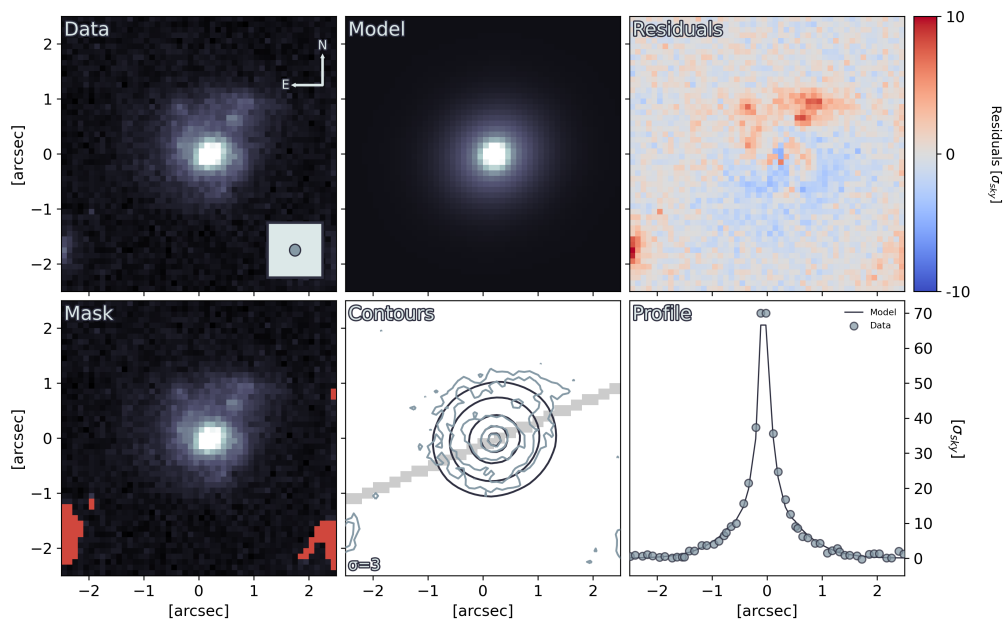


Figure C.43: The results of fitting source 12 with GALFIT. **Data**: A cutout of the source. The colour scale for the *Data*, *Model* and *Mask* panels are defined from this map, using a linear scale. The direction towards celestial north and east are displayed by the arrows. The fitted FWHM of the PSF is displayed in the inset in the bottom right. **Mask**: Masked out sources and dead pixels are displayed in red. **Model**: The fitted model convolved with the PSF. **Contours**: Contours of the *Data* panel in blue. Contours of the *Model* panel in black. Contour levels start at the value annotated in the bottom left, and increase by a factor of two for each subsequent level. The shaded region indicates where the 1D profile was extracted from. **Residuals**: The *Data* subtracted by the *Model*. **Profile**: A one-dimensional profile extracted along the semi-major axis of the *Model*.

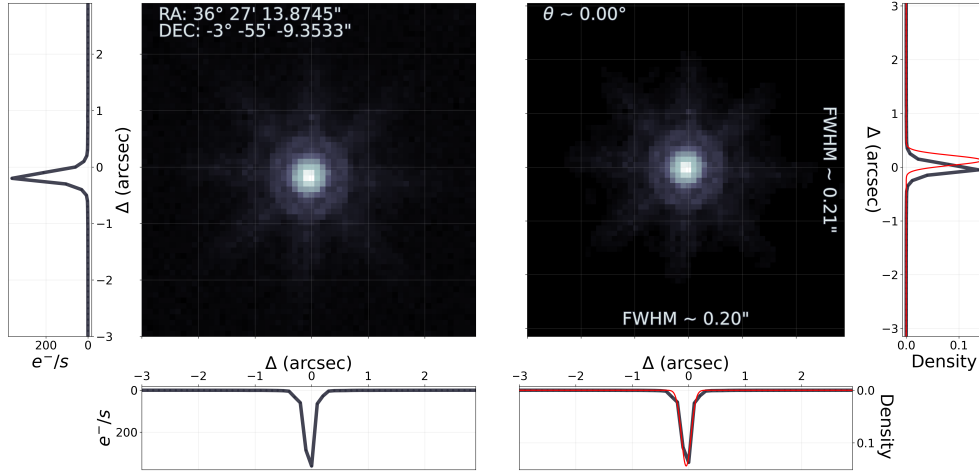


Figure C.44: From point-source to PSF. **Left**: The map displays the source used to create the PSF, for the mosaic containing source 12, in a logarithmic colour scale. The left and bottom panels shows the profile through the pixel of the highest value. The annotated coordinates are the coordinates of the centre of the map. **Right**: The map displays the PSF created from the left figure. The annotated FWHM along each axis are calculated by fitting a two-dimensional Gaussian to the map. The right and bottom panel shows the profile through the highest value pixel in black and the profile of the fitted two-dimensional Gaussian in red. The annotated angle describes the position angle of the fitted two-dimensional Gaussian counterclockwise from the positive x-axis.

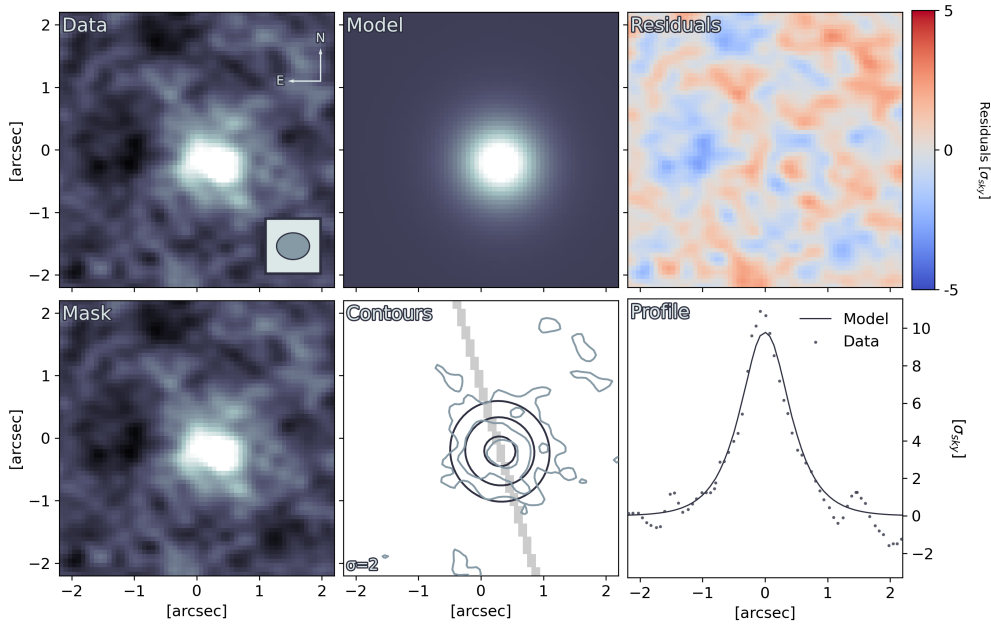


Figure C.45: The results of fitting the CO(2-1) ALMA map for source 12 with GALFIT. **Data**: A cutout of the source. The colour scale for the *Data*, *Model* and *Mask* panels are defined from this map, using a linear scale. The direction towards celestial north and east are displayed by the arrows. The FWHM of the synthetic beam is displayed in the inset on the lower right. **Mask**: Masked out sources and dead pixels are displayed in red. **Model**: The fitted model convolved with the PSF. **Contours**: Contours of the *Data* panel in blue. Contours of the *Model* panel in black. Contour levels start at the value annotated in the bottom left, and increase by a factor of two for each subsequent level. The shaded region indicates where the 1D profile was extracted from. **Residuals**: The *Data* subtracted by the *Model*. **Profile**: A one-dimensional profile extracted along the semi-major axis of the *Model*.

Source 13

Table C.11: Photometric data collected for source 13. The observation column lists the facility, instrument and filter used to make the observation. The code column connects the filter transmission curve with the correct one in Stardust. The reference column lists references to the works from which the observations were collected. Observations without an uncertainty corresponds to 3σ upper limits.

Observation	Flux [Jy]		Uncertainty [Jy]		Code	Reference
	Value	Order	Value	Order		
CFHT/MegaCam/u*	8.941	10^{-7}	8.919	10^{-9}	352	Weaver et al. 2022
CFHT/MegaCam/u	8.982	10^{-7}	1.666	10^{-8}	353	Weaver et al. 2022
Subaru/HSC/g	1.004	10^{-6}	1.710	10^{-8}	314	Weaver et al. 2022
Subaru/HSC/r	1.466	10^{-6}	2.036	10^{-8}	315	Weaver et al. 2022
Subaru/HSC/i	2.467	10^{-6}	2.374	10^{-8}	316	Weaver et al. 2022
Subaru/HSC/z	3.828	10^{-6}	3.531	10^{-8}	317	Weaver et al. 2022
Subaru/HSC/y	4.522	10^{-6}	5.003	10^{-8}	318	Weaver et al. 2022
VISTA/VIRCAM/Y	4.839	10^{-6}	4.342	10^{-8}	256	Weaver et al. 2022
VISTA/VIRCAM/J	6.973	10^{-6}	5.209	10^{-8}	257	Weaver et al. 2022
VISTA/VIRCAM/H	1.070	10^{-5}	7.614	10^{-8}	258	Weaver et al. 2022
VISTA/VIRCAM/Ks	1.767	10^{-5}	1.082	10^{-7}	259	Weaver et al. 2022
Subaru/Suprime-Cam/IB427	6.964	10^{-7}	8.466	10^{-8}	181	Weaver et al. 2022
Subaru/Suprime-Cam/IB464	9.642	10^{-7}	1.252	10^{-7}	183	Weaver et al. 2022
Subaru/Suprime-Cam/IA484	9.773	10^{-7}	5.644	10^{-8}	184	Weaver et al. 2022
Subaru/Suprime-Cam/IB505	1.051	10^{-6}	7.359	10^{-8}	185	Weaver et al. 2022
Subaru/Suprime-Cam/IA527	1.091	10^{-6}	5.998	10^{-8}	186	Weaver et al. 2022
Subaru/Suprime-Cam/IB574	1.209	10^{-6}	1.061	10^{-7}	188	Weaver et al. 2022
Subaru/Suprime-Cam/IA624	1.393	10^{-6}	5.910	10^{-8}	190	Weaver et al. 2022
Subaru/Suprime-Cam/IA679	1.517	10^{-6}	1.025	10^{-7}	192	Weaver et al. 2022
Subaru/Suprime-Cam/IB709	1.699	10^{-6}	9.177	10^{-8}	193	Weaver et al. 2022
Subaru/Suprime-Cam/IA738	1.881	10^{-6}	8.436	10^{-8}	194	Weaver et al. 2022
Subaru/Suprime-Cam/IA767	2.574	10^{-6}	1.368	10^{-7}	195	Weaver et al. 2022
Subaru/Suprime-Cam/IB827	3.234	10^{-6}	1.226	10^{-7}	197	Weaver et al. 2022
Subaru/Suprime-Cam/NB711	1.655	10^{-6}	1.292	10^{-7}	322	Weaver et al. 2022
Subaru/Suprime-Cam/NB816	2.869	10^{-6}	1.150	10^{-7}	319	Weaver et al. 2022
VISTA/VIRCAM/NB118	6.454	10^{-6}	2.042	10^{-7}	321	Weaver et al. 2022
Subaru/Suprime-Cam/B	8.747	10^{-7}	1.809	10^{-8}	114	Weaver et al. 2022
Subaru/Suprime-Cam/V	1.130	10^{-6}	3.825	10^{-8}	115	Weaver et al. 2022
Subaru/Suprime-Cam/r+	1.445	10^{-6}	3.550	10^{-8}	116	Weaver et al. 2022
Subaru/Suprime-Cam/i+	2.304	10^{-6}	3.838	10^{-8}	117	Weaver et al. 2022
Subaru/Suprime-Cam/z++	3.638	10^{-6}	1.741	10^{-7}	118	Weaver et al. 2022
Spitzer/IRAC/ch1	4.161	10^{-5}	5.050	10^{-8}	18	Weaver et al. 2022
Spitzer/IRAC/ch2	5.196	10^{-5}	6.986	10^{-8}	19	Weaver et al. 2022
GALEX/GALEX/FUV	8.737	10^{-8}	4.294	10^{-8}	120	Weaver et al. 2022
GALEX/GALEX/NUV	9.846	10^{-8}	5.923	10^{-8}	121	Weaver et al. 2022
SPITZER/MIPS/24	5.023	10^{-4}	5.153	10^{-5}	325	Jin et al. 2018
JCMT/SCUBA2/850GHz	4.120	10^{-3}	1.099	10^{-3}	324	Jin et al. 2018
VLA/3GHz	2.990	10^{-5}	2.600	10^{-6}		Jin et al. 2018
VLA/1.5GHz	2.747	10^{-5}	1.302	10^{-5}		Jin et al. 2018
Meerkat/1.3GHz	5.995	10^{-5}				Jin et al. 2018
VLA/3GHz	2.990	10^{-5}	2.600	10^{-6}		Smolčić et al. 2017
ALMA/1.3mm	8.920	10^{-4}	1.000	10^{-4}		Zavala et al. 2019
IRAC/ch3	6.350	10^{-5}	5.590	10^{-6}	20	Nayyeri et al. 2017
IRAC/ch4	3.490	10^{-5}	6.090	10^{-6}	21	Nayyeri et al. 2017

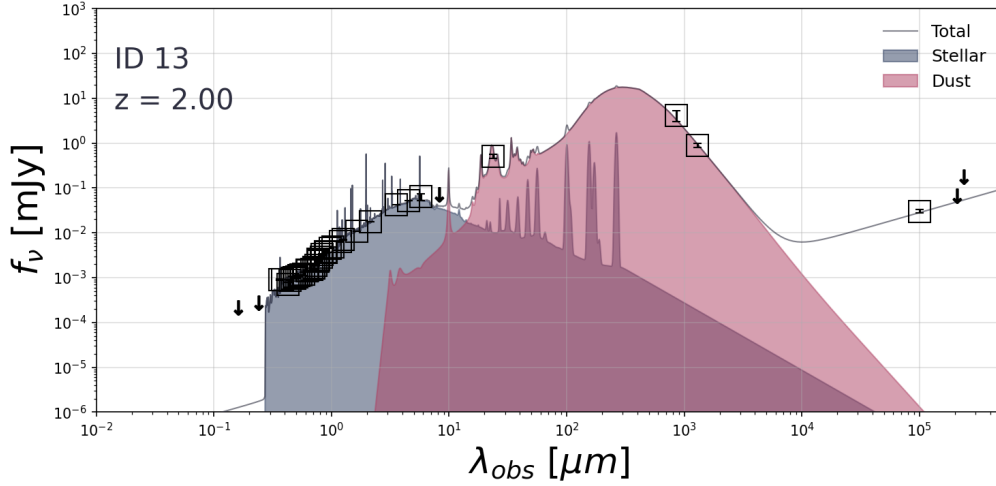


Figure C.46: The SED of source 13 as fitted with STARDUST, assuming that there's no significant AGN contribution. The squares are marked around observations with a SNR > 3. Arrows indicate 3σ upper limits of observations with SNR < 3 or non-detections.

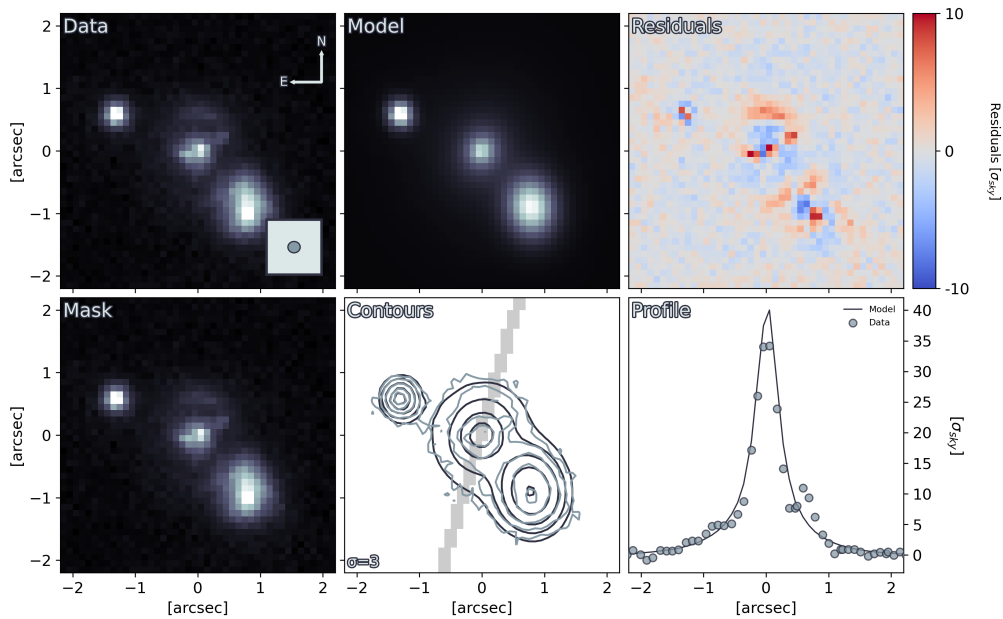


Figure C.47: The results of fitting source 13 with GALFIT. **Data**: A cutout of the source. The colour scale for the *Data*, *Model* and *Mask* panels are defined from this map, using a linear scale. The direction towards celestial north and east are displayed by the arrows. The fitted FWHM of the PSF is displayed in the inset in the bottom right. **Mask**: Masked out sources and dead pixels are displayed in red. **Model**: The fitted model convolved with the PSF. **Contours**: Contours of the *Data* panel in blue. Contours of the *Model* panel in black. Contour levels start at the value annotated in the bottom left, and increase by a factor of two for each subsequent level. The shaded region indicates where the 1D profile was extracted from. **Residuals**: The *Data* subtracted by the *Model*. **Profile**: A one-dimensional profile extracted along the semi-major axis of the *Model*.

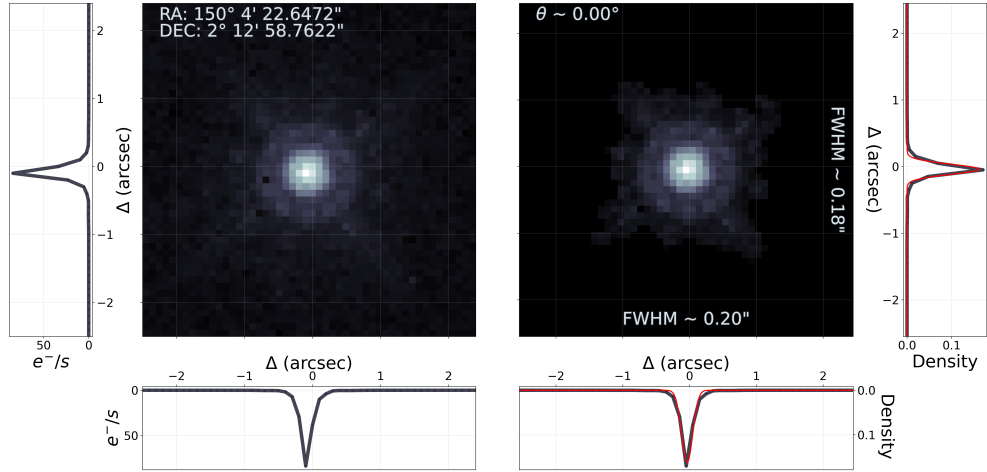


Figure C.48: From point-source to PSF. **Left:** The map displays the source used to create the PSF, for the mosaic containing source 13, in a logarithmic colour scale. The left and bottom panels shows the profile through the pixel of the highest value. The annotated coordinates are the coordinates of the centre of the map. **Right:** The map displays the PSF created from the left figure. The annotated FWHM along each axis are calculated by fitting a two-dimensional Gaussian to the map. The right and bottom panel shows the profile through the highest value pixel in black and the profile of the fitted two-dimensional Gaussian in red. The annotated angle describes the position angle of the fitted two-dimensional Gaussian counterclockwise from the positive x-axis.

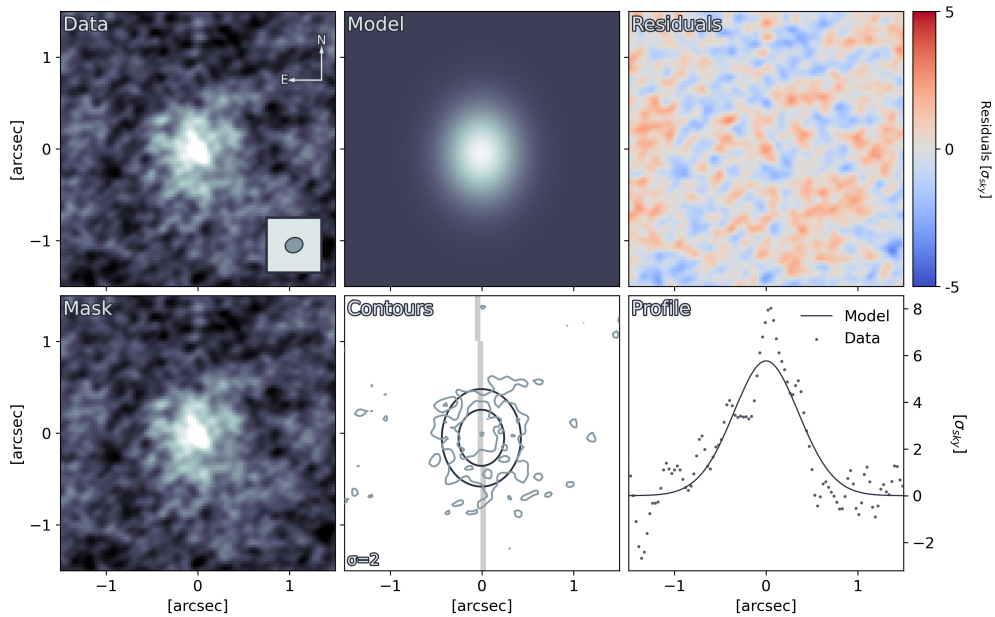


Figure C.49: The results of fitting the [CI](2-1) ALMA map for source 13 with GALFIT. **Data:** A cutout of the source. The colour scale for the *Data*, *Model* and *Mask* panels are defined from this map, using a linear scale. The direction towards celestial north and east are displayed by the arrows. The FWHM of the synthetic beam is displayed in the inset on the lower right. **Mask:** Masked out sources and dead pixels are displayed in red. **Model:** The fitted model convolved with the PSF. **Contours:** Contours of the *Data* panel in blue. Contours of the *Model* panel in black. Contour levels start at the value annotated in the bottom left, and increase by a factor of two for each subsequent level. The shaded region indicates where the 1D profile was extracted from. **Residuals:** The *Data* subtracted by the *Model*. **Profile:** A one-dimensional profile extracted along the semi-major axis of the *Model*.

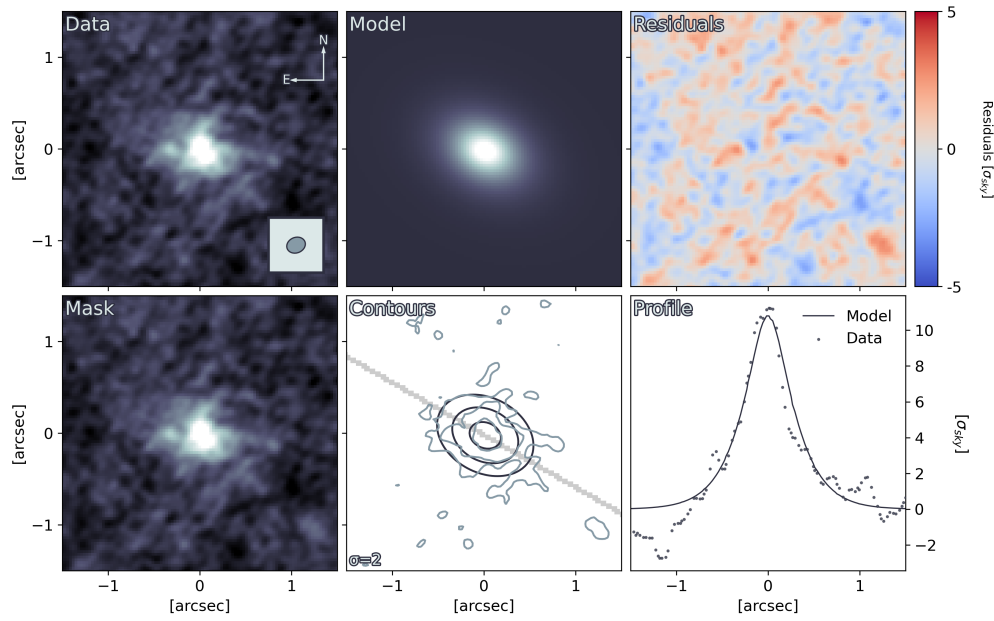


Figure C.50: The results of fitting the dust continuum ALMA map for source 13 with GALFIT. **Data**: A cutout of the source. The colour scale for the *Data*, *Model* and *Mask* panels are defined from this map, using a linear scale. The direction towards celestial north and east are displayed by the arrows. The FWHM of the synthetic beam is displayed in the inset on the lower right. **Mask**: Masked out sources and dead pixels are displayed in red. **Model**: The fitted model convolved with the PSF. **Contours**: Contours of the *Data* panel in blue. Contours of the *Model* panel in black. Contour levels start at the value annotated in the bottom left, and increase by a factor of two for each subsequent level. The shaded region indicates where the 1D profile was extracted from. **Residuals**: The *Data* subtracted by the *Model*. **Profile**: A one-dimensional profile extracted along the semi-major axis of the *Model*.

Source 14

Table C.12: Photometric data collected for source 14. The observation column lists the facility, instrument and filter used to make the observation. The code column connects the filter transmission curve with the correct one in Stardust. The reference column lists references to the works from which the observations were collected. Observations without an uncertainty corresponds to 3σ upper limits.

Observation	Flux [Jy]		Uncertainty [Jy]		Code	Reference
	Value	Order	Value	Order		
IRAM/PdBI/150GHz	4.100	10^{-4}	9.000	10^{-5}		Brisbin et al. 2019
IRAM/PdBI/250GHz	2.390	10^{-3}	3.100	10^{-4}		Brisbin et al. 2019
HST/NICMOS2/F160W	5.432	10^{-6}	3.002	10^{-7}	110	Schreiber et al. 2011
Palomar/WIRC/Ks	1.380	10^{-5}	2.672	10^{-7}	359	Erb et al. 2006
Palomar/WIRC/J	4.089	10^{-6}	1.365	10^{-7}	358	Erb et al. 2006
SPITZER/MIPS/24	5.610	10^{-4}	1.400	10^{-5}	325	Spitzer Science Center (SSC) and Infrared Science Archive (IRSA) 2021
SPITZER/IRAC/4.5	3.060	10^{-5}	4.000	10^{-7}	19	Spitzer Science Center (SSC) and Infrared Science Archive (IRSA) 2021
WISE/band-1	1.640	10^{-5}	2.100	10^{-6}	244	Marocco et al. 2021
WISE/band-2	2.630	10^{-5}	4.000	10^{-6}	245	Marocco et al. 2021

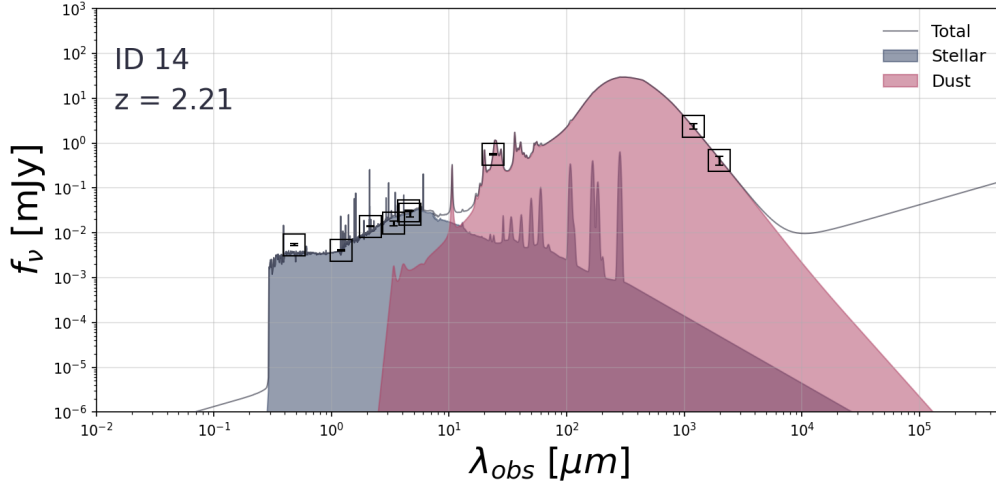


Figure C.51: The SED of source 14 as fitted with STARDUST, assuming that there's no significant AGN contribution. The squares are marked around observations with a SNR > 3. Arrows indicate 3σ upper limits of observations with SNR < 3 or non-detections.

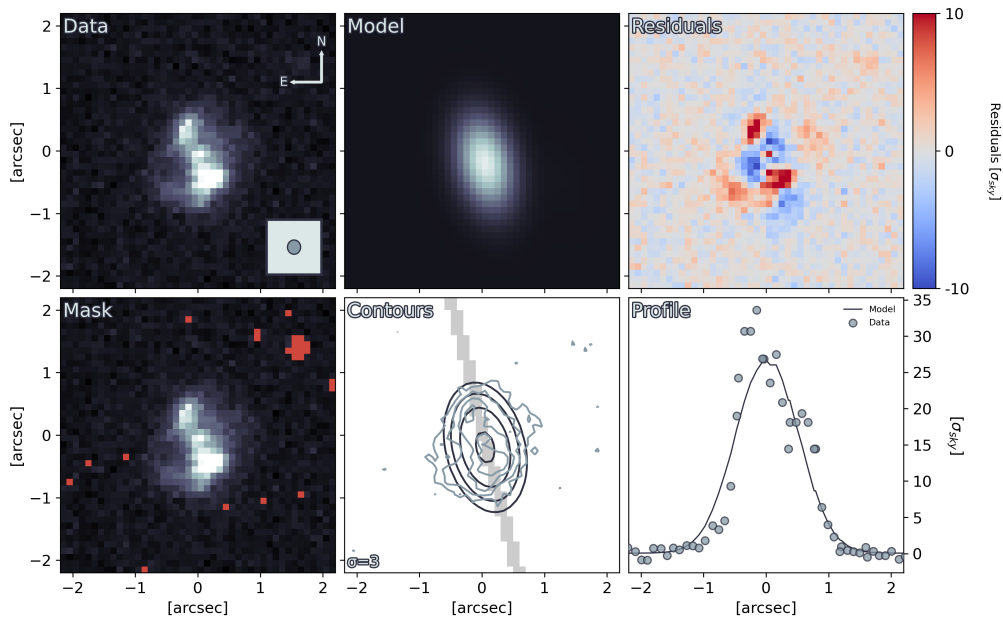


Figure C.52: The results of fitting source 14 with GALFIT. **Data**: A cutout of the source. The colour scale for the *Data*, *Model* and *Mask* panels are defined from this map, using a linear scale. The direction towards celestial north and east are displayed by the arrows. The fitted FWHM of the PSF is displayed in the inset in the bottom right. **Mask**: Masked out sources and dead pixels are displayed in red. **Model**: The fitted model convolved with the PSF. **Contours**: Contours of the *Data* panel in blue. Contours of the *Model* panel in black. Contour levels start at the value annotated in the bottom left, and increase by a factor of two for each subsequent level. The shaded region indicates where the 1D profile was extracted from. **Residuals**: The *Data* subtracted by the *Model*. **Profile**: A one-dimensional profile extracted along the semi-major axis of the *Model*.

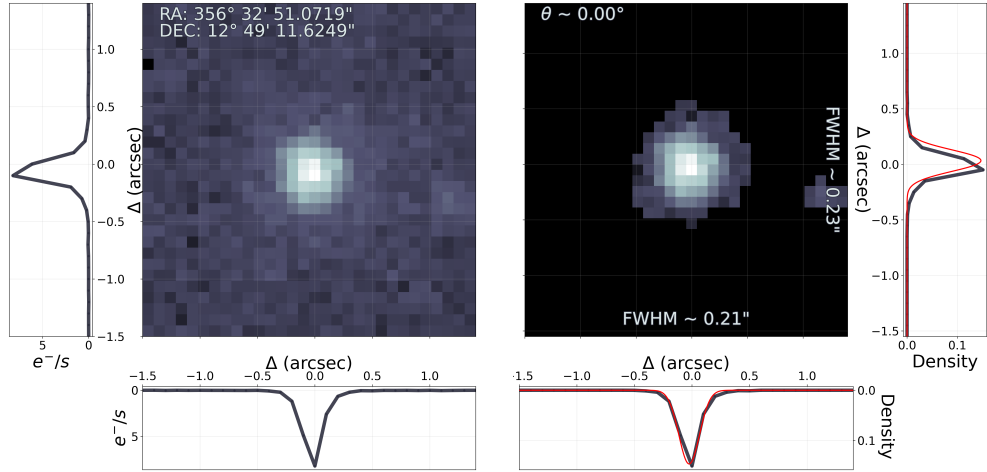


Figure C.53: From point-source to PSF. **Left:** The map displays the source used to create the PSF, for the mosaic containing source 14, in a logarithmic colour scale. The left and bottom panels shows the profile through the pixel of the highest value. The annotated coordinates are the coordinates of the centre of the map. **Right:** The map displays the PSF created from the left figure. The annotated FWHM along each axis are calculated by fitting a two-dimensional Gaussian to the map. The right and bottom panel shows the profile through the highest value pixel in black and the profile of the fitted two-dimensional Gaussian in red. The annotated angle describes the position angle of the fitted two-dimensional Gaussian counterclockwise from the positive x-axis.

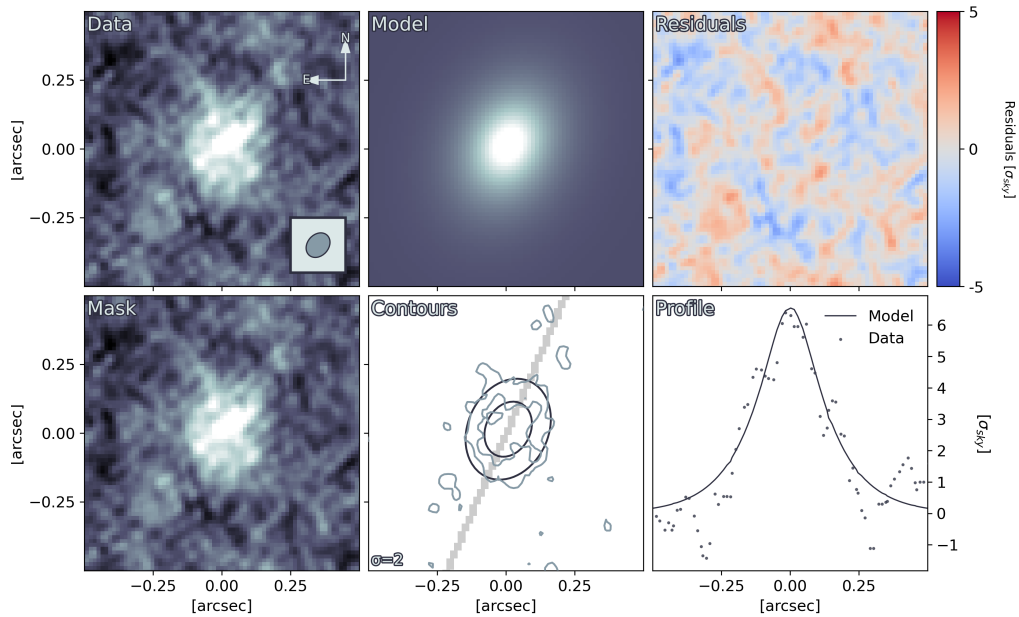


Figure C.54: The results of fitting the [CI](1-0) ALMA map for source 14 with GALFIT. **Data:** A cutout of the source. The colour scale for the *Data*, *Model* and *Mask* panels are defined from this map, using a linear scale. The direction towards celestial north and east are displayed by the arrows. The FWHM of the synthetic beam is displayed in the inset on the lower right. **Mask:** Masked out sources and dead pixels are displayed in red. **Model:** The fitted model convolved with the PSF. **Contours:** Contours of the *Data* panel in blue. Contours of the *Model* panel in black. Contour levels start at the value annotated in the bottom left, and increase by a factor of two for each subsequent level. The shaded region indicates where the 1D profile was extracted from. **Residuals:** The *Data* subtracted by the *Model*. **Profile:** A one-dimensional profile extracted along the semi-major axis of the *Model*.

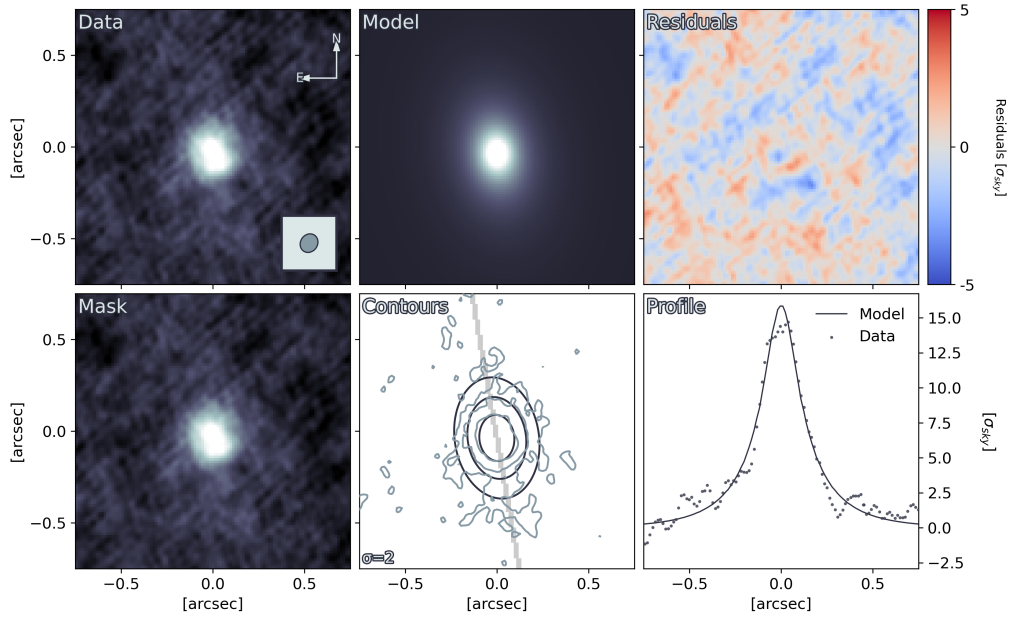


Figure C.55: The results of fitting the CO(4-3) ALMA map for source 14 with GALFIT. **Data**: A cutout of the source. The colour scale for the *Data*, *Model* and *Mask* panels are defined from this map, using a linear scale. The direction towards celestial north and east are displayed by the arrows. The FWHM of the synthetic beam is displayed in the inset on the lower right. **Mask**: Masked out sources and dead pixels are displayed in red. **Model**: The fitted model convolved with the PSF. **Contours**: Contours of the *Data* panel in blue. Contours of the *Model* panel in black. Contour levels start at the value annotated in the bottom left, and increase by a factor of two for each subsequent level. The shaded region indicates where the 1D profile was extracted from. **Residuals**: The *Data* subtracted by the *Model*. **Profile**: A one-dimensional profile extracted along the semi-major axis of the *Model*.

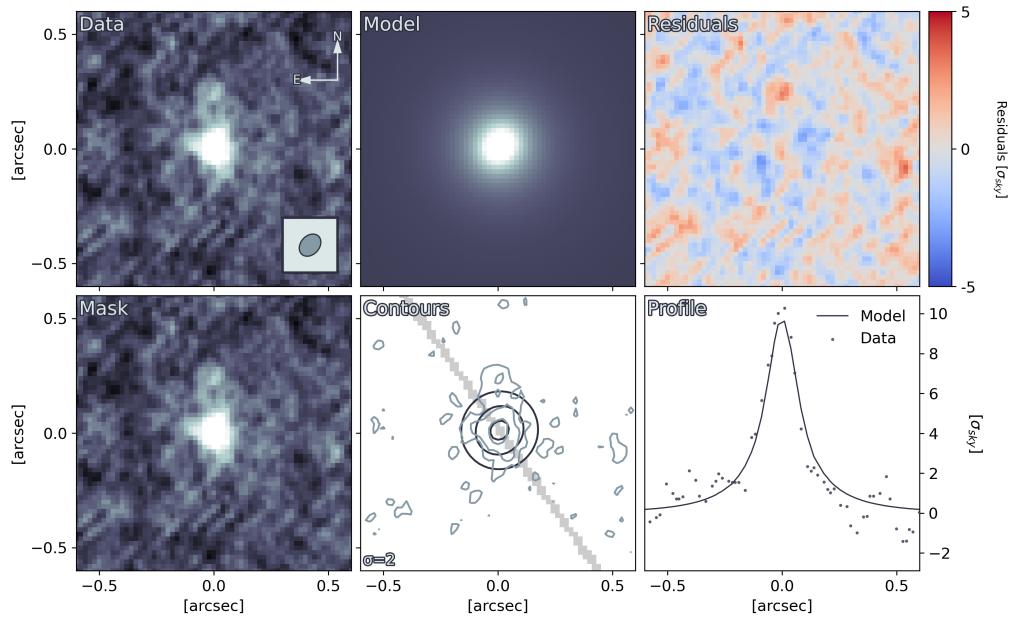


Figure C.56: The results of fitting the dust continuum ALMA map for source 14 with GALFIT. **Data**: A cutout of the source. The colour scale for the *Data*, *Model* and *Mask* panels are defined from this map, using a linear scale. The direction towards celestial north and east are displayed by the arrows. The FWHM of the synthetic beam is displayed in the inset on the lower right. **Mask**: Masked out sources and dead pixels are displayed in red. **Model**: The fitted model convolved with the PSF. **Contours**: Contours of the *Data* panel in blue. Contours of the *Model* panel in black. Contour levels start at the value annotated in the bottom left, and increase by a factor of two for each subsequent level. The shaded region indicates where the 1D profile was extracted from. **Residuals**: The *Data* subtracted by the *Model*. **Profile**: A one-dimensional profile extracted along the semi-major axis of the *Model*.

Source 15

Table C.13: Photometric data collected for source 15. The observation column lists the facility, instrument and filter used to make the observation. The code column connects the filter transmission curve with the correct one in Stardust. The reference column lists references to the works from which the observations were collected. Observations without an uncertainty corresponds to 3σ upper limits.

Observation	Flux [Jy]		Uncertainty [Jy]		Code	Reference
	Value	Order	Value	Order		
WHT/LIRIS/Ks	2.250	10^{-5}	3.400	10^{-6}	355	Fu et al. 2013
GALEX/NUV/0.23um	5.000	10^{-7}			121	Fu et al. 2013
CFHT/u*	2.000	10^{-7}			352	Fu et al. 2013
CFHT/g	2.000	10^{-7}			74	Fu et al. 2013
CFHT/r	2.000	10^{-7}	1.000	10^{-7}	75	Fu et al. 2013
CFHT/i	5.000	10^{-7}			76	Fu et al. 2013
CFHT/z	6.000	10^{-7}	3.000	10^{-7}	77	Fu et al. 2013
HST/wfc3/F110W/1.16um	1.600	10^{-6}	2.000	10^{-7}	241	Fu et al. 2013
WHT/LIRIS/J	1.700	10^{-6}	5.000	10^{-7}	354	Fu et al. 2013
WHT/LIRIS/Ks	7.600	10^{-6}	2.000	10^{-6}	355	Fu et al. 2013
Spitzer/IRAC/3.6	2.220	10^{-5}	5.000	10^{-6}	18	Fu et al. 2013
Spitzer/IRAC/4.5	2.940	10^{-5}	5.000	10^{-6}	19	Fu et al. 2013
Spitzer/IRAC/5.8	5.150	10^{-5}	6.800	10^{-6}	20	Fu et al. 2013
Spitzer/IRAC/8.0	4.110	10^{-5}	6.700	10^{-6}	21	Fu et al. 2013
SMA/880um	9.300	10^{-3}	1.200	10^{-3}		Fu et al. 2013
VLA/1.4GHz	4.200	10^{-4}				Fu et al. 2013

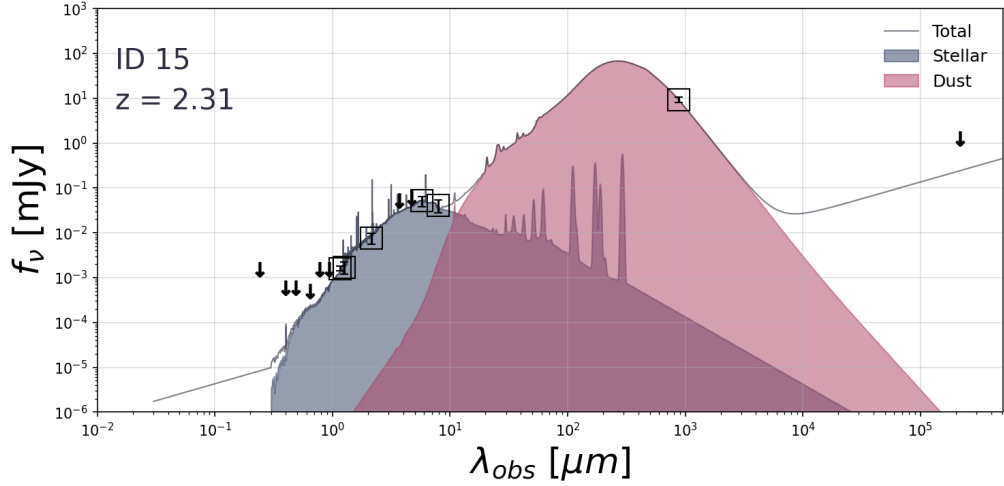


Figure C.57: The SED of source 15 as fitted with STARDUST, assuming that there's no significant AGN contribution. The squares are marked around observations with a $\text{SNR} > 3$. Arrows indicate 3σ upper limits of observations with $\text{SNR} < 3$ or non-detections.

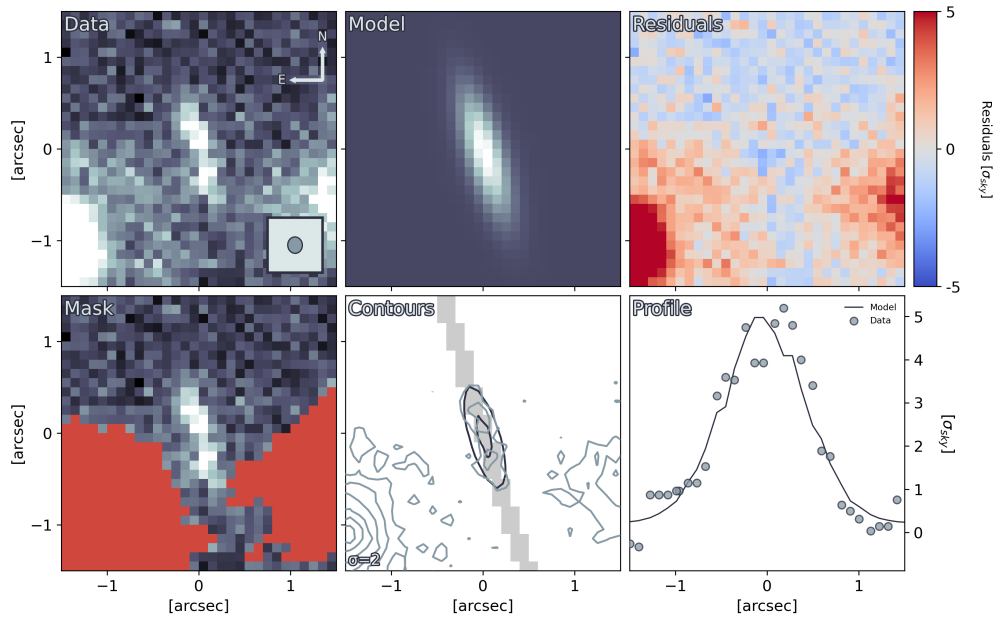


Figure C.58: The results of fitting source 15 with GALFIT. **Data**: A cutout of the source. The colour scale for the *Data*, *Model* and *Mask* panels are defined from this map, using a linear scale. The direction towards celestial north and east are displayed by the arrows. The fitted FWHM of the PSF is displayed in the inset in the bottom right. **Mask**: Masked out sources and dead pixels are displayed in red. **Model**: The fitted model convolved with the PSF. **Contours**: Contours of the *Data* panel in blue. Contours of the *Model* panel in black. Contour levels start at the value annotated in the bottom left, and increase by a factor of two for each subsequent level. The shaded region indicates where the 1D profile was extracted from. **Residuals**: The *Data* subtracted by the *Model*. **Profile**: A one-dimensional profile extracted along the semi-major axis of the *Model*.

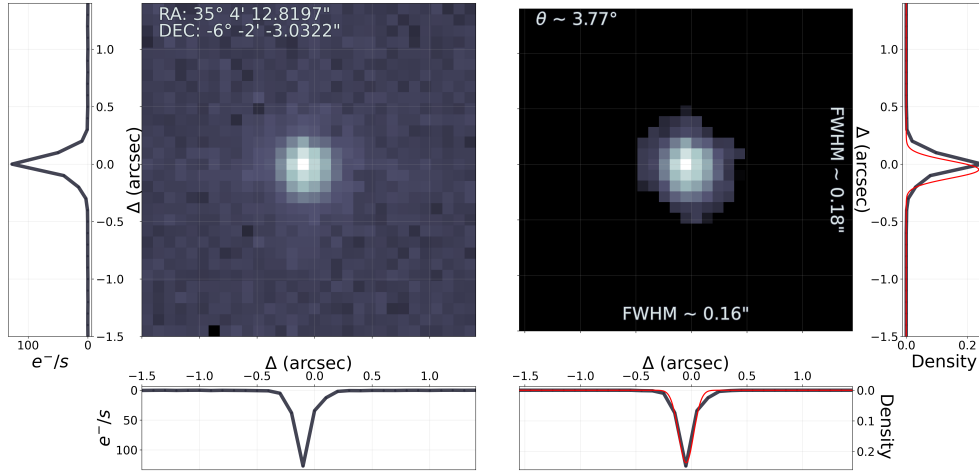


Figure C.59: From point-source to PSF. **Left:** The map displays the source used to create the PSF, for the mosaic containing source 15, in a logarithmic colour scale. The left and bottom panels shows the profile through the pixel of the highest value. The annotated coordinates are the coordinates of the centre of the map. **Right:** The map displays the PSF created from the left figure. The annotated FWHM along each axis are calculated by fitting a two-dimensional Gaussian to the map. The right and bottom panel shows the profile through the highest value pixel in black and the profile of the fitted two-dimensional Gaussian in red. The annotated angle describes the position angle of the fitted two-dimensional Gaussian counterclockwise from the positive x-axis.

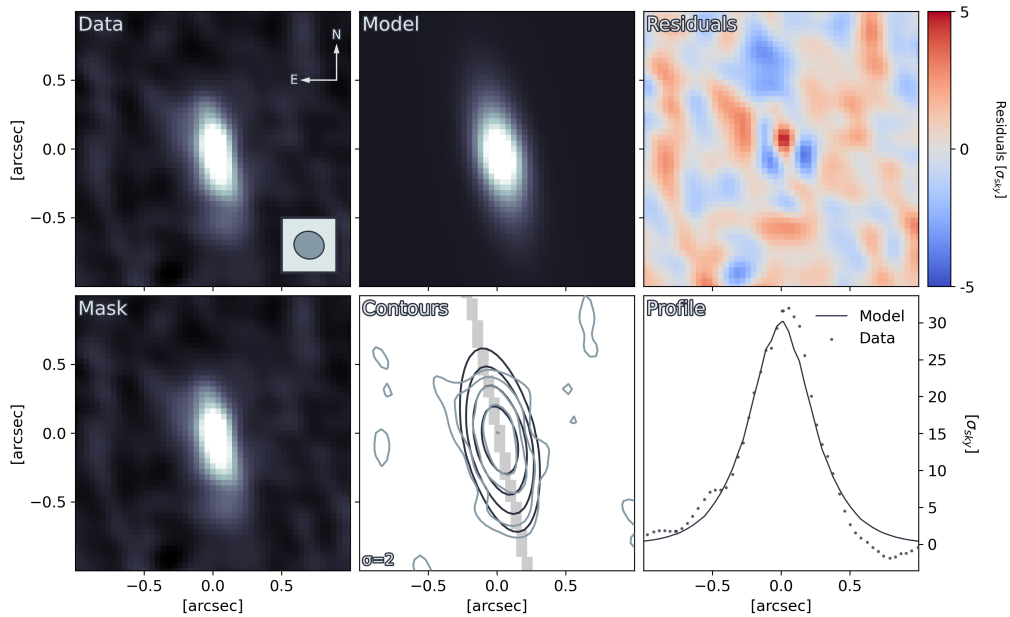


Figure C.60: The results of fitting the [CI](2-1) ALMA map for source 15 with GALFIT. **Data:** A cutout of the source. The colour scale for the *Data*, *Model* and *Mask* panels are defined from this map, using a linear scale. The direction towards celestial north and east are displayed by the arrows. The FWHM of the synthetic beam is displayed in the inset on the lower right. **Mask:** Masked out sources and dead pixels are displayed in red. **Model:** The fitted model convolved with the PSF. **Contours:** Contours of the *Data* panel in blue. Contours of the *Model* panel in black. Contour levels start at the value annotated in the bottom left, and increase by a factor of two for each subsequent level. The shaded region indicates where the 1D profile was extracted from. **Residuals:** The *Data* subtracted by the *Model*. **Profile:** A one-dimensional profile extracted along the semi-major axis of the *Model*.

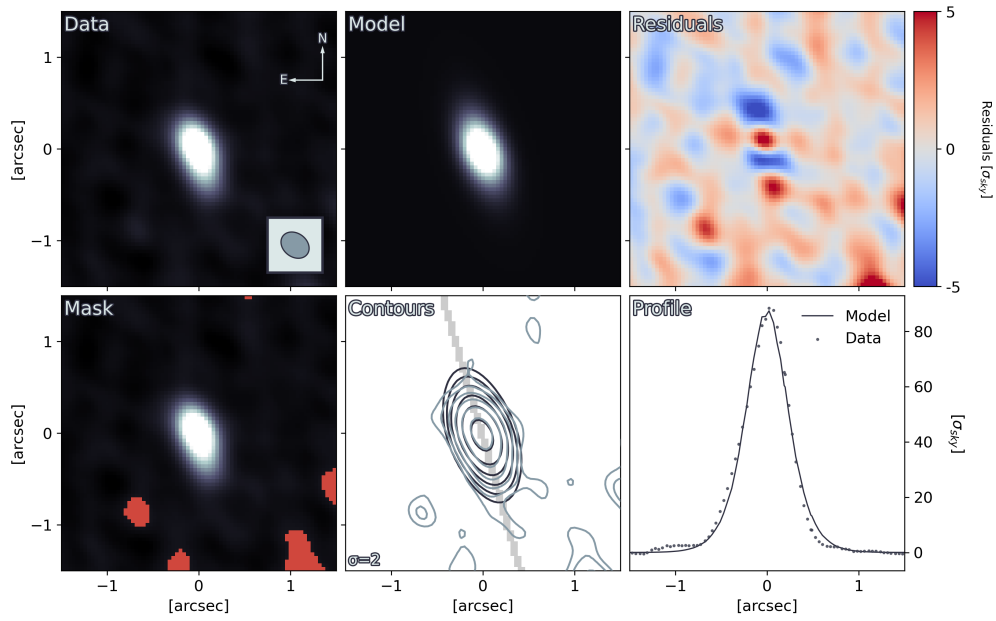


Figure C.61: The results of fitting the dust continuum ALMA map for source 15 with GALFIT. **Data**: A cutout of the source. The colour scale for the *Data*, *Model* and *Mask* panels are defined from this map, using a linear scale. The direction towards celestial north and east are displayed by the arrows. The FWHM of the synthetic beam is displayed in the inset on the lower right. **Mask**: Masked out sources and dead pixels are displayed in red. **Model**: The fitted model convolved with the PSF. **Contours**: Contours of the *Data* panel in blue. Contours of the *Model* panel in black. Contour levels start at the value annotated in the bottom left, and increase by a factor of two for each subsequent level. The shaded region indicates where the 1D profile was extracted from. **Residuals**: The *Data* subtracted by the *Model*. **Profile**: A one-dimensional profile extracted along the semi-major axis of the *Model*.

Source 16

Table C.14: Photometric data collected for source 16. The observation column lists the facility, instrument and filter used to make the observation. The code column connects the filter transmission curve with the correct one in Stardust. The reference column lists references to the works from which the observations were collected. Observations without an uncertainty corresponds to 3σ upper limits.

Observation	Flux [Jy]		Uncertainty [Jy]		Code	Reference
	Value	Order	Value	Order		
GALEX/NUV/0.23um	5.000	10^{-7}			121	Fu et al. 2013
CFHT/u*	5.000	10^{-7}	1.000	10^{-7}	352	Fu et al. 2013
CFHT/g	1.200	10^{-6}	1.000	10^{-7}	74	Fu et al. 2013
CFHT/r	2.100	10^{-6}	2.000	10^{-7}	75	Fu et al. 2013
CFHT/i	2.300	10^{-6}	3.000	10^{-7}	76	Fu et al. 2013
CFHT/z	3.200	10^{-6}	6.000	10^{-7}	77	Fu et al. 2013
HST/wfc3/F110W/1.16um	4.700	10^{-6}	3.000	10^{-7}	241	Fu et al. 2013
WHT/LIRIS/J	5.100	10^{-6}	6.000	10^{-7}	354	Fu et al. 2013
WHT/LIRIS/Ks	1.490	10^{-5}	2.700	10^{-6}	355	Fu et al. 2013
Spitzer/IRAC/3.6	2.640	10^{-5}	2.800	10^{-6}	18	Fu et al. 2013
Spitzer/IRAC/4.5	3.470	10^{-5}	2.900	10^{-6}	19	Fu et al. 2013
Spitzer/IRAC/5.8	6.040	10^{-5}	9.600	10^{-6}	20	Fu et al. 2013
Spitzer/IRAC/8.0	4.580	10^{-5}	1.060	10^{-5}	21	Fu et al. 2013
SMA/880um	8.300	10^{-3}	1.100	10^{-3}		Fu et al. 2013
VLA/1.4GHz	4.200	10^{-4}				Fu et al. 2013

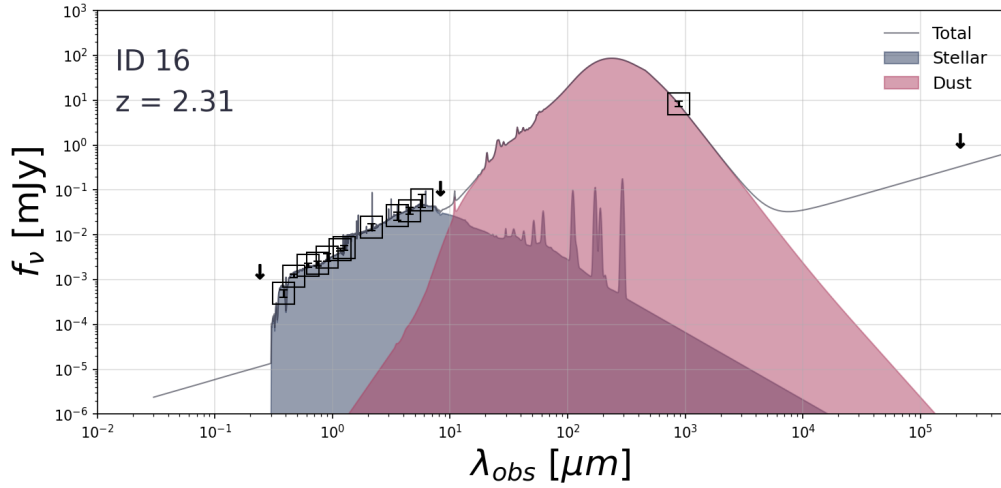


Figure C.62: The SED of source 16 as fitted with STARDUST, assuming that there's no significant AGN contribution. The squares are marked around observations with a $\text{SNR} > 3$. Arrows indicate 3σ upper limits of observations with $\text{SNR} < 3$ or non-detections.

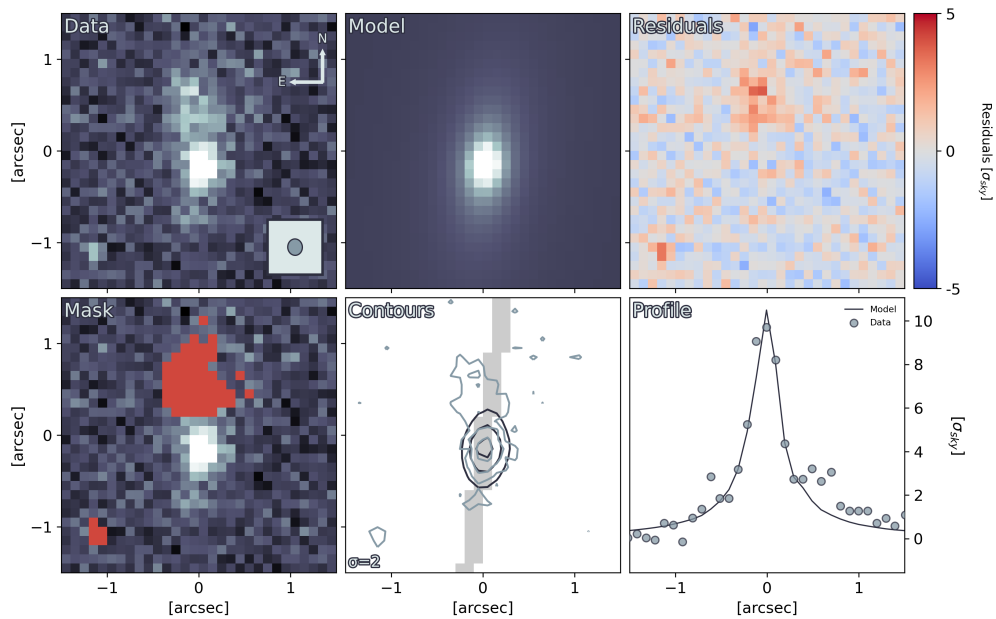


Figure C.63: The results of fitting source 16 with GALFIT. **Data**: A cutout of the source. The colour scale for the *Data*, *Model* and *Mask* panels are defined from this map, using a linear scale. The direction towards celestial north and east are displayed by the arrows. The fitted FWHM of the PSF is displayed in the inset in the bottom right. **Mask**: Masked out sources and dead pixels are displayed in red. **Model**: The fitted model convolved with the PSF. **Contours**: Contours of the *Data* panel in blue. Contours of the *Model* panel in black. Contour levels start at the value annotated in the bottom left, and increase by a factor of two for each subsequent level. The shaded region indicates where the 1D profile was extracted from. **Residuals**: The *Data* subtracted by the *Model*. **Profile**: A one-dimensional profile extracted along the semi-major axis of the *Model*.

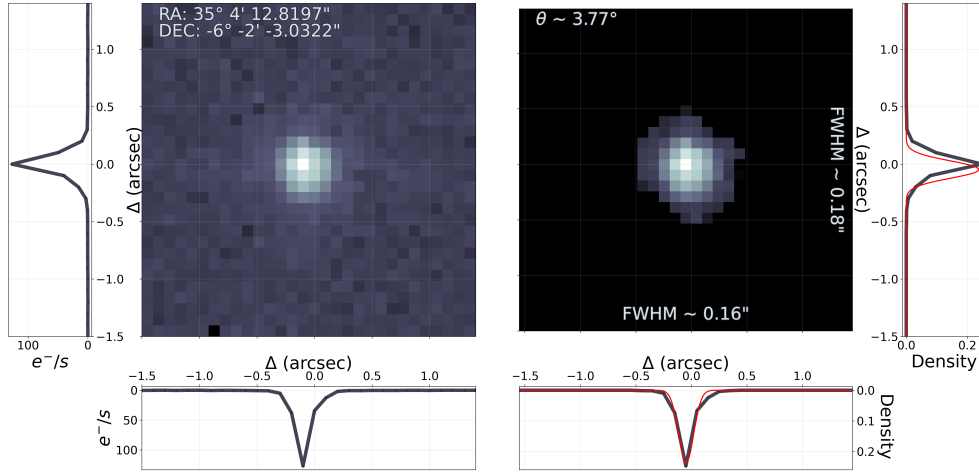


Figure C.64: From point-source to PSF. **Left:** The map displays the source used to create the PSF, for the mosaic containing source 16, in a logarithmic colour scale. The left and bottom panels shows the profile through the pixel of the highest value. The annotated coordinates are the coordinates of the centre of the map. **Right:** The map displays the PSF created from the left figure. The annotated FWHM along each axis are calculated by fitting a two-dimensional Gaussian to the map. The right and bottom panel shows the profile through the highest value pixel in black and the profile of the fitted two-dimensional Gaussian in red. The annotated angle describes the position angle of the fitted two-dimensional Gaussian counterclockwise from the positive x-axis.

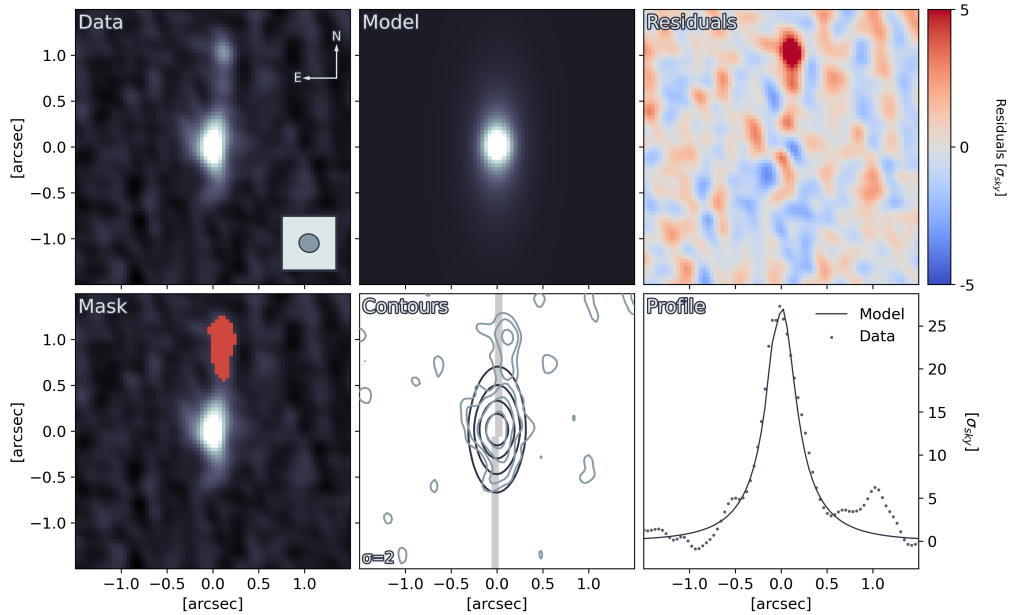


Figure C.65: The results of fitting the [CI](2-1) ALMA map for source 16 with GALFIT. **Data:** A cutout of the source. The colour scale for the *Data*, *Model* and *Mask* panels are defined from this map, using a linear scale. The direction towards celestial north and east are displayed by the arrows. The FWHM of the synthetic beam is displayed in the inset on the lower right. **Mask:** Masked out sources and dead pixels are displayed in red. **Model:** The fitted model convolved with the PSF. **Contours:** Contours of the *Data* panel in blue. Contours of the *Model* panel in black. Contour levels start at the value annotated in the bottom left, and increase by a factor of two for each subsequent level. The shaded region indicates where the 1D profile was extracted from. **Residuals:** The *Data* subtracted by the *Model*. **Profile:** A one-dimensional profile extracted along the semi-major axis of the *Model*.

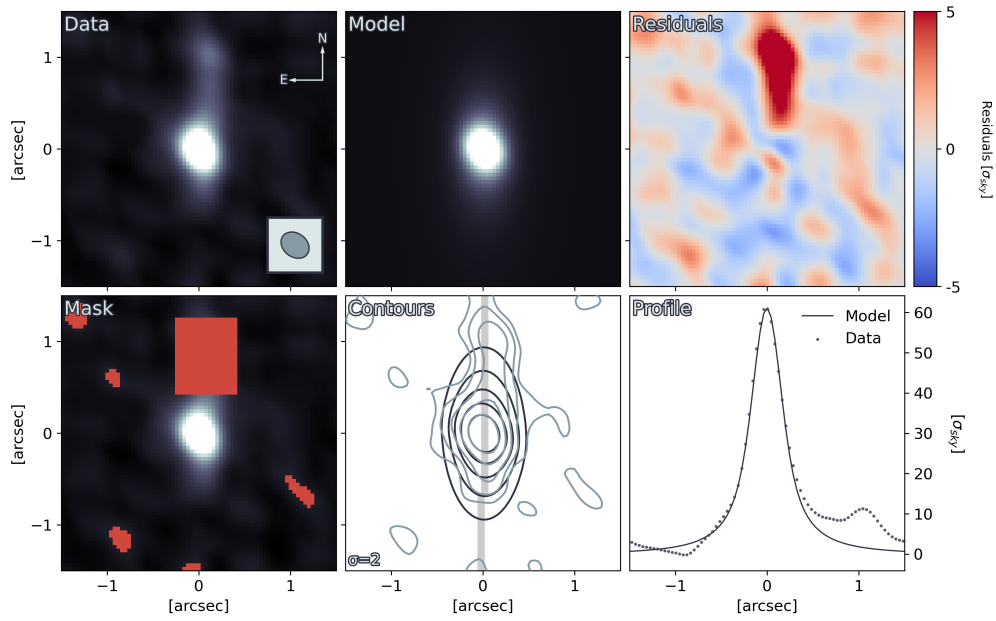


Figure C.66: The results of fitting the dust continuum ALMA map for source 16 with GALFIT. **Data**: A cutout of the source. The colour scale for the *Data*, *Model* and *Mask* panels are defined from this map, using a linear scale. The direction towards celestial north and east are displayed by the arrows. The FWHM of the synthetic beam is displayed in the inset on the lower right. **Mask**: Masked out sources and dead pixels are displayed in red. **Model**: The fitted model convolved with the PSF. **Contours**: Contours of the *Data* panel in blue. Contours of the *Model* panel in black. Contour levels start at the value annotated in the bottom left, and increase by a factor of two for each subsequent level. The shaded region indicates where the 1D profile was extracted from. **Residuals**: The *Data* subtracted by the *Model*. **Profile**: A one-dimensional profile extracted along the semi-major axis of the *Model*.

Source 17

Table C.15: Photometric data collected for source 17. The observation column lists the facility, instrument and filter used to make the observation. The code column connects the filter transmission curve with the correct one in Stardust. The reference column lists references to the works from which the observations were collected. Observations without an uncertainty corresponds to 3σ upper limits.

Observation	Flux [Jy]		Uncertainty [Jy]		Code	Reference
	Value	Order	Value	Order		
VISTA/Z	8.160	10^{-6}	1.370	10^{-6}	356	Ivison et al. 2013
VISTA/Y	1.050	10^{-5}	1.800	10^{-6}	256	Ivison et al. 2013
HST/wfc3/F110W	1.360	10^{-5}	2.300	10^{-6}	241	Ivison et al. 2013
VISTA/J	1.680	10^{-5}	2.800	10^{-6}	257	Ivison et al. 2013
VISTA/H	2.350	10^{-5}	4.000	10^{-6}	258	Ivison et al. 2013
VISTA/Ks	3.810	10^{-5}	6.400	10^{-6}	259	Ivison et al. 2013
IRAC/3.6	6.710	10^{-5}	1.860	10^{-5}	18	Ivison et al. 2013
IRAC/4.5	7.660	10^{-5}	2.010	10^{-5}	19	Ivison et al. 2013
Herschel/PACS/100	2.300	10^{-2}	7.000	10^{-3}	329	Ivison et al. 2013
Herschel/PACS/160	9.100	10^{-2}	1.200	10^{-2}	330	Ivison et al. 2013
SMA/870	2.500	10^{-2}	2.000	10^{-3}		Ivison et al. 2013
IRAM/PdBI/1360	8.300	10^{-3}	5.000	10^{-4}		Ivison et al. 2013
IRAM/PdBI/2210	1.100	10^{-3}	1.000	10^{-4}		Ivison et al. 2013
CARMA/3000	3.300	10^{-4}	1.400	10^{-4}		Ivison et al. 2013
JVLA/8800	4.300	10^{-5}	1.000	10^{-5}		Ivison et al. 2013
JVLA/59000	1.770	10^{-4}	1.500	10^{-5}		Ivison et al. 2013

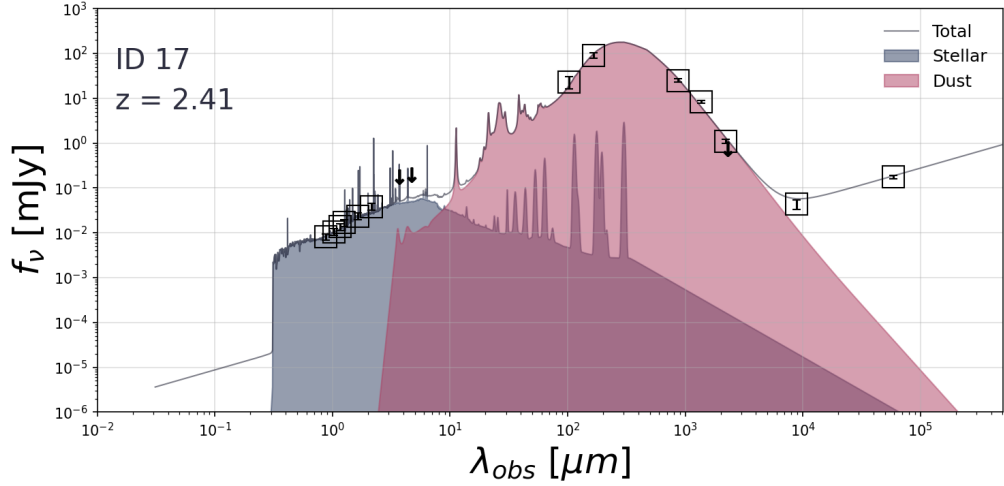


Figure C.67: The SED of source 17 as fitted with STARDUST, assuming that there's no significant AGN contribution. The squares are marked around observations with a $\text{SNR} > 3$. Arrows indicate 3σ upper limits of observations with $\text{SNR} < 3$ or non-detections.

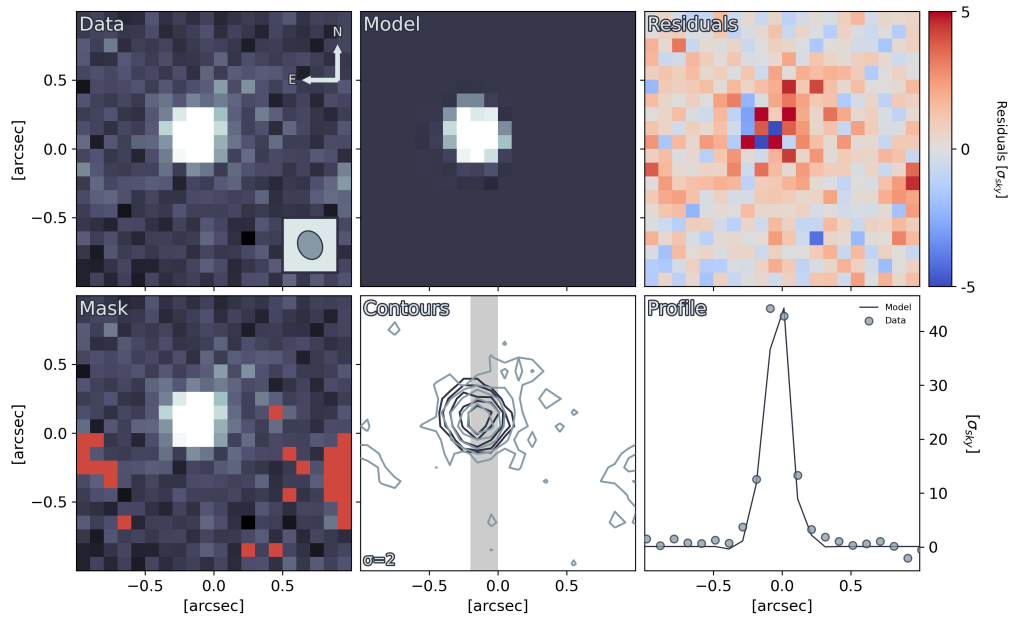


Figure C.68: The results of fitting source 17 with GALFIT. **Data**: A cutout of the source. The colour scale for the *Data*, *Model* and *Mask* panels are defined from this map, using a linear scale. The direction towards celestial north and east are displayed by the arrows. The fitted FWHM of the PSF is displayed in the inset in the bottom right. **Mask**: Masked out sources and dead pixels are displayed in red. **Model**: The fitted model convolved with the PSF. **Contours**: Contours of the *Data* panel in blue. Contours of the *Model* panel in black. Contour levels start at the value annotated in the bottom left, and increase by a factor of two for each subsequent level. The shaded region indicates where the 1D profile was extracted from. **Residuals**: The *Data* subtracted by the *Model*. **Profile**: A one-dimensional profile extracted along the semi-major axis of the *Model*.

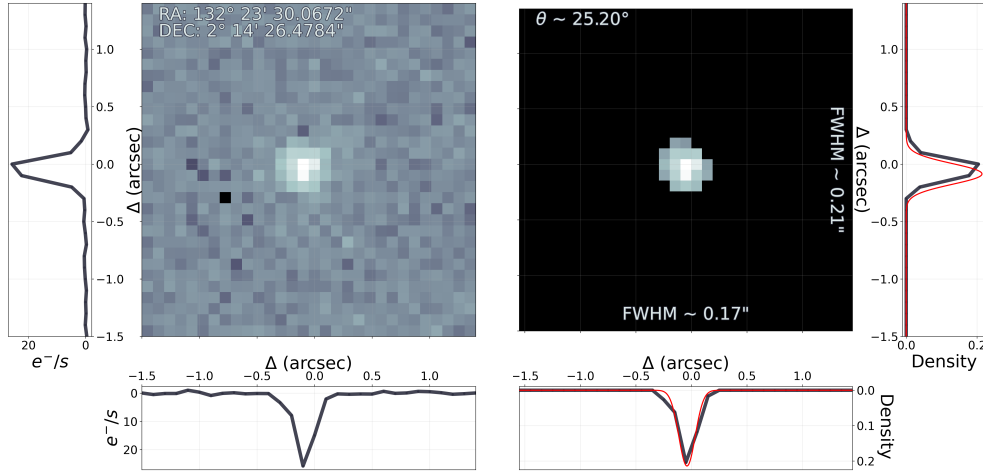


Figure C.69: From point-source to PSF. **Left:** The map displays the source used to create the PSF, for the mosaic containing source 17, in a logarithmic colour scale. The left and bottom panels shows the profile through the pixel of the highest value. The annotated coordinates are the coordinates of the centre of the map. **Right:** The map displays the PSF created from the left figure. The annotated FWHM along each axis are calculated by fitting a two-dimensional Gaussian to the map. The right and bottom panel shows the profile through the highest value pixel in black and the profile of the fitted two-dimensional Gaussian in red. The annotated angle describes the position angle of the fitted two-dimensional Gaussian counterclockwise from the positive x-axis.

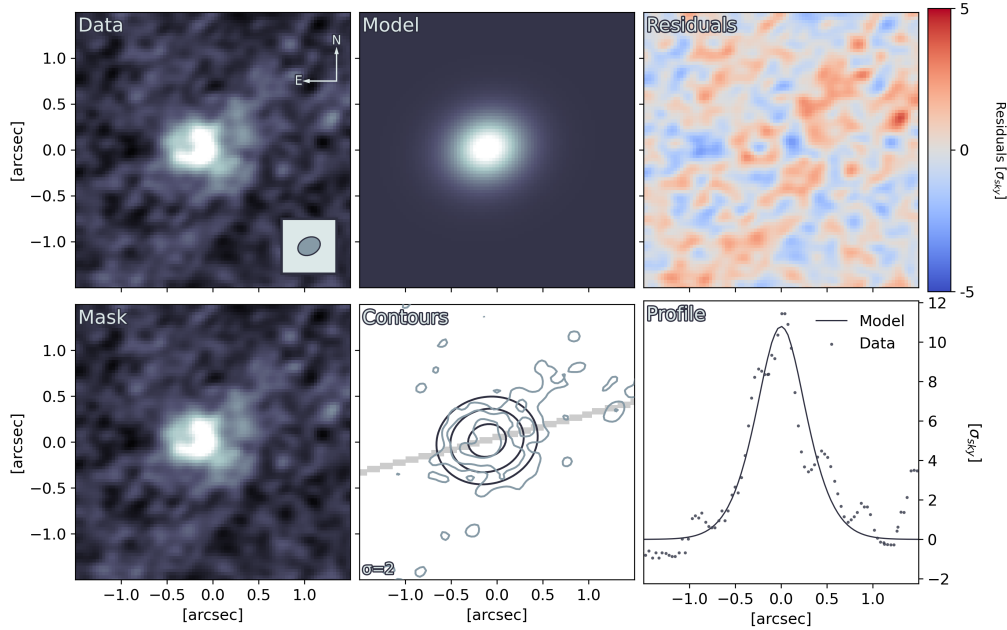


Figure C.70: The results of fitting the [CI](1-0) ALMA map for source 17 with GALFIT. **Data:** A cutout of the source. The colour scale for the *Data*, *Model* and *Mask* panels are defined from this map, using a linear scale. The direction towards celestial north and east are displayed by the arrows. The FWHM of the synthetic beam is displayed in the inset on the lower right. **Mask:** Masked out sources and dead pixels are displayed in red. **Model:** The fitted model convolved with the PSF. **Contours:** Contours of the *Data* panel in blue. Contours of the *Model* panel in black. Contour levels start at the value annotated in the bottom left, and increase by a factor of two for each subsequent level. The shaded region indicates where the 1D profile was extracted from. **Residuals:** The *Data* subtracted by the *Model*. **Profile:** A one-dimensional profile extracted along the semi-major axis of the *Model*.

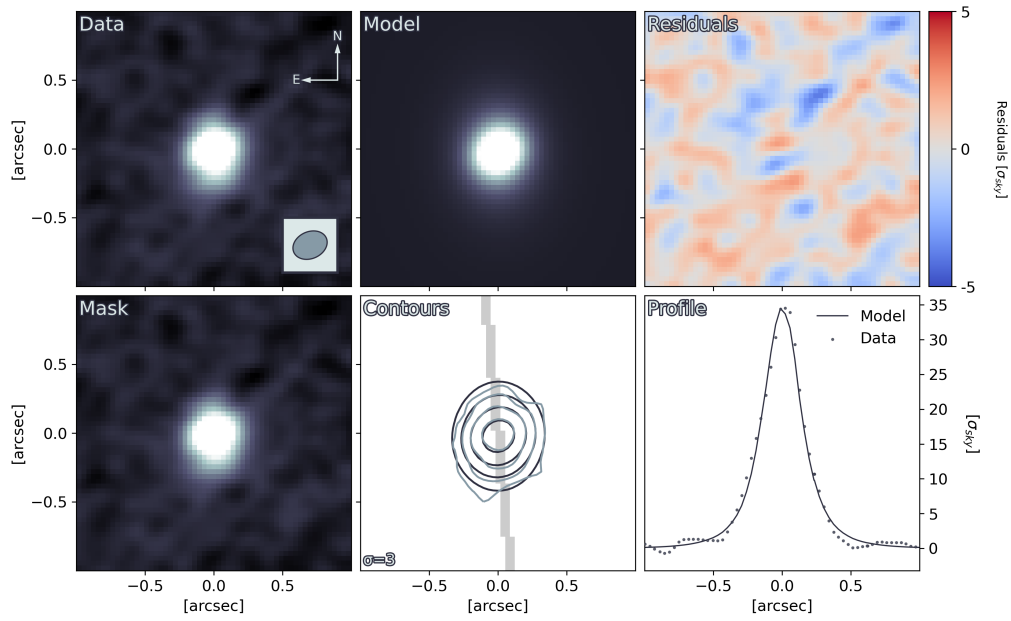


Figure C.71: The results of fitting the dust continuum ALMA map for source 17 with GALFIT. **Data**: A cutout of the source. The colour scale for the *Data*, *Model* and *Mask* panels are defined from this map, using a linear scale. The direction towards celestial north and east are displayed by the arrows. The FWHM of the synthetic beam is displayed in the inset on the lower right. **Mask**: Masked out sources and dead pixels are displayed in red. **Model**: The fitted model convolved with the PSF. **Contours**: Contours of the *Data* panel in blue. Contours of the *Model* panel in black. Contour levels start at the value annotated in the bottom left, and increase by a factor of two for each subsequent level. The shaded region indicates where the 1D profile was extracted from. **Residuals**: The *Data* subtracted by the *Model*. **Profile**: A one-dimensional profile extracted along the semi-major axis of the *Model*.

Source 18

Table C.16: Photometric data collected for source 18. The observation column lists the facility, instrument and filter used to make the observation. The code column connects the filter transmission curve with the correct one in Stardust. The reference column lists references to the works from which the observations were collected. Observations without an uncertainty corresponds to 3σ upper limits.

Observation	Flux [Jy]		Uncertainty [Jy]		Code	Reference
	Value	Order	Value	Order		
VISTA/Z	5.800	10^{-6}	9.800	10^{-7}	356	Ivison et al. 2013
VISTA/Y	8.650	10^{-6}	1.450	10^{-6}	256	Ivison et al. 2013
HST/wfc3/F110W	1.120	10^{-5}	1.900	10^{-6}	241	Ivison et al. 2013
VISTA/J	1.300	10^{-5}	2.200	10^{-6}	257	Ivison et al. 2013
VISTA/H	1.920	10^{-5}	3.200	10^{-6}	258	Ivison et al. 2013
VISTA/Ks	2.610	10^{-5}	4.400	10^{-6}	259	Ivison et al. 2013
IRAC/3.6	4.770	10^{-5}	1.740	10^{-5}	18	Ivison et al. 2013
IRAC/4.5	4.580	10^{-5}	1.520	10^{-5}	19	Ivison et al. 2013
Herschel/PACS/100	1.900	10^{-2}	7.000	10^{-3}	329	Ivison et al. 2013
Herschel/PACS/160	4.000	10^{-2}	1.200	10^{-2}	330	Ivison et al. 2013
SMA/870	1.900	10^{-2}	2.000	10^{-3}		Ivison et al. 2013
IRAM/PdBI/1360	7.500	10^{-3}	5.000	10^{-4}		Ivison et al. 2013
IRAM/PdBI/2210	8.000	10^{-4}	1.000	10^{-4}		Ivison et al. 2013
CARMA/3000	4.200	10^{-4}				Ivison et al. 2013
JVLA/8800	3.000	10^{-5}				Ivison et al. 2013
JVLA/59000	6.500	10^{-5}	1.500	10^{-5}		Ivison et al. 2013

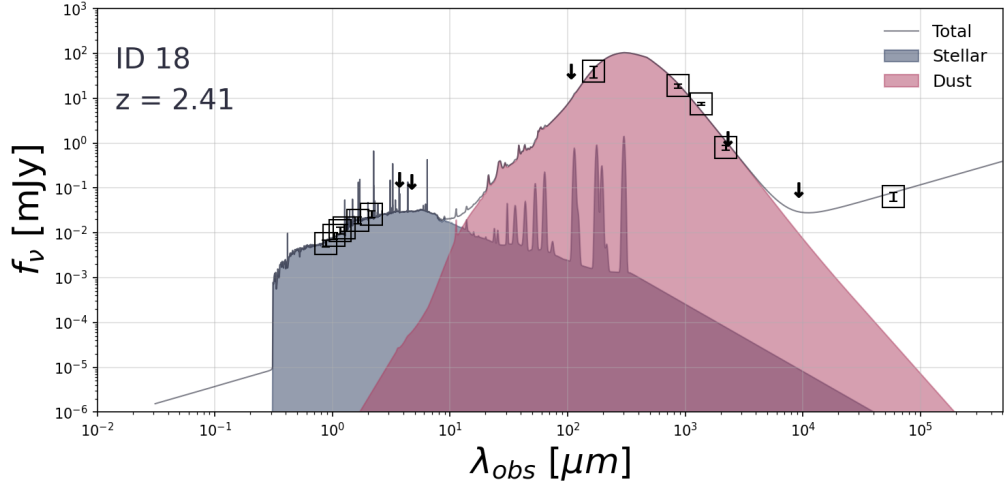


Figure C.72: The SED of source 18 as fitted with STARDUST, assuming that there's no significant AGN contribution. The squares are marked around observations with a $\text{SNR} > 3$. Arrows indicate 3σ upper limits of observations with $\text{SNR} < 3$ or non-detections.

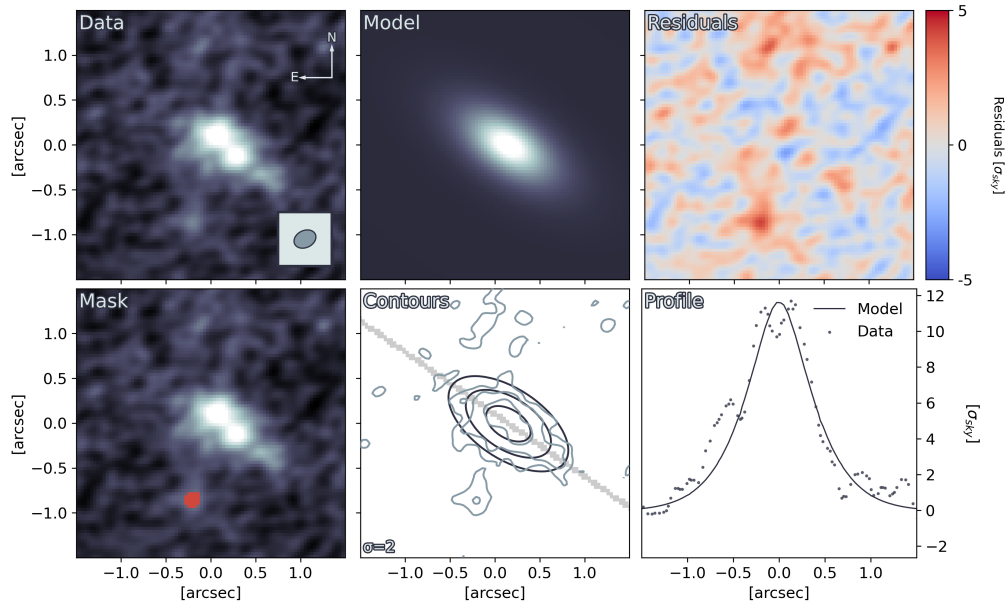


Figure C.73: The results of fitting the $[\text{CI}](1-0)$ ALMA map for source 18 with GALFIT. **Data**: A cutout of the source. The colour scale for the *Data*, *Model* and *Mask* panels are defined from this map, using a linear scale. The direction towards celestial north and east are displayed by the arrows. The FWHM of the synthetic beam is displayed in the inset on the lower right. **Mask**: Masked out sources and dead pixels are displayed in red. **Model**: The fitted model convolved with the PSF. **Contours**: Contours of the *Data* panel in blue. Contours of the *Model* panel in black. Contour levels start at the value annotated in the bottom left, and increase by a factor of two for each subsequent level. The shaded region indicates where the 1D profile was extracted from. **Residuals**: The *Data* subtracted by the *Model*. **Profile**: A one-dimensional profile extracted along the semi-major axis of the *Model*.

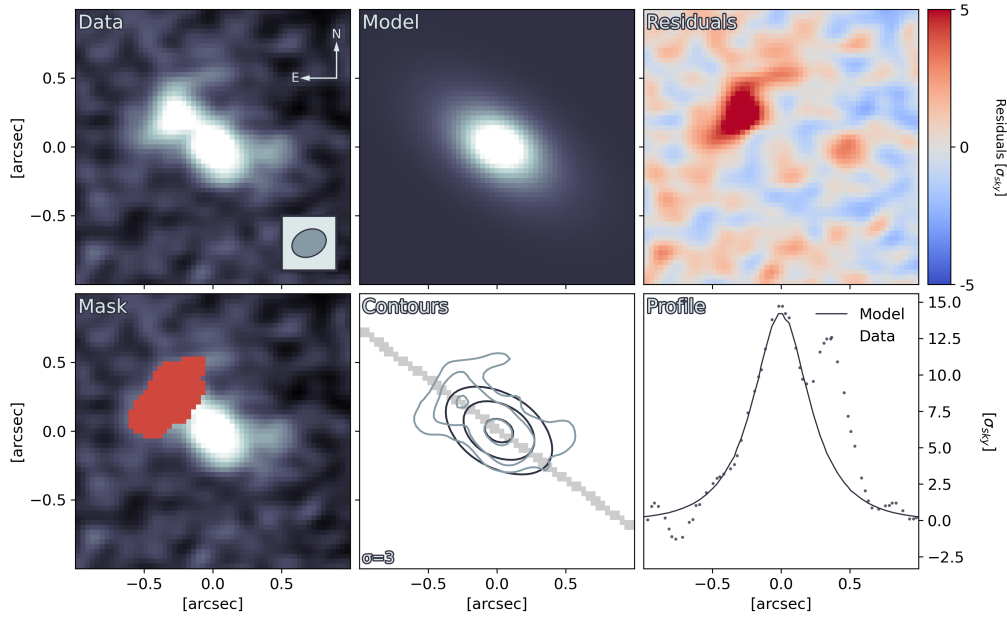


Figure C.74: The results of fitting the dust continuum ALMA map for source 18 with GALFIT. **Data**: A cutout of the source. The colour scale for the *Data*, *Model* and *Mask* panels are defined from this map, using a linear scale. The direction towards celestial north and east are displayed by the arrows. The FWHM of the synthetic beam is displayed in the inset on the lower right. **Mask**: Masked out sources and dead pixels are displayed in red. **Model**: The fitted model convolved with the PSF. **Contours**: Contours of the *Data* panel in blue. Contours of the *Model* panel in black. Contour levels start at the value annotated in the bottom left, and increase by a factor of two for each subsequent level. The shaded region indicates where the 1D profile was extracted from. **Residuals**: The *Data* subtracted by the *Model*. **Profile**: A one-dimensional profile extracted along the semi-major axis of the *Model*.

Source 19

Table C.17: Photometric data collected for source 19. The observation column lists the facility, instrument and filter used to make the observation. The code column connects the filter transmission curve with the correct one in Stardust. The reference column lists references to the works from which the observations were collected. Observations without an uncertainty corresponds to 3σ upper limits.

Observation	Flux [Jy]		Uncertainty [Jy]		Code	Reference
	Value	Order	Value	Order		
CFHT/MegaCam/u*	4.008	10^{-7}	2.539	10^{-8}	352	Weaver et al. 2022
CFHT/MegaCam/u	3.358	10^{-7}	3.787	10^{-8}	353	Weaver et al. 2022
Subaru/HSC/g	5.262	10^{-7}	2.413	10^{-8}	314	Weaver et al. 2022
Subaru/HSC/r	8.510	10^{-7}	2.964	10^{-8}	315	Weaver et al. 2022
Subaru/HSC/i	1.120	10^{-6}	3.328	10^{-8}	316	Weaver et al. 2022
Subaru/HSC/z	1.544	10^{-6}	5.083	10^{-8}	317	Weaver et al. 2022
Subaru/HSC/y	3.469	10^{-6}	9.506	10^{-8}	318	Weaver et al. 2022
VISTA/VIRCAM/Y	1.960	10^{-6}	1.592	10^{-7}	256	Weaver et al. 2022
VISTA/VIRCAM/J	3.570	10^{-6}	1.907	10^{-7}	257	Weaver et al. 2022
VISTA/VIRCAM/H	6.972	10^{-6}	2.818	10^{-7}	258	Weaver et al. 2022
VISTA/VIRCAM/Ks	1.260	10^{-5}	2.833	10^{-7}	259	Weaver et al. 2022
Subaru/Suprime-Cam/IB427	4.909	10^{-7}	1.998	10^{-7}	181	Weaver et al. 2022
Subaru/Suprime-Cam/IA484	5.650	10^{-7}	1.355	10^{-7}	184	Weaver et al. 2022
Subaru/Suprime-Cam/IB505	3.482	10^{-7}	1.831	10^{-7}	185	Weaver et al. 2022
Subaru/Suprime-Cam/IA527	5.498	10^{-7}	1.495	10^{-7}	186	Weaver et al. 2022
Subaru/Suprime-Cam/IB574	8.166	10^{-7}	2.751	10^{-7}	188	Weaver et al. 2022
Subaru/Suprime-Cam/IA624	7.683	10^{-7}	1.565	10^{-7}	190	Weaver et al. 2022
Subaru/Suprime-Cam/IA679	5.951	10^{-7}	2.560	10^{-7}	192	Weaver et al. 2022
Subaru/Suprime-Cam/IB709	5.760	10^{-7}	2.320	10^{-7}	193	Weaver et al. 2022
Subaru/Suprime-Cam/IA738	1.140	10^{-6}	2.038	10^{-7}	194	Weaver et al. 2022
Subaru/Suprime-Cam/IA767	7.262	10^{-7}	3.181	10^{-7}	195	Weaver et al. 2022
Subaru/Suprime-Cam/IB827	1.302	10^{-6}	3.374	10^{-7}	197	Weaver et al. 2022
Subaru/Suprime-Cam/NB711	6.699	10^{-7}	3.614	10^{-7}	322	Weaver et al. 2022
Subaru/Suprime-Cam/NB816	1.295	10^{-6}	2.713	10^{-7}	319	Weaver et al. 2022
VISTA/VIRCAM/NB118	2.367	10^{-6}	7.762	10^{-7}	321	Weaver et al. 2022
Subaru/Suprime-Cam/B	4.203	10^{-7}	3.957	10^{-8}	114	Weaver et al. 2022
Subaru/Suprime-Cam/V	4.519	10^{-7}	8.931	10^{-8}	115	Weaver et al. 2022
Subaru/Suprime-Cam/r+	7.407	10^{-7}	8.517	10^{-8}	116	Weaver et al. 2022
Subaru/Suprime-Cam/i+	1.018	10^{-6}	1.389	10^{-7}	117	Weaver et al. 2022
Subaru/Suprime-Cam/z++	1.729	10^{-6}	4.195	10^{-7}	118	Weaver et al. 2022
Spitzer/IRAC/ch1	1.658	10^{-5}	1.086	10^{-7}	18	Weaver et al. 2022
SPITZER/MIPS/24	2.941	10^{-4}	3.243	10^{-5}	325	Jin et al. 2018
VLA/3GHz	3.950	10^{-5}	3.100	10^{-6}		Jin et al. 2018
VLA/1.5GHz	4.083	10^{-5}	7.486	10^{-6}		Jin et al. 2018
Meerkat/1.3GHz	2.198	10^{-4}				Jin et al. 2018
ALMA/870um	5.260	10^{-3}	2.600	10^{-4}		Bussmann et al. 2015

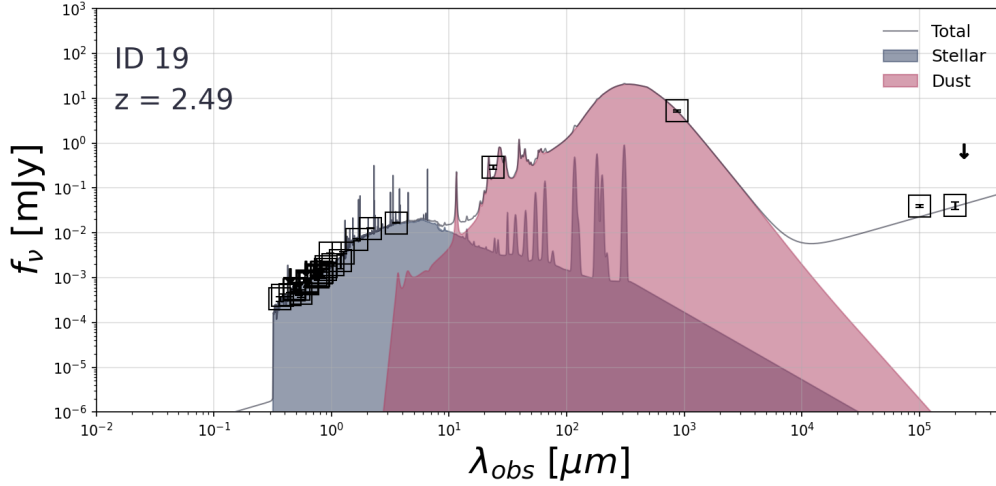


Figure C.75: The SED of source 19 as fitted with STARDUST, assuming that there's no significant AGN contribution. The squares are marked around observations with a SNR > 3. Arrows indicate 3σ upper limits of observations with SNR < 3 or non-detections.

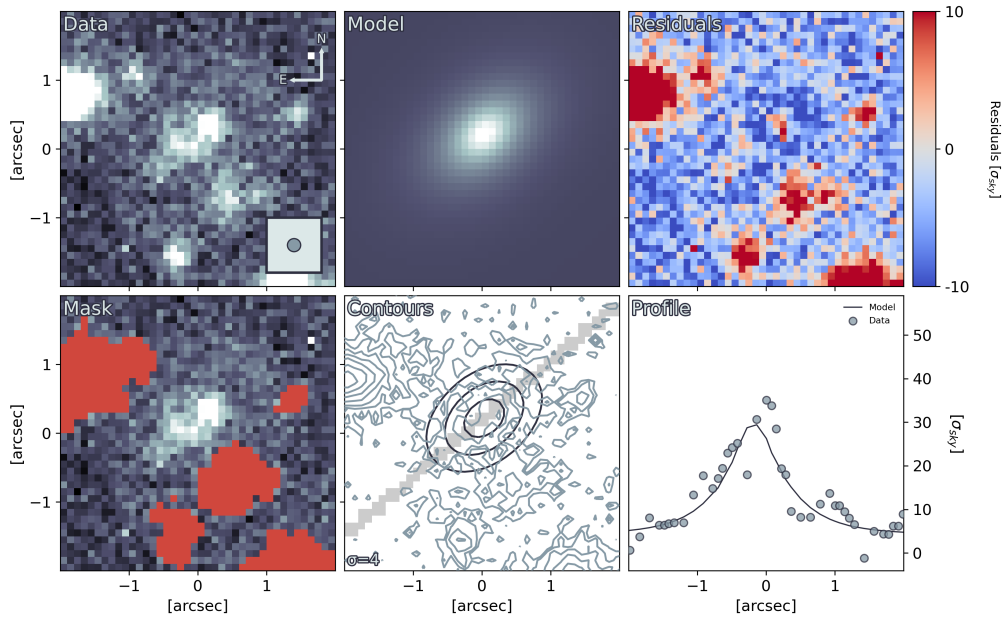


Figure C.76: The results of fitting source 19 with GALFIT. **Data**: A cutout of the source. The colour scale for the *Data*, *Model* and *Mask* panels are defined from this map, using a linear scale. The direction towards celestial north and east are displayed by the arrows. The fitted FWHM of the PSF is displayed in the inset in the bottom right. **Mask**: Masked out sources and dead pixels are displayed in red. **Model**: The fitted model convolved with the PSF. **Contours**: Contours of the *Data* panel in blue. Contours of the *Model* panel in black. Contour levels start at the value annotated in the bottom left, and increase by a factor of two for each subsequent level. The shaded region indicates where the 1D profile was extracted from. **Residuals**: The *Data* subtracted by the *Model*. **Profile**: A one-dimensional profile extracted along the semi-major axis of the *Model*.

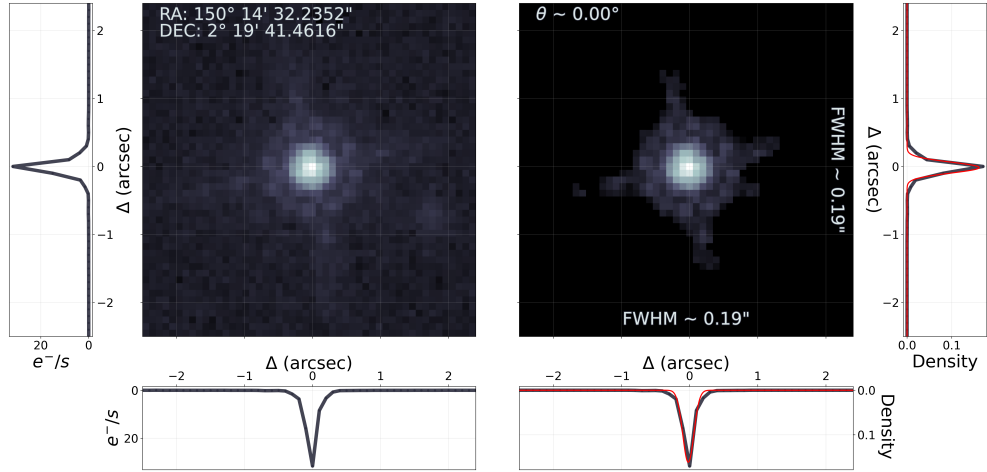


Figure C.77: From point-source to PSF. **Left:** The map displays the source used to create the PSF, for the mosaic containing source 19, in a logarithmic colour scale. The left and bottom panels shows the profile through the pixel of the highest value. The annotated coordinates are the coordinates of the centre of the map. **Right:** The map displays the PSF created from the left figure. The annotated FWHM along each axis are calculated by fitting a two-dimensional Gaussian to the map. The right and bottom panel shows the profile through the highest value pixel in black and the profile of the fitted two-dimensional Gaussian in red. The annotated angle describes the position angle of the fitted two-dimensional Gaussian counterclockwise from the positive x-axis.

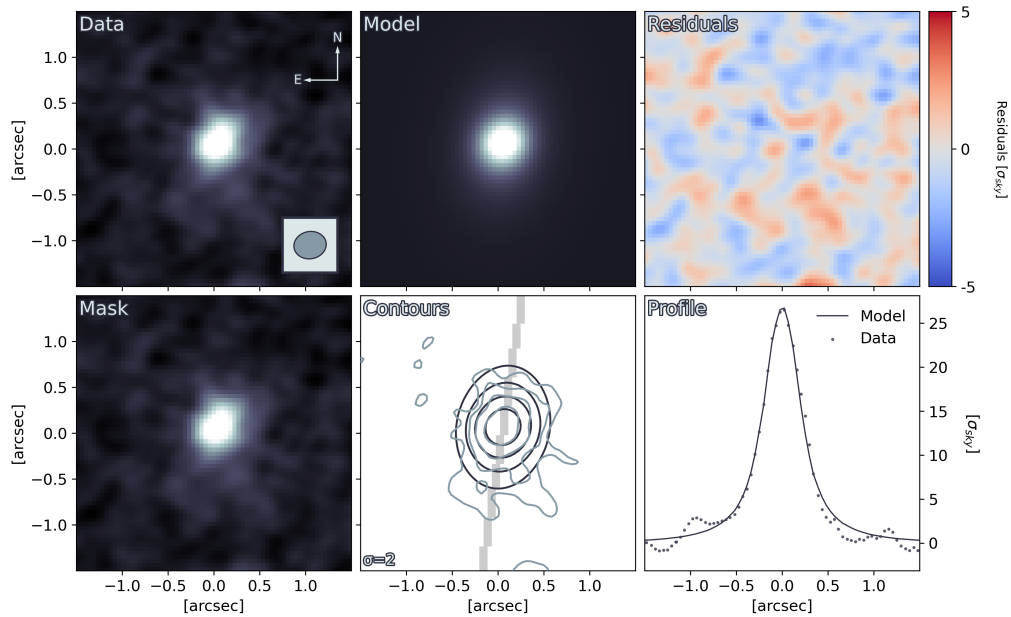


Figure C.78: The results of fitting the CO(3-2) ALMA map for source 19 with GALFIT. **Data:** A cutout of the source. The colour scale for the *Data*, *Model* and *Mask* panels are defined from this map, using a linear scale. The direction towards celestial north and east are displayed by the arrows. The FWHM of the synthetic beam is displayed in the inset on the lower right. **Mask:** Masked out sources and dead pixels are displayed in red. **Model:** The fitted model convolved with the PSF. **Contours:** Contours of the *Data* panel in blue. Contours of the *Model* panel in black. Contour levels start at the value annotated in the bottom left, and increase by a factor of two for each subsequent level. The shaded region indicates where the 1D profile was extracted from. **Residuals:** The *Data* subtracted by the *Model*. **Profile:** A one-dimensional profile extracted along the semi-major axis of the *Model*.

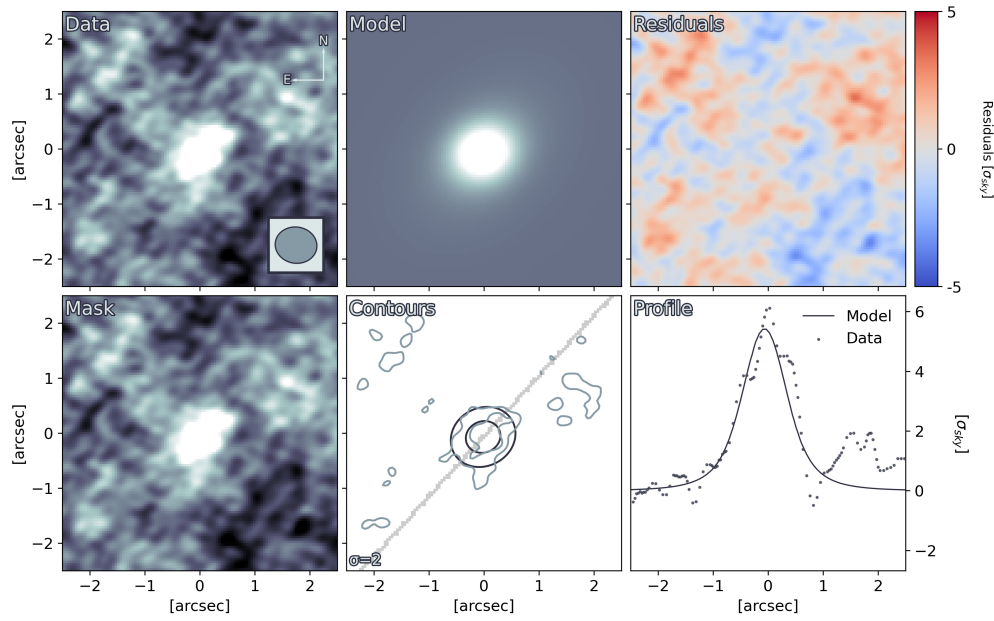


Figure C.79: The results of fitting the dust continuum ALMA map for source 19 with GALFIT. **Data**: A cutout of the source. The colour scale for the *Data*, *Model* and *Mask* panels are defined from this map, using a linear scale. The direction towards celestial north and east are displayed by the arrows. The FWHM of the synthetic beam is displayed in the inset on the lower right. **Mask**: Masked out sources and dead pixels are displayed in red. **Model**: The fitted model convolved with the PSF. **Contours**: Contours of the *Data* panel in blue. Contours of the *Model* panel in black. Contour levels start at the value annotated in the bottom left, and increase by a factor of two for each subsequent level. The shaded region indicates where the 1D profile was extracted from. **Residuals**: The *Data* subtracted by the *Model*. **Profile**: A one-dimensional profile extracted along the semi-major axis of the *Model*.

Source 20

Table C.18: Photometric data collected for source 20. The observation column lists the facility, instrument and filter used to make the observation. The code column connects the filter transmission curve with the correct one in Stardust. The reference column lists references to the works from which the observations were collected. Observations without an uncertainty corresponds to 3σ upper limits.

Observation	Flux [Jy]		Uncertainty [Jy]		Code	Reference
	Value	Order	Value	Order		
CFHT/MegaCam/u*	1.350	10^{-7}	1.735	10^{-8}	352	Weaver et al. 2022
CFHT/MegaCam/u	1.172	10^{-7}	2.622	10^{-8}	353	Weaver et al. 2022
Subaru/HSC/g	3.794	10^{-7}	1.684	10^{-8}	314	Weaver et al. 2022
Subaru/HSC/r	7.509	10^{-7}	2.194	10^{-8}	315	Weaver et al. 2022
Subaru/HSC/i	1.047	10^{-6}	2.482	10^{-8}	316	Weaver et al. 2022
Subaru/HSC/z	1.531	10^{-6}	3.791	10^{-8}	317	Weaver et al. 2022
Subaru/HSC/y	2.439	10^{-6}	6.590	10^{-8}	318	Weaver et al. 2022
VISTA/VIRCAM/Y	2.301	10^{-6}	1.093	10^{-7}	256	Weaver et al. 2022
VISTA/VIRCAM/J	5.084	10^{-6}	1.315	10^{-7}	257	Weaver et al. 2022
VISTA/VIRCAM/H	1.446	10^{-5}	1.955	10^{-7}	258	Weaver et al. 2022
VISTA/VIRCAM/Ks	2.184	10^{-5}	1.958	10^{-7}	259	Weaver et al. 2022
Subaru/Suprime-Cam/IB464	3.368	10^{-7}	2.203	10^{-7}	183	Weaver et al. 2022
Subaru/Suprime-Cam/IA484	4.791	10^{-7}	9.380	10^{-8}	184	Weaver et al. 2022
Subaru/Suprime-Cam/IB505	5.283	10^{-7}	1.259	10^{-7}	185	Weaver et al. 2022
Subaru/Suprime-Cam/IA527	2.095	10^{-7}	1.030	10^{-7}	186	Weaver et al. 2022
Subaru/Suprime-Cam/IB574	4.156	10^{-7}	1.910	10^{-7}	188	Weaver et al. 2022
Subaru/Suprime-Cam/IA624	5.790	10^{-7}	1.103	10^{-7}	190	Weaver et al. 2022
Subaru/Suprime-Cam/IA679	7.361	10^{-7}	1.751	10^{-7}	192	Weaver et al. 2022
Subaru/Suprime-Cam/IB709	6.927	10^{-7}	1.624	10^{-7}	193	Weaver et al. 2022
Subaru/Suprime-Cam/IA738	8.714	10^{-7}	1.403	10^{-7}	194	Weaver et al. 2022
Subaru/Suprime-Cam/IA767	7.132	10^{-7}	2.170	10^{-7}	195	Weaver et al. 2022
Subaru/Suprime-Cam/IB827	9.661	10^{-7}	2.115	10^{-7}	197	Weaver et al. 2022
Subaru/Suprime-Cam/NB711	5.763	10^{-7}	2.483	10^{-7}	322	Weaver et al. 2022
Subaru/Suprime-Cam/NB816	1.269	10^{-6}	1.853	10^{-7}	319	Weaver et al. 2022
VISTA/VIRCAM/NB118	4.227	10^{-6}	5.402	10^{-7}	321	Weaver et al. 2022
Subaru/Suprime-Cam/B	2.701	10^{-7}	2.731	10^{-8}	114	Weaver et al. 2022
Subaru/Suprime-Cam/V	4.081	10^{-7}	5.910	10^{-8}	115	Weaver et al. 2022
Subaru/Suprime-Cam/r+	6.615	10^{-7}	5.870	10^{-8}	116	Weaver et al. 2022
Subaru/Suprime-Cam/i+	1.129	10^{-6}	9.545	10^{-8}	117	Weaver et al. 2022
Subaru/Suprime-Cam/z++	1.458	10^{-6}	2.806	10^{-7}	118	Weaver et al. 2022
Spitzer/IRAC/ch1	3.364	10^{-5}	4.987	10^{-8}	18	Weaver et al. 2022
Spitzer/IRAC/ch2	4.002	10^{-5}	2.894	10^{-7}	19	Weaver et al. 2022
SPITZER/MIPS/24	1.896	10^{-4}	2.106	10^{-5}	325	Jin et al. 2018
JCMT/SCUBA2/850GHz	2.282	10^{-13}	3.298	10^{-3}	324	Jin et al. 2018
VLA/3GHz	9.978	10^{-6}	3.212	10^{-6}		Jin et al. 2018
VLA/1.5GHz	2.538	10^{-5}	6.020	10^{-6}		Jin et al. 2018
Meerkat/1.3GHz	1.116	10^{-4}				Jin et al. 2018
Herschel/PACS/100	1.669	10^{-8}	3.871	10^{-3}	329	Liu et al. 2019
Herschel/PACS/160	3.554	10^{-3}	6.406	10^{-3}	330	Liu et al. 2019
Herschel/SPIRE/250	1.311	10^{-2}	1.194	10^{-2}	331	Liu et al. 2019

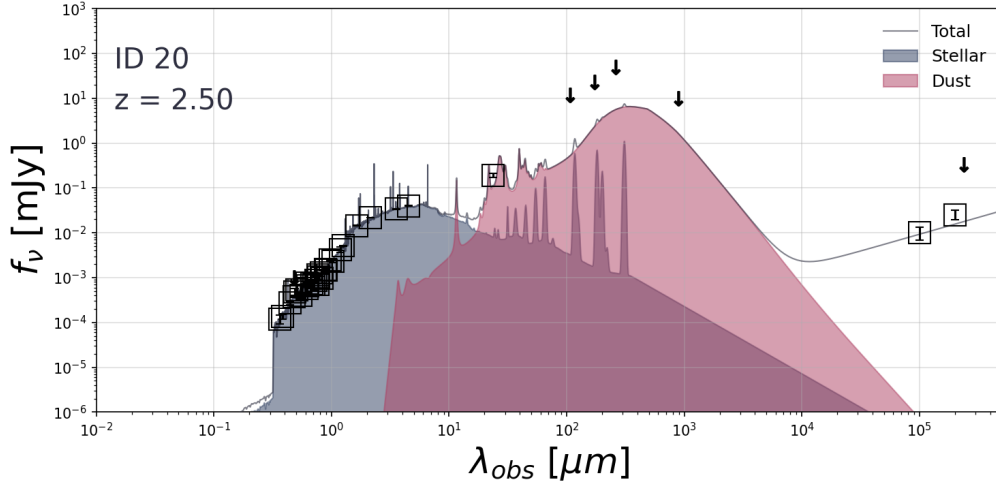


Figure C.80: The SED of source 20 as fitted with STARDUST, assuming that there's no significant AGN contribution. The squares are marked around observations with a SNR > 3. Arrows indicate 3σ upper limits of observations with SNR < 3 or non-detections.

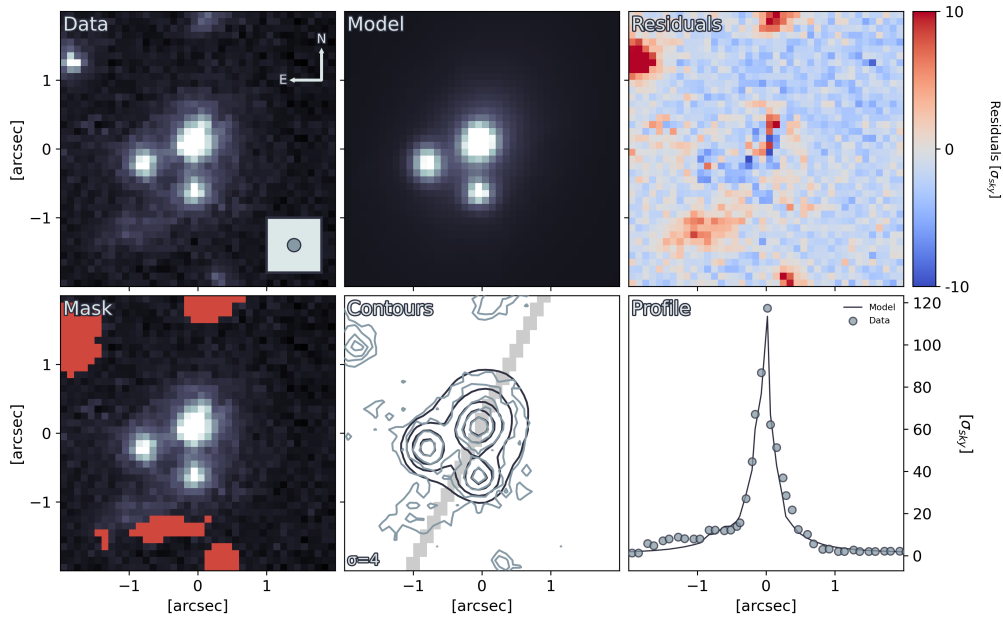


Figure C.81: The results of fitting source 20 with GALFIT. **Data**: A cutout of the source. The colour scale for the *Data*, *Model* and *Mask* panels are defined from this map, using a linear scale. The direction towards celestial north and east are displayed by the arrows. The fitted FWHM of the PSF is displayed in the inset in the bottom right. **Mask**: Masked out sources and dead pixels are displayed in red. **Model**: The fitted model convolved with the PSF. **Contours**: Contours of the *Data* panel in blue. Contours of the *Model* panel in black. Contour levels start at the value annotated in the bottom left, and increase by a factor of two for each subsequent level. The shaded region indicates where the 1D profile was extracted from. **Residuals**: The *Data* subtracted by the *Model*. **Profile**: A one-dimensional profile extracted along the semi-major axis of the *Model*.

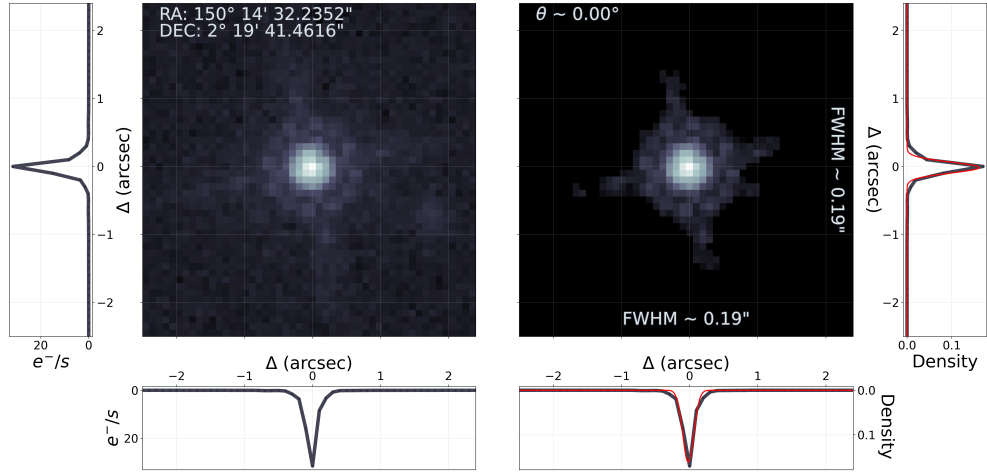


Figure C.82: From point-source to PSF. **Left:** The map displays the source used to create the PSF, for the mosaic containing source 20, in a logarithmic colour scale. The left and bottom panels shows the profile through the pixel of the highest value. The annotated coordinates are the coordinates of the centre of the map. **Right:** The map displays the PSF created from the left figure. The annotated FWHM along each axis are calculated by fitting a two-dimensional Gaussian to the map. The right and bottom panel shows the profile through the highest value pixel in black and the profile of the fitted two-dimensional Gaussian in red. The annotated angle describes the position angle of the fitted two-dimensional Gaussian counterclockwise from the positive x-axis.

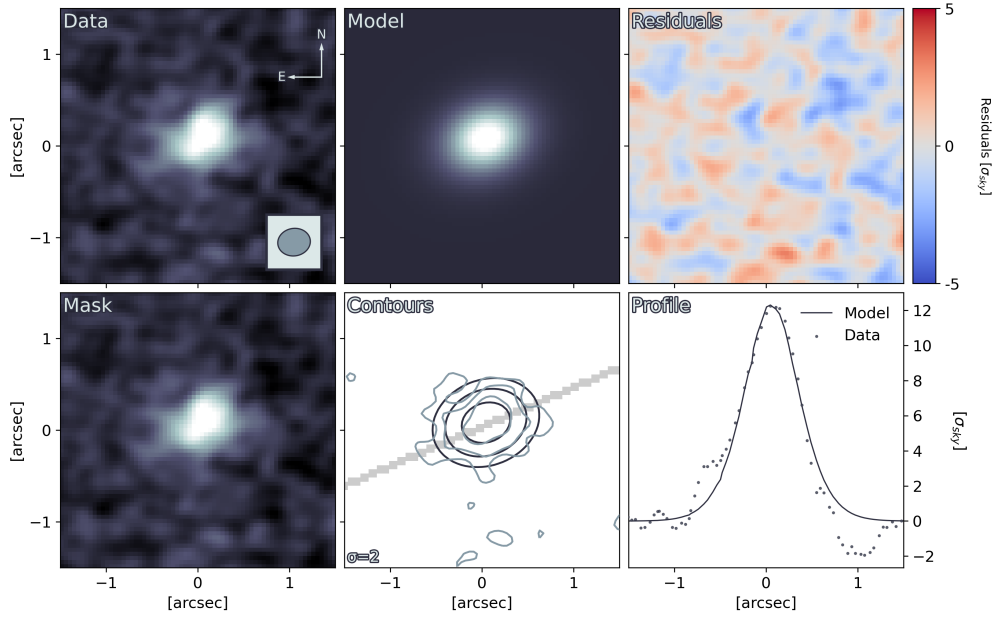


Figure C.83: The results of fitting the CO(3-2) ALMA map for source 20 with GALFIT. **Data:** A cutout of the source. The colour scale for the *Data*, *Model* and *Mask* panels are defined from this map, using a linear scale. The direction towards celestial north and east are displayed by the arrows. The FWHM of the synthetic beam is displayed in the inset on the lower right. **Mask:** Masked out sources and dead pixels are displayed in red. **Model:** The fitted model convolved with the PSF. **Contours:** Contours of the *Data* panel in blue. Contours of the *Model* panel in black. Contour levels start at the value annotated in the bottom left, and increase by a factor of two for each subsequent level. The shaded region indicates where the 1D profile was extracted from. **Residuals:** The *Data* subtracted by the *Model*. **Profile:** A one-dimensional profile extracted along the semi-major axis of the *Model*.

Source 21

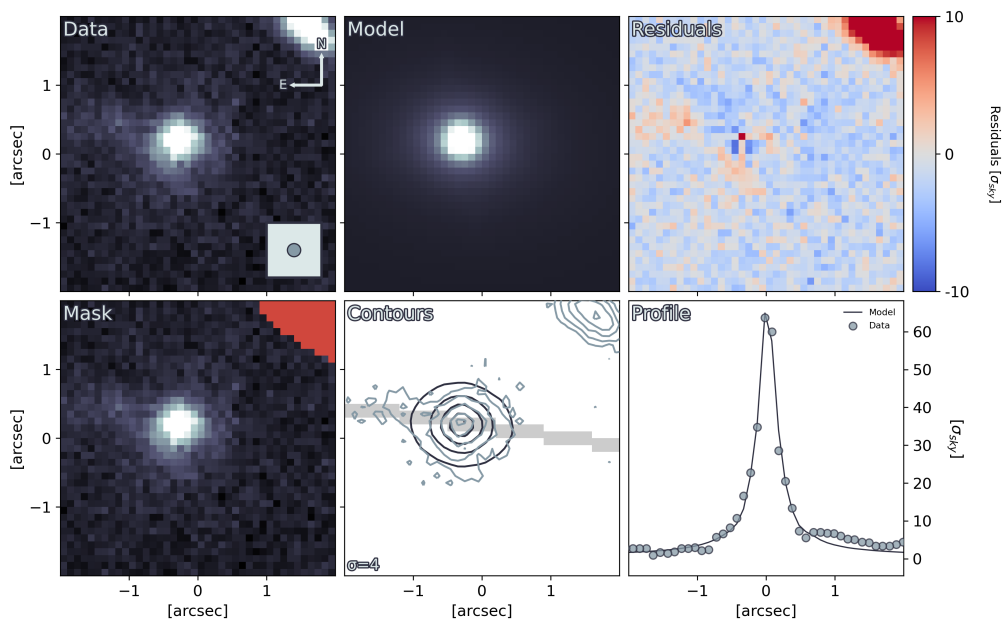


Figure C.84: The results of fitting source 21 with GALFIT. **Data**: A cutout of the source. The colour scale for the *Data*, *Model* and *Mask* panels are defined from this map, using a linear scale. The direction towards celestial north and east are displayed by the arrows. The fitted FWHM of the PSF is displayed in the inset in the bottom right. **Mask**: Masked out sources and dead pixels are displayed in red. **Model**: The fitted model convolved with the PSF. **Contours**: Contours of the *Data* panel in blue. Contours of the *Model* panel in black. Contour levels start at the value annotated in the bottom left, and increase by a factor of two for each subsequent level. The shaded region indicates where the 1D profile was extracted from. **Residuals**: The *Data* subtracted by the *Model*. **Profile**: A one-dimensional profile extracted along the semi-major axis of the *Model*.

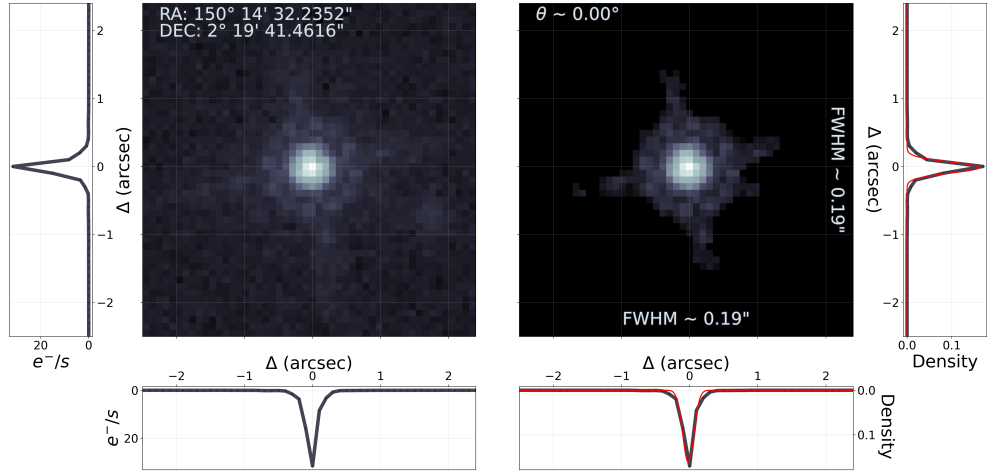


Figure C.85: From point-source to PSF. **Left:** The map displays the source used to create the PSF, for the mosaic containing source 21, in a logarithmic colour scale. The left and bottom panels shows the profile through the pixel of the highest value. The annotated coordinates are the coordinates of the centre of the map. **Right:** The map displays the PSF created from the left figure. The annotated FWHM along each axis are calculated by fitting a two-dimensional Gaussian to the map. The right and bottom panel shows the profile through the highest value pixel in black and the profile of the fitted two-dimensional Gaussian in red. The annotated angle describes the position angle of the fitted two-dimensional Gaussian counterclockwise from the positive x-axis.

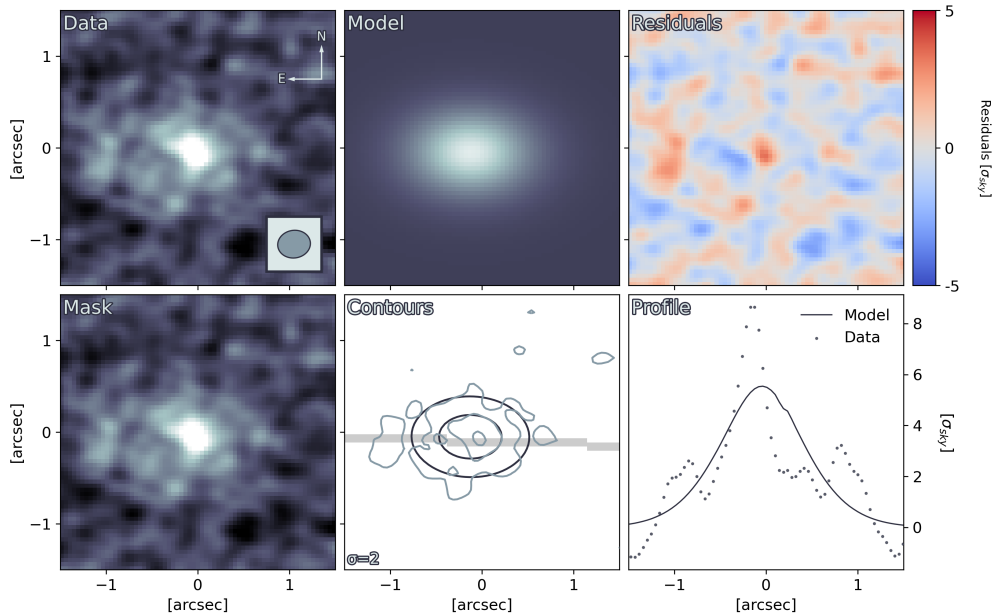


Figure C.86: The results of fitting the CO(3-2) ALMA map for source 21 with GALFIT. **Data:** A cutout of the source. The colour scale for the *Data*, *Model* and *Mask* panels are defined from this map, using a linear scale. The direction towards celestial north and east are displayed by the arrows. The FWHM of the synthetic beam is displayed in the inset on the lower right. **Mask:** Masked out sources and dead pixels are displayed in red. **Model:** The fitted model convolved with the PSF. **Contours:** Contours of the *Data* panel in blue. Contours of the *Model* panel in black. Contour levels start at the value annotated in the bottom left, and increase by a factor of two for each subsequent level. The shaded region indicates where the 1D profile was extracted from. **Residuals:** The *Data* subtracted by the *Model*. **Profile:** A one-dimensional profile extracted along the semi-major axis of the *Model*.

Source 22

Table C.19: Photometric data collected for source 20. The observation column lists the facility, instrument and filter used to make the observation. The code column connects the filter transmission curve with the correct one in Stardust. The reference column lists references to the works from which the observations were collected. Observations without an uncertainty corresponds to 3σ upper limits.

Observation	Flux [Jy]		Uncertainty [Jy]		Code	Reference
	Value	Order	Value	Order		
CFHT/MegaCam/u*	6.401	10^{-7}	1.961	10^{-8}	352	Weaver et al. 2022
CFHT/MegaCam/u	6.094	10^{-7}	2.952	10^{-8}	353	Weaver et al. 2022
Subaru/HSC/g	7.353	10^{-7}	2.266	10^{-8}	314	Weaver et al. 2022
Subaru/HSC/r	9.204	10^{-7}	2.558	10^{-8}	315	Weaver et al. 2022
Subaru/HSC/i	1.161	10^{-6}	2.799	10^{-8}	316	Weaver et al. 2022
Subaru/HSC/z	1.681	10^{-6}	4.255	10^{-8}	317	Weaver et al. 2022
Subaru/HSC/y	1.706	10^{-6}	6.993	10^{-8}	318	Weaver et al. 2022
VISTA/VIRCAM/Y	1.698	10^{-6}	1.353	10^{-7}	256	Weaver et al. 2022
VISTA/VIRCAM/J	3.004	10^{-6}	1.612	10^{-7}	257	Weaver et al. 2022
VISTA/VIRCAM/H	6.415	10^{-6}	2.392	10^{-7}	258	Weaver et al. 2022
VISTA/VIRCAM/Ks	1.133	10^{-5}	2.278	10^{-7}	259	Weaver et al. 2022
Subaru/Suprime-Cam/IB427	7.258	10^{-7}	1.540	10^{-7}	181	Weaver et al. 2022
Subaru/Suprime-Cam/IB464	2.273	10^{-7}	2.483	10^{-7}	183	Weaver et al. 2022
Subaru/Suprime-Cam/IA484	6.947	10^{-7}	1.061	10^{-7}	184	Weaver et al. 2022
Subaru/Suprime-Cam/IB505	7.037	10^{-7}	1.427	10^{-7}	185	Weaver et al. 2022
Subaru/Suprime-Cam/IA527	6.894	10^{-7}	1.167	10^{-7}	186	Weaver et al. 2022
Subaru/Suprime-Cam/IB574	6.842	10^{-7}	2.125	10^{-7}	188	Weaver et al. 2022
Subaru/Suprime-Cam/IA624	7.905	10^{-7}	1.220	10^{-7}	190	Weaver et al. 2022
Subaru/Suprime-Cam/IA679	9.510	10^{-7}	1.980	10^{-7}	192	Weaver et al. 2022
Subaru/Suprime-Cam/IB709	1.075	10^{-6}	1.788	10^{-7}	193	Weaver et al. 2022
Subaru/Suprime-Cam/IA738	1.060	10^{-6}	1.585	10^{-7}	194	Weaver et al. 2022
Subaru/Suprime-Cam/IA767	1.250	10^{-6}	2.461	10^{-7}	195	Weaver et al. 2022
Subaru/Suprime-Cam/IB827	8.767	10^{-7}	2.387	10^{-7}	197	Weaver et al. 2022
Subaru/Suprime-Cam/NB711	1.176	10^{-6}	2.813	10^{-7}	322	Weaver et al. 2022
Subaru/Suprime-Cam/NB816	1.193	10^{-6}	2.180	10^{-7}	319	Weaver et al. 2022
VISTA/VIRCAM/NB118	2.740	10^{-6}	6.778	10^{-7}	321	Weaver et al. 2022
Subaru/Suprime-Cam/B	6.559	10^{-7}	3.095	10^{-8}	114	Weaver et al. 2022
Subaru/Suprime-Cam/V	6.613	10^{-7}	6.661	10^{-8}	115	Weaver et al. 2022
Subaru/Suprime-Cam/r+	8.530	10^{-7}	5.066	10^{-8}	116	Weaver et al. 2022
Subaru/Suprime-Cam/i+	1.099	10^{-6}	6.984	10^{-8}	117	Weaver et al. 2022
Subaru/Suprime-Cam/z++	1.476	10^{-6}	3.116	10^{-7}	118	Weaver et al. 2022
Spitzer/IRAC/ch1	3.102	10^{-5}	4.627	10^{-8}	18	Weaver et al. 2022
Spitzer/IRAC/ch2	4.374	10^{-5}	7.172	10^{-8}	19	Weaver et al. 2022
GALEX/GALEX/NUV	1.985	10^{-7}	7.858	10^{-8}	121	Weaver et al. 2022
SPITZER/MIPS/24	2.261	10^{-4}	2.640	10^{-5}	325	Jin et al. 2018
JCMT/SCUBA2/850GHz	2.282	10^{-13}	1.016	10^{-3}	324	Jin et al. 2018
VLA/3GHz	2.060	10^{-5}	2.500	10^{-6}		Jin et al. 2018
VLA/1.5GHz	2.512	10^{-5}	6.153	10^{-6}		Jin et al. 2018
Meerkat/1.3GHz	7.921	10^{-5}				Jin et al. 2018
Herschel/PACS/100	1.669	10^{-8}	3.635	10^{-3}	329	Liu et al. 2019
Herschel/PACS/160	1.694	10^{-2}	6.137	10^{-3}	330	Liu et al. 2019
Herschel/SPIRE/250	1.342	10^{-2}	1.571	10^{-3}	331	Liu et al. 2019

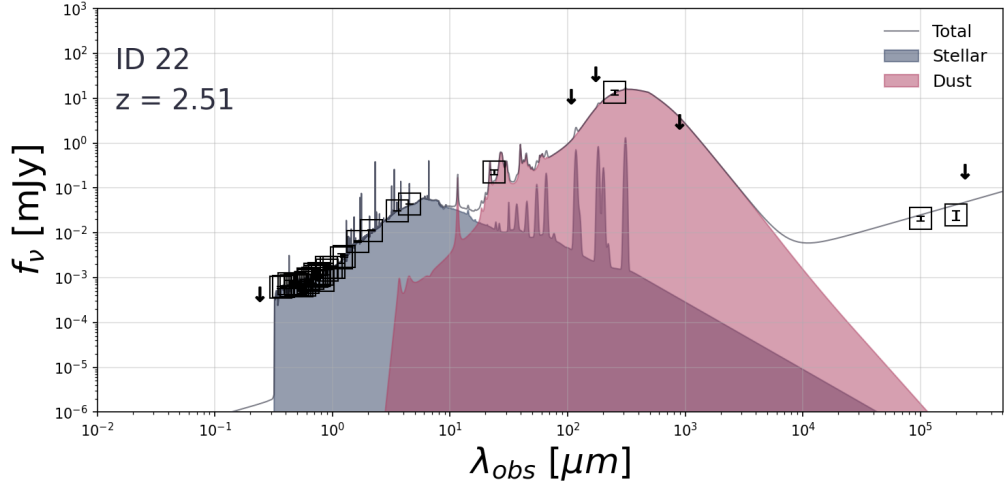


Figure C.87: The SED of source 22 as fitted with STARDUST, assuming that there's no significant AGN contribution. The squares are marked around observations with a SNR > 3. Arrows indicate 3σ upper limits of observations with SNR < 3 or non-detections.

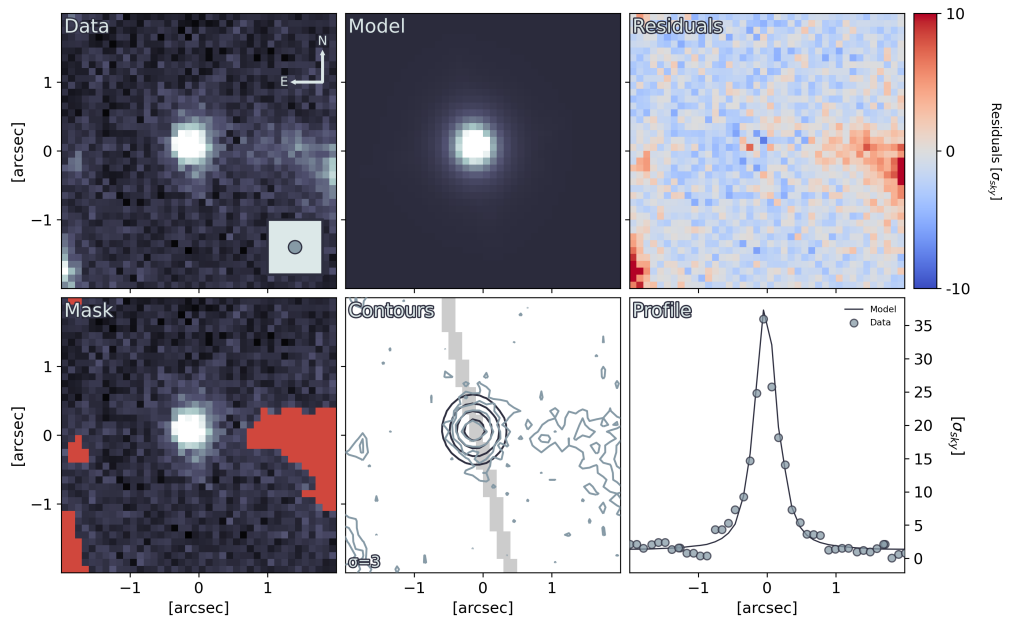


Figure C.88: The results of fitting source 22 with GALFIT. **Data**: A cutout of the source. The colour scale for the *Data*, *Model* and *Mask* panels are defined from this map, using a linear scale. The direction towards celestial north and east are displayed by the arrows. The fitted FWHM of the PSF is displayed in the inset in the bottom right. **Mask**: Masked out sources and dead pixels are displayed in red. **Model**: The fitted model convolved with the PSF. **Contours**: Contours of the *Data* panel in blue. Contours of the *Model* panel in black. Contour levels start at the value annotated in the bottom left, and increase by a factor of two for each subsequent level. The shaded region indicates where the 1D profile was extracted from. **Residuals**: The *Data* subtracted by the *Model*. **Profile**: A one-dimensional profile extracted along the semi-major axis of the *Model*.

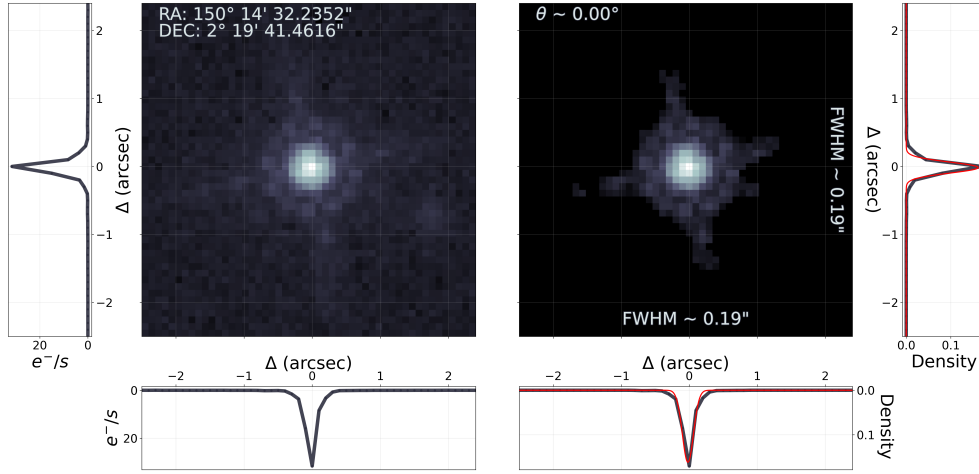


Figure C.89: From point-source to PSF. **Left:** The map displays the source used to create the PSF, for the mosaic containing source 22, in a logarithmic colour scale. The left and bottom panels shows the profile through the pixel of the highest value. The annotated coordinates are the coordinates of the centre of the map. **Right:** The map displays the PSF created from the left figure. The annotated FWHM along each axis are calculated by fitting a two-dimensional Gaussian to the map. The right and bottom panel shows the profile through the highest value pixel in black and the profile of the fitted two-dimensional Gaussian in red. The annotated angle describes the position angle of the fitted two-dimensional Gaussian counterclockwise from the positive x-axis.

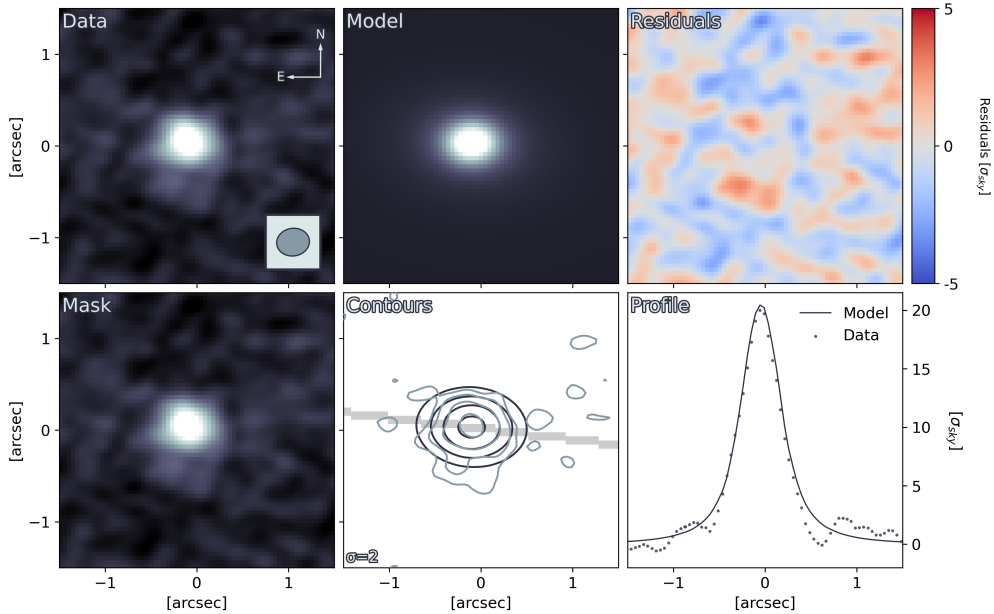


Figure C.90: The results of fitting the CO(3-2) ALMA map for source 22 with GALFIT. **Data:** A cutout of the source. The colour scale for the *Data*, *Model* and *Mask* panels are defined from this map, using a linear scale. The direction towards celestial north and east are displayed by the arrows. The FWHM of the synthetic beam is displayed in the inset on the lower right. **Mask:** Masked out sources and dead pixels are displayed in red. **Model:** The fitted model convolved with the PSF. **Contours:** Contours of the *Data* panel in blue. Contours of the *Model* panel in black. Contour levels start at the value annotated in the bottom left, and increase by a factor of two for each subsequent level. The shaded region indicates where the 1D profile was extracted from. **Residuals:** The *Data* subtracted by the *Model*. **Profile:** A one-dimensional profile extracted along the semi-major axis of the *Model*.

Source 24

Table C.20: Photometric data collected for source 24. The observation column lists the facility, instrument and filter used to make the observation. The code column connects the filter transmission curve with the correct one in Stardust. The reference column lists references to the works from which the observations were collected. Observations without an uncertainty corresponds to 3σ upper limits.

Observation	Flux [Jy]		Uncertainty [Jy]		Code	Reference
	Value	Order	Value	Order		
CFHT/MegaCam/u*	2.121	10^{-7}	8.260	10^{-9}	352	Weaver et al. 2022
CFHT/MegaCam/u	1.240	10^{-7}	1.257	10^{-8}	353	Weaver et al. 2022
Subaru/HSC/g	7.198	10^{-7}	1.312	10^{-8}	314	Weaver et al. 2022
Subaru/HSC/r	1.272	10^{-6}	1.683	10^{-8}	315	Weaver et al. 2022
Subaru/HSC/i	1.445	10^{-6}	1.681	10^{-8}	316	Weaver et al. 2022
Subaru/HSC/z	1.535	10^{-6}	2.219	10^{-8}	317	Weaver et al. 2022
Subaru/HSC/y	1.585	10^{-6}	3.335	10^{-8}	318	Weaver et al. 2022
VISTA/VIRCAM/Y	1.635	10^{-6}	1.098	10^{-7}	256	Weaver et al. 2022
VISTA/VIRCAM/J	2.013	10^{-6}	1.242	10^{-7}	257	Weaver et al. 2022
VISTA/VIRCAM/H	3.264	10^{-6}	1.764	10^{-7}	258	Weaver et al. 2022
VISTA/VIRCAM/Ks	4.113	10^{-6}	1.175	10^{-7}	259	Weaver et al. 2022
Subaru/Suprime-Cam/IB427	5.414	10^{-7}	6.320	10^{-8}	181	Weaver et al. 2022
Subaru/Suprime-Cam/IB464	4.320	10^{-7}	9.342	10^{-8}	183	Weaver et al. 2022
Subaru/Suprime-Cam/IA484	4.246	10^{-7}	3.663	10^{-8}	184	Weaver et al. 2022
Subaru/Suprime-Cam/IB505	9.247	10^{-7}	5.415	10^{-8}	185	Weaver et al. 2022
Subaru/Suprime-Cam/IA527	1.073	10^{-6}	4.087	10^{-8}	186	Weaver et al. 2022
Subaru/Suprime-Cam/IB574	1.229	10^{-6}	7.874	10^{-8}	188	Weaver et al. 2022
Subaru/Suprime-Cam/IA624	1.224	10^{-6}	4.133	10^{-8}	190	Weaver et al. 2022
Subaru/Suprime-Cam/IA679	1.521	10^{-6}	7.024	10^{-8}	192	Weaver et al. 2022
Subaru/Suprime-Cam/IB709	1.469	10^{-6}	6.767	10^{-8}	193	Weaver et al. 2022
Subaru/Suprime-Cam/IA738	1.439	10^{-6}	5.509	10^{-8}	194	Weaver et al. 2022
Subaru/Suprime-Cam/IA767	1.480	10^{-6}	8.226	10^{-8}	195	Weaver et al. 2022
Subaru/Suprime-Cam/IB827	1.405	10^{-6}	9.262	10^{-8}	197	Weaver et al. 2022
Subaru/Suprime-Cam/NB711	1.347	10^{-6}	1.063	10^{-7}	322	Weaver et al. 2022
Subaru/Suprime-Cam/NB816	1.522	10^{-6}	7.855	10^{-8}	319	Weaver et al. 2022
Subaru/Suprime-Cam/B	4.767	10^{-7}	1.215	10^{-8}	114	Weaver et al. 2022
Subaru/Suprime-Cam/V	1.167	10^{-6}	2.581	10^{-8}	115	Weaver et al. 2022
Subaru/Suprime-Cam/r+	1.313	10^{-6}	1.797	10^{-8}	116	Weaver et al. 2022
Subaru/Suprime-Cam/i+	1.492	10^{-6}	2.454	10^{-8}	117	Weaver et al. 2022
Subaru/Suprime-Cam/z++	1.544	10^{-6}	1.042	10^{-7}	118	Weaver et al. 2022
Spitzer/IRAC/ch1	9.238	10^{-6}	1.890	10^{-8}	18	Weaver et al. 2022
Spitzer/IRAC/ch2	1.405	10^{-5}	3.602	10^{-8}	19	Weaver et al. 2022
SPITZER/MIPS/24	1.719	10^{-4}	1.514	10^{-5}	325	Jin et al. 2018
VLA/3GHz	3.380	10^{-5}	2.900	10^{-6}		Jin et al. 2018
Meerkat/1.3GHz	2.739	10^{-4}				Jin et al. 2018
Herschel/PACS/100	6.276	10^{-3}	1.625	10^{-3}	329	Liu et al. 2019
Herschel/PACS/160	1.142	10^{-2}	4.362	10^{-3}	330	Liu et al. 2019
Spitzer/IRAC/ch3	1.241	10^{-5}	2.330	10^{-6}	20	Laigle et al. 2016
Spitzer/IRAC/ch4	1.293	10^{-5}	4.020	10^{-6}	21	Laigle et al. 2016
Herschel/SPIRE/200	2.496	10^{-2}	7.400	10^{-4}	331	Laigle et al. 2016
Herschel/SPIRE/350	3.328	10^{-2}	1.110	10^{-3}	332	Laigle et al. 2016
Herschel/SPIRE/500	2.390	10^{-2}	1.090	10^{-3}	333	Laigle et al. 2016

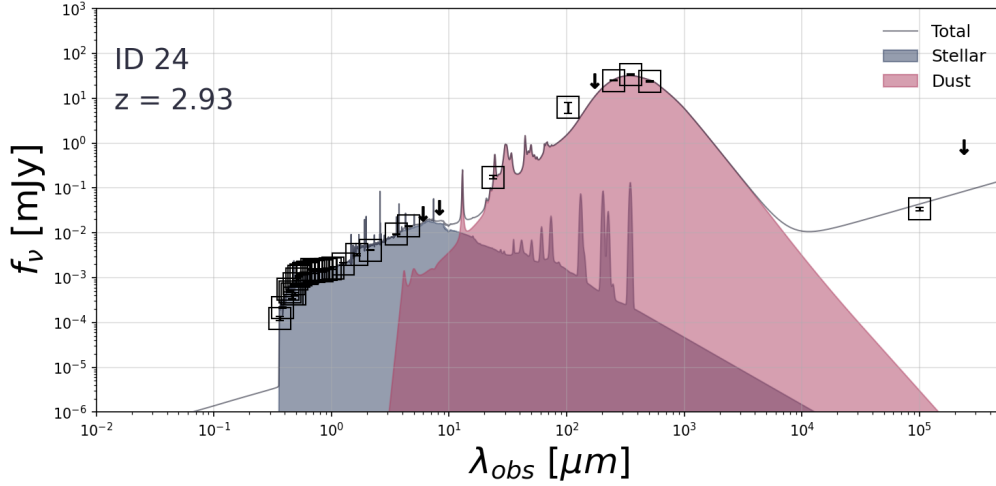


Figure C.91: The SED of source 24 as fitted with STARDUST, assuming that there's no significant AGN contribution. The squares are marked around observations with a SNR > 3. Arrows indicate 3σ upper limits of observations with SNR < 3 or non-detections.

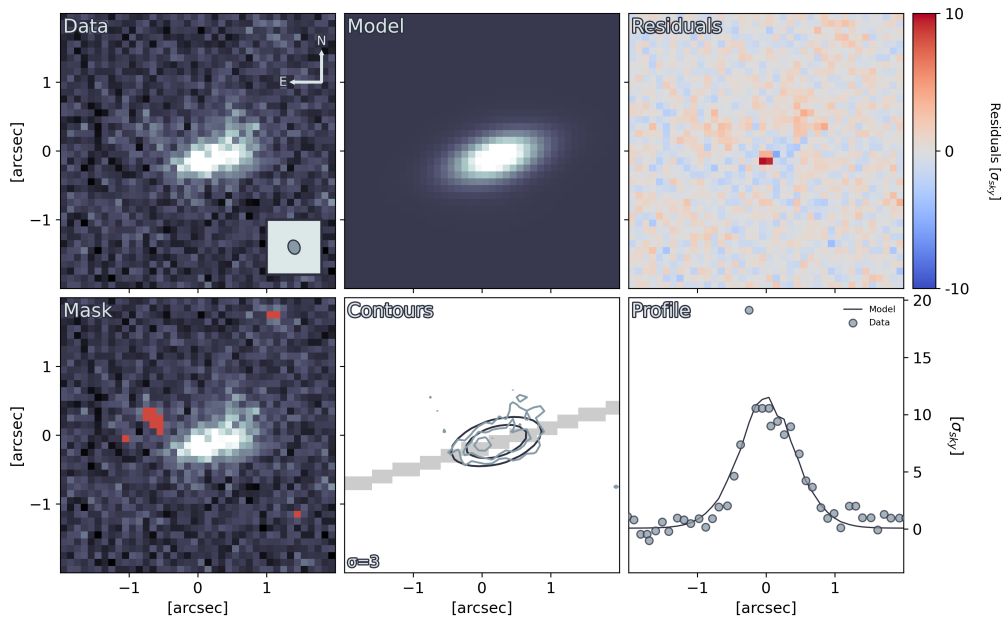


Figure C.92: The results of fitting source 24 with GALFIT. **Data**: A cutout of the source. The colour scale for the *Data*, *Model* and *Mask* panels are defined from this map, using a linear scale. The direction towards celestial north and east are displayed by the arrows. The fitted FWHM of the PSF is displayed in the inset in the bottom right. **Mask**: Masked out sources and dead pixels are displayed in red. **Model**: The fitted model convolved with the PSF. **Contours**: Contours of the *Data* panel in blue. Contours of the *Model* panel in black. Contour levels start at the value annotated in the bottom left, and increase by a factor of two for each subsequent level. The shaded region indicates where the 1D profile was extracted from. **Residuals**: The *Data* subtracted by the *Model*. **Profile**: A one-dimensional profile extracted along the semi-major axis of the *Model*.

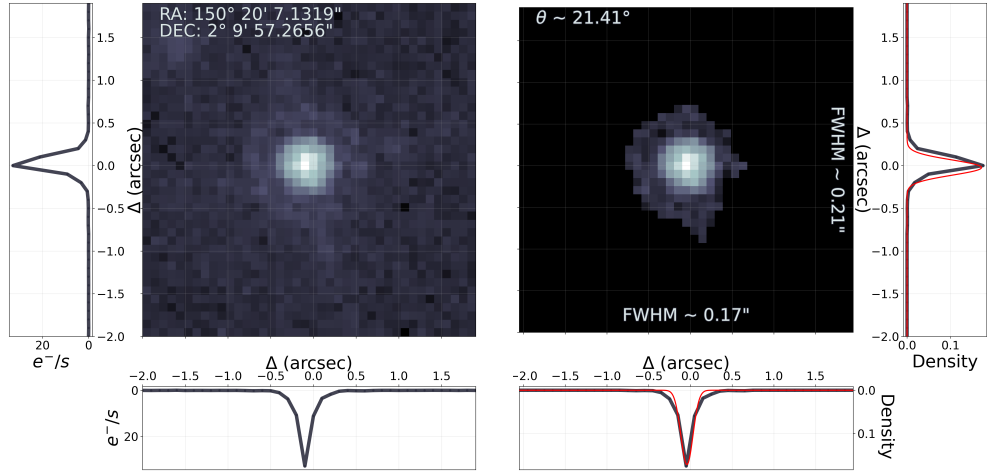


Figure C.93: From point-source to PSF. **Left:** The map displays the source used to create the PSF, for the mosaic containing source 24, in a logarithmic colour scale. The left and bottom panels shows the profile through the pixel of the highest value. The annotated coordinates are the coordinates of the centre of the map. **Right:** The map displays the PSF created from the left figure. The annotated FWHM along each axis are calculated by fitting a two-dimensional Gaussian to the map. The right and bottom panel shows the profile through the highest value pixel in black and the profile of the fitted two-dimensional Gaussian in red. The annotated angle describes the position angle of the fitted two-dimensional Gaussian counterclockwise from the positive x-axis.

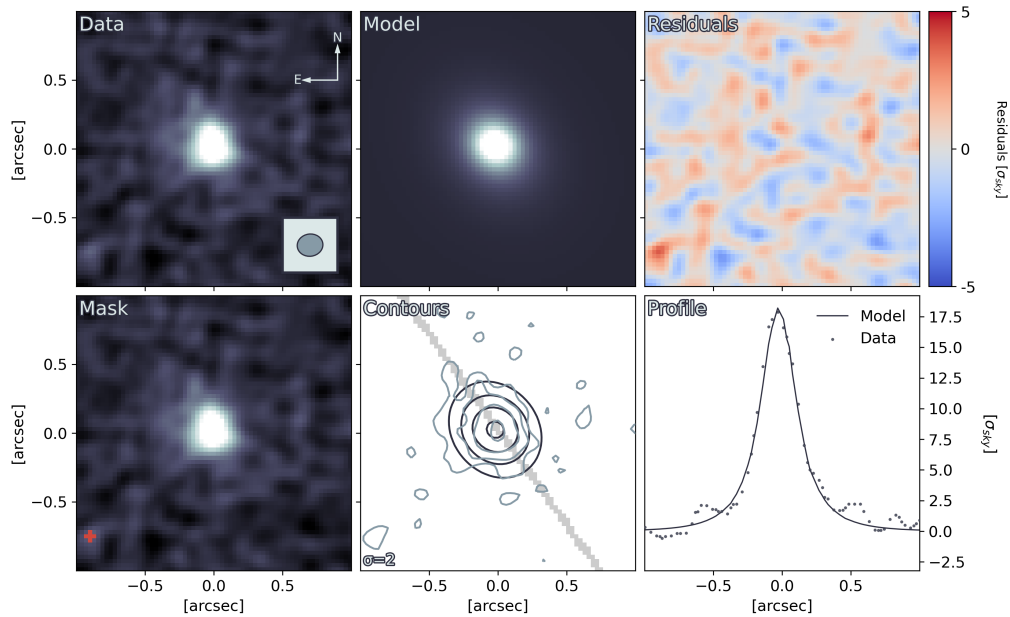


Figure C.94: The results of fitting the CO(5-4) ALMA map for source 24 with GALFIT. **Data:** A cutout of the source. The colour scale for the *Data*, *Model* and *Mask* panels are defined from this map, using a linear scale. The direction towards celestial north and east are displayed by the arrows. The FWHM of the synthetic beam is displayed in the inset on the lower right. **Mask:** Masked out sources and dead pixels are displayed in red. **Model:** The fitted model convolved with the PSF. **Contours:** Contours of the *Data* panel in blue. Contours of the *Model* panel in black. Contour levels start at the value annotated in the bottom left, and increase by a factor of two for each subsequent level. The shaded region indicates where the 1D profile was extracted from. **Residuals:** The *Data* subtracted by the *Model*. **Profile:** A one-dimensional profile extracted along the semi-major axis of the *Model*.

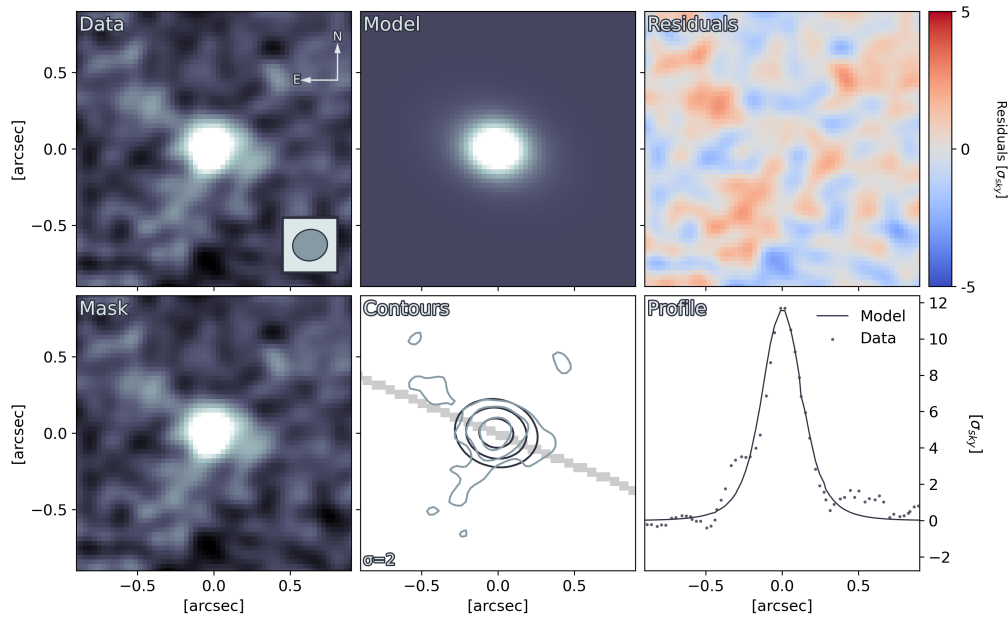


Figure C.95: The results of fitting the dust continuum ALMA map for source 24 with GALFIT. **Data**: A cutout of the source. The colour scale for the *Data*, *Model* and *Mask* panels are defined from this map, using a linear scale. The direction towards celestial north and east are displayed by the arrows. The FWHM of the synthetic beam is displayed in the inset on the lower right. **Mask**: Masked out sources and dead pixels are displayed in red. **Model**: The fitted model convolved with the PSF. **Contours**: Contours of the *Data* panel in blue. Contours of the *Model* panel in black. Contour levels start at the value annotated in the bottom left, and increase by a factor of two for each subsequent level. The shaded region indicates where the 1D profile was extracted from. **Residuals**: The *Data* subtracted by the *Model*. **Profile**: A one-dimensional profile extracted along the semi-major axis of the *Model*.

Source 25

Table C.21: Photometric data collected for source 24. The observation column lists the facility, instrument and filter used to make the observation. The code column connects the filter transmission curve with the correct one in Stardust. The reference column lists references to the works from which the observations were collected. Observations without an uncertainty corresponds to 3σ upper limits.

Observation	Flux [Jy]		Uncertainty [Jy]		Code	Reference
	Value	Order	Value	Order		
Spitzer/IRAC/5.8	8.610	10 ⁻⁶	1.540	10 ⁻⁶	20	Leung et al. 2019
Spitzer/IRAC/8.0	8.140	10 ⁻⁶	4.480	10 ⁻⁶	21	Leung et al. 2019
Spitzer/MIPS/24um	1.080	10 ⁻³	2.000	10 ⁻⁵	325	Leung et al. 2019
Herschel/PACS/160um	8.630	10 ⁻²	1.790	10 ⁻²	330	Leung et al. 2019
Herschel/SPIRE/250um	1.060	10 ⁻¹	7.000	10 ⁻³	331	Leung et al. 2019
Herschel/SPIRE/350um	1.200	10 ⁻¹	1.000	10 ⁻²	332	Leung et al. 2019
Herschel/SPIRE/500um	9.210	10 ⁻²	7.600	10 ⁻³	333	Leung et al. 2019
ALMA/635um	5.250	10 ⁻²	5.900	10 ⁻³		Leung et al. 2019
ALMA/870um	1.800	10 ⁻²	4.000	10 ⁻⁴		Leung et al. 2019
SMA/870um	2.150	10 ⁻²	3.100	10 ⁻³		Leung et al. 2019
ALMA-ACA/1037um	1.180	10 ⁻²	8.000	10 ⁻⁴		Leung et al. 2019
IRAM/MAMBO/1200um	8.900	10 ⁻³	9.000	10 ⁻⁴		Leung et al. 2019
CARMA/3000um	5.000	10 ⁻⁴	1.100	10 ⁻⁴		Leung et al. 2019
VLA/9586.8um	1.840	10 ⁻⁵	3.140	10 ⁻⁶		Leung et al. 2019
GALEX/FUV	2.290	10 ⁻⁶			120	Leung et al. 2019
GALEX/NUV	2.290	10 ⁻⁶			121	Leung et al. 2019
CFHT/MegaCam/u*	1.900	10 ⁻⁷			352	Leung et al. 2019
CFHT/MegaCam/g'	1.400	10 ⁻⁷			89	Leung et al. 2019
CFHT/MegaCam/r'	2.000	10 ⁻⁷			90	Leung et al. 2019
CFHT/MegaCam/i'	2.400	10 ⁻⁷			91	Leung et al. 2019
CFHT/MegaCam/z'	3.500	10 ⁻⁷			92	Leung et al. 2019
VISTA/VIRCAM/Z	1.100	10 ⁻⁷			356	Leung et al. 2019
VISTA/VIRCAM/Y	3.100	10 ⁻⁷			256	Leung et al. 2019
VISTA/VIRCAM/J	3.500	10 ⁻⁷			257	Leung et al. 2019
VISTA/VIRCAM/H	5.500	10 ⁻⁷			258	Leung et al. 2019
VISTA/VIRCAM/Ks	7.800	10 ⁻⁷			259	Leung et al. 2019
Spitzer/IRAC/3.6	1.250	10 ⁻⁶			18	Leung et al. 2019
Spitzer/IRAC/4.5	1.250	10 ⁻⁶			19	Leung et al. 2019
WISE/band-1	2.000	10 ⁻⁴			244	Leung et al. 2019
WISE/band-2	1.900	10 ⁻⁴			245	Leung et al. 2019
WISE/band-3	5.200	10 ⁻⁴			245	Leung et al. 2019
WISE/band-4	3.240	10 ⁻³			246	Leung et al. 2019

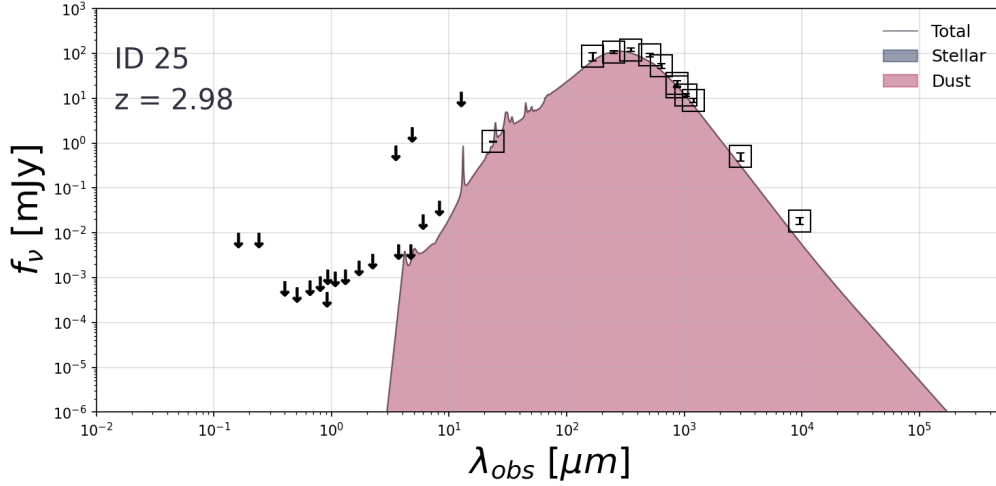


Figure C.96: The SED of source 24 as fitted with STARDUST, assuming that there's no significant AGN contribution. The squares are marked around observations with a SNR > 3. Arrows indicate 3σ upper limits of observations with SNR < 3 or non-detections.

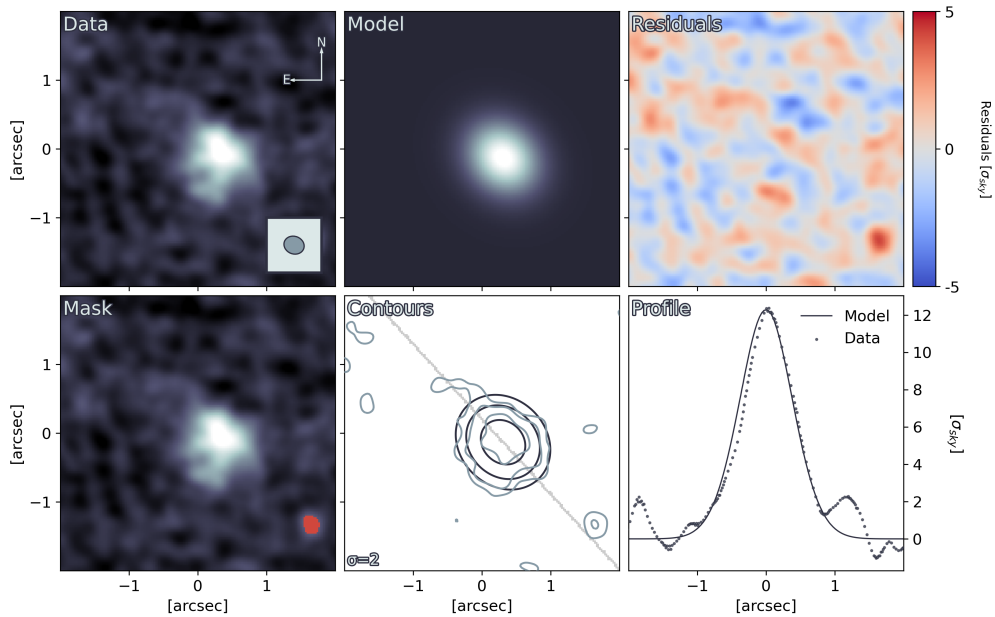


Figure C.97: The results of fitting the [CII](1-0) ALMA map for source 25 with GALFIT. **Data**: A cutout of the source. The colour scale for the *Data*, *Model* and *Mask* panels are defined from this map, using a linear scale. The direction towards celestial north and east are displayed by the arrows. The FWHM of the synthetic beam is displayed in the inset on the lower right. **Mask**: Masked out sources and dead pixels are displayed in red. **Model**: The fitted model convolved with the PSF. **Contours**: Contours of the *Data* panel in blue. Contours of the *Model* panel in black. Contour levels start at the value annotated in the bottom left, and increase by a factor of two for each subsequent level. The shaded region indicates where the 1D profile was extracted from. **Residuals**: The *Data* subtracted by the *Model*. **Profile**: A one-dimensional profile extracted along the semi-major axis of the *Model*.

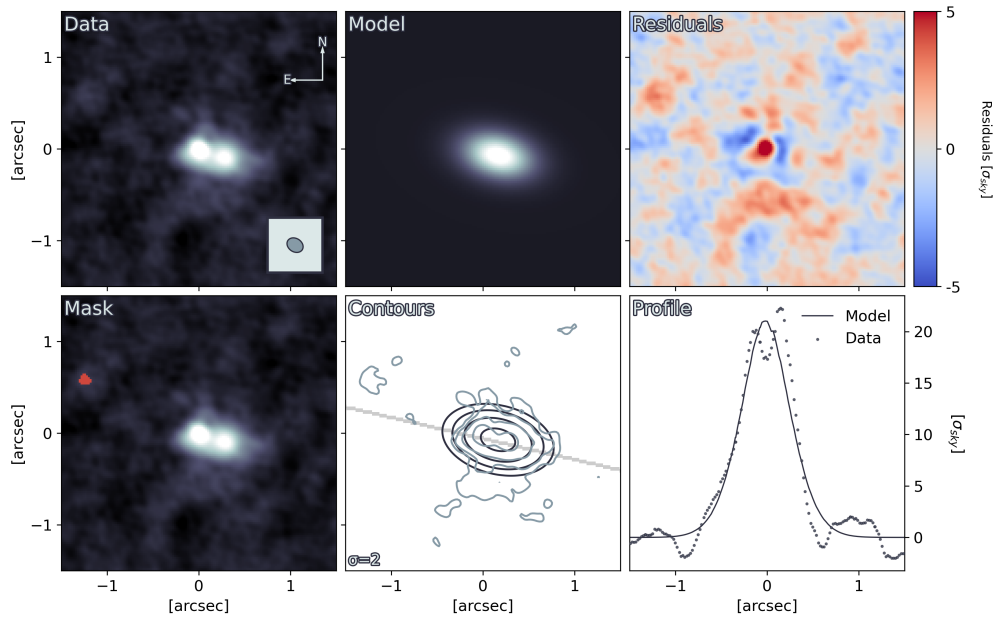


Figure C.98: The results of fitting the dust continuum ALMA map for source 25 with GALFIT. **Data**: A cutout of the source. The colour scale for the *Data*, *Model* and *Mask* panels are defined from this map, using a linear scale. The direction towards celestial north and east are displayed by the arrows. The FWHM of the synthetic beam is displayed in the inset on the lower right. **Mask**: Masked out sources and dead pixels are displayed in red. **Model**: The fitted model convolved with the PSF. **Contours**: Contours of the *Data* panel in blue. Contours of the *Model* panel in black. Contour levels start at the value annotated in the bottom left, and increase by a factor of two for each subsequent level. The shaded region indicates where the 1D profile was extracted from. **Residuals**: The *Data* subtracted by the *Model*. **Profile**: A one-dimensional profile extracted along the semi-major axis of the *Model*.

Source 26

Table C.22: Photometric data collected for source 26. The observation column lists the facility, instrument and filter used to make the observation. The code column connects the filter transmission curve with the correct one in Stardust. The reference column lists references to the works from which the observations were collected. Observations without an uncertainty corresponds to 3σ upper limits.

Observation	Flux [Jy]		Uncertainty [Jy]		Code	Reference
	Value	Order	Value	Order		
ALMA/1140um	5.600	10^{-3}	1.300	10^{-4}		Umehata et al. 2017
VLA/200000	4.200	10^{-5}	1.200	10^{-5}		Tamura et al. 2010
ASTE/AzTEC/1100/db	8.200	10^{-3}	1.000	10^{-3}		Tamura et al. 2010
SMA/860	1.220	10^{-2}	2.700	10^{-3}		Tamura et al. 2010
SPITZER/MIPS/24	1.420	10^{-4}	1.800	10^{-5}	325	Tamura et al. 2010
SPITZER/IRAC/8.0	3.259	10^{-5}	2.270	10^{-6}	21	Tamura et al. 2010
SPITZER/IRAC/5.8	2.224	10^{-5}	1.870	10^{-6}	20	Tamura et al. 2010
SPITZER/IRAC/4.5	1.446	10^{-5}	7.600	10^{-7}	19	Tamura et al. 2010
SPITZER/IRAC/3.6	7.800	10^{-6}	5.000	10^{-7}	18	Tamura et al. 2010
Subaru/MOIRCS/Ks	2.710	10^{-6}	6.300	10^{-7}	226	Tamura et al. 2010
Subaru/MOIRCS/H	2.130	10^{-6}	7.100	10^{-7}	225	Tamura et al. 2010
Subaru/MOIRCS/J	1.680	10^{-6}			224	Tamura et al. 2010
Subaru/S-CAM/z'	1.200	10^{-7}			199	Tamura et al. 2010
Subaru/S-CAM/i'	6.300	10^{-8}			195	Tamura et al. 2010
Subaru/S-CAM/R	4.800	10^{-8}			162	Tamura et al. 2010
Subaru/S-CAM/V	5.250	10^{-8}			187	Tamura et al. 2010
Subaru/HSC/NB497	7.500	10^{-8}			357	Tamura et al. 2010
Subaru/S-CAM/B	5.700	10^{-8}			182	Tamura et al. 2010
ALMA/3mm	1.170	10^{-4}	1.400	10^{-5}		This work

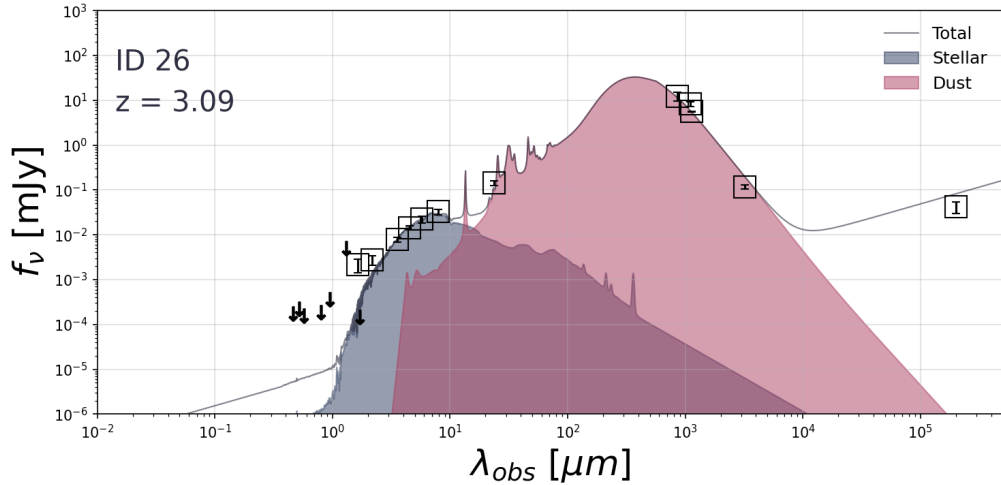


Figure C.99: The SED of source 26 as fitted with STARDUST, assuming that there's no significant AGN contribution. The squares are marked around observations with a SNR > 3. Arrows indicate 3σ upper limits of observations with SNR < 3 or non-detections.

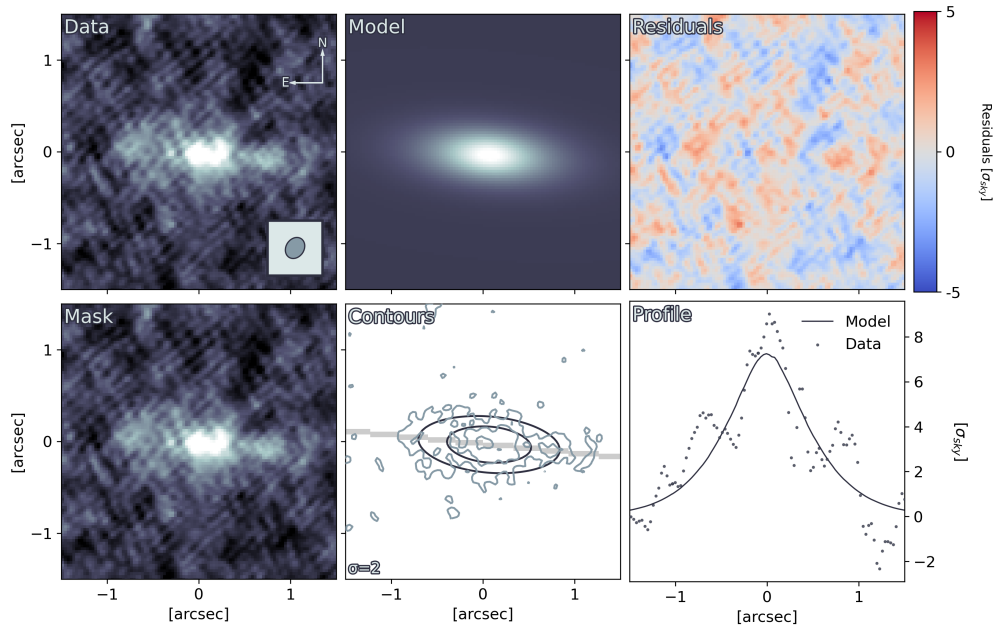


Figure C.100: The results of fitting the CO(3-2) ALMA map for source 26 with GALFIT. **Data**: A cutout of the source. The colour scale for the *Data*, *Model* and *Mask* panels are defined from this map, using a linear scale. The direction towards celestial north and east are displayed by the arrows. The FWHM of the synthetic beam is displayed in the inset on the lower right. **Mask**: Masked out sources and dead pixels are displayed in red. **Model**: The fitted model convolved with the PSF. **Contours**: Contours of the *Data* panel in blue. Contours of the *Model* panel in black. Contour levels start at the value annotated in the bottom left, and increase by a factor of two for each subsequent level. The shaded region indicates where the 1D profile was extracted from. **Residuals**: The *Data* subtracted by the *Model*. **Profile**: A one-dimensional profile extracted along the semi-major axis of the *Model*.

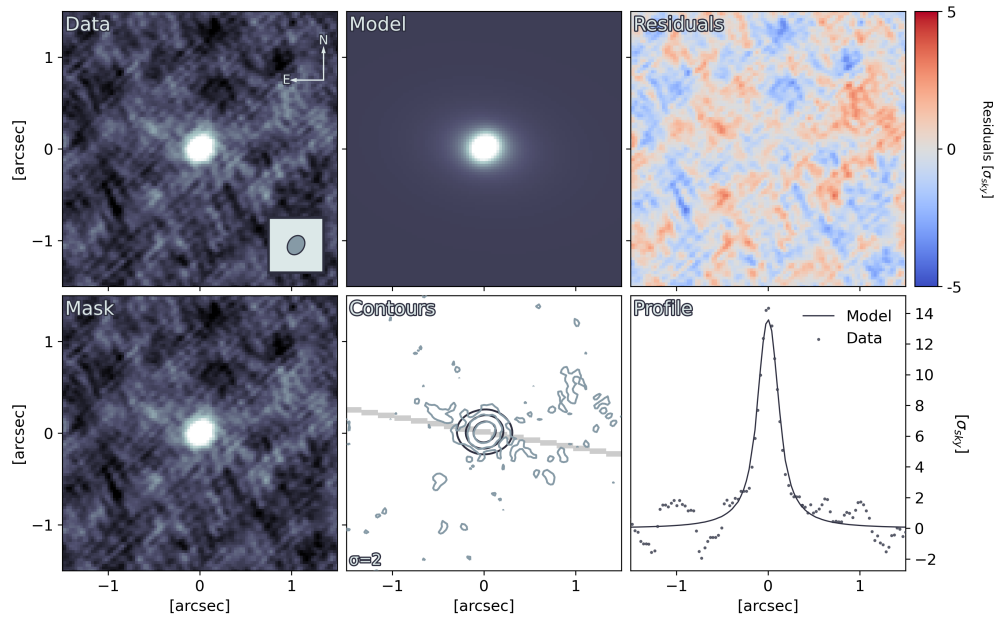


Figure C.101: The results of fitting the dust continuum ALMA map for source 26 with GALFIT. **Data**: A cutout of the source. The colour scale for the *Data*, *Model* and *Mask* panels are defined from this map, using a linear scale. The direction towards celestial north and east are displayed by the arrows. The FWHM of the synthetic beam is displayed in the inset on the lower right. **Mask**: Masked out sources and dead pixels are displayed in red. **Model**: The fitted model convolved with the PSF. **Contours**: Contours of the *Data* panel in blue. Contours of the *Model* panel in black. Contour levels start at the value annotated in the bottom left, and increase by a factor of two for each subsequent level. The shaded region indicates where the 1D profile was extracted from. **Residuals**: The *Data* subtracted by the *Model*. **Profile**: A one-dimensional profile extracted along the semi-major axis of the *Model*.

Source 27

Table C.23: Photometric data collected for source 27. The observation column lists the facility, instrument and filter used to make the observation. The code column connects the filter transmission curve with the correct one in Stardust. The reference column lists references to the works from which the observations were collected. Observations without an uncertainty corresponds to 3σ upper limits.

Observation	Flux [Jy]		Uncertainty [Jy]		Code	Reference
	Value	Order	Value	Order		
ALMA/1140um	1.650	10^{-3}	7.000	10^{-5}		Umehata et al. 2017
SPITZER/IRAC/8.0	1.230	10^{-5}	8.000	10^{-7}	21	Spitzer Science Center (SSC) and Infrared Science Archive (IRSA) 2021
SPITZER/IRAC/5.8	7.760	10^{-6}	4.400	10^{-7}	20	Spitzer Science Center (SSC) and Infrared Science Archive (IRSA) 2021
SPITZER/IRAC/4.5	6.770	10^{-6}	9.000	10^{-8}	19	Spitzer Science Center (SSC) and Infrared Science Archive (IRSA) 2021
SPITZER/IRAC/3.6	5.460	10^{-6}	6.000	10^{-8}	18	Spitzer Science Center (SSC) and Infrared Science Archive (IRSA) 2021
HST/wfc3/F160W	9.908	10^{-7}	1.091	10^{-6}	205	This work
HST/wfc3/F814W	1.086	10^{-7}	1.316	10^{-7}	217	This work

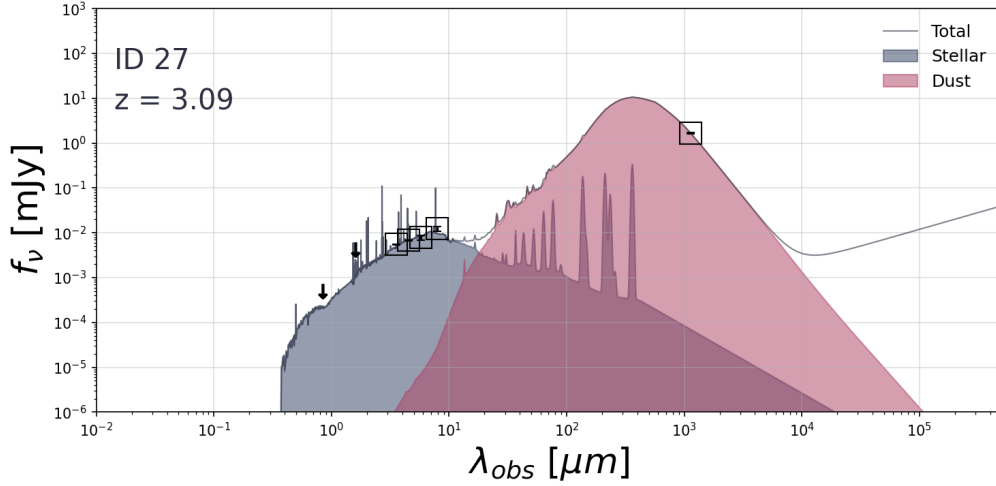


Figure C.102: The SED of source 24 as fitted with STARDUST, assuming that there's no significant AGN contribution. The squares are marked around observations with a SNR > 3. Arrows indicate 3σ upper limits of observations with SNR < 3 or non-detections.

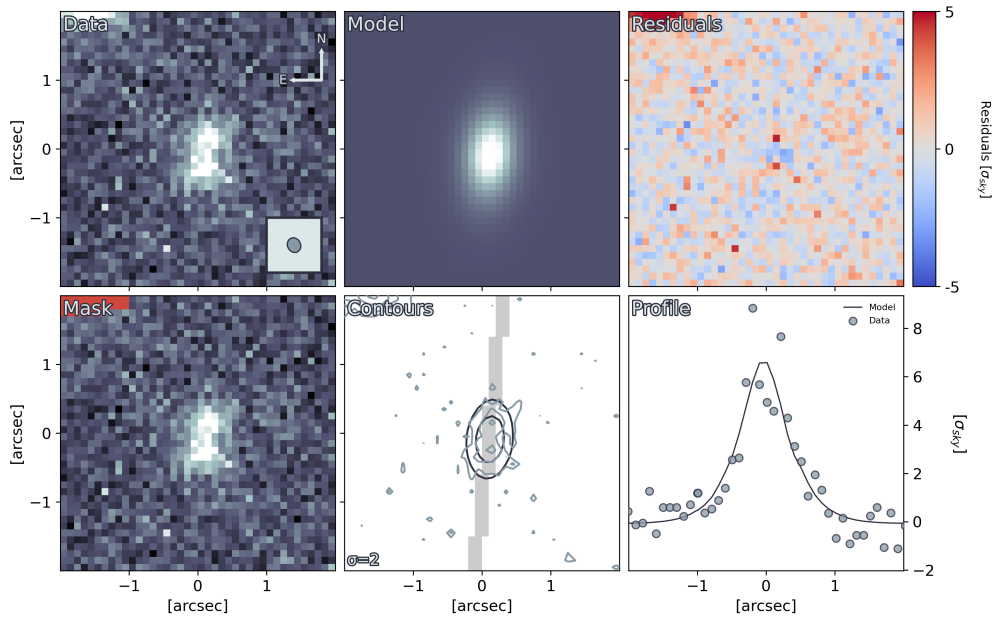


Figure C.103: The results of fitting source 27 with GALFIT. **Data**: A cutout of the source. The colour scale for the *Data*, *Model* and *Mask* panels are defined from this map, using a linear scale. The direction towards celestial north and east are displayed by the arrows. The fitted FWHM of the PSF is displayed in the inset in the bottom right. **Mask**: Masked out sources and dead pixels are displayed in red. **Model**: The fitted model convolved with the PSF. **Contours**: Contours of the *Data* panel in blue. Contours of the *Model* panel in black. Contour levels start at the value annotated in the bottom left, and increase by a factor of two for each subsequent level. The shaded region indicates where the 1D profile was extracted from. **Residuals**: The *Data* subtracted by the *Model*. **Profile**: A one-dimensional profile extracted along the semi-major axis of the *Model*.

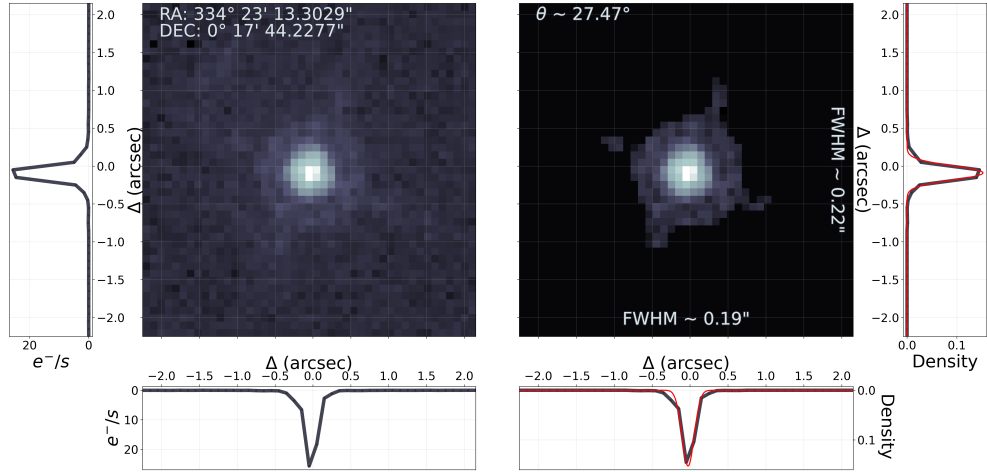


Figure C.104: From point-source to PSF. **Left:** The map displays the source used to create the PSF, for the mosaic containing source 27, in a logarithmic colour scale. The left and bottom panels shows the profile through the pixel of the highest value. The annotated coordinates are the coordinates of the centre of the map. **Right:** The map displays the PSF created from the left figure. The annotated FWHM along each axis are calculated by fitting a two-dimensional Gaussian to the map. The right and bottom panel shows the profile through the highest value pixel in black and the profile of the fitted two-dimensional Gaussian in red. The annotated angle describes the position angle of the fitted two-dimensional Gaussian counterclockwise from the positive x-axis.

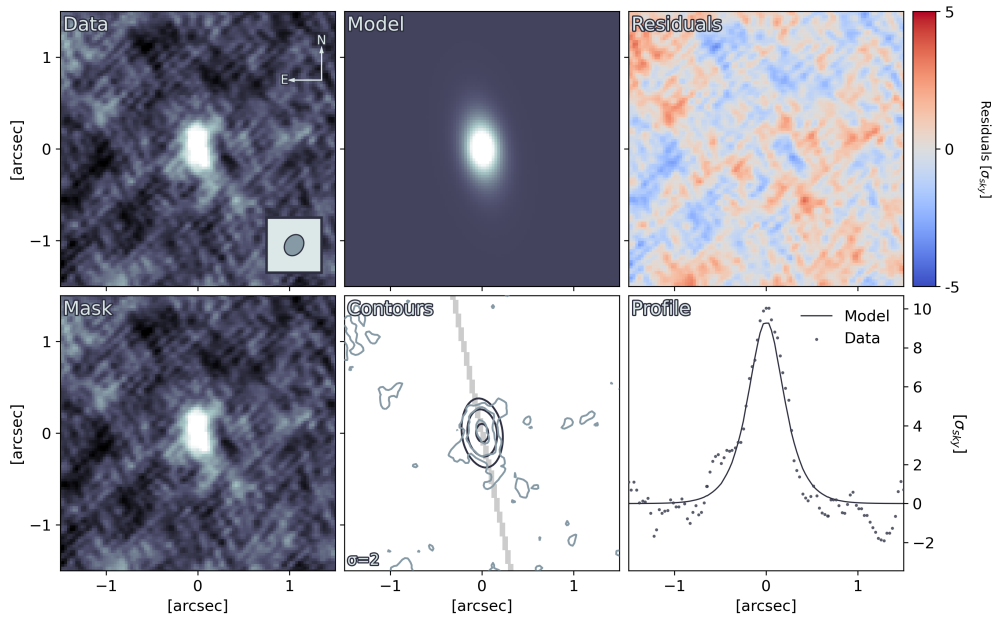


Figure C.105: The results of fitting the CO(3-2) ALMA map for source 27 with GALFIT. **Data:** A cutout of the source. The colour scale for the *Data*, *Model* and *Mask* panels are defined from this map, using a linear scale. The direction towards celestial north and east are displayed by the arrows. The FWHM of the synthetic beam is displayed in the inset on the lower right. **Mask:** Masked out sources and dead pixels are displayed in red. **Model:** The fitted model convolved with the PSF. **Contours:** Contours of the *Data* panel in blue. Contours of the *Model* panel in black. Contour levels start at the value annotated in the bottom left, and increase by a factor of two for each subsequent level. The shaded region indicates where the 1D profile was extracted from. **Residuals:** The *Data* subtracted by the *Model*. **Profile:** A one-dimensional profile extracted along the semi-major axis of the *Model*.

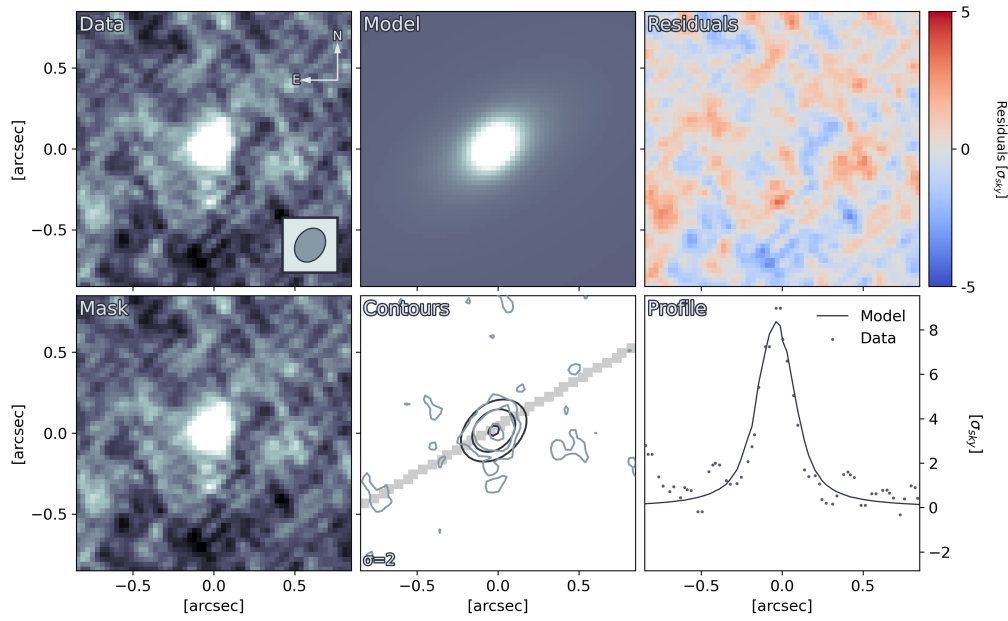


Figure C.106: The results of fitting the dust continuum ALMA map for source 27 with GALFIT. **Data**: A cutout of the source. The colour scale for the *Data*, *Model* and *Mask* panels are defined from this map, using a linear scale. The direction towards celestial north and east are displayed by the arrows. The FWHM of the synthetic beam is displayed in the inset on the lower right. **Mask**: Masked out sources and dead pixels are displayed in red. **Model**: The fitted model convolved with the PSF. **Contours**: Contours of the *Data* panel in blue. Contours of the *Model* panel in black. Contour levels start at the value annotated in the bottom left, and increase by a factor of two for each subsequent level. The shaded region indicates where the 1D profile was extracted from. **Residuals**: The *Data* subtracted by the *Model*. **Profile**: A one-dimensional profile extracted along the semi-major axis of the *Model*.

Source 28

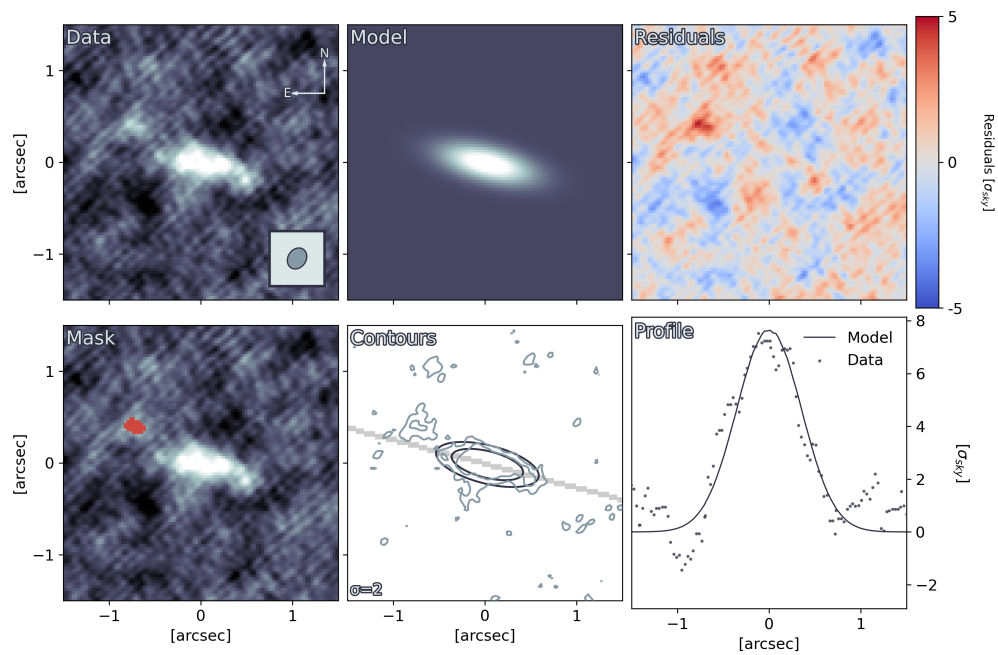


Figure C.107: The results of fitting the CO(3-2) ALMA map for source 28 with GALFIT. **Data**: A cutout of the source. The colour scale for the *Data*, *Model* and *Mask* panels are defined from this map, using a linear scale. The direction towards celestial north and east are displayed by the arrows. The FWHM of the synthetic beam is displayed in the inset on the lower right. **Mask**: Masked out sources and dead pixels are displayed in red. **Model**: The fitted model convolved with the PSF. **Contours**: Contours of the *Data* panel in blue. Contours of the *Model* panel in black. Contour levels start at the value annotated in the bottom left, and increase by a factor of two for each subsequent level. The shaded region indicates where the 1D profile was extracted from. **Residuals**: The *Data* subtracted by the *Model*. **Profile**: A one-dimensional profile extracted along the semi-major axis of the *Model*.

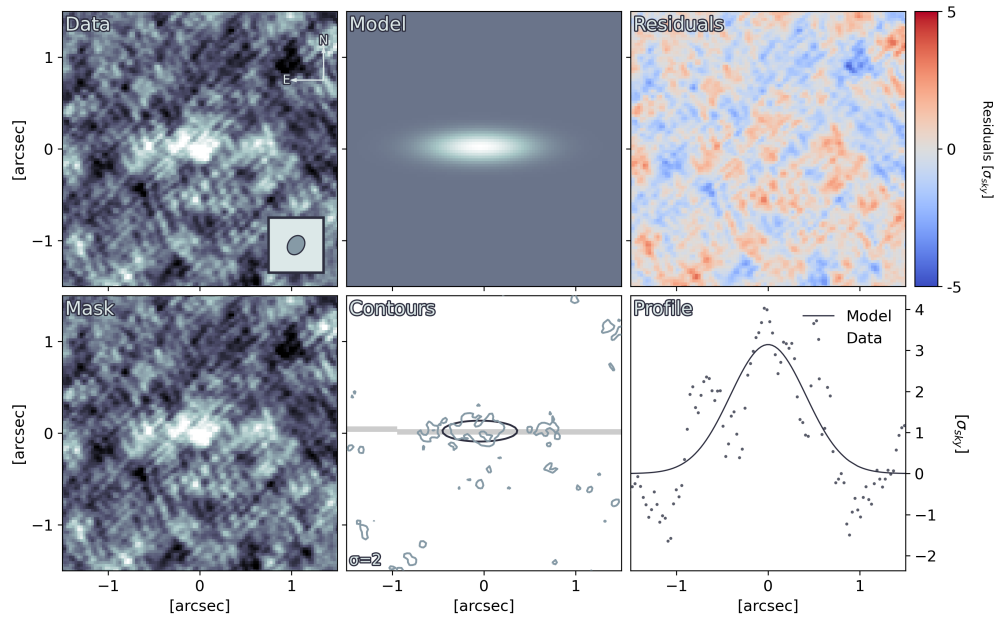


Figure C.108: The results of fitting the dust continuum ALMA map for source 28 with GALFIT. **Data**: A cutout of the source. The colour scale for the *Data*, *Model* and *Mask* panels are defined from this map, using a linear scale. The direction towards celestial north and east are displayed by the arrows. The FWHM of the synthetic beam is displayed in the inset on the lower right. **Mask**: Masked out sources and dead pixels are displayed in red. **Model**: The fitted model convolved with the PSF. **Contours**: Contours of the *Data* panel in blue. Contours of the *Model* panel in black. Contour levels start at the value annotated in the bottom left, and increase by a factor of two for each subsequent level. The shaded region indicates where the 1D profile was extracted from. **Residuals**: The *Data* subtracted by the *Model*. **Profile**: A one-dimensional profile extracted along the semi-major axis of the *Model*.

Source 29

Table C.24: Photometric data collected for source 29. The observation column lists the facility, instrument and filter used to make the observation. The code column connects the filter transmission curve with the correct one in Stardust. The reference column lists references to the works from which the observations were collected. Observations without an uncertainty corresponds to 3σ upper limits.

Observation	Flux [Jy]		Uncertainty [Jy]		Code	Reference
	Value	Order	Value	Order		
CFHT/MegaCam/u*	3.588	10^{-7}	9.609	10^{-9}	352	Weaver et al. 2022
CFHT/MegaCam/u	3.493	10^{-7}	1.416	10^{-8}	353	Weaver et al. 2022
Subaru/HSC/g	4.727	10^{-7}	1.270	10^{-8}	314	Weaver et al. 2022
Subaru/HSC/r	9.498	10^{-7}	1.647	10^{-8}	315	Weaver et al. 2022
Subaru/HSC/i	1.442	10^{-6}	1.865	10^{-8}	316	Weaver et al. 2022
Subaru/HSC/z	1.623	10^{-6}	2.534	10^{-8}	317	Weaver et al. 2022
Subaru/HSC/y	1.675	10^{-6}	3.859	10^{-8}	318	Weaver et al. 2022
VISTA/VIRCAM/Y	1.866	10^{-6}	9.064	10^{-8}	256	Weaver et al. 2022
VISTA/VIRCAM/J	2.504	10^{-6}	1.075	10^{-7}	257	Weaver et al. 2022
VISTA/VIRCAM/H	4.066	10^{-6}	1.602	10^{-7}	258	Weaver et al. 2022
VISTA/VIRCAM/Ks	5.155	10^{-6}	1.279	10^{-7}	259	Weaver et al. 2022
Subaru/Suprime-Cam/IB427	2.867	10^{-7}	6.621	10^{-8}	181	Weaver et al. 2022
Subaru/Suprime-Cam/IB464	3.961	10^{-7}	1.043	10^{-7}	183	Weaver et al. 2022
Subaru/Suprime-Cam/IA484	4.910	10^{-7}	4.473	10^{-8}	184	Weaver et al. 2022
Subaru/Suprime-Cam/IB505	4.653	10^{-7}	6.056	10^{-8}	185	Weaver et al. 2022
Subaru/Suprime-Cam/IA527	5.715	10^{-7}	4.830	10^{-8}	186	Weaver et al. 2022
Subaru/Suprime-Cam/IB574	6.732	10^{-7}	8.696	10^{-8}	188	Weaver et al. 2022
Subaru/Suprime-Cam/IA624	8.923	10^{-7}	4.912	10^{-8}	190	Weaver et al. 2022
Subaru/Suprime-Cam/IA679	1.189	10^{-6}	7.548	10^{-8}	192	Weaver et al. 2022
Subaru/Suprime-Cam/IB709	1.102	10^{-6}	7.320	10^{-8}	193	Weaver et al. 2022
Subaru/Suprime-Cam/IA738	1.362	10^{-6}	6.423	10^{-8}	194	Weaver et al. 2022
Subaru/Suprime-Cam/IA767	1.437	10^{-6}	1.005	10^{-7}	195	Weaver et al. 2022
Subaru/Suprime-Cam/IB827	1.623	10^{-6}	1.045	10^{-7}	197	Weaver et al. 2022
Subaru/Suprime-Cam/NB711	1.468	10^{-6}	1.071	10^{-7}	322	Weaver et al. 2022
Subaru/Suprime-Cam/NB816	1.415	10^{-6}	9.416	10^{-8}	319	Weaver et al. 2022
VISTA/VIRCAM/NB118	1.520	10^{-6}	5.985	10^{-7}	321	Weaver et al. 2022
Subaru/Suprime-Cam/B	4.159	10^{-7}	1.354	10^{-8}	114	Weaver et al. 2022
Subaru/Suprime-Cam/V	6.517	10^{-7}	2.725	10^{-8}	115	Weaver et al. 2022
Subaru/Suprime-Cam/r+	9.874	10^{-7}	2.207	10^{-8}	116	Weaver et al. 2022
Subaru/Suprime-Cam/i+	1.446	10^{-6}	2.877	10^{-8}	117	Weaver et al. 2022
Subaru/Suprime-Cam/z++	1.468	10^{-6}	1.325	10^{-7}	118	Weaver et al. 2022
Spitzer/IRAC/ch1	9.335	10^{-6}	1.648	10^{-8}	18	Weaver et al. 2022
Spitzer/IRAC/ch2	1.350	10^{-5}	1.004	10^{-7}	19	Weaver et al. 2022
GALEX/GALEX/NUV	3.244	10^{-7}	7.990	10^{-8}	121	Weaver et al. 2022
SPITZER/MIPS/24	8.167	10^{-5}	1.313	10^{-5}	325	Jin et al. 2018
JCMT/SCUBA2/850GHz	5.419	10^{-3}	1.392	10^{-3}	324	Jin et al. 2018
VLA/3GHz	1.900	10^{-5}	2.400	10^{-6}		Jin et al. 2018
VLA/1.5GHz	2.945	10^{-5}	1.330	10^{-5}		Jin et al. 2018
Meerkat/1.3GHz	1.430	10^{-4}				Jin et al. 2018
Herschel/PACS/100	1.828	10^{-3}	1.680	10^{-3}	329	Liu et al. 2019
Herschel/PACS/160	1.126	10^{-2}	3.352	10^{-3}	330	Liu et al. 2019
Herschel/SPIRE/250	2.532	10^{-2}	2.456	10^{-3}	331	Liu et al. 2019

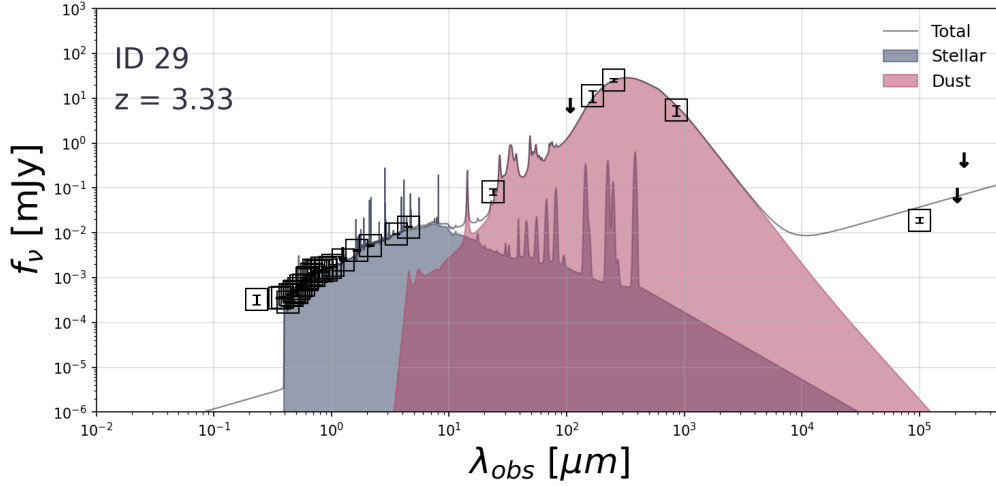


Figure C.109: The SED of source 29 as fitted with STARDUST, assuming that there's no significant AGN contribution. The squares are marked around observations with a SNR > 3. Arrows indicate 3σ upper limits of observations with SNR < 3 or non-detections.

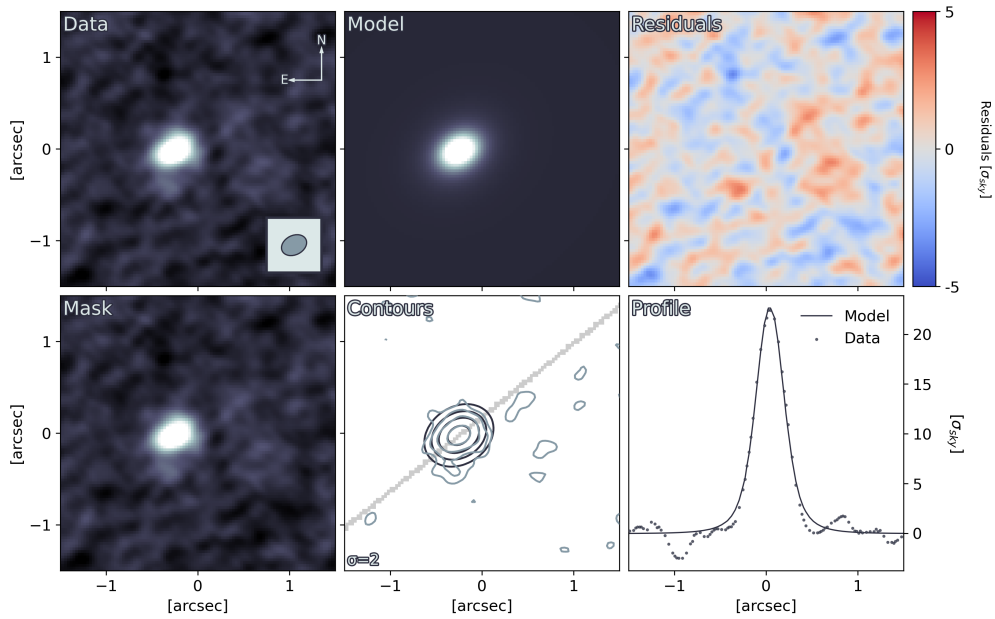


Figure C.110: The results of fitting the CO(5-4) ALMA map for source 29 with GALFIT. **Data**: A cutout of the source. The colour scale for the *Data*, *Model* and *Mask* panels are defined from this map, using a linear scale. The direction towards celestial north and east are displayed by the arrows. The FWHM of the synthetic beam is displayed in the inset on the lower right. **Mask**: Masked out sources and dead pixels are displayed in red. **Model**: The fitted model convolved with the PSF. **Contours**: Contours of the *Data* panel in blue. Contours of the *Model* panel in black. Contour levels start at the value annotated in the bottom left, and increase by a factor of two for each subsequent level. The shaded region indicates where the 1D profile was extracted from. **Residuals**: The *Data* subtracted by the *Model*. **Profile**: A one-dimensional profile extracted along the semi-major axis of the *Model*.

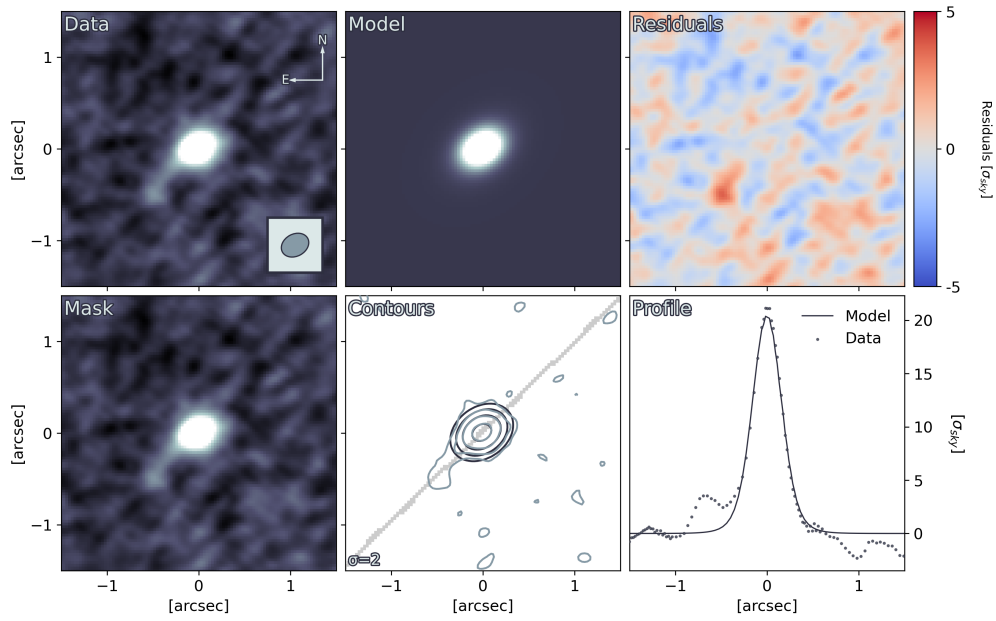


Figure C.111: The results of fitting the dust continuum ALMA map for source 29 with GALFIT. **Data**: A cutout of the source. The colour scale for the *Data*, *Model* and *Mask* panels are defined from this map, using a linear scale. The direction towards celestial north and east are displayed by the arrows. The FWHM of the synthetic beam is displayed in the inset on the lower right. **Mask**: Masked out sources and dead pixels are displayed in red. **Model**: The fitted model convolved with the PSF. **Contours**: Contours of the *Data* panel in blue. Contours of the *Model* panel in black. Contour levels start at the value annotated in the bottom left, and increase by a factor of two for each subsequent level. The shaded region indicates where the 1D profile was extracted from. **Residuals**: The *Data* subtracted by the *Model*. **Profile**: A one-dimensional profile extracted along the semi-major axis of the *Model*.

Source 30

Table C.25: Photometric data collected for source 30. The observation column lists the facility, instrument and filter used to make the observation. The code column connects the filter transmission curve with the correct one in Stardust. The reference column lists references to the works from which the observations were collected. Observations without an uncertainty corresponds to 3σ upper limits.

Observation	Flux [Jy]		Uncertainty [Jy]		Code	Reference
	Value	Order	Value	Order		
CFHT/MegaCam/u*	1.377	10^{-8}	8.815	10^{-9}	352	Weaver et al. 2022
CFHT/MegaCam/u	1.952	10^{-8}	1.371	10^{-8}	353	Weaver et al. 2022
Subaru/HSC/g	4.309	10^{-7}	1.079	10^{-8}	314	Weaver et al. 2022
Subaru/HSC/r	8.118	10^{-7}	1.399	10^{-8}	315	Weaver et al. 2022
Subaru/HSC/i	1.028	10^{-6}	1.489	10^{-8}	316	Weaver et al. 2022
Subaru/HSC/z	1.109	10^{-6}	2.004	10^{-8}	317	Weaver et al. 2022
Subaru/HSC/y	1.126	10^{-6}	3.211	10^{-8}	318	Weaver et al. 2022
VISTA/VIRCAM/Y	9.520	10^{-7}	1.121	10^{-7}	256	Weaver et al. 2022
VISTA/VIRCAM/J	1.411	10^{-6}	1.317	10^{-7}	257	Weaver et al. 2022
VISTA/VIRCAM/H	2.694	10^{-6}	1.858	10^{-7}	258	Weaver et al. 2022
VISTA/VIRCAM/Ks	3.806	10^{-6}	1.179	10^{-7}	259	Weaver et al. 2022
Subaru/Suprime-Cam/IB427	2.744	10^{-7}	6.149	10^{-8}	181	Weaver et al. 2022
Subaru/Suprime-Cam/IB464	3.740	10^{-7}	1.018	10^{-7}	183	Weaver et al. 2022
Subaru/Suprime-Cam/IA484	4.735	10^{-7}	5.148	10^{-8}	184	Weaver et al. 2022
Subaru/Suprime-Cam/IB505	4.155	10^{-7}	5.743	10^{-8}	185	Weaver et al. 2022
Subaru/Suprime-Cam/IA527	5.530	10^{-7}	5.512	10^{-8}	186	Weaver et al. 2022
Subaru/Suprime-Cam/IB574	6.969	10^{-7}	8.799	10^{-8}	188	Weaver et al. 2022
Subaru/Suprime-Cam/IA624	8.384	10^{-7}	4.432	10^{-8}	190	Weaver et al. 2022
Subaru/Suprime-Cam/IA679	8.685	10^{-7}	7.796	10^{-8}	192	Weaver et al. 2022
Subaru/Suprime-Cam/IB709	9.372	10^{-7}	7.436	10^{-8}	193	Weaver et al. 2022
Subaru/Suprime-Cam/IA738	1.005	10^{-6}	6.381	10^{-8}	194	Weaver et al. 2022
Subaru/Suprime-Cam/IA767	1.040	10^{-6}	9.757	10^{-8}	195	Weaver et al. 2022
Subaru/Suprime-Cam/IB827	9.035	10^{-7}	9.998	10^{-8}	197	Weaver et al. 2022
Subaru/Suprime-Cam/NB711	8.728	10^{-7}	1.034	10^{-7}	322	Weaver et al. 2022
Subaru/Suprime-Cam/NB816	1.078	10^{-6}	8.815	10^{-8}	319	Weaver et al. 2022
Subaru/Suprime-Cam/B	2.812	10^{-7}	1.159	10^{-8}	114	Weaver et al. 2022
Subaru/Suprime-Cam/V	6.884	10^{-7}	2.521	10^{-8}	115	Weaver et al. 2022
Subaru/Suprime-Cam/r+	8.308	10^{-7}	2.154	10^{-8}	116	Weaver et al. 2022
Subaru/Suprime-Cam/i+	1.049	10^{-6}	2.586	10^{-8}	117	Weaver et al. 2022
Subaru/Suprime-Cam/z++	1.078	10^{-6}	1.336	10^{-7}	118	Weaver et al. 2022
Spitzer/IRAC/ch1	6.790	10^{-6}	2.202	10^{-8}	18	Weaver et al. 2022
Spitzer/IRAC/ch2	1.100	10^{-5}	2.032	10^{-8}	19	Weaver et al. 2022
SPITZER/MIPS/24	2.852	10^{-4}	4.161	10^{-5}	325	Jin et al. 2018
JCMT/SCUBA2/850GHz	4.340	10^{-3}	8.235	10^{-4}	324	Jin et al. 2018
VLA/3GHz	3.410	10^{-5}	2.900	10^{-6}		Jin et al. 2018
VLA/1.5GHz	4.276	10^{-5}	1.680	10^{-5}		Jin et al. 2018
Meerkat/1.3GHz	2.276	10^{-4}				Jin et al. 2018
Herschel/PACS/100	1.579	10^{-3}	2.590	10^{-3}	329	Liu et al. 2019
Herschel/PACS/160	2.969	10^{-2}	4.544	10^{-3}	330	Liu et al. 2019
Herschel/SPIRE/250	3.268	10^{-2}	1.528	10^{-3}	331	Liu et al. 2019

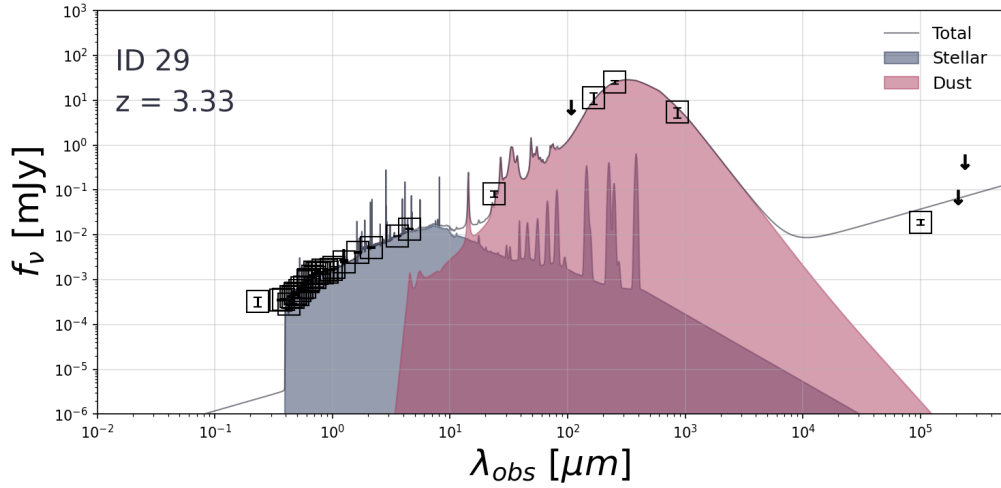


Figure C.112: The SED of source 29 as fitted with STARDUST, assuming that there's no significant AGN contribution. The squares are marked around observations with a SNR > 3. Arrows indicate 3σ upper limits of observations with SNR < 3 or non-detections.

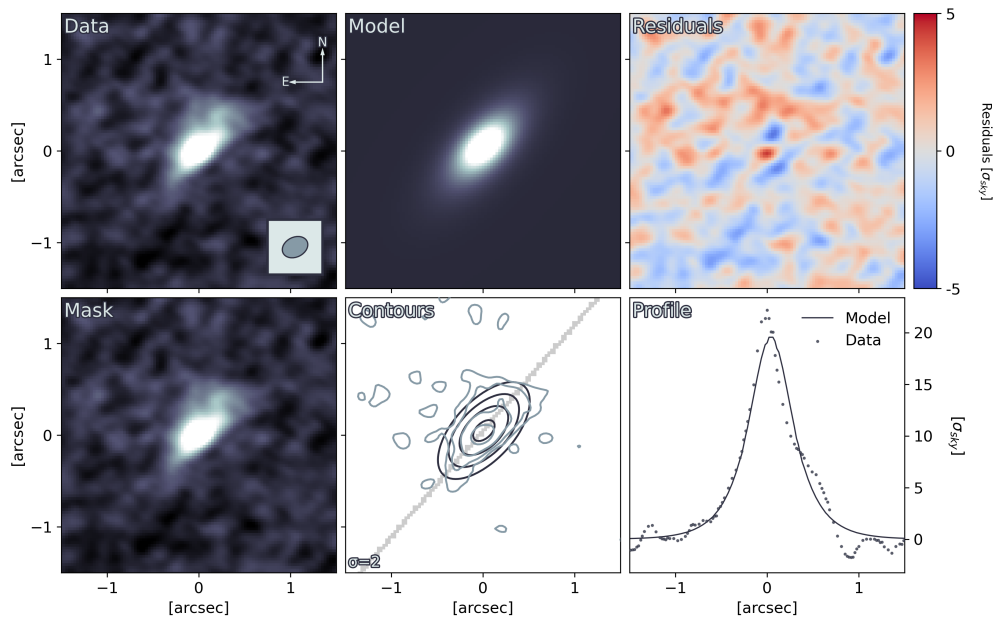


Figure C.113: The results of fitting the CO(5-4) ALMA map for source 30 with GALFIT. **Data**: A cutout of the source. The colour scale for the *Data*, *Model* and *Mask* panels are defined from this map, using a linear scale. The direction towards celestial north and east are displayed by the arrows. The FWHM of the synthetic beam is displayed in the inset on the lower right. **Mask**: Masked out sources and dead pixels are displayed in red. **Model**: The fitted model convolved with the PSF. **Contours**: Contours of the *Data* panel in blue. Contours of the *Model* panel in black. Contour levels start at the value annotated in the bottom left, and increase by a factor of two for each subsequent level. The shaded region indicates where the 1D profile was extracted from. **Residuals**: The *Data* subtracted by the *Model*. **Profile**: A one-dimensional profile extracted along the semi-major axis of the *Model*.

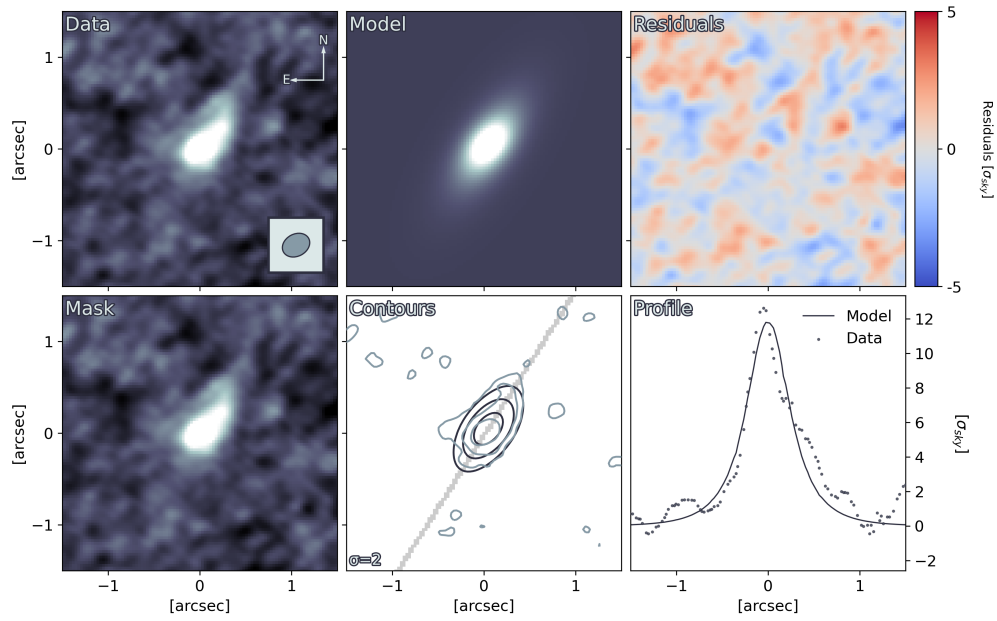


Figure C.114: The results of fitting the dust continuum ALMA map for source 30 with GALFIT. **Data**: A cutout of the source. The colour scale for the *Data*, *Model* and *Mask* panels are defined from this map, using a linear scale. The direction towards celestial north and east are displayed by the arrows. The FWHM of the synthetic beam is displayed in the inset on the lower right. **Mask**: Masked out sources and dead pixels are displayed in red. **Model**: The fitted model convolved with the PSF. **Contours**: Contours of the *Data* panel in blue. Contours of the *Model* panel in black. Contour levels start at the value annotated in the bottom left, and increase by a factor of two for each subsequent level. The shaded region indicates where the 1D profile was extracted from. **Residuals**: The *Data* subtracted by the *Model*. **Profile**: A one-dimensional profile extracted along the semi-major axis of the *Model*.

D Statistical Analyses

D.1 Spearman's Rank Order Correlation

In the discussion section of this thesis, we compare different fitted variables for our entire sample. Additionally, we want to calculate whether there's a statistical significant relation between those variables. For that purpose, we apply Spearman's rank order correlation.

Spearman's rank order correlation is a non-parametric version of the Pearson Product-Moment Correlation. It measures how well the relationship between two variables can be described by a monotonic function. A monotonic function is a function for which the increase in one variable will always result in either an increase or decrease in the other variable. Essentially, the function is either entirely increasing or decreasing. Consequently, Spearman's rank order correlation essentially measures the association between the paired variables.

The correlation, ρ , between two variables, X and Y , is calculated by first ranking the data independently for each variable. Each of the N data points are ranked from 1 (highest) to N (lowest) in each variable. We represent the ranking algorithm with an R . For example,

$$R([10, 30, 50, 20, 40]) = [5, 3, 1, 4, 2] \quad (\text{D.1})$$

The rank order correlation between the two variables are then given by,

$$\rho = \frac{\text{cov}(R(X), R(Y))}{\sigma_{R(X)}\sigma_{R(Y)}}, \quad (\text{D.2})$$

where $\sigma_{R(K)}$ is the standard deviation of the ranking of the K^{th} variable. Additionally, the covariance is calculated in the following way for two variables I and J ,

$$\text{cov}(I, J) = \frac{1}{N-1} \sum_i^N (I_i - \mu_I) \cdot (J_i - \mu_J), \quad (\text{D.3})$$

where i represents the i^{th} pair of data points and μ_K represents the mean of the K^{th} variable. The rank order correlation takes on a range of values $\rho \in [-1, 1]$. A value close to zero indicates no monotonic association between the variables. Additionally, a positive value indicates a positive monotonic association while a negative value indicates a negative monotonic association. Moreover, we adopt the following interpretation of the rank order correlation,

- Very weak correlation: $0 \leq |\rho| < 0.2$
- Weak correlation: $0.2 < |\rho| < 0.4$
- Moderate correlation: $0.4 < |\rho| < 0.6$
- Strong correlation: $0.6 < |\rho| < 0.8$
- Very strong correlation: $0.8 < |\rho| \leq 1$

The rank order correlation is accompanied by a p-value, which roughly describes the probability of an uncorrelated dataset having a rank order correlation at least as extreme as the one calculated from the dataset. The p-value is calculated from the t-distributed statistic,

$$t = \rho \sqrt{\frac{\nu}{1 - \rho^2}}, \quad (\text{D.4})$$

by integrating from the calculated rank order correlation to infinity. In the above equation, $\nu = N - 2$, is the degree of freedom.

D.2 Monte Carlo Method

In this thesis, we use the MC method to estimate how uncertainties propagate through a non-trivial operation. For example, we use it to investigate how the choice of PSF affects the uncertainties of the parameters recovered from fitting the surface brightness profile with GALFIT. Additionally, we will be using it to estimate the uncertainty of the median of an uncertain variable in chapter 4.

In short, the MC method estimates the output distribution by randomly sampling the input variable, assuming a Normal distribution centred on the actual variable of the input variable. The standard deviation of that Normal distribution is then set to reflect the uncertainty of the variable. By iteratively sampling the input space and calculating the output, we build an output distribution of variables.

The uncertainty on the output variable can then be calculated by finding the upper and lower limit of the output distribution, as defined by the 84th and 16th percentile respectively.

University of Copenhagen
Faculty of Science
Niels Bohr Institute

Jagtvej 155A
2200 København

<https://nbi.ku.dk/>